EXPERIMENTAL AND NUMERICAL STUDY ON THE EXTREME BEHAVIORS OF SLIDING ISOLATION BEARINGS

EXPERIMENTAL AND NUMERICAL STUDY ON THE EXTREME BEHAVIORS OF SLIDING ISOLATION BEARINGS

BY

Yu Bao

B.Eng., M.Sc. (Huazhong University of Science and Technology)

A Thesis Submitted to the School of Graduate Studies in Partial Fulfilment of the Requirements for the Degree of Doctor of Philosophy

Doctor of Philosophy (2017)   McMaster University

(Civil Engineering)   Hamilton, Ontario

TITLE: Experimental and Numerical Study on the Extreme

                        Behaviors of Sliding Isolation Bearings

AUTHOR: Yu Bao

                        B.Eng. (Civil Engineering)

                        M.Sc. (Structural Engineering)

                        Huazhong University of Science and Technology, China

SUPERVISOR: Dr. Tracy C. Becker

NUMBER OF PAGES: xx, 237

To My Beloved Parents…

谨以此献给我的父亲和母亲

Abstract

Sliding isolation bearings are used widely around the world to minimize damage to structures and their contents during earthquakes. Past studies have typically focused on the behavior of sliding isolation bearing under design conditions; however, as the performance-based earthquake engineering advances, it is necessary and critical to understand the ultimate or even failure behavior, of structural systems under extreme conditions. Using a double friction pendulum bearing with non-articulated slider as an example, this thesis comprehensively investigates the extreme behavior of the sliding bearing components as well as steel frame buildings isolated using these bearings.

This thesis is comprised of two major parts. The first includes numerical and experimental studies of double friction pendulum bearings at the component-level. Finite element investigation shows that depending on the superstructure mass there are two major failure modes for the double friction pendulum bearings. When the superstructure mass is sufficiently large, the failure mode is dominated by the restraining rim yielding; however, when the mass is relatively small, its failure mode shifts to bearing uplift. A simplified analytical model which can directly simulate the impact and uplift behavior of double friction pendulum bearing is also implemented, comparing well to the finite element analysis. Then, to validate the ability of the models to predict extreme behavior as well as to investigate the effect of the restraining rim design, which varies around the world, an experimental study was carried out. Uplift behavior and significant rim yielding were observed during the shake table tests. Moreover, other response parameters, including uplift and shear forces, are evaluated and compared among different rim

designs. It is found the restraining rim design has a substantial influence on the bearing's extreme behavior.

The second part of the thesis investigates the system-level behavior of steel frame buildings isolated with double friction pendulum bearings. It is found that the stiffness of the superstructure largely dictates the system-level failure modes and collapse probability. Initially, bearings with rigid restraining rims are investigated. For flexible moment-resisting frames, the system-level failure modes are mixed: both the bearing uplift and superstructure yielding contribute; also, using current code-minimum design results in acceptably low probability of collapse. However, for stiff concentrically-braced frames, the impact force can impose large ductility demands on the superstructure regardless of its strength. As a result, the system-level failure comes exclusively from superstructure yielding, and only by increasing bearing's displacement capacity beyond the minimum code allowed can the design meet as acceptably low collapse probability. When flat rims are used instead for the bearing design, the failure modes for both building types are exclusively bearing failure. Furthermore, while it is more apparent for concentrically-braced frames, using flat rims for the bearings can reduce the collapse probability compared to using rigid rims.

Acknowledgements

First of all, I would like to take this opportunity to give my sincerest gratitude to my advisor, Dr. Tracy Becker, for her truly amazing and exceptional guidance throughout my PhD study at McMaster University. I really appreciate every productive discussion and constructive suggestion during my weekly meeting with her. Her passion and enthusiasm always inspire me to achieve more on my research and help me discover my real potential. Without her dedication and support, my study at McMaster University would not have been so joyful and successful. Her contributions go beyond her academic role and for which I will be grateful for all my life.

Secondly, I want to thank my supervisory committee members, Drs. Michael Tait and Stan Pietruszczak, for their insightful and invaluable comments and advice on my research work. Their encouragement and guidance are greatly appreciated.

I am also truly grateful for those who helped me during my experimental study, including undergraduate students Ridhwan Khan and Griffin Dow. Special thanks must be given to our technicians of the Applied Dynamics Laboratory (ADL): Kent Wheeler, Paul Heerema and Peter Koudys. My experimental study would have been impossible without their professional supports.

Then I would like to thank all my friends and colleagues during my stay at McMaster University, as well as all the professors who greatly expanded my knowledge, including Drs. Lydell Wiebe, Dimitrios Konstantinidis, Michael Tait and Ghani Razaqpur.

Lastly and most importantly, I am deeply indebted to my parents who never waive their support of me.

Table of Contents

List of Figures

List of Tables

Co-Authorship

This thesis has been prepared in accordance with the regulations for a "sandwich thesis" format as stipulated by the School of Graduate Studies at McMaster University. The thesis has been co-authored as:

Chapter 2: Failure of double friction pendulum bearings under pulse-type motions

Authors: Yu Bao, Tracy C. Becker and Hiroki Hamaguci

The numerical model was implemented by Yu Bao and the numerical analyses were conducted by Yu Bao, both under the supervision of Dr. Tracy Becker. The manuscript was written by Yu Bao and modifications were completed by Dr. Tracy Becker and Mr. Hiroki Hamaguchi.

This paper has been published in *Earthquake Engineering and Structural Dynamics* (Vol. 46, Issue 5, Pages: 715-732).

Chapter 3: Experimental study of the effect of restraining rim design on the extreme behavior of friction pendulum bearings

Authors: Yu Bao, Tracy C. Becker, Takayuki Sone and Hiroki Hamaguchi

The experimental study and data analyses were carried out by Yu Bao under the supervision of Dr. Tracy Becker. The isolation bearing design was conducted by Mr. Takayuki Sone. The manuscript was written by Yu Bao, modifications and suggestions were contributed from Dr. Tracy Becker, Mr. Takayuki Sone and Mr. Hiroki Hamaguchi.

This paper has been published in *Earthquake Engineering and Structural Dynamics*, available online. DOI:10.1002/eqe.2997.

Chapter 4: State-space formulation of a two-dimensional Euler-Bernoulli beam element for the simulation of steel frames

Authors: Yu Bao and Tracy C.Becker

The formulation of the element was developed by Yu Bao. The manuscript was written by Yu Bao under the supervision of Dr. Tracy Becker. Editorial suggestions and revisions were provided by Dr. Tracy Becker.

This paper will be submitted to an international journal for review and possible publication.

Chapter 5: Effect of design methodology on the collapse of friction pendulum isolated moment-resisting and concentrically-braced frames

Authors: Yu Bao and Tracy C. Becker

The numerical model and analyses for the isolated frames were performed by Yu Bao under the supervision of Dr. Tracy Becker. The manuscript was written by Yu Bao and modifications were completed by Dr. Tracy Becker.

This paper has been submitted to *Journal of Structural Engineering (ASCE)* for review and possible publication.

Chapter 6: To limit forces or displacements: comparative study of steel frames isolated by sliding bearings with and without restraining rims

Authors: Yu Bao, Tracy C. Becker, Takayuki Sone and Hiroki Hamaguchi

The design of isolated frames was provided by Yu Bao. The numerical model and analyses were performed by Yu Bao, the manuscript was written by Yu Bao as well, both

under the supervision of Dr. Tracy Becker. Modifications to the manuscript were provided by Dr. Tracy Becker and Mr. Takayuki Sone and Mr. Hiroki Hamaguchi.

This paper has been submitted to *Soil Dynamics and Earthquake Engineering* for review and possible publication.

Appendix: Extreme behavior in a triple friction pendulum isolated frame

Authors: Tracy C. Becker, Yu Bao and Stephen A. Mahin

The experimental study was carried out by Drs. Tracy Becker and Stephen Mahin at University of California, Berkeley. The numerical model was implemented by Yu Bao and numerical analyses were conducted by Yu Bao, both under the supervision of Dr. Tracy Becker. The manuscript was written by Dr. Tracy Becker and modifications were completed by Yu Bao and Dr. Stephen Mahin.

This paper has been published in *Earthquake Engineering and Structural Dynamics*, 2017, 46(15): 2683-2698.

Chapter 1 Introduction

1.1 Background

Seismic isolation is a novel design strategy that can provide enhanced seismic performance and mitigate the potential seismic losses. The idea of seismic isolation is to use horizontally flexible and vertically stiff devices to uncouple the structure from the horizontal ground motion, thereby protecting both the structural and non-structural components from damage. The beneficial effects of seismic isolation may be explained from the response spectrum: by elongating the natural period of isolated structures, the maximum base shear can be significantly reduced, as shown in the left side of Figure 1-1. Although the concept of seismic isolation can be dated back around 100 years ago (Bechtold 1907), only in the past three decades have seismically isolated structures been widely adopted. In this time, several constructed isolated structures have been subjected to real earthquakes and recorded data has demonstrated the superior performance of isolated structures compared to fixed base structures. For example, Tohoku University located in Sendai Japan during an earthquake in 1987 had a maximum ground acceleration of 0.04 g, the recorded maximum roof acceleration of isolated structure was only 0.04 g while the adjacent fixed-base structure had a value as large as 0.27 g. A Coal Storage Silo located in Takenaka Technical Research Laboratory during the 1985 earthquake had the similar observation; the recorded maximum ground acceleration was

0.09 *g*, the fixed-base structure had a recorded maximum roof acceleration of 0.16 *g*, however, the isolated structure only experienced 0.05 *g*. (Buckle and Mayes 1990).

Researchers have tended to compare the seismic performance between isolated and fixed-base structures under design level ground motions (e.g. Erduran et al. 2011; Ordonez et al. 2003; Sayani et al. 2011; Shenton and Lin 1993; Su and Ahmadi 1989; Su and Ahmadi 1990). However, as performance-based earthquake engineering (PBEE) develops, more emphases have been focused on examining the seismic performance of structures under extreme conditions. For traditional fixed-base structures, in order to dissipate the energy and achieve the specific seismic performance objective, capacity design approach is usually adopted. The idea of capacity design is to select a ductile failure mechanism to limit the maximum forces in the seismic resisting system and detail this mechanism, so that the system can withstand inelastic deformations and other failure mechanisms which would result in non-ductile behavior are avoided. One prominent example of capacity design is the so-called 'strong column-weak beam' mechanism when designing moment resisting frames. Compared to 'weak column-strong beam' mechanism, the preferred 'strong column-weak beam' mechanism can undergo larger inelastic deformations and dissipate more energy before collapse occurs. For traditional fixed-base structures, seismic design codes specify the desired inelastic mechanism for different types of structures and provide associated detailing requirements to achieve this mechanism. For isolated structures, however, current seismic design codes do not provide any guidelines for capacity design. Rather, they focus separately on the isolation bearings and the superstructure, limiting failure in each while ignoring their interaction.

As isolated structures have elongated natural periods, consequently, large horizontal displacements at the isolation level are expected, as shown in the right side of Figure 1-1. Excessive horizontal displacements can be detrimental to the integrity of isolated structures. They can cause pounding of isolated structures with adjacent structures or its surrounding moat wall, or direct failure of the isolation devices. The general effects of pounding of isolated buildings with adjacent buildings have been examined by Komodromos et al. (2007) and Matsagar and Jangid (2003). Both studies conclude that impact force will increase floor accelerations and excite undesirable higher modes; however, these studies use simple lumped-mass models and assume elastic behavior of superstructure even after impact. Recently, the effects of pounding against the moat wall have been investigated both experimentally and numerically by Masroor and Mosqueda (2012, 2013 and 2015) and numerically by Qu et al. (2013). These studies include the inelastic behavior of superstructure and they found that moat-wall impact can induce yielding of superstructure and increase the collapse probability of isolated structures. However, no system-level studies have included modeling of the failure of the isolation bearings themselves.

There are two major categories of seismic isolation bearings: elastomeric bearings and sliding isolation bearings. There have been considerably more studies on elastomeric bearings (Kelly and Konstantinidis 2011); this includes the mechanical behavior of rubber bearings under compression, bending, or a combination of both, the buckling behavior of elastomeric bearings, cavitation, etc. Additionally, many studies, both numerical and experimental, have been conducted on the stability of elastomeric bearings

at component level (Buckle et al. 2002; Sanchez et al. 2013; Han and Warn 2014; Monzon et al. 2016). However, for friction pendulum bearings there have been very limited numbers of studies conducted to investigate their behavior under extreme conditions. As the two bearing types differ in design and material, their mechanics and the resulting failure modes are dissimilar. To the best of the author's knowledge, beyond to the work presented in this thesis, only Sarlis et al. (2013) has conducted dynamic tests to investigate the extreme behavior of triple friction pendulum isolators. However, in their study, the motions were moderately intensive so that only minor uplift of the isolation bearing was observed and the bearings did not fail.

As PBEE advances, the need to understand the extreme behavior and even the failure mechanisms of friction pendulum bearings and friction pendulum isolated systems is critical. Such knowledge will help structural engineers to understand the safety margin inherent in designs of isolated structures and allow for the minimization of collapse probabilities. To this end, this thesis attempts to provide a comprehensive study on the extreme behavior of friction pendulum bearings using both numerical and experimental studies. Furthermore, this thesis investigates the influence of design choices for both bearing and superstructure properties and how they affect the probability and mode of collapse. It is expected to provide insights for engineers to better design of structures isolated by these bearings.
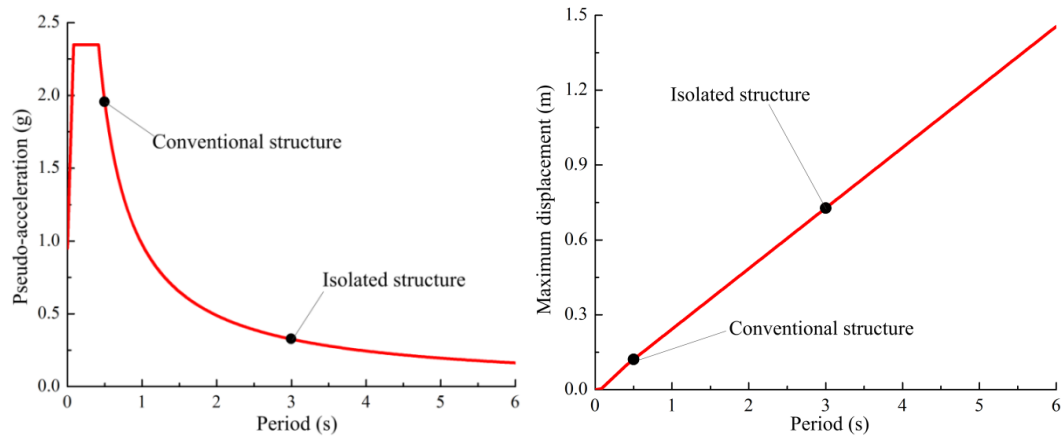
Figure 1-1: Response spectra of conventional and isolated structures

1.2 Friction pendulum bearings

Friction pendulum bearings, which usually consist of an inner slider and one or more concave plates, are shown from Figure 1-2 to Figure 1-4. Common designs include single friction pendulum bearings, double friction pendulum bearings, and triple friction pendulum bearings. The single friction pendulum bearing, as depicted in Figure 1-2, was first described by Zayas et al. (1987). It is comprised of a concave sliding plate which has a constant radius of curvature R and an articulated inner slider. Once the friction force is reached or exceeded, the inner slider starts to move on the concave surface. After the initiation of the sliding, the bearing has a tangent stiffness proportional to the inverse of the radius of the concave surface. This provides a bilinear hysteresis loop and the amplitude directly depends on the weight supported by the bearing, as a result the natural period of the single friction pendulum bearing is independent of the supported mass and it can be expressed as: $T = 2\pi\sqrt{R/g}$.

Similar to the single friction pendulum bearings, double friction pendulum bearings consist of two concave plates and an inner slider, as shown in Figure 1-3. For

the double friction pendulum bearings shown in Figure 1-3, there are two main types, the difference between which lies in the configuration of inner slider: the articulated inner slider is very common in the United States while the non-articulated inner slider is available in Japan. The mechanical behavior of double friction pendulum bearings with a non-articulated slider is identical to the single; with a bilinear hysteresis loop. It has an independent natural period $T = 2\pi\sqrt{2R/g}$ and an has a increased displacement capacity compared to a single pendulum bearing of similar diameter due to motion on the top and bottom plates (Fenz and Constantinou 2006).

The triple friction pendulum bearing (Figure 1-4) has more complicated behavior. Several studies have investigated this bearing both analytically and experimentally (Fenz and Constantinou 2008a; Fenz and Constatinou 2008b; Tsai et al. 2010; Becker and Mahin 2012). Compared to single and double friction pendulum bearings, the triple friction pendulum bearings can provide adaptive behavior with increased displacement due to the presence of multiple spherical concave surfaces. This feature may allow structural designer to achieve multiple seismic performance objectives (Morgan and Mahin 2010).

All the friction pendulum isolators shown in Figure 1-2 to Figure 1-4 have fully-connected restraining rims, which are representative of these bearings in the United States. These restraining rims aim to prevent the inner slider from moving beyond the concave plates when excessive horizontal displacement occurs. In the other regions of the world, different restraining rim designs are available. For example, in Europe the seismic design code explicitly prohibits the use of any restraining rim in an isolator (European

committee for standardization, 2009); instead a flat rim bearing is available, and as a result the potential impact force is eliminated. In Japan, however, both flat rim bearings and bearings with bolted rims are available. Since past studies on friction pendulum bearings rarely focus on extreme events, the effects of different restraining rim designs have been largely ignored. When examining the extreme behaviors of these isolation bearings, it is essential to consider the variation in rim designs.

This thesis utilizes the double friction pendulum bearing with the non-articulated slider, shown on the right side of Figure 1.3. This bearing is the only commercially available sliding isolation bearing in Japan. Considering that Japan has significantly more isolated structures compared to the rest of the world, this study bearing design is meaningful. Although the extreme behavior for friction pendulum bearings with other configurations are not studied, the general findings made in this thesis should be applicable.

Figure 1-2: Single friction pendulum bearing with articulated slider

Figure 1-3: Double friction pendulum bearing with different inner sliders (left: articulated slider; right: non-articulated slider)
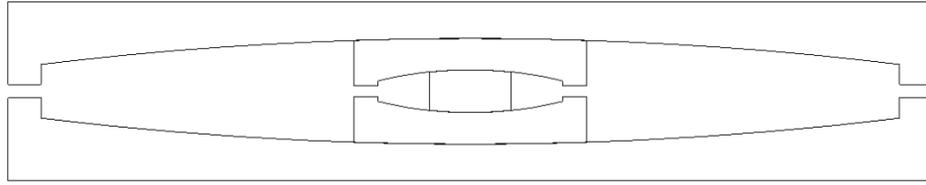
Figure 1-4: Triple friction pendulum bearing

1.3 Organization of the thesis

This dissertation is prepared in accordance with the regulation of a "sandwich" thesis format which includes previously published, submitted, or to-be-submitted journal papers. There are seven chapters in the thesis. Chapter 2 to Chapter 6 and the Appendix are prepared as standalone documents, each chapter has its own introduction, body, conclusion, and references. As a result, some overlaps may be observed between each chapter, especially in the introductions. The contributions of the author to each paper have been outlined at the beginning of each chapter.

This thesis can be roughly divided into two parts. Part I consists of Chapter 2 and 3, which systematically investigates the extreme behavior of double friction pendulum bearing when its physical displacement limit is reached or exceeded. This component-level study is the first step to fully understanding the extreme behavior of the sliding isolation bearings. Part II is comprised of Chapter 5, Chapter 6, and the Appendix, which present a system-level study of friction pendulum isolated buildings considering both the extreme behavior of isolation bearing as well as the degrading nonlinear behavior of the superstructure.

Chapter 2 presents a numerical study of double friction pendulum bearings subjected to both analytical Ricker pulses and pulse-like ground motions. This study is

motivated from the concerns that isolated structures are vulnerable to long-period content in pulse-like motions as they can impose large displacement demands in the isolators. At first, finite element analyses are conducted to study the failure modes of double friction pendulum bearings at the component level. It is found that, depending on the superstructure mass, failure modes can either be significant yielding of the restraining rim or the uplift of isolation bearing. Then, in order to perform parametric study, a rigid body model which can directly simulate the impact and uplift behavior of double friction pendulum bearings is implemented. Using this model, influences of different design parameters on the failure modes are examined.

Chapter 3 describes an experimental study on the extreme behavior of double friction pendulum bearings. There are two purposes in this study: 1) to verify the extreme behavior mechanisms of the double friction pendulum bearings predicted by the finite element analysis; and 2) to evaluate the accuracy of the developed numerical model (i.e. the rigid body model in Chapter 2) and identify possible drawbacks if using such numerical model in the system-level studies. In this experimental study four different restraining rim designs are considered and tested. These rim designs represent sliding isolation bearings available in Europe, Japan, and North America. Experimental observations made from two high speed cameras show that restraining rim designs have substantial effects on the extreme behavior of sliding isolation bearings. Uplift and rim yielding were observed during the shake table test. Key response parameters, including horizontal and vertical displacement, peak shear force, floor response spectra are also evaluated and compared between different isolation bearings.

The rigid body model used in Chapter 2 is implemented in the state-space form. In order to perform a system-level study that includes the nonlinear behavior of the superstructure, Chapter 4 reports the formulation of a two-dimensional Euler-Bernoulli beam element in the state-space form. The developed beam element can explicitly incorporate the strength and stiffness degradation, second-order effects and internal force interaction. As a result, this element is used extensively for the numerical simulation together with the rigid body model of sliding isolation bearing. As shown in this chapter, this element can simulate the flexural behavior of moment-resisting frames quite well and it can also be adopted to simulate the inelastic buckling behavior of concentrically-braced frames with reasonable accuracy.

Chapter 5 presents a system-level study of moment-resisting and concentrically-braced frames isolated with double friction pendulum bearings. The two-dimensional Euler-Bernoulli beam element developed in Chapter 4 is used to model the superstructure and isolation bearings are represented by the rigid body models. As a result, this study is more comprehensive due to the inclusion of possible uplift failure of the isolation bearing. Fourteen pairs of near-fault pulse-like ground motions and the methodology recommended by FEMA P695 (ATC 2009) is used to investigate the collapse risk of isolated frames and it is found that the stiffness of the superstructure largely dictates its collapse risk. For flexible moment-resisting frames, the system-level failure modes are mixed: both bearing uplift failure and superstructure yielding can contribute, and designed moment-resisting frames meet the requirement of acceptable collapse probability (i.e. less than 10% at MCE level). For the stiff concentrically-braced frames

the impact force tends to impose large ductility demands on the superstructure, as a result the system-level failure mode comes solely from the excessive superstructure yielding. Moreover, only by increasing bearing's displacement capacity can the designed braced frame have an acceptably low collapse probability.

Chapter 6 is the second part of the system-level study of steel frame structures isolated by double friction pendulum bearings. In this chapter the collapse risk of moment-resisting and concentrically-braced frames isolated by double friction pendulum bearings with two different rim designs are studied: one is the rigid rim design and the other is the flat rim design. Fourteen pairs of near-fault pulse-like ground motions are used as the input motions. For the rigid rim bearings, the findings are similar to those in Chapter 5. For the flat rim bearings, due to the elimination of the impact force, the maximum drift of the superstructure is limited so system-level failure comes only from the instability of the isolation bearings. The flat rim bearings result in lower probabilities of failure for the frames under the design level earthquake.

The Appendix I presents an experimental and numerical study of the failure of a moment-resisting frame isolated by six triple friction pendulum bearings. This chapter is included because it is relevant to the scope of this thesis. In this study, a shake table test was conducted to investigate the system-level failure mechanism in a triple friction pendulum isolated frame. A numerical model is developed and verified using the experimental data. Compared to the experimental observation, the numerical model can predict the failure behavior of triple friction pendulum bearing.

References

Anderson TL (1989). Seismic isolation for the Los Angeles County fire command and control facility. *Proceedings ASCE Structures Congress: Seismic Engineering Research and Practice*: 605-624.

Applied Technology Council (2009). FEMA P695: Quantification of building seismic performance factors, Washington, D.C, USA.

Asher JW (1989). Seismic isolation of the USC University Hospital. *Proceedings ASCE Structures Congress: Seismic Engineering Research and Practice*: 605-614.

Bechtold J (1907). Earthquake-proof building. US Patent No. 845046.

Becker TC and Mahin SA (2012). Experimental and analytical study of the bi-directional behavior of the triple friction pendulum isolator. *Earthquake Engineering and Structural Dynamics*, 41:355-373.

Buckle IG and Mayes RL (1989). The application of seismic isolation to bridges. *Proceedings ASCE Structures Congress: Seismic Engineering Research and Practice*: 633-642.

Buckle IG and Mayes RL (1990). Seismic isolation: history, application and performance – A world view. *Earthquake Spectra*, 6(2): 161-201.

Buckle IG, Nagarajaiah S and Ferrell K (2002). Stability of elastomeric seismic isolation bearings: experimental study. *Journal of Structural Engineering*, 128: 3-11.

Erduran E, Dao ND and Ryan KL (2011). Comparative response assessment of minimally compliant low-rise conventional and base-isolated steel frames. *Earthquake Engineering and Structural Dynamics*, 40: 1123-1141.

European committee for standardization (2009). European standard 15129: Anti-seismic devices (English version), Brussels, Belgium.

Fenz DM and Constantinou MC (2006). Behaviour of the double concave friction pendulum bearing. *Earthquake Engineering and Structural Dynamics*, 35: 1403-1424.

Fenz DM, Constantinou MC (2008a). Spherical sliding isolation bearings with adaptive behavior: Theory. *Earthquake Engineering and Structural Dynamics*, 37:163-183.

Fenz DM, Constantinou MC (2008b). Spherical sliding isolation bearings with adaptive behavior: Experimental verification. *Earthquake Engineering and Structural Dynamics*, 37:185-205.

Han X and Warn GP (2014). Mechanistic model for simulating critical behavior in elastomeric bearings. *Journal of Structural Engineering*, 141(5): 04014140.

Kelly JM and Konstantinids D (2011). Mechanics of rubber bearings for seismic and vibration isolation. Wiley: Chichester, UK.

Komodromos P, Polycarpou PC, Papaloizou L and Phocas MC (2007). Response of seismically isolated buildings considering poundings. *Earthquake Engineering and Structural Dynamics*, 36: 1605-1622.

Li L (1984). Base isolation measure for seismic buildings in China. *Proceedings Eighth World Conference on Earthquake Engineering*, San Francisco: 791-798.

Masroor A and Mosqueda G (2012). Experimental simulation of base-isolated buildings pounding against moat wall and effects on superstructure response. *Earthquake Engineering and Structural Dynamics*, 41: 2093-2109.

Masroor A and Mosqueda G (2013). Impact model for simulation of base-isolated buildings impacting flexible moat walls. *Earthquake Engineering and Structural Dynamics*, 42: 357-376.

Masroor A and Mosqueda G (2015). Assessing the collapse probability of base-isolated buildings considering pounding to moat walls using FEMA P695 methodology. *Earthquake Spectra*, 31(4): 2069-2086.

Matsagar VA and Jangid RS (2003). Seismic response of base-isolated structures during impact with adjacent structures. *Engineering Structures*, 25: 1311-1323.

Miyazaki M (1978). Design and analysis of a base isolated building using lead-rubber bearings. Sumitomo Construction Co., Tokyo, 7 pages.

Monzon EV, Buckle IG and Itani AM (2016). Seismic performance and response of seismically isolated curved steel I-girded bridge. *Journal of Structural Engineering*, 142(12): 04016121.

Morgan TA and Mahin SA (2010). Achieving reliable seismic performance enhancement using multi-stage friction pendulum isolators. *Earthquake Engineering and Structural Dynamics*, 39: 1443-1461.

Ordonez D, Foti D and Bozzo L (2003). Comparative study of the inelastic response of base isolated buildings. *Earthquake Engineering and Structural Dynamics*, 32: 151-164.

Qu Z, Kishiki S and Nakazawa T (2013). Influence of isolation gap size on the collapse performance of seismically base-isolated buildings. *Earthquake Spectra*, 29(4): 1477-1494.

Sanchez J, Masroor A, Mosqueda G and Ryan KL (2014). Static and dynamic stability of elastomeric bearings for seismic protection of structures. *Journal of Structural Engineering*, 2013: 1149-1159.

Sarlis AA, Constantinou M, Reinhorn A (2013). Shake table testing of triple friction pendulum isolators under extreme conditions. Report No. MCEER-13-0011, University at Buffalo, Buffalo, NY, USA.

Sayani PJ, Erduran E and Ryan KL (2011). Comparative response assessment of minimally compliant low-rise base-isolated and conventional steel moment-resisting frame buildings. *Journal of Structural Engineering*, 137(10): 1118-1131.

Shenton HW and Lin AN (1993). Relative performance of fixed-base and base-isolated concrete frames. *Journal of Structural Engineering*, 119(10): 2952-2968.

Su L and Ahmadi G (1989). A comparative study of performances of various base isolation systems, part I: shear beam structures. *Earthquake Engineering and Structural Dynamics*, 18: 11-32.

Su L and Ahmadi G (1990). A comparative study of performances of various base isolation systems, part II: sensitivity analysis. *Earthquake Engineering and Structural Dynamics*, 19: 21-33.

Tsai CS, Lin YC and Su HC (2010). Characterization and modeling of multiple friction pendulum isolation system with numerous sliding interfaces. *Earthquake Engineering and Structural Dynamics*, 39:1463-1491.

Zayas VA, Low SS and Mahin SA (1987). The FPS earthquake resisting system. Report No.EERC 87-01. Earthquake Engineering Research Center, Berkeley, USA.

Chapter 2 Failure of Double Friction Pendulum Bearings Under Pulse-type Motions

Abstract

Although the behavior of friction sliding bearings is well understood, the failure behavior has not been thoroughly investigated. However, predicting and understanding the failure of bearings is an important key in designing isolated structures to minimize their collapse in extreme events, and thus, this study is critical. Because of its relative simplicity and particular availability in certain markets, the failure of the double friction pendulum (DFP) bearing at its physical displacement limit is investigated. The bearing is modeled with a rigid body model including inertia for each of the bearing components. A nonlinear viscoelastic impact model is included to simulate the impact between bearing components. As isolation systems are particularly vulnerable to long-period excitations, analytical pulses are used as input excitations to investigate the influences of pulse parameters on the failure of DFP bearing. The influences of DFP design parameters are investigated as well. To confirm that the response to the analytical pulses correctly represents the behavior under long-period ground motions, wavelet analysis is performed

on 14 pairs of pulse-type ground motion records to extract their pulses, and the failure prediction made from the extracted analytical pulse is compared with the failure from the real ground motions. It is found that using the extracted pulses provides a good estimation for the failure prediction of the ground motions.

2.1 Introduction

Seismic isolation is an effective technology for improving the seismic performance of structures and mitigating seismic hazards. There are two main categories of isolation bearings, rubber bearings and friction sliding bearings, and their mechanical properties have been widely investigated by many researchers. Even though the superiority of seismic isolation technology has been demonstrated over traditional fixed base structures, there are still many important issues that must be addressed, including understanding and predicting the failure mechanism of isolated structures, which is an essential step for performance based earthquake design. Global failure mechanisms are complex and involve interaction between the isolation layer, sub and superstructure, and potentially moat walls. However, to look at the problem thoroughly, the failure of each component must be understood, and so this study will look at the first step, the failure of individual isolation bearings. The failure of isolation bearings is important from a system failure standpoint but also because more buildings are being constructed with midstory isolation. And while there is no consensus on whether isolation displacement should be limited by isolator capacity or the distance to the moat wall, the latter is not an option for midstory isolation.

There has been significantly more study on the failure of rubber bearings than friction sliding bearings, and the shear failure and buckling failure behavior of rubber bearings is well understood (Kelly and Konstantinidis 2011). Researchers have even investigated the behavior of rubber isolated buildings in which large displacements cause pounding against the moat wall (Pant and Wijeyewickerma 2014; Masroor and Mosqueda 2012). However, there has been minimal study on the failure of friction sliding bearings. Sliding bearings are often made up of multiple components and the failure of sliding bearings is highly dependent on the interactions, including impact between components. Thus, the expected failure behavior is completely different from rubber bearings.

This paper will first look at the failure behavior of individual double friction pendulum bearing (DFP). The DFP, shown in Figure 2-1, consists of a top plate, inner slider and bottom plate. The top and bottom plate have restraining rims to limit the displacement of the bearings. These bearings have been selected as they are currently the only commercially available sliding bearings in Japan which has a significantly larger number of isolation projects compared to the majority of the world. Also, DFP have relatively simple geometry compared to other sliding bearings, such as triple friction pendulums, which helps to condense the problem. Unlike DFP produced in the United States, these bearings do not have an articulated inner slider. When the bearing reaches its maximum displacement, the restrainer forces create a couple on the slider (see Figure 2-2), which, because the slider is not articulated, results in yielding of the restraining rim, a sharp increase in the vertical displacement, or both. The yielding or uplift caused by the strong impact can lead to bearing failure.
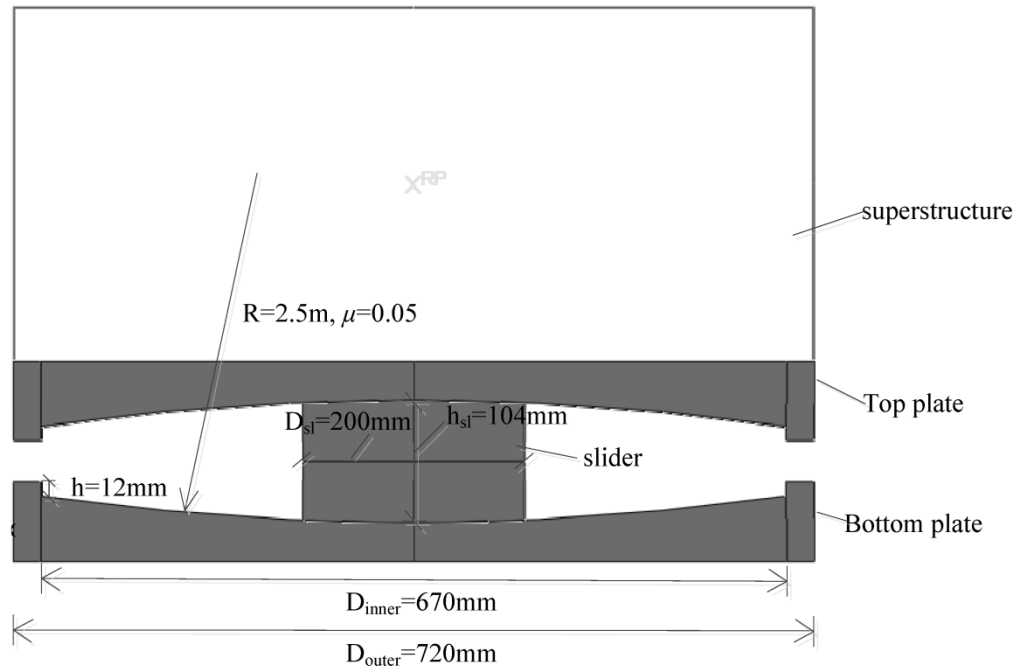
Figure 2-1 Baseline configuration of double friction pendulum
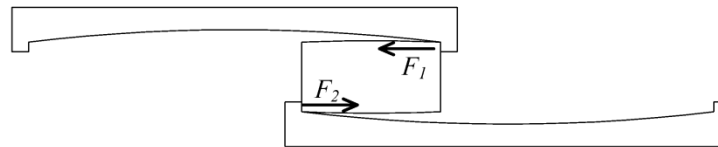
Figure 2-2 Illustration of double friction pendulum impact

The influence of different design parameters of the DFP on the failure behavior is investigated using Ricker pulses as inputs to approximate long period pulse-type ground motions. These pulse-type ground motions have been shown to be of particular concern for isolation systems as the systems themselves have long natural periods (Vassiliou et al. 2013). The failure predictions using Ricker pulses are shown to give a good approximation for time history response.

2.2 Rigid Body Model

For initial investigation, a finite element model of the bearing was created in Abaqus. However, this model required significant computational time. Thus, a rigid body model that is capable of simulating sliding, impact, and uplift behavior was selected. The numerical model used herein is based on the work of Sarlis and Constantinou (2013) which employs rigid body kinematics, rigid body dynamics and contact mechanics. Each component of the DFP is considered as a rigid body, the top plate and bottom plate are assumed to only have two translation degrees of freedom (horizontal and vertical), the slider has two translation and one rotation degrees of freedom, all motions are measured at the centroid of each component. The normal forces, friction forces and potential impact forces acting on the slider are assumed to concentrate on the four vertexes. In order to develop normal forces and impact forces, small penetrations are allowed between the components and resulting forces are directly related to the penetration depth. Arbitrary damping forces are also included in the expression of normal forces.

While this is the only existing analytical model that is capable of considering impact and uplift behavior directly, a major issue is that it is hard to quantify the energy dissipation during impact between bearing components. This is because the model specifies an arbitrary damping constant in the vertical direction and does not consider energy dissipation in the horizontal direction. In order to address this limitation, the Hertz's contact law with non-linear parallel damper (Muthukumar and DesRoches 2006) is added to Sarlis and Constantinou's model in order to consider the energy dissipation

during the impact for all surfaces. For the Hertz's contact law, the impact force during the

approaching phase once contact is detected can be calculated as:

$$F_{impact}(t) = k\delta(t)^{1.5} + c\dot{\delta}(t) \tag{1}$$

Then, the impact force during the restitution phase can be determined as:

$$F_{impact}(t) = k\delta(t)^{1.5} \tag{2}$$

where k is the penalty stiffness, c is the damping coefficient, and δ is the penetration

depth. According to Jankowski (2005 and 2006), the damping coefficient c can be

determined through the coefficient of restitution e as:

$$c = 2\xi\sqrt{k\sqrt{\delta(t)}\frac{m_1 m_2}{m_1 + m_2}} \tag{3}$$

$$\xi = \frac{9\sqrt{5}\left(1 - e^2\right)}{2e\left(e\left(9\pi - 16\right) + 16\right)} \tag{4}$$

The coefficient of restitution e represents the amount of energy dissipated during

impact, $e = 1$ means a completely elastic impact (i.e. no energy dissipation) while $e = 0$

means a fully plastic impact (i.e. all energy is dissipated). Jankowski (2010) has

experimentally determined the value of coefficient of restitution for different materials

and it is found that for steel this coefficient of restitution e ranges from 0.4 to 0.7 and

decreases as the impact velocity increases. During numerical impact simulations, the

value of coefficient of restitution e is usually arbitrarily selected (for example, see

Komodromos et al. 2007; Anagnostopoulos 1988), in this paper the value of coefficient

of restitution is selected as $e = 0.65$, and it will be demonstrated later in this section this

value provides a good estimation compared to detailed finite element analysis.

2.2.1 Validation of rigid body model

The failure predicted using the rigid body model was compared against a detailed finite element analysis for model validation. The design parameters selected for the DFP are shown in Figure 2-1; these parameters are chosen from a standard configuration available. The radius of curvature R is 2.5 m, the outer diameter of the isolator is 720 mm, the width of the slider is 200 mm, the height of the slider is 104 mm and the restrainer height is 12 mm. These properties result in a second-slope period of $T_b = 4.5$ s, where $T_b = 2\pi\sqrt{2R/g}$, and a displacement capacity $D = 450$ mm. The friction coefficient is assumed to be constant with $\mu = 0.05$.

The finite element model was created in Abaqus/Explicit using quadrilateral elements. Plasticity with isotropic hardening was included in the material model to consider potential yielding of the restrainers. The yielding stress and ultimate stress of the steel are 345 MPa and 450 MPa respectively, the ratio of post yield stiffness to elastic stiffness is assumed to be 0.01. The bearing supports a superstructure, which is considered as a rigid mass with the rotational degree of freedom restrained. Finite element analysis indicates that yielding can affect the failure behavior of DFP significantly. Under small masses (resulting in pressured less than roughly 10 MPa), the impact causes negligible yielding of the restrainers and uplift after the impact leads to dynamic instability of the DFP. However, when the mass is large (e.g. resulting in a slider pressure of 50 MPa), impact causes significant yielding and potential fracture of the restrainers, and the uplift behavior is reduced. These two situations result in different failure behavior, shown in Figure 2-3. The left failure behavior is the slider goes beyond

the restrainer of top plate due to the uplift after the impact; the right failure is due to the

significant yielding of the bottom plate restrainer rim. Failure of the DFP is characterized

as when one of the vertexes of the inner slider goes beyond the restrainer rim of the top or

bottom plate.

Figure 2-3 Different failure behaviors of double friction pendulum (left: due to uplift; right: due to yielding)

The rigid body model can capture the first failure behavior but cannot simulate

the latter. The model does not include yielding, and thus, the failure behavior of DFP

using the rigid body model is almost independent of the superstructure mass. Therefore,

to compare between the two models, a slider pressure of 10 MPa is used. Discussion of

how ignoring yielding changes failure predictions is given in section 2.3.4.

Twenty eight (14 pairs) pulse-type ground motion records taken from FEMA

P695 (ATC 2009) are used as input ground motions. The scaling method of the 28 pulse-

type ground motions can also be found in FEMA P695. The ground motions are scaled up

using an increment of 0.1 g in the pseudo acceleration at the period of the bearing $SA(T_b)$.

Figure 2-4 shows the critical $SA(T_b)$ predicted from the rigid body model with coefficient

of restitution $e = 0.65$ and finite element analysis. The rigid body model provides a good

prediction. Only five out of the 28 ground motions are incorrect predictions, and of these, four conservatively underestimate the critical $SA(T_b)$.
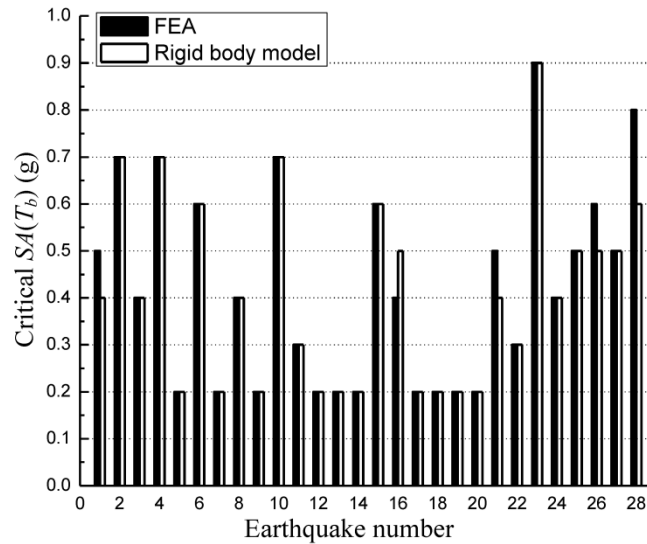
Figure 2-4 Comparison of rigid body model and finite element analysis

2.3 Failure of Double Friction Pendulum Bearing Due to Analytical Pulse Excitation

As isolated structures have relatively long natural periods, it is reasonable to believe the seismic response of isolated structures is dominated by long period pulses. As ground motions have highly variable characteristics, the behavior of DFP under simplified analytical pulses is first investigated to gain insight into likely demands of pulse-type ground motions.

2.3.1 Analytical Ricker pulse

There are several analytical pulses in the existing literature (Mavroeidis and Papageorgiou 2003). In this study Ricker pulses are used as the analytical pulse excitations for two reasons: 1) Ricker pulses are governed by only two parameters

(amplitude A_p and period T_p), which makes its mathematical representation very simple

and 2) many ground motions identified as pulse type can be idealized by a Ricker pulse,

for example, Figure 2-5 shows two different ground motions approximated by analytical

Ricker pulses.
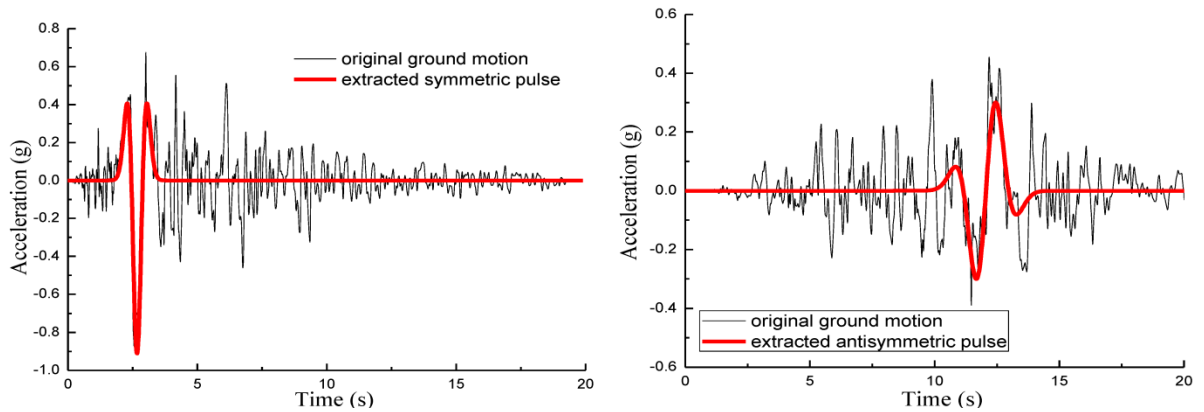
Figure 2-5 Ground motion records approximated by Ricker pulses (left: symmetric; right: antisymmetric)

The mathematical formulations of symmetric and antisymmetric Ricker pulses

(Ricker 1944; Ricker 1943) are given by:

$$\ddot{u}_g = A_p \left(1 - \frac{2\pi^2 t^2}{T_p^2}\right) e^{-\frac{\pi^2 t^2}{T_p^2}} \tag{5}$$

$$\ddot{u}_g = \frac{A_p}{1.38} \left(\frac{4\pi^2 t^2}{3T_p^2} - 3\right) \frac{2\pi t}{\sqrt{3}T_p} e^{-\frac{2\pi^2 t^2}{3T_p^2}} \tag{6}$$

where T_p and A_p are the amplitude and period of Ricker pulse, respectively.

2.3.2 Maximum impact velocity spectrum

The impact velocity spectrum, proposed by Davis (1992) for building pounding,

describes the velocity of the top plate relative to the bottom plate at every occurrence of

impact during one input excitation. The analyses are run with the rigid body model using

the bearing depicted in Figure 2-1. Figure 2-6 shows the impact velocity spectra under

Ricker pulses $A_p = 0.8$ g. Each dot represents an impact after which failure does not occur;

the crosses indicate impact which is followed by failure. The period ratio is the ratio of natural period of DFP (i.e. 4.5 s in this case) to the period of Ricker pulse, therefore the lower this period ratio, the longer the period of the Ricker pulse. Note, in these impact velocity spectra the lower bound of period ratio is limited to 0.6 which corresponds to a pulse period of 7.5 s, pulses longer than this are not investigated.
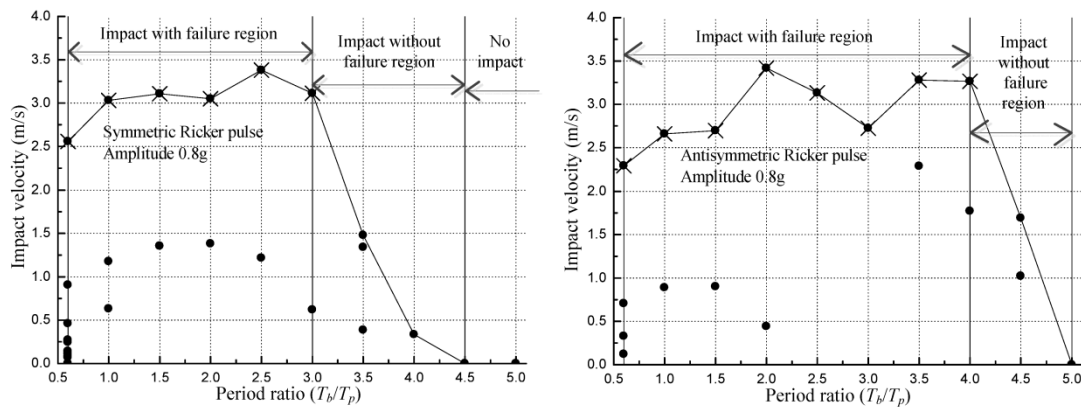
Figure 2-6 Impact velocity spectra under Ricker pulses of amplitude 0.8 g

The impact velocity spectrum provides interesting information regarding the pounding and failure of DFP. During one specific pulse excitation there may be multiple incidents of impact but only an impact with significant velocity results in failure. Failure of the bearing is a complex phenomenon that involves interactions among bearing components, including the uplift and bouncing of the top plate, and rocking, uplift, and bouncing of the slider. Figure 2-7 shows the horizontal displacement of the top plate relative to the bottom plate and the corresponding ground displacement (i.e. bottom plate displacement) during two antisymmetric Ricker pulses. At high period ratios (see (b) in Figure 2-7) there is often an initial impact, the energy from which increases the velocity of the second impact, causing uplift after which the top plate of the bearing moves in the

opposite direction until it is beyond the slider. However, at lower period ratios (see (a) in Figure 2-7), because of the long duration of the pulse, the bearing reaches the maximum displacement and maintains this displacement in a series of impacts, then after reversal of motion impact leading to failure occurs at the other restrainer. On this reversal of motion, the bearing again would have a series of impacts with the restrainer; however, the impact causes large enough uplift of the top slider that the failure occurs. While uplifting of the top plate causes failure is both circumstances, it is difficult to pinpoint the specific trigger for failure.

Figure 2-8 shows the horizontal displacement of the same bearing under the same motions as shown in Figure 2-7 but with a large mass resulting in sliding surface pressures of 50 MPa, the analysis of which was done using the finite element model. The response for the bearings with large and small masses is almost identical for the long period ground motion (see (a) in both figures). The only difference is that in the bearing with small mass uplift and a slight rebound occur before failure while in the bearing with large mass, the slider yields the restraining rim and thus no rebound occurs. For the short period ground motion (see (b) in both figures), the behavior changes greatly. Failure for the bearing with large mass occurs on the first impact as the restraining rim yields; however, for the bearing with small mass uplift does not occur until after the second impact event.
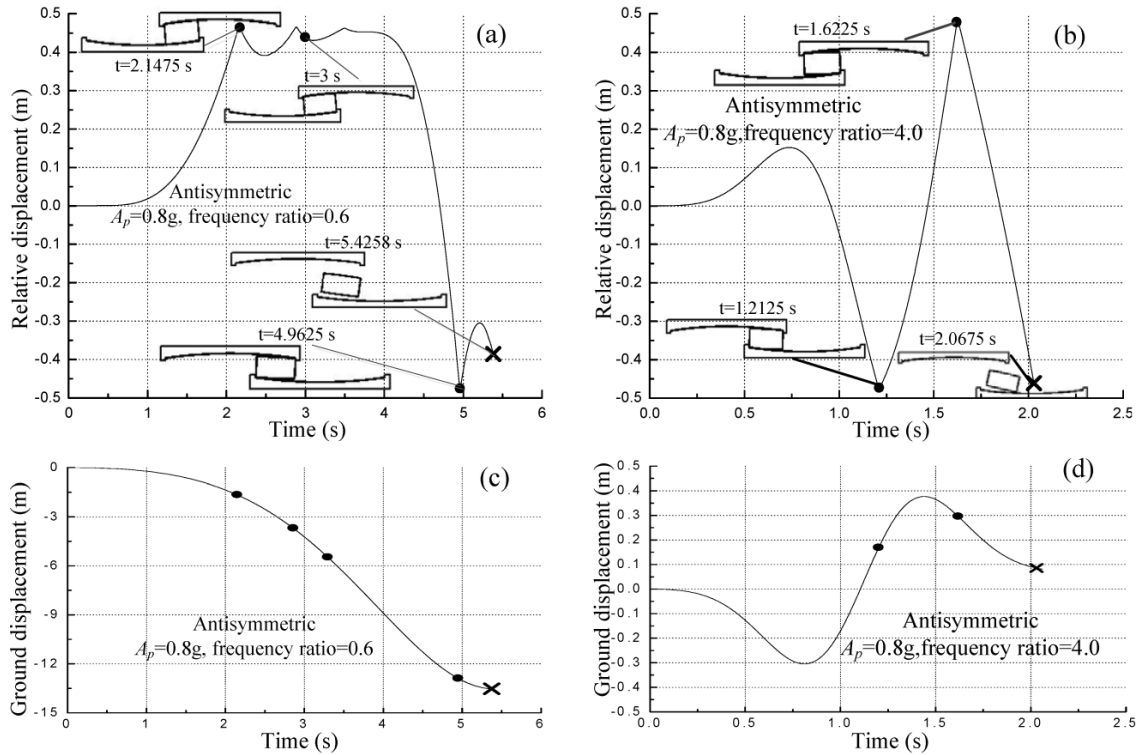
Figure 2-7 Relative bearing displacement and ground displacement time histories and under antisymmetric

Ricker pulses of (a, c) period ratio 0.6 and (b, d) period ratio of 4.0

Since only the strongest impact is of real concern, it is natural to construct the maximum impact velocity spectrum, which is similar to the impact velocity spectrum but only describes the maximum impact velocity during each specific pulse excitation. In Figure 2-6 the line represents the maximum impact velocity spectra under Ricker pulses with different amplitudes. Figure 2-9 presents the maximum impact velocity spectra for increasing pulse amplitudes. Again, the crosses in both figures indicate failure of double friction pendulum bearing occurs.
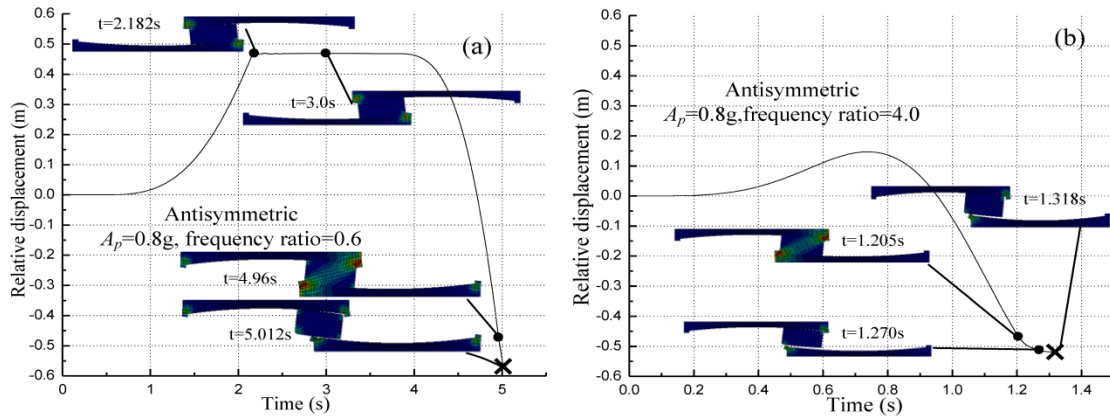
Figure 2-8 Relative displacement time histories under antisymmetric Ricker pulses with large mass

2.3.3 Impact region spectrum

In the maximum impact velocity spectra shown in Figure 2-9, it is observed that the period ratio can be divided into three different regions, a region where impact results in failure, region where impact occurs but does not result in failure, and a region with no impact. These regions are also illustrated in Figure 2-6. From this, the impact region spectrum can be derived. Unlike the maximum impact velocity spectrum which describes the maximum impact velocity given a specific Ricker pulse, the impact region spectrum describes the behavior of the bearing directly given any amplitude and period (or period ratio) combination. Figure 2-10 shows the impact region spectra derived from the maximum impact velocity spectra in Figure 2-9. Similarly there are three regions in the impact region spectrum: 1) the vertical hatch represents the impact with failure region, which means if the bearing is subjected to a pulse with amplitude and period that fall in this area then failure will occur, 2) the horizontal hatch represents the impact without failure region, and 3) the white area is the region where impact will not occur. The impact

region spectrum can be used to directly determine the final status of the DFP when subjected to Ricker pulse excitations. The shape of impact regions will be influenced by the design parameters of DFP.
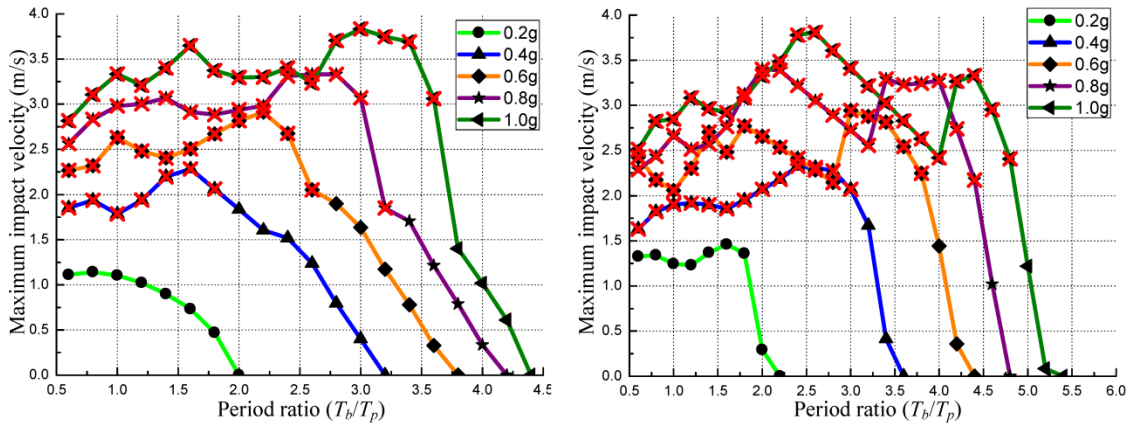
Figure 2-9 Maximum impact velocity spectrum under Ricker pulses (left:symmetric; right: antisymmetric)
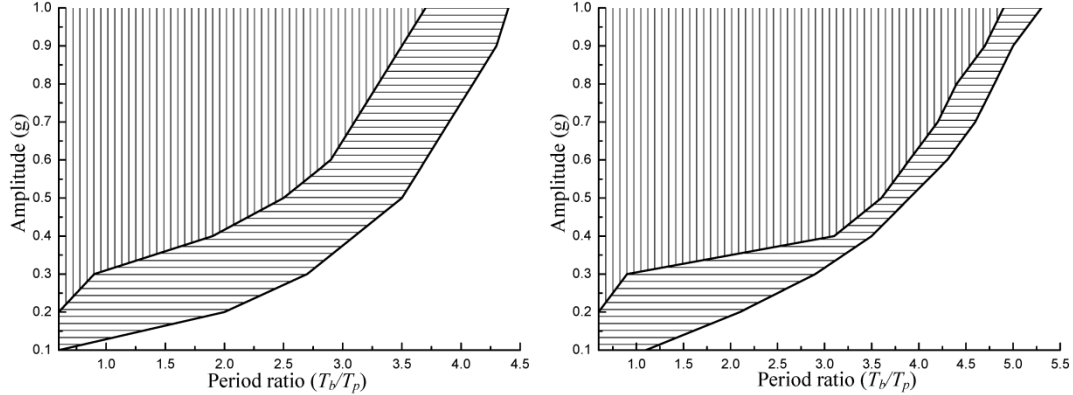
Figure 2-10 Impact region spectra (left: symmetric Ricker pulse; right: antisymmetric Ricker pulse)

For sliding bearings without restraining rims, as are common in Europe, a conservative method would be to assume failure when the bearing reached impact. This would reduce the impact region spectra to two regions: no impact and failure.

2.3.4 Effect of yielding on failure

The rigid body model is incapable of considering potential yielding of the restrainer rims during the impact. To explore how including yielding would affect the impact region spectra created using the rigid body model, two different values of superstructure mass *M* are investigated with the finite element model, resulting in slider pressures of 10 MPa and 50 MPa. Figure 2-11 shows the impact region spectra for different superstructure mass values. As expected, as the superstructure mass increases, the impact with failure region shifts to the right (note, in the impact region spectra, lines shifting to the left indicate a larger region of stability), which means increasing the superstructure mass is detrimental for avoiding failure. This is because as the superstructure mass increases, the impact force will cause significant yielding of the restrainers, resulting in failure. Interestingly, under the lighter mass, the rigid body model is more conservative. This may be that due to the fact the same uplift failure mechanism is observed, yet some energy is dissipated during the impact in the finite element model. In both cases, compared to the predictions from finite element analysis, the rigid body model provides a satisfactory estimation of the impact regions, and the rigid body model will be used for the remained of the investigation.
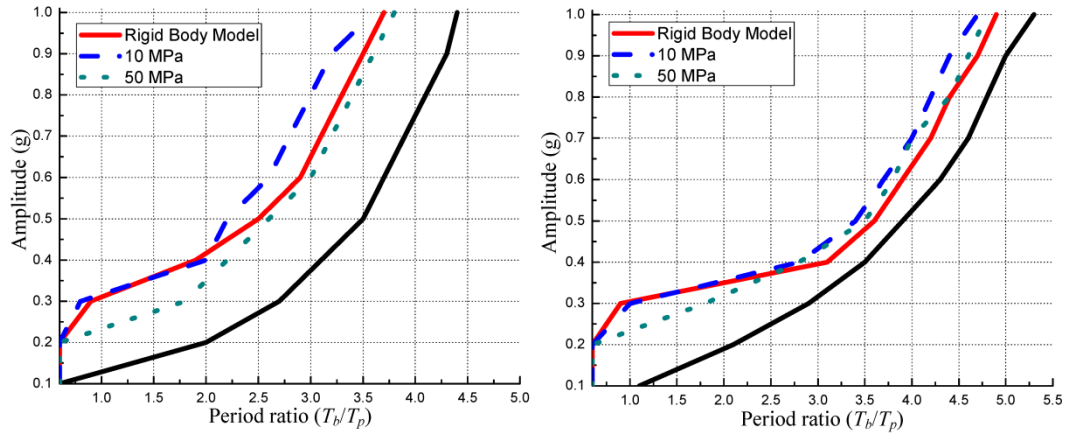
Figure 2-11 Impact region spextra comparing the rigid body model to the finite element model with

different superstructure masses (left: symmetric; right: antisymmetric)

2.4 Influences of Design Parameters on the Impact Region Spectrum

In this section the influence of the bearing design parameters, including friction

coefficient μ, radius of curvature R, diameter D, restrainer height h, and aspect ratio of

slider ρ, on the shape of impact regions will be investigated. Using the configuration

shown in Figure 2-1 as a baseline, each design parameter is varied and descriptions of

their effects can be found in the corresponding subsection.

2.4.1 Friction coefficient

Three different friction coefficient values $\mu = 0.02$, 0.05, and 0.08 are examined in this

study. Figure 2-12 shows the impact region spectra with different friction coefficient

values under Ricker pulses. At the first glance, the influence of the friction coefficient is

complex: 1) for both symmetric and antisymmetric Ricker pulses with low period ratio

(e.g. 2.0), increasing the friction coefficient is beneficial for avoiding impact and failure,

2) for symmetric Ricker pulses with high period ratio (e.g. 3.8), increasing the friction

coefficient is beneficial for avoiding failure but detrimental for avoiding impact, 3)

however, for antisymmetric Ricker pulse with high period ratio, increasing the friction coefficient is detrimental for avoiding both impact and failure.

To better understand how the friction coefficient affects the behavior of DFP, it is beneficial to look at the impact region spectrum with the aid of dimensional analysis. Ignoring potential impact, the maximum displacement response D_{max} of DFP can be expressed as below:

$$D_{\max} = f\left(T_b, \mu, A_p, T_p\right) \tag{7}$$

Using Buckingham π theorem with appropriate π terms, Equation (7) can be expressed as:

$$\frac{D_{\max}}{A_p T_p^2} = f\left(\frac{T_b}{T_p}, \frac{A_p}{\mu g}\right) \tag{8}$$

The first π term is the period ratio used in the impact region spectrum, the second π term is the amplitude ratio. For DFP with constant friction coefficient, there is no particular advantage to changing the pulse amplitude A_p to the amplitude ratio $A_p/\mu g$ in the impact region spectrum, however, as the friction coefficient varies doing so will reveal remarkable simplicity, as shown in Figure 2-13. It is clear that as the friction coefficient increases the impact region shifts to the right side in the spectra. This can be easily explained in the context of dimensional analysis. Given the same period ratio T_b/T_p and amplitude ratio $A_p/\mu g$, the normalized maximum displacement should remain identical. As the friction coefficient μ increases, the pulse amplitude A_p must increase accordingly to keep the second π term the same. This means the maximum displacement D_{max} must also increase as the friction coefficient increases. Since the physical

displacement of the DFP is a constant value, 450 mm in this case, increasing the friction coefficient will shift the impact region to the right side in the spectrum.
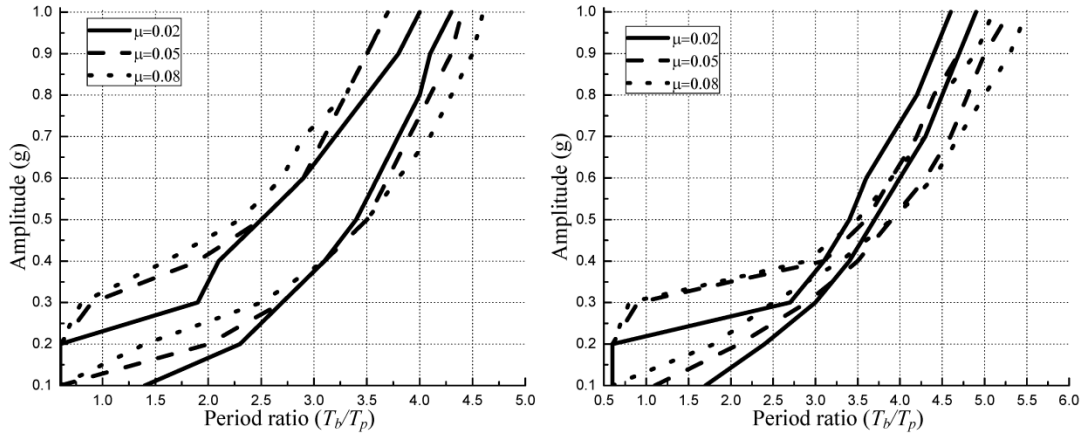
Figure 2-12 Impact region spectra with different friction coefficients (left: symmetric; right: antisymmetric)
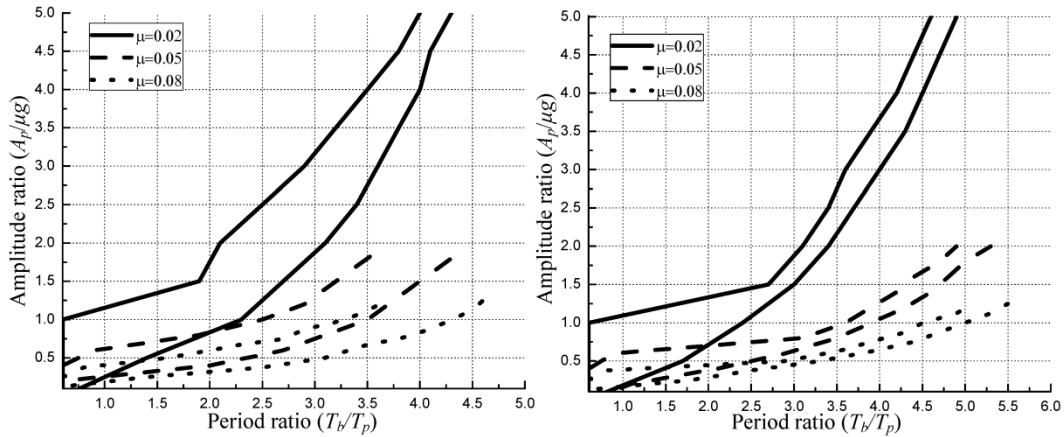
Figure 2-13 Impact region spectra with different friction coefficients using amplitude ratio (left: symmetric; right: antisymmetric)

2.4.2 Radius of curvature

Three different radius of curvature values, $R = 1.12$ m, $R = 2.5$ m and $R = 4.5$ m, are investigated, which result in second slope periods T_b of 3.0 s, 4.5 s and 6.0 s. The impact region spectra with different radius of curvatures are presented in Figure 2-14. It is notable that as the natural period of DFP increases, the bearing is more vulnerable to

Ricker pulses with higher period ratios. This observation is reasonable from a physical point of view; as the radius of curvature increases (i.e. natural period of DFP increases) the plate surface becomes flatter and a smaller force (smaller acceleration) is required to push the bearing to its displacement limit.
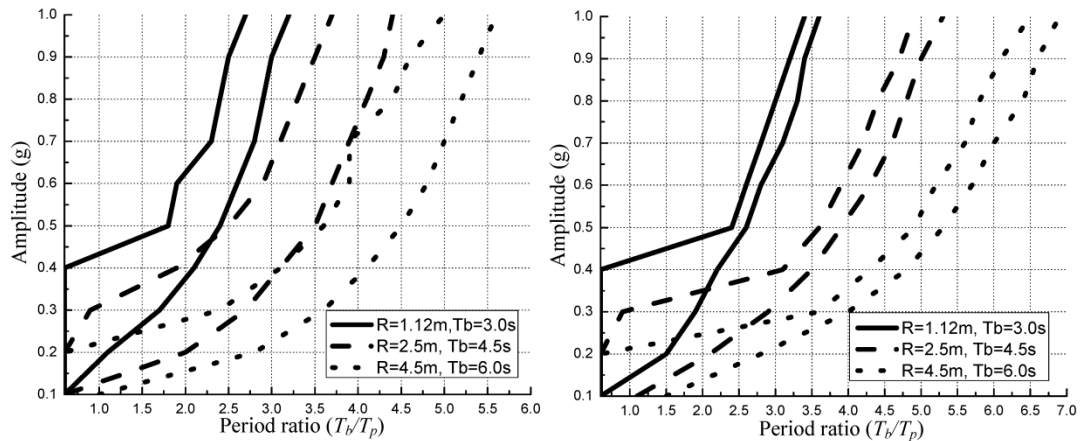
Figure 2-14 Impact region spectra with different radius of curvatures (left: symmetric; right: antisymmetric)

This phenomenon can be also understood by dimensional analysis. Referring to Equation (8) above, initial impact occurs when the maximum displacement reaches then displacement limit, 450 mm in this case. Given the same period ratio T_b/T_p and amplitude ratio $A_p/\mu g$, the normalized maximum displacement should be the same. On the other side, as the natural period of DFP T_b increases, to maintain the same period ratio T_p must increase as well, therefore the maximum displacement D_{max} increases as T_b increases. Also as the natural period of the DFP increases, the input pulse amplitude A_p to reach the same level of displacement lowers. Therefore, as the radius of curvature increases the impact region spectrum shifts to the right. Even though this cannot directly explain the failure, it is reasonable to presume that the earlier bearing reaches its displacement limit, the easier failure of the bearing occurs.

2.4.3 Bearing diameter

Three different bearing diameters of the outer sliding plates are investigated, $D = 620$ mm, 720 mm and 820 mm. The corresponding impact region spectra are presented in Figure 2-15. Even though the results are straightforward: increasing the bearing diameter will shift the impact region spectra to the right side, which means bearing are safer when subjected to the same Ricker pulse excitation, there is still one interesting observation: as the period ratio increases, the benefit of selecting a larger diameter also increases. There is much smaller benefit at low period ratios.
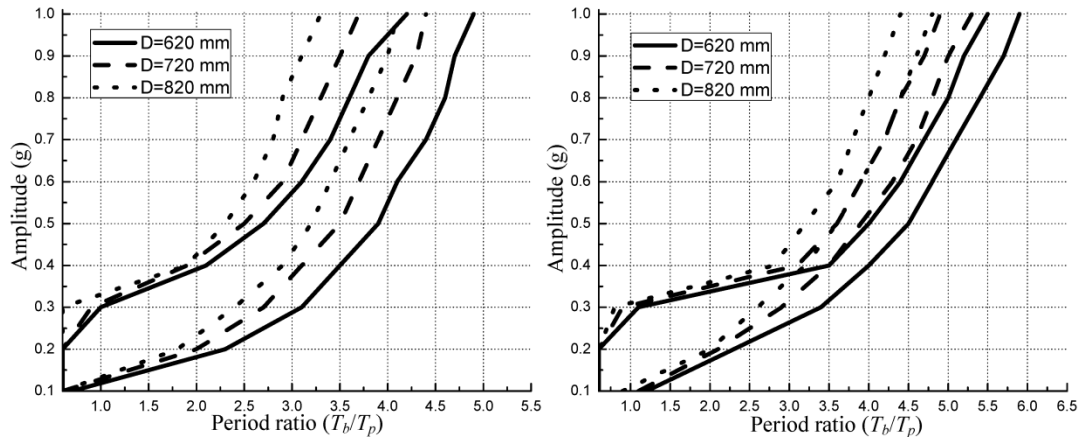
Figure 2-15 Impact region spectra with different bearing diameters (left: symmetric; right: antisymmetric)

2.4.4 Restrainer height

Three configurations of restrainer height $h = 9$ mm, 12 mm, and 15 mm are investigated. Intuitively, increasing the restrainer height will be beneficial for avoiding failure, however, Figure 2-16 demonstrates that the restrainer height has limited influence on the failure. This is because the failure is predominantly caused by uplift, and the amount of vertical displacement that occurs after high velocity impacts generally exceeds typical restrainer heights.
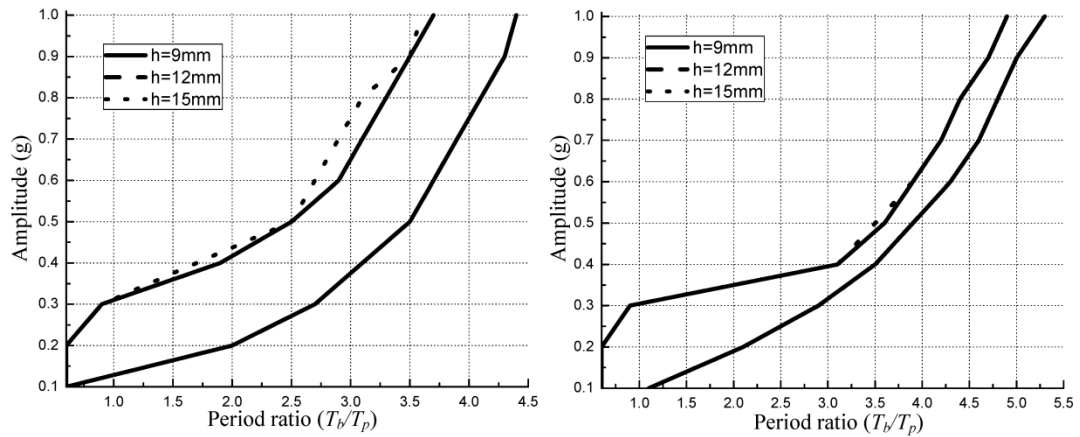
Figure 2-16 Impact region spectra with different restrainer heights (left: symmetric; right: antisymmetric)

2.4.5 Aspect ratio of slider

The aspect ratio of the slider ρ is defined as the ratio of the slider height h_{sl} to the slider width D_{sl}, (see Figure 2-1). Three distinct aspect ratio values are studied: 1) the slider height h_{sl} = 200 mm, the slider width D_{sl} = 200 mm, ρ = 1; 2) the slider height h_{sl} = 104 mm, the slider width D_{sl} = 200 mm, ρ = 0.52; 3) the slider height h_{sl} = 164 mm, the slider width D_{sl} = 500 mm, ρ = 0.328. The latter two combinations were taken from commercially available dimensions while the first was chosen in order to explore a large aspect ratio. To illustrate the influence of the aspect ratio on the failure of DFP, it is better to start with the maximum impact velocity spectra, which is shown in Figure 2-17 for three different aspect ratios with pulse amplitude 0.7 g. As before, the crosses indicate failure occurs.
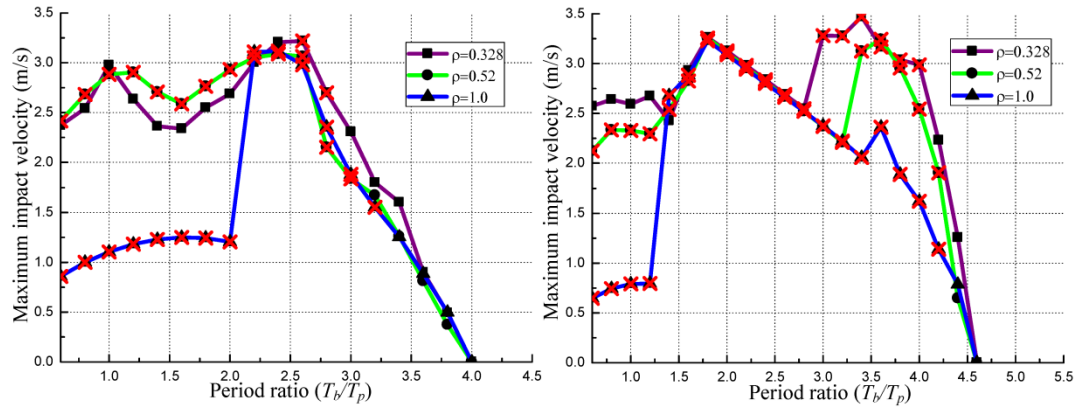
Figure 2-17 Maximum impact velocity spectra under Ricker pulses of amplitude 0.7 g with different slider

aspect ratios (left: symmetric; right: antisymmetric)

The maximum impact velocity spectra provide useful information regarding how

the aspect ratio affects the failure of the DFP. When $\rho = 1.0$, at relatively low period

ratios, the impact velocity that leads to failure decreases dramatically compared to when

$\rho = 0.52$. This is because at large aspect ratios smaller rotation is required for the inner

slider to become unstable, resulting in failure. When $\rho = 0.328$, compared to $\rho = 0.52$ the

failure region decreases dramatically. For symmetric Ricker pulses, only the period ratio

range from 2.6 to 2.8 results in failure, and for antisymmetric Ricker pulses, the period

ratio range from 2.0 to 4.0 results in failure. This suggests that by decreasing the aspect

ratio of the inner slider, the failure region can be significantly reduced as a larger rotation

is necessary to cause instability. This is especially beneficial for avoiding failure in long

period pulses.

Based on the maximum impact velocity spectra the impact region spectra can be

constructed, however, for $\rho = 0.328$ the impact region spectra will not be continuous.

Thus, it is proposed that for $\rho = 0.328$ once failure occurs at a certain period ratio for a

specific amplitude, pulses of the same amplitude at lower period ratios will be grouped

into the failure region (see Figure 2-18). Of course this is not true, but this is a more

conservative estimation and makes the impact region spectra easier to construct and use.

Moreover, as will be presented in Section 2.5.3, compared to the impact region spectrum

based on the actual failure region, the impact region spectrum based on this proposed

failure region provides better predictions.
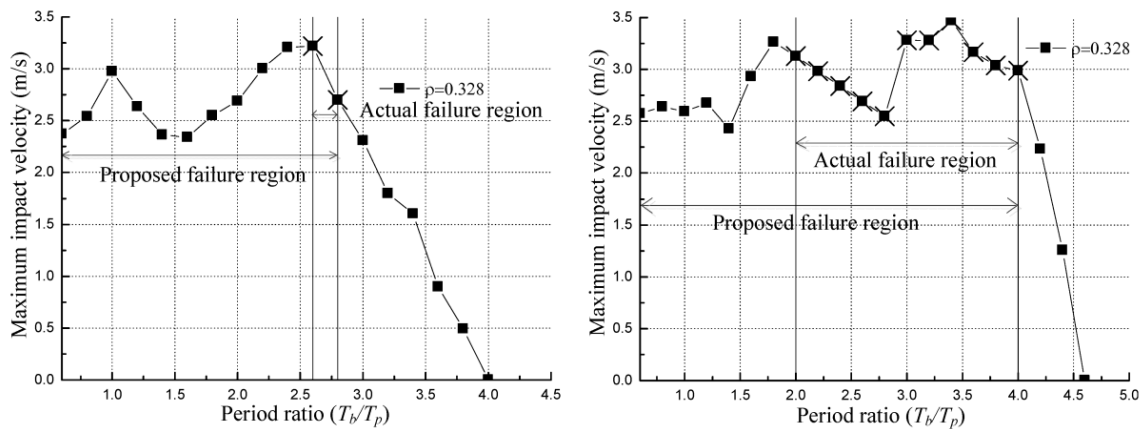
Figure 2-18 Actual and proposed failure region for aspect ratio ρ = 0.328 under 0.7 g amplitude pluses (left:

symmetric; right: antisymmetric)

The impact region spectra for different aspect ratios are shown in Figure 2-19. As

expected, the period ratio that determines impact remains almost identical, but the period

ratio that results in failure moves to the left as the aspect ratio decreases, indicating

improved performance. This effect is largest for low amplitude pulses.
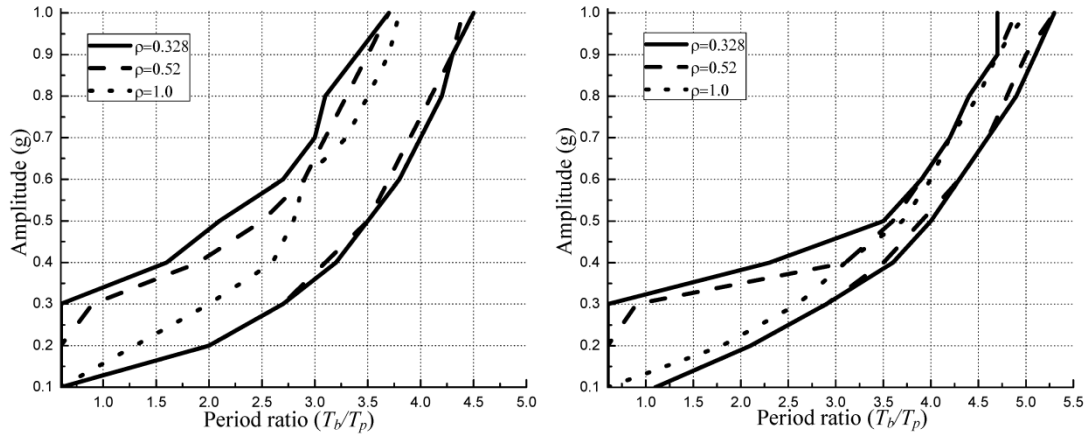
Figure 2-19 Impact region spectra for different aspect ratios (left: symmetric; right: antisymmetric)

2.5 Failure Prediction for Pulse-Type Ground Motions

The impact region spectra are useful for determining the failure of a DFP under a Ricker pulse. However, to be useful in design, these spectra must be able to predict failure under ground motions. Here the best method to extract the pulse from the ground motion for use in the impact region spectra is investigated, and the ability of the spectra to predict failure in pulse-type ground motions is evaluated.

2.5.1 Wavelet analysis of pulse-type ground motions

Wavelet analysis has been widely used in signal processing and data analysis. Baker (2007) used wavelet analysis on the velocity time histories to determine whether a ground motion can be classified as pulse-type. Vassiliou and Makris (2011) used wavelet analysis with different weighting functions to extract pulses of different natures from acceleration records directly. Both the symmetric and antisymmetric Ricker pulses, which are also known as the second and third derivatives of the Gaussian respectively, meet the mathematical requirements for wavelet analysis, so they can be used as mother wavelets

to extract pulses from ground motions. This can be implemented by performing the following integral:

$$C(s,\xi) = w(s) \int_{-\infty}^{+\infty} f(t)\Psi\left(\frac{t-\xi}{s}\right) dt \qquad (9)$$

Where $f(t)$ is either the acceleration or velocity time history, $\psi(\bullet)$ is the mother wavelet function, $w(s)$ is the weighting function, and s and ξ are constants that control the dilation and translation of the mother wavelet. While Baker (2007) used the weighting function $w(s) = 1/\sqrt{s}$ with the velocity record, Vassiliou and Makris (2011) proposed three different weighting functions $w(s)$: $w(s) = 1/\sqrt{s}$, $w(s) = 1/s$, $w(s) = 1$. These weighting functions can be used with acceleration or velocity records.

The 28 pulse-type ground motions used originally in the model validation are analyzed with wavelet analysis. For a sample ground motion, Figure 2-20 shows the Ricker pulses extracted from the velocity records, using three different weighting functions, the right hand figures are the velocity time history and the left hand figures are the corresponding acceleration time history. When pulses are extracted from the velocity time history, in order to find a symmetric Ricker acceleration pulse, the first derivative of the Gaussian is used as the mother wavelet for the velocity record; similarly, to find an antisymmetric Ricker acceleration pulse, the second derivative of the Gaussian is used as the mother wavelet for the velocity record. Note the symmetric and antisymmetric annotations in Figure 2-20 are in terms of the final acceleration pulse (not velocity).
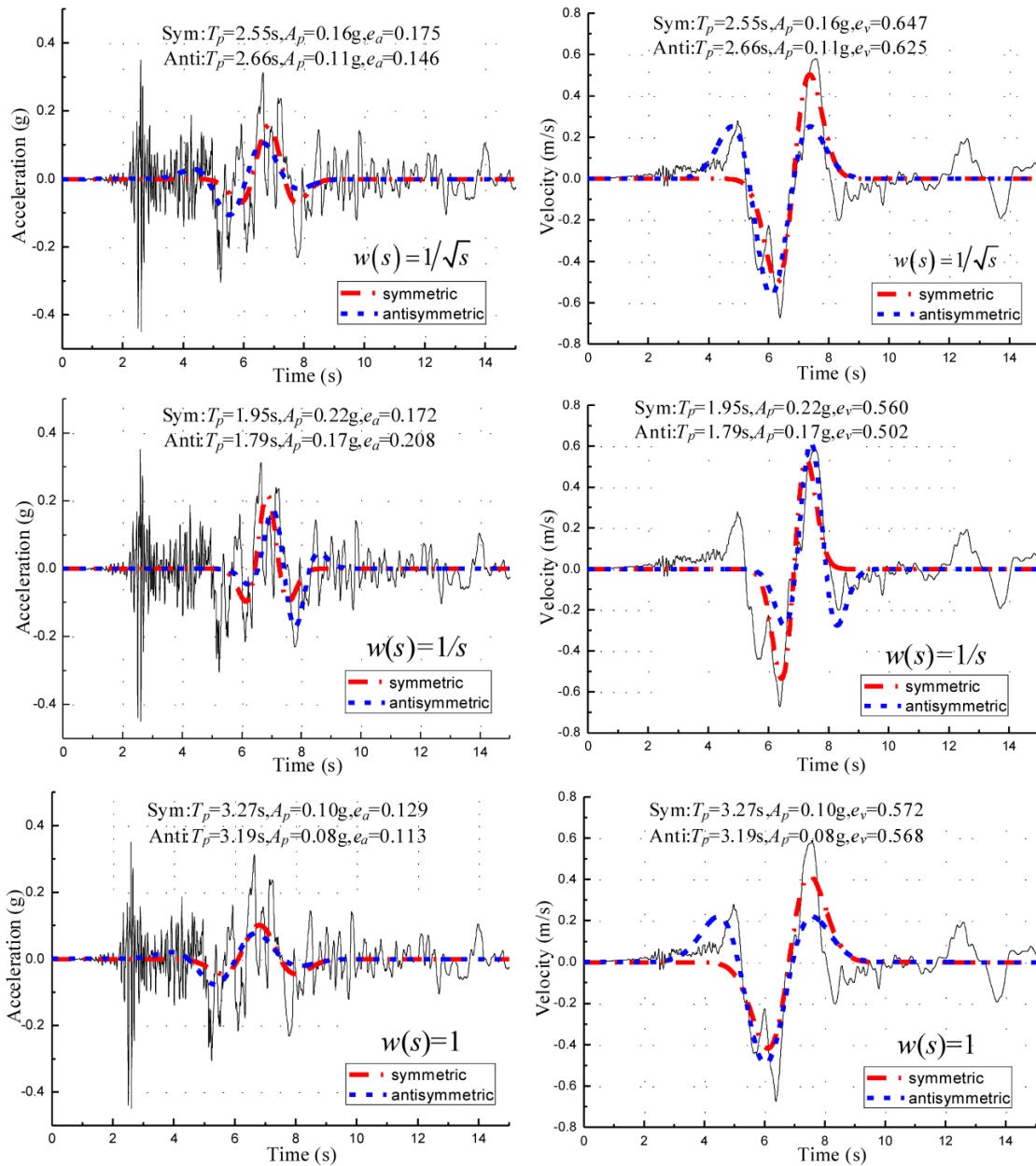
Figure 2-20 Extracted pulses from velocity records using three different weighting functions

2.5.2 Best match analytical pulse selection

In order to evaluate to what extent these extracted pulses match with the original ground

motions, two indexes can be used: the acceleration index e_a and the velocity index e_v:

$$e_a = \frac{\int_{-\infty}^{+\infty} \ddot{u}_g(t)\ddot{u}_{pulse}(t)dt}{\int_{-\infty}^{+\infty} [\ddot{u}_g(t)]^2 dt} \qquad (10)$$

$$e_v = \frac{\int_{-\infty}^{+\infty} \dot{u}_g(t)\dot{u}_{pulse}(t)dt}{\int_{-\infty}^{+\infty} [\dot{u}_g(t)]^2 dt} \qquad (11)$$

There are four possibilities for selecting the best analytical pulse: 1) The pulse extracted from the acceleration time history that corresponds to the maximum acceleration index. 2) The pulse extracted from the acceleration time history that corresponds to the maximum velocity index. 3) The pulse extracted from the velocity time history that corresponds to the maximum acceleration index. 4) The pulse extracted from the velocity time history that corresponds to the maximum velocity index. The predicted results from these four selection criteria are compared in the following section.

2.5.3 Prediction results

With the best match extracted pulse, then it is easy to predict the critical value of $SA(T_b)$ that results in failure using impact region spectra. For example, the best match pulse corresponding to selection criterion No.3 for the original sample ground motion is the antisymmetric Ricker pulse found with weighting function $w(s) = 1/s$, as shown in Figure 2-20, with amplitude $A_p = 0.17$ g and period $T_p = 1.79$ s. The original sample ground motion is scaled initially to so that the pseudo acceleration at the period $T_b = 4.5$ s is equal to 0.1 g. The motion is then scaled up with an increment of 0.1 g at T_b, and the amplitude associated with the best match pulse is scaled by the same magnitude. As shown in Figure 2-21, when the sample ground motion is scaled to $SA(4.5\text{s}) = 0.2$ g, the best match pulse, with an amplitude of 0.28 g falls in the impact without failure region.

When the motion is scaled to $SA(4.5s) = 0.3$ g, the pulse amplitude is 0.42 g, falling in the failure region. Therefore, the predicted critical $SA(T_b)$ is 0.3 g.
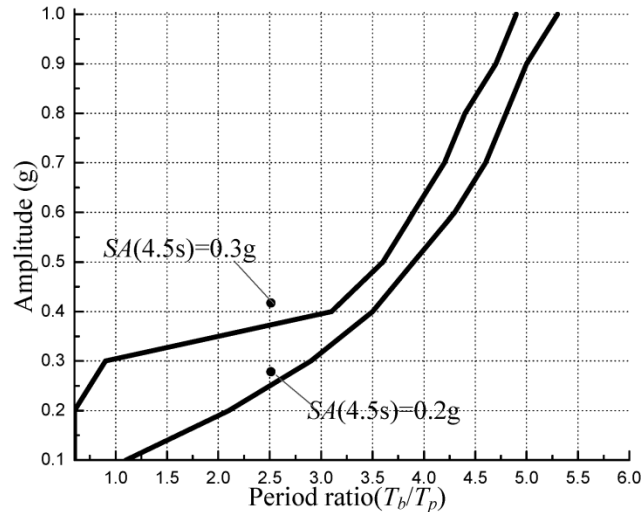
Figure 2-21 Example of failure prediction using impact region spectra

Figure 2-22 compares the predicted and actual critical $SA(T_b)$ for the baseline configuration of DFP. In the study presented here, it is clear that selection criterion No. 3 offers the best prediction results for the fourteen pairs of pulse-like ground motions recommended by FEMA P695; only 7 out of 28 pulse-type ground motions are overestimation of the critical $SA(T_b)$ compared to real ground motions. Another study conducted by Bao and Becker (2016) found that criterion No. 4 gave the best estimation for a set of Japanese ground motions. Although the best match pulse selection criterion is different for the two sets of ground motions, it is apparent that the analytical pulse extracted from the velocity record provides better prediction than that from acceleration record. This finding is consistent with the methodology proposed by Baker (2007). Bao and Becker (2016) found that for the Japanese ground motion set, using criterion No. 3 resulted in several very short period pulses (much less than 0.5 s), which could not well

predict the failure of the baseline DFP. While this did not occur for the FEMA ground motions with either criterion Nos. 3 or 4, it was true of criterion Nos. 1 and 2 which resulted and many very short period pulses along with many poor estimations. Examining the pulses selected from the FEMA motions using criterion No. 3, long period pulses are usually associated with low amplitudes, the longest period Ricker pulse is 5.14 s with an amplitude of 0.056 g, while the shortest period is 0.52 s with an amplitude of 0.61 g.

Using criteria No.3 resulted in using the pulse coming from the weighting function $w(s)=1/s$ for approximately 90% of the motions. Criteria No.4 resulted in using the weighting function $w(s) = 1/\sqrt{s}$ for all motions. The weighting function $w(s) = 1$ never resulted in the best match pulse. The subject of how to select the most representative analytical pulse from a real ground motion still needs more future study, especially as performance predictions are highly dependent on the pulse period, amplitude, and shape.

When the bearing design parameters vary, the comparisons between the predicted and actual critical $SA(T_b)$ using the pulses from criteria No.3 can be found in Table 2-1. It is found that generally the prediction results are good, the number of overestimation of critical $SA(T_b)$ is usually around seven. When the aspect ratio $\rho = 0.328$, the predictions based on the actual and proposed impact region spectrum discussed in Section 2.4.4 are compared. It is shown that the prediction made from the proposed impact region spectrum is significantly better.
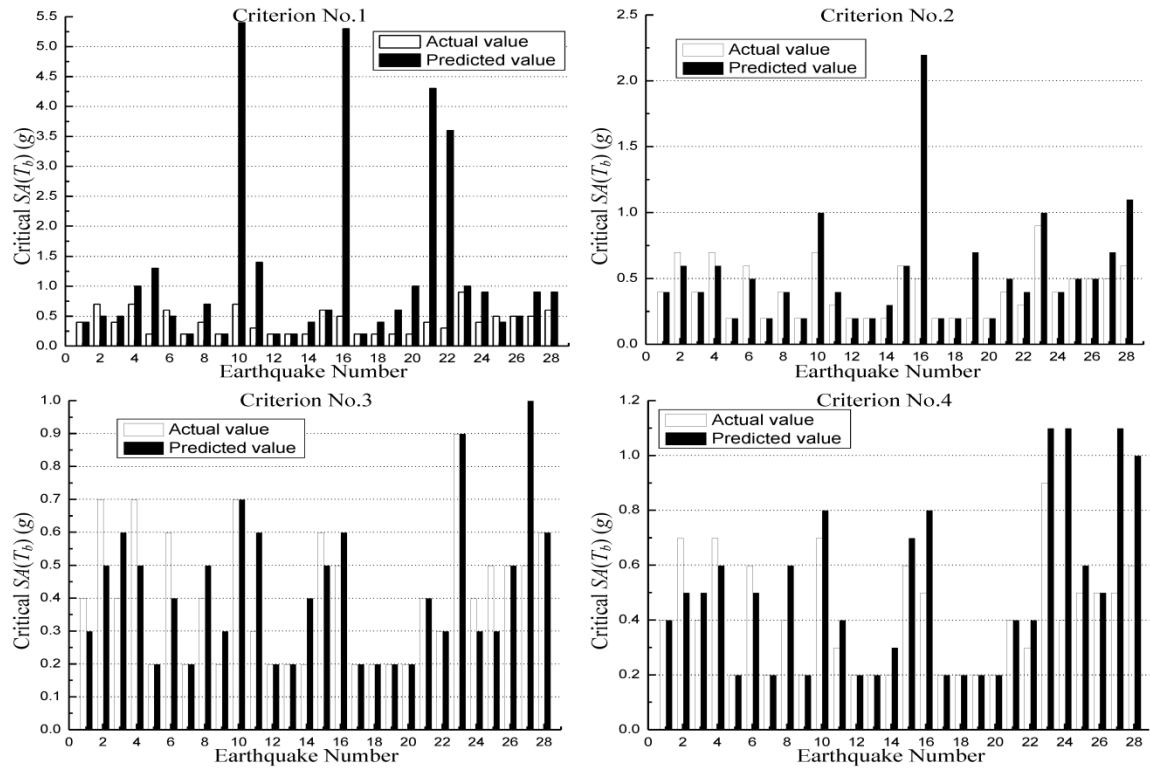
Figure 2-22 Comparsion of predicted and actual critical SA for the baseline configuration of double friction

pendulum

In Japan, where these specific bearings are manufactured, there are a set number of design parameters that have been approved for sale by the government, as each design offered for sale must pass rigorous governmental testing similar to prototype testing in the US but not done on a case-by-case basis. Thus, the impact region spectra could be provided up front for each bearing design. The impact region spectrum could then be used by designers for incremental analysis as shown previously, or the designer could simply plot the period and amplitude of the best match extracted pulse of a design ground motion on the impact region spectra to find the expected performance. The impact region spectrum is also useful for quick calculation of the collapse margin ratio, assuming

structural failure is dominated by the isolation system failure. For countries in which a wider variety of bearing designs are available, a finite number of impact region spectra could help inform initial bearing design.

Table 2-1 Comparison of the predicted and actual spectral acceleration for different design parameters

Design parameters	Underestimation of critical $SA(T_b)$	Exact estimation of critical $SA(T_b)$	Overestimation of critical $SA(T_b)$	Median value of $SA(T_b)$ overestimates
Baseline design	7	14	7	0.2g
Change with friction coefficient μ				
$\mu = 0.02$	10	12	6	0.2g
$\mu = 0.08$	5	17	6	0.15g
Change with radius of curvature R				
$R = 3.5$ m	5	15	8	0.1g
$R = 4.5$ m	4	17	7	0.1g
Change with bearing diameter D				
$D = 620$ mm	6	13	9	0.1 g
$D = 820$ mm	8	12	8	0.15 g
Change with restrainer height h				
$h = 9$ mm	10	11	7	0.2g
$h = 15$ mm	8	15	5	0.2g
Change with slider aspect ratio ρ				
$\rho = 0.328$ (actual)	5	7	16	0.25g
$\rho = 0.328$ (proposed)	14	7	7	0.2g
$\rho = 1.0$	3	15	10	0.1g

2.6 Conclusions

In this paper the failure of the double friction pendulum bearings (DFP) subjected to pulse-type ground motions was analyzed. The DFP was originally investigated under Ricker pulses because these pulses are mathematically simple, with only amplitude and period as parameters, and they can be used for wavelet analysis. Compared to detailed finite element analysis, it was found that the rigid body model provides a good estimation of when failure occurs. It was found that for short period pulses, the failure of the DFP was usually caused by one strong impact, however, for long period pulses, the failure happened after rebound from a prolonged impact.

After analysis of the failure of the DFP subjected to Ricker pulses with a range of amplitudes and period ratios, an impact region spectrum was developed to efficiently determine the response of the DFP (i.e. no impact, impact without failure, or impact with failure) to a particular pulse. Using the impact region spectra, the influences of several design parameters on the stability of the DFP were investigated. It was found that:

1) Large masses caused yielding of restraining rims, which can change the failure behavior of the bearing from uplift to failure of the restraining rims. This increases the failure region, particularly in the region of long period pulses.

2) Friction coefficient has a complex influence on the shape of impact region spectra. However, if presented in the dimensionless terms, the effect become clearer, and increasing the friction coefficient increases the regions of impact and failure when the acceleration amplitude is normalized through the friction coefficient.

3) Increasing the radius of curvature makes DFP bearings more vulnerable to Ricker pulses with high period ratios, which means it is detrimental for avoiding both impact and failure. However, when considering the pulse period rather than the period ration, changing the radius of curvature had little to no benefit in avoiding impact of failure.

4) The influence of the restrainer height within normal design ranges was insignificant.

5) Decreasing the aspect ratio of the slider had the largest effect in decreasing regions of impact and failure as the sliders with lower aspect ratio have greater stability.

To validate the use of Ricker pulses and their associated impact region spectra for the prediction of DFP bearing failure, 28 pulse-type ground motion records were analyzed with wavelet analysis to extract analytical Ricker pulses, and the best match extracted pulses were used to estimate the critical pseudo acceleration that results in the failure. It was found that using extracted Ricker pulses with the impact region spectrum provides a good estimation for failure prediction. Given impact region spectra for a number of existing bearing designs, this method offers a relatively simple yet effective way to predict the critical responses.

Acknowledgements

References

Anagnostopoulos SA (1988). Pounding of buildings in series during earthquakes. *Earthquake Engineering and Structural Dynamics*,16:443-456.

Applied Technology Council (2009). FEMA P695: Quantification of building seismic performance factors. Washington, D.C, USA.

Baker JW (2007). Quantitative classification of near-fault ground motions using wavelet analysis. *Bulletin of the Seismological Society of America*, 97(5):1486-1501.

Bao Y and Becker TC (2016). Predicting failure in sliding isolation bearings under long-period motions. *CSCE 5th International structural specialty conference*. London, Ontario, Canada, June 1-4.

Davis RO (1992). Pounding of buildings modelled by an impact oscillator. *Earthquake Engineering and Structural Dynamics*, 21:253-274.

Jankowski R (2005). Non-linear viscoelastic modelling of earthquake-induced structural pounding. *Earthquake Engineering and Structural Dynamics*, 34:595-611.

Jankowski R (2006). Analytical expression between the impact damping ratio and the coefficient of restitution in the non-linear viscoelastic model of structural pounding. *Earthquake Engineering and Structural Dynamics*, 35:517-524.

Jankowski R (2010). Experimental study on earthquake-induced pounding between structural elements made of different building materials. *Earthquake Engineering and Structural Dynamics*, 39:343-354.

Kelly JM, Konstantinidis D (2011). Mechanics of Rubber Bearings for Seismic and Vibration Isolation. Wiley.

Komodromos P, Polycarpou PC, Papaloizou L and Phocas MC (2007). Response of seismically isolated buildings considering poundings. *Earthquake Engineering and Structural Dynamics*, 36:1605-1622.

Masroor A. and Mosqueda G (2012). Experimental simulation of base-isolated buildings pounding against moat wall and effects on superstructure response. *Earthquake Engineering and Structural Dynamics*, 41: 2093–2109.

Mavroeidis GP and Papageorgiou AS (2003). A mathematical representation of near-fault ground motions. *Bulletin of the Seismological Society of America*, 93(3):1099-1131.

Muthukumar S, DesRoches R (2006). A Hertz contact model with non-linear damping for pounding simulation. *Earthquake Engineering and Structural Dynamics*, 35:811-828.

Pant DR, Wijeyewickrema AC (2014). Performance of base-isolated reinforced concrete buildings under bidirectional seismic excitation considering pounding with retaining walls including friction effects. *Earthquake Engineering and Structural Dynamics*, 43: 1521-1541.

Ricker N (1944). Wavelet functions and their polynomials. *Geophysic*s ,9:314-323.

Ricker N (1943). Further developments in the wavelet theory of seismogram structure. *Bulletin of the Seismological Society of America*, 33:197-228.

Sarlis AA and Constantinou MC (2013). Model of triple friction pendulum bearing for general geometric and frictional parameters and for uplift conditions. Technical report MCEER-13-0010, Buffalo, NY, USA.

Vassiliou MF, Tsiavos A and Stojadinovic B (2013). Dynamics of inelastic base-isolated structures subjected to analytical pulse ground motions. *Earthquake Engineering and Structural Dynamics*, 42: 2043-2060. DOI: 10.1002/eqe.2311.

Vassiliou MF and Makris N (2011). Estimating time scales and length scales in pulselike earthquake acceleration records with wavelet analysis. *Bulletin of the Seismological Society of America*, 101(2):596-618. DOI: 10.1785/0120090387.

Chapter 3 Experimental Study of the Effect of Restraining Rim Design on the Extreme Behavior of Friction Pendulum Bearings

Abstract

While the performance of sliding isolator has been extensively validated under typical levels of ground motion, there have been very few experimental studies on the extreme behavior of sliding isolation bearings when the displacement limit is reached. However, in order to appropriately design isolated systems, from selecting the size of the bearing to sizing the superstructure members, the behavior of the bearing as it reaches, and in some cases exceeds, the displacement limit should be well understood. A series of shake table tests to investigate the extreme behavior of double pendulum sliding bearings under strong ground motions were conducted at McMaster University. One major difference in sliding bearings around the world is how the motion of the bearing is restrained at the bearing's displacement capacity. Scaled bearings with four different types of restraining rim designs were included, representing typical sliding restraining rims found in Europe,

Japan, and the United States. Experimental observation shows that the restraining rim has a significant influence on the extreme behavior of sliding isolation bearing. Key response parameters such as impact force and uplift are evaluated and compared between the different sliding bearing designs. While the bearing with flat rim bearing imparts the lowest forces to the superstructure, it loses its functionality at a lower amplitude input than all the other rim types. For the other rim designs, the impact forces are significantly higher but they remained operational although damaged.

3.1 Introduction

It is well known that seismic isolation can elongate the natural period of structures and thus substantially reduces the base shear; however, this usually comes at the expense of large horizontal displacements. Excessive displacements are a potential issue for the safety of the isolated superstructure. They can result in the failure of isolation bearing itself or cause the superstructure to impact against the surrounding moat wall, which may damage or even induce collapse of the superstructure. Masroor and Mosqueda have experimentally studied the effect the impact of isolated structure against the moat on the superstructure response (Masroor and Mosqueda 2012), they found the impact force can significantly increase the peak acceleration at the first floor, resulting in considerable yielding and residual drift in the superstructure. They have also developed an impact model to capture both the global and local responses of the moat wall during impact (Masroor and Mosqueda 2013).

Sliding isolation bearings consist of one or more sliders with friction liners and corresponding concave sliding plates. Often there is a restraining rim along the perimeter of the sliding plate to prevent the slider from exceeding the displacement capacity and dropping off the sliding surface. The study here focuses on a non-articulated double pendulum sliding bearing shown in Figure 3-1, which has one slider with concave sliding plates on the top and bottom. The articulated double friction pendulum bearing, which is more common in the United States (Fenz and Constantinou 2006), is also shown in Figure 3-1 for comparison. A previous study (Bao et al. 2017) on the failure mechanism of double pendulum sliding bearings with fully connected restraining rims showed that there are two types of failure modes for the bearings: one due to uplift and the other due to yielding of the restraining rim. Yielding versus uplift behavior was dependent on the mass of the superstructure. However, this study did not consider other restraining rim design in the world and lacks of supporting experimental evidence.

Past experimental studies (Morgan 2008; Fenz and Constantinou 2007; Becker and Mahin 2012; Sasaki et al. 2012) have focused on the sliding isolation response under typical conditions, either to examine seismic performance or verify bearing model theories. There has been very limited experimental study on the extreme behavior of sliding isolation bearings. Sarlis et al. (2013) tested the triple pendulum sliding bearing until the isolation bearing impacted its restrainer. In their experiment, they observed the isolation bearing uplifted due to the impact. However, impacts were minor and the isolation bearing was never tested to failure. Additionally, the effect of the restraining rim design was not investigated. Becker et al. (2017) experimentally and numerically

investigated the extreme performance of a steel frame isolated on six triple pendulum sliding bearings. This investigation looked at the failure of triple pendulum sliding bearings which included both bolt shear and slider uplift. Again this study looked only at one type of restraining rim.

This paper presents an experimental study on the extreme behavior of double pendulum sliding bearings with the intent of better understanding the margin of safety available in designs. Four sliding isolation bearings all with identical friction coefficient, sliding radius, and displacement capacity were tested. However, each bearing had a different restraining rim design, representative of sliding bearings in Europe, Japan and the United States. In Europe sliding isolation bearings are not permitted to include a restraining rim (European committee for standardization 2009) to ensure that no impact force will be transferred to superstructure. However, there is nothing to limit the internal slider from sliding beyond the bearing causing loss of functionality of the isolator. In the United States, sliding isolation bearings include fully connected restraining rims to limit the displacement of the bearing in an extreme event. In Japan bearings with separate restraining rims bolted to the sliding surface are available as well as bearings with no restraining rims. Experimental observations gained through two high speed cameras demonstrate that the different restraining rim designs have significant influence on the extreme behavior of double pendulum sliding bearings. Key response parameters, including peak shear force, peak axial force and uplift displacement, are also evaluated and compared between different types of sliding bearings.

3.2 Experimental Setup

The sliding isolation experiments were conducted at the Applied Dynamic Laboratory at McMaster University using a bidirectional shake table with a displacement capacity of 350 mm. Only uniaxial input was used in the North-South direction. The three-dimensional schematic drawing and real experimental setup are shown in Figure 3-2. In order to concentrate on the extreme behavior of the isolation bearings only two isolators were tested at a time, aligned in the North-South direction, and a rigid block constructed from two concrete blocks was used to provide adequate pressure on the two bearings. Each block was 2.8 m x 2.0 m x 0.4 m and together weighed approximately 110 kN. As the concrete blocks were only supported along a line, they were inherently unstable in the East-West direction. To constrain the out-of-plane behavior of the concrete blocks, two reaction frames were designed with four roller bearings on each frame to restrain the concrete blocks while allowing them to move in the North-South direction. The roller bearings imparted significant forces on the blocks that were unfortunately not able to be measured. The three catching beams in the setup were to protect the shake table in the event that the isolation bearings lost their load-carrying capacities. The connection of an isolation bearing between the shake table and concrete block is shown in Figure 3-1.
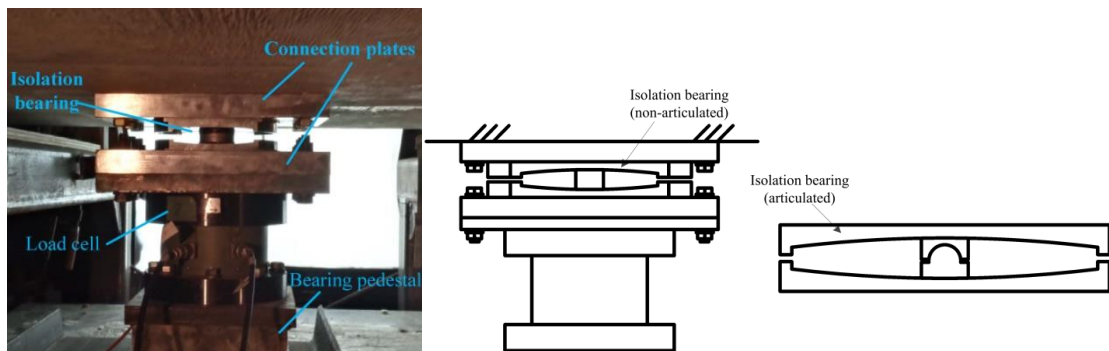
Figure 3-1 Connection of isolation bearing with shake table and concrete block
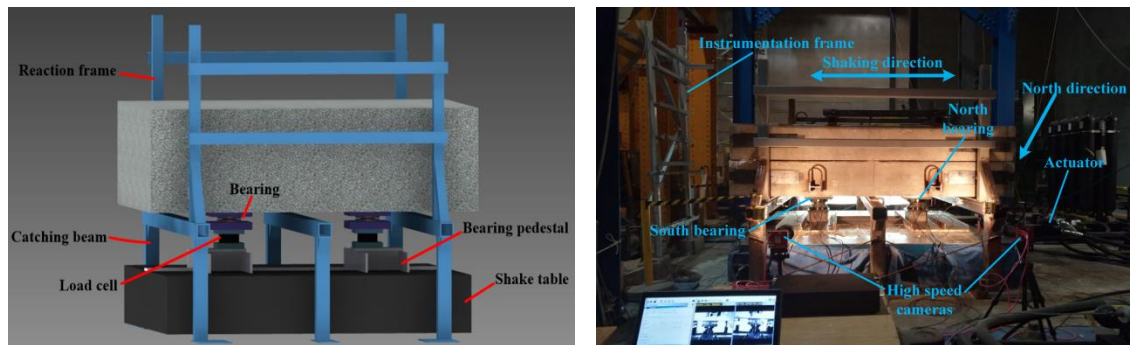
Figure 3-2 Three-dimension and real experimental setup

3.2.1 Sliding bearing specimens

The sliding bearing model properties were based on commercially available prototype bearings. Considering the displacement capacity of the shake table and load capacity of the actuator, a length scale, defining the ratio of the dimensions of the prototype bearing to the model bearings, of $L = 3.5$ was selected. The geometric properties of prototype bearing, based on the dimensions of a commercially available bearing, and scaled model bearing are listed in Table 3-1. While the properties for the sliding surfaces remained the same, four different types of restraining rims were designed for this experiment, depicted in Figure 3-3:

1) Specimen A does not have a restraining rim, instead it has a flat periphery with 10 mm width beyond the sliding surface, similar to those allowed in Europe (European committee for standardization 2009). These bearings are also available in Japan.

2) Specimen B has a stopper ring bolted at eight points around the perimeter using M3 screws (M8 bolts in prototype bearing). These bearings are available in Japan.

3) Specimen C has the sliding surface and rim milled from a single piece of steel; thus, the restraining rim is fully connected, as is common in sliding bearings in the United States. The rim thickness was selected to be 5 mm.

4) Similar to Specimen C, Specimen D also has a fully restraining rim; however, the rim thickness was selected to be 10 mm for comparison.

Specimen C and D have rims of varying thickness in order to observe the effect on rim yielding on impact behavior. In order to design the thickness of the fully connected rims, a two-dimensional finite element model of double pendulum sliding bearings was created in ABAQUS, following the modeling described in Bao et al. (2017). It was found that for rim thickness of 5 mm its primary failure mode is rim yielding with minor uplift, and for 10 mm thickness uplift is the major failure mode with minor rim yielding, as shown in Figure 3-4.

For Specimen A, C, and D, the sides of the isolation bearing were cut off during manufacturing to aid in visual observation of the extreme behavior. As the ground motion input was unidirectional, this did not affect sliding behavior. To justify that this would not affect the impact behavior, a three-dimensional finite element model was used to investigate the stress distribution when the impact occurred. The maximum impact force

from the two-dimensional case was used as a static force applied to the three-dimensional model. The resultant Von Mises stress distribution shown in Figure 3-4. It was observed that the regions of large stress are well within the impact region of the rim.

Table 3-1 Geometric properties of prototype bearing and model bearing

Bearing property	Prototype bearing	Model bearing with length scale $L = 3.5$
Radius of curvature R (m)	2.5	0.714
Inner slider diameter D_{sl} (mm)	200	57.1
Inner slider height h_{sl} (mm)	104	29.7
Plate inner diameter D (mm)	670	191.4
Restraining rim height h (mm)	12	3.4
Displacement capacity (mm)	450	130
Second stiffness period (s)	4.5	2.41
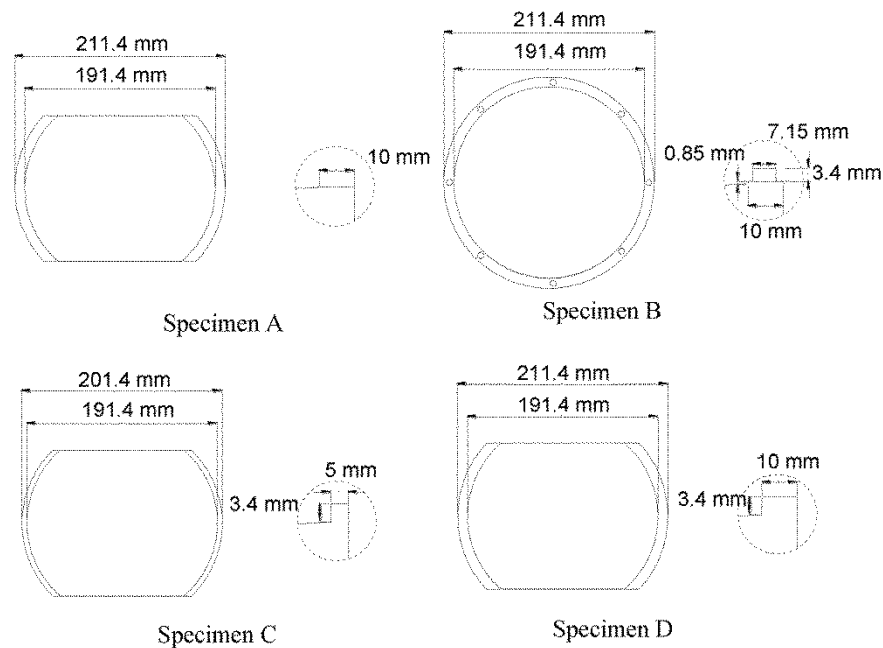
Figure 3-3 Sliding bearing specimen dimensions with the restraining rim detail magnified
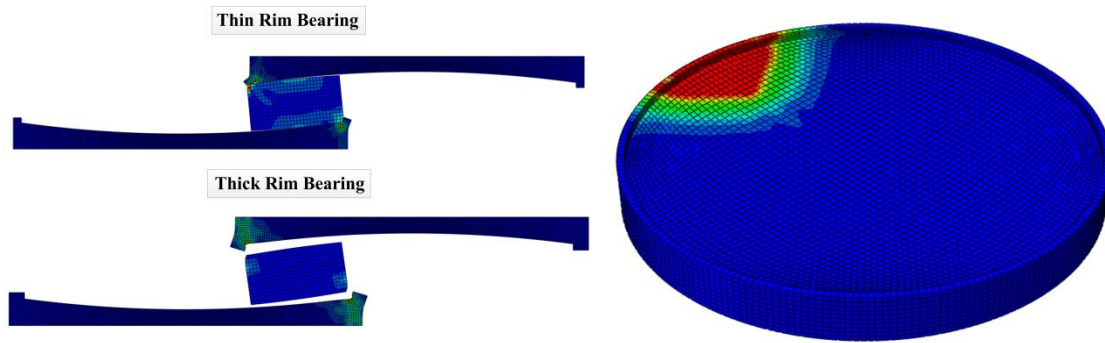
Figure 3-4 Preliminary finite element analysis results. Left: failure modes; Right: Von Mises stress distribution under statically applied impact forces

The friction coefficient is dependent on bearing pressure, sliding velocity, and temperature (Constantinou et al. 1990). Properties provided by the bearing manufacturer state that under 60 MPa pressure, 400 mm/s, and 20 ℃ the friction coefficient is nominally 0.06. Each specimen was tested with a new slider, all sliders had identical lining material. The friction coefficient was measured by calibrating a simple bilinear model using test data from the ground motions which did not cause impact. The calculation of the friction coefficient was based on approximately equating the hysteretic energy between the numerical model and experimental results. The friction coefficient did not vary significantly between the tested isolation bearings: the lowest measured friction coefficient was 0.123 for the Specimen B north bearing, and the highest was 0.133 for the Specimen A south bearing. On average for all of the bearings, the friction coefficient was 0.126. This high friction coefficient may be attributed to the lower pressure (22 MPa), relatively low temperature (roughly 15 ℃ to 20 ℃) during test.

3.2.2 Instrumentation

The schematic drawing of the locations of all sensors are shown in Figure 3-5. Two high speed cameras recording at 350 frames per second were used to capture the behavior of the bearings throughout the motion. For all other sensors, a sampling rate of 500 samples per second was used if the bearing displacement was far from impact. For ground motions likely to cause impact, a rate of 2000 samples per second was used. The individual sensors included:

- Four wire potentiometers to measure the displacement of the shake table and the concrete blocks. The potentiometers were located so that rocking and potential torsion of the blocks could be measured.

- Two accelerometers, located on the south surface of the concrete blocks, to measure horizontal acceleration, and two more located on the top surface of the concrete blocks to measure vertical acceleration. Again, these were located so that torsion and twist could be identified. All accelerometers have a range of 10 g and measure up to 350 Hz.

- Four laser transducers, mounted to the catching beams, to measure the vertical displacement of the concrete blocks due to uplift or in- or out-of-plane rocking of the concrete blocks.

•   Load cells, installed below the double pendulum sliding bearings, to measure the

horizontal shear force and the vertical axial force in the bearings during the test.
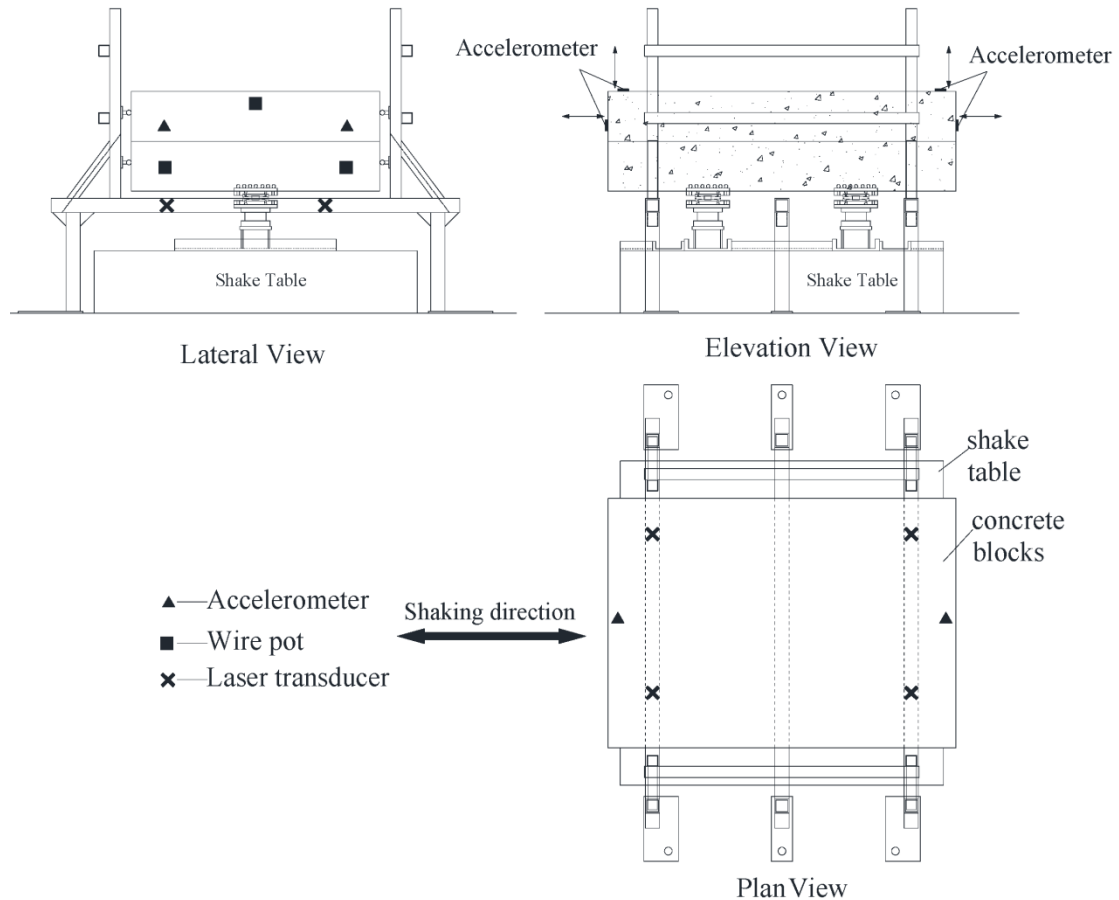
Figure 3-5 Schematic drawing of instrumentation

3.2.3 Input motion and test procedures

The East-West component of the 1995 Kobe earthquake recorded at Takatori station was

selected as the input ground motion. This ground motion was measured near to the fault

and contains a strong velocity pulse. A time scale $T=\sqrt{L}=1.87$ was used to scale the

original ground motion to meet the similitude requirement. In the unscaled ground

motion, referred to as the baseline, the pseudo-acceleration at the model-bearing second

stiffness period (i.e. 2.405 s) is 0.11 g. The acceleration, velocity, displacement time histories, and 5% damped response spectrum are plotted in Figure 3-6. All the input ground motions were amplitude scaled based on the baseline ground motion. Under this motion, the numerical model predicts a maximum displacement of 117 mm with a friction coefficient of 0.125, just 10% below the displacement limit of 130 mm. The margin of safety between the design ground motion displacement and the bearing limit varies greatly depending on the regional design code.

There are two aims to this experimental study: the first is to study the behavior of sliding bearings when they reach their maximum displacement; the second is to compare the performance of the isolation bearings with different rims at maximum displacement. When the bearing impacts its restraining rim, it is possible to damage the rim and affect the bearing's further performance. Thus, it was desirable to limit the number of input motions that involve impact to avoid cumulative damage. As a result, the following test protocol was used: for the bearings with rims, Specimen B, C, and D, 70% of the baseline motion was run and then scaled up with an increment of 20%. At 110% the bearings had just reached or were very close to their maximum displacement, this was dependent on slight variations in slider offsets and friction coefficient. Then, 115% of the motion was run to observe minor impact. After, the ground motion was amplified considerably (155% for Specimen C and D and 135% for Specimen B) to observe the extreme behavior of the different restraining rim designs. For Specimen A, there was no rim to damage, and thus the ground motion was amplified in increments of 5% until the slider displaced outside of the sliding surface. During the sequential tests within each bearing specimen, after each

test was performed, there was an interval to examine the setup conditions and recorded data.

After the extreme behavior tests, only Specimen D was deemed sufficiently undamaged so that further impact testing could be done. This time, after initial impact was detected, the input motion was amplified in increments of 9% to investigate how the maximum impact force and horizontal displacement varied with the increasing excitation. These response parameters were also compared between different bearing specimens to explore the influence of different restraining rim designs.
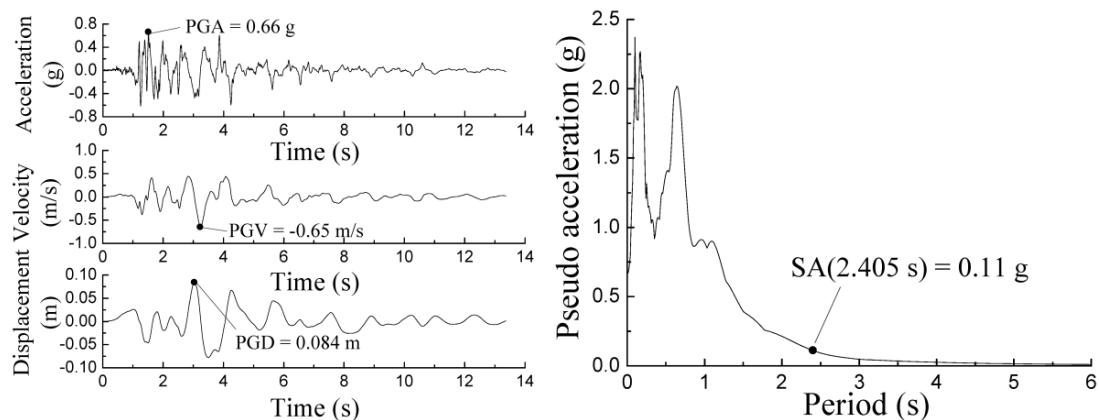
Figure 3-6 Time histories and 5% damped response spectrum of the time-scaled baseline ground motion

3.3 Experimental Observations

In this section the general experimental observations of the isolation bearing's extreme behavior are presented, this includes both the images captured by high speed cameras during the shake table test and physical inspections of isolation bearings after the test.

3.3.1 Specimen A: sliding bearing without a restraining rim

For the bearing with no restraining rim, theoretically, when the slider's center of gravity exceeds the displacement limit of the top or bottom plate, the slider will fall and causing

failure of the bearing. During the test at 115% of the baseline ground motion, the inner slider reached the displacement limit of the spherical sliding surface and just began to move on to the flat 10 mm wide rim. The motion was then incremented at 5%. At 140% of the motion, there was severe abrasion of the friction liners on the inner slider; this was due to the shearing mechanism of flat periphery against the convex slider when excessive horizontal displacement occurred. After this motion, a new set of sliders was installed. At 150% of the motion, high speed cameras show the center of the slider moved past the bottom plate (see Figure 3-7), but inertial forces caused the bearing to reverse; thus, the isolation bearing remained functional after the test.

At 155% of the baseline motion, the slider displaced completely beyond the bottom plate, but, interestingly, the sliders sat on the adjacent connection bolts and the top plate continued to slide, much like a single pendulum sliding bearing, until the test was stopped. Figure 3-8 depicts the behavior of isolation bearing Specimens A under 155% baseline ground motion, and Figure 3-9 shows the isolators directly after motion was stopped. After removing the isolation bearings, inspection showed the surfaces of the inner sliders were severely damaged; the friction liner was sheared and there were indents from where the sliders sat on the connection bolts, as shown in Figure 3-10.
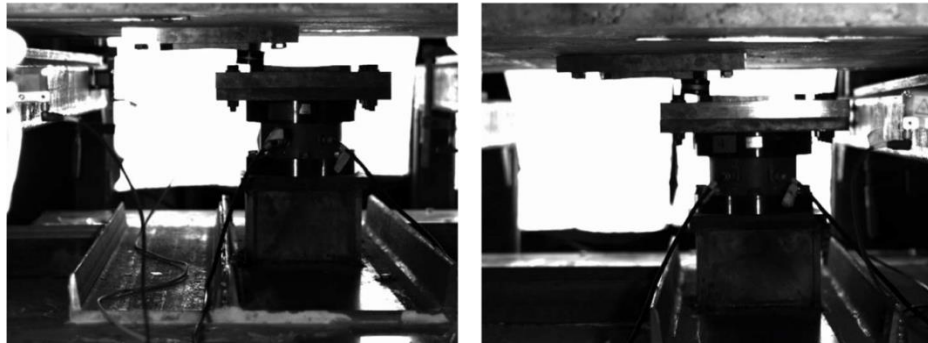
Figure 3-7 Specimen A under 150% baseline motion (left: south bearing, right: north bearing)

Figure 3-8 Specimen A at increasing time steps under 155% baseline motion (left column: south bearing,

right column: north bearing)
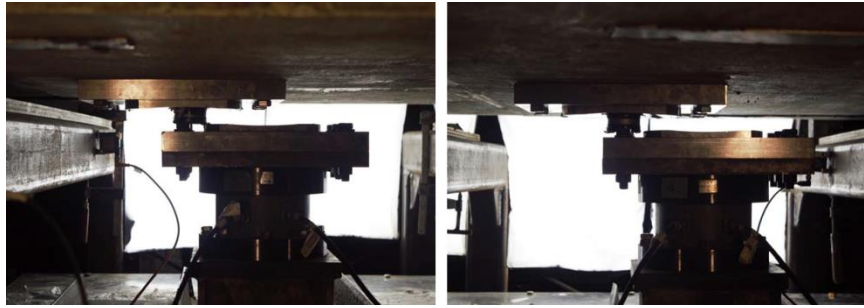
Figure 3-9 Position of Specimen A after 155% baseline motion (left: south bearing, right: north bearing)

Figure 3-10 Inspection of Specimen A

3.3.2 Specimen B: sliding bearing with a bolted restraining rim

As the stopper ring of Specimen B is connected with only eight M3 screws, Specimen B is not expected to carry as large a shear force as Specimen C or D. In reality, impact can occur at any place along the stopper ring; however, in this study the rim was oriented so that the impact occurs directly in the middle of two bolts.

At 115% of the baseline motion, the south bearing experienced slight impact which caused a permanent uplift of the stopper ring so that there was 0.25 mm gap between the ring and the sliding plate. Afterwards, the input motion was then directly scaled up to 135% baseline motion to observe the extreme behavior. Choosing 135% baseline motion is because it is the median value of 115% and 155% baseline motion. Figure 3-11 presents the behavior of the bearing during and shortly after the impact.

There are several noticeable observations: 1) during the impact the behavior of the two bearings was almost identical, there was no major rocking or uplift observed; 2) after the impact, the slider of the north bearing became stuck in the stopper ring of the upper sliding surface. This can be observed in the fourth and fifth image in Figure 3-11, where the slider location varies significantly between the north and south bearing. After this test, 70% of the baseline motion was run without re-centering the isolation bearing; both isolation bearings remained functional although major impact had occurred.

Figure 3-11 Specimen B at increasing time steps under 135% baseline motion (left column: south bearing, right column: north bearing)

The bearings after testing are shown in Figure 3-12, the stopper rings of both isolation bearings experienced large yielding during impact, and two screws from the topper ring of the south isolation bearing were sheared off. During the impact, the sliders were significantly damaged to the point that, during the 70% ground motion, they gouged the steel sliding surfaces. The scratch trace can be seen in Figure 3-12. The damage to the slider surface and scratched concave surface resulted in a higher friction coefficient. Comparison of hysteresis loops from the damaged and undamaged slider under the same ground motion showed the damaged slider increased the friction coefficient by 10% to 15%.
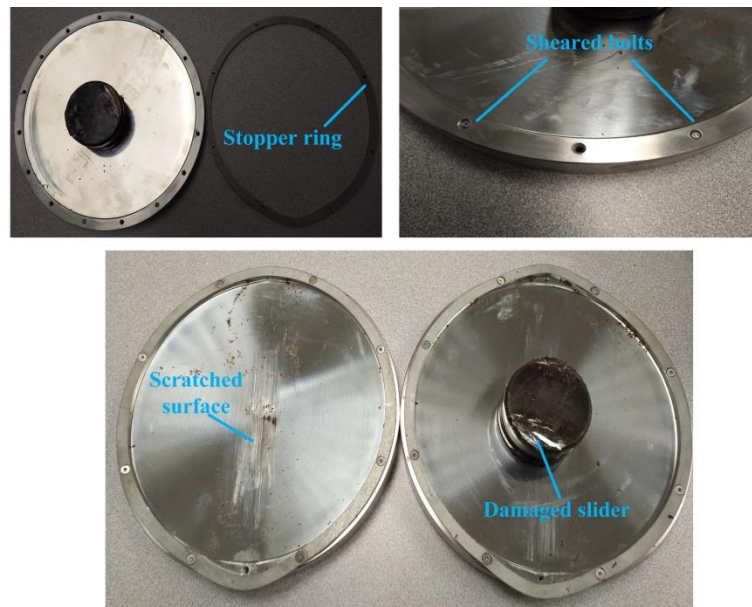
Figure 3-12 Inspection of Specimen B after test

3.3.3 Specimen C: sliding bearing with a thin restraining rim

For this bearing specimen, the rim thickness is only 5 mm, and preliminary finite element analysis predicted that the impact force would cause significant yielding. The first minor impact was observed at 115% of the baseline motion, then the motion was scaled directly

up to 155%. The extreme behavior of bearing Specimen C is presented in Figure 3-13. Compared to Specimen A and B, there are some distinct features associated with behavior of Specimen C: 1) after impact, the slider immediately rebounded; 2) the north and south bearings exhibited different behavior. The north isolation bearing experienced noticeable uplift during impact while the south bearing did not. Figure 3-14 shows the condition of the north isolation bearing after test. As expected, the restraining rim experienced considerable plastic deformation during the impact, and, although hard to notice in Figure 3-14, the opposite side of the restraining rim also developed a smaller amount of plastic deformation during the rebound and impact. The condition of the sliders was significantly better than Specimen B after the extreme motion, only the edges that hit the rims suffered some damage; the remainder of the slider was undamaged. While Specimen C would still be functional for following earthquakes, its performance in subsequent extreme events would be altered if the same portion of the rim was impacted. However, this would not be a likely event.
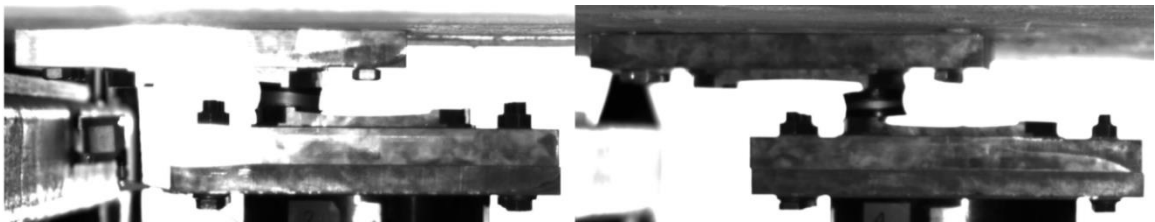
Figure 3-13 Specimen C at increasing time steps under 155% baseline motion (left: south bearing, right: north bearing)

Figure 3-14 Inspection of Specimen C after test (two plates from north isolation bearing)

3.3.4 Specimen D: sliding bearing with a thick restraining rim

Similar to bearing Specimen C, bearing Specimen D also has a fully connected restraining rim, but it is twice as thick, with a thickness of 10 mm. From finite element analysis it was expected that this bearing specimen would exhibit noticeable uplift and would have minimal yielding of the restraining rim during impact. The isolation bearing first exhibited minor impact at 110% of the baseline motion, a very minor dent was noticed in the rim under 115% of the motion. To compare between Specimen C and D, the motion was then directly scaled to 155%. The bearing's behavior is shown in Figure 3-15. Similar to Specimen C, the north and south bearings had different behavior: the north isolation bearing underwent substantial uplift during the impact while the south isolation bearing maintained contact. One observation for the north isolation bearing is that the impact force was large enough to cause the bearing support, designed primarily to transfer the shear force to the table, to rotate, which was only noticeable in the high speed camera footage. How this rotation affects the extreme behavior of isolation bearing remains to be investigated. Afterwards, 70% of the baseline motion was run. The

bearings were completely functional under this motion. Further comparison of hysteresis loops from the same ground motion showed the friction coefficient increased around 5% due to the damaged slider surface. The relatively smaller increase in friction coefficient compared to Specimen B with the bolted rims was consistent with the extent of slider surface damage. Physical inspection of Specimen D after 155% is shown in Figure 3-16; compared to Specimen C this bearing specimen had significantly less plastic deformation.
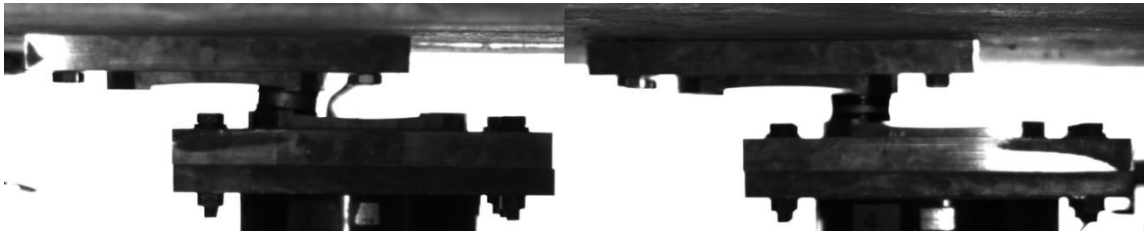
Figure 3-15 Specimen D at increasing time steps under 155% baseline motion (left: south bearing, right: north bearing)
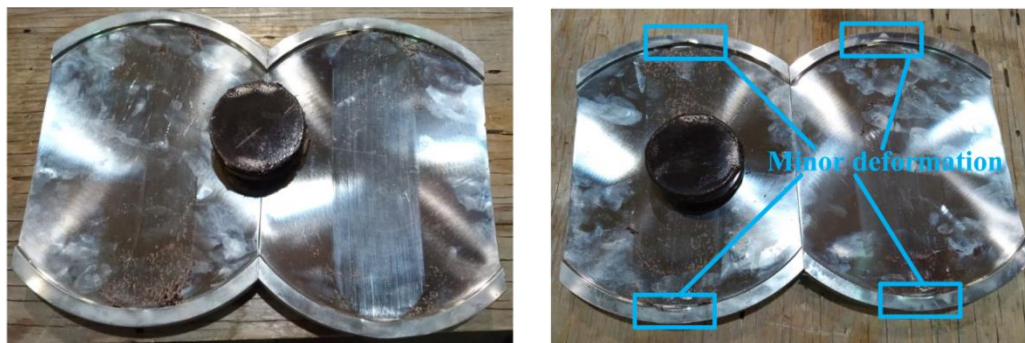
Figure 3-16 Inspection of Specimen D after test (two plates from north isolation bearing)

3.4 Experimental Results

In this section key seismic response parameters from the isolation bearings under extreme conditions are presented, including the horizontal and vertical displacement, axial and shear force, and floor response spectra.

3.4.1 Horizontal and vertical displacement

The horizontal and vertical displacement time histories for each bearing's maximum scaled ground motion are shown in Figure 3-17 and Figure 3-18 respectively. The two dotted lines in Figure 3-17 represent the physical displacement limit of the isolation bearing (i.e. 130 mm) and the dotted line in Figure 3-18 is the vertical displacement of the bearing when it reaches its horizontal displacement with no uplift, determined through the bearing's geometry. The rim design affects the specimen behavior in both horizontal and vertical directions.

From the geometry of bearing Specimen A (see Table 3-1 and Figure 3-3), the maximum displacement is between 180 mm and 210 mm before it is no longer statically stable. At 150% baseline motion this limit was already reached but the inertia force drove the slider back. At 155% baseline motion the slider moved beyond the bottom plate and sat on a connection bolt. After the slider rested on the adjacent bolt, sliding continued on the top sliding surface; this behavior was not predicted. As the pendulum motion on the bottom sliding surface was lost, there was significant residual displacement. Moving beyond the capacity of the sliding surface also caused a large vertical displacement. However, the difference in the vertical displacements between the north and south bearings was only 1.4 mm, indicating that no significant rocking or uplift occurred.

For bearing Specimen B, C and D, the horizontal displacement histories for the maximum motion were very similar, all had three impacts during the ground motion. The maximum horizontal displacements for them were 150.2 mm, 147 mm and 145.5 mm, respectively. Compared to the physical displacement limit of 130 mm, the large

horizontal displacement may come from a combination of rim yielding and slider rotation during uplift. While Specimen B had the smallest input motion (135% as compared to 155% for the other two specimens), it had the largest plastic deformation. Specimen D had the smallest rim deformation. The yielding in the restraining rim acted as a damper; after the third impact, Specimen C had a smaller rebound displacement than Specimen D. Specimen B has a much smaller rebound; however, this may come from the stopper ring dissipating more kinetic energy or due to the smaller ground motion input. When comparing the vertical displacement history, these three specimens had very different behavior. The vertical displacement difference between the north and south bearings was only 0.7 mm for Specimen B but was as large as 14.6 mm for Specimen C and 15.9 mm for Specimen D. The large vertical displacement associated with Specimen D may be attributed to its thicker rim, which results in uplift rather than rim yielding.
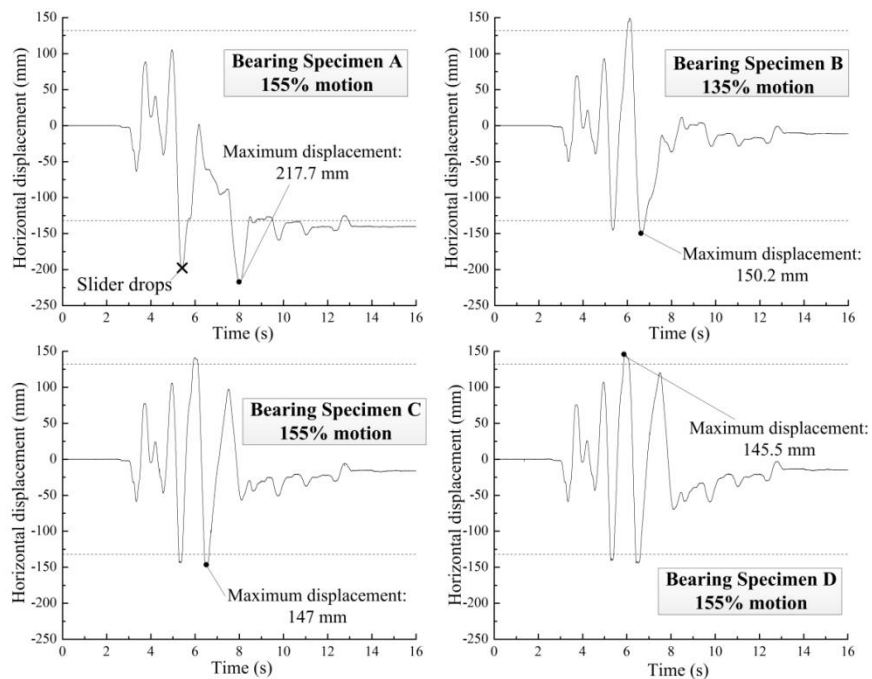
Figure 3-17 Isolation bearing horizontal displacement responses
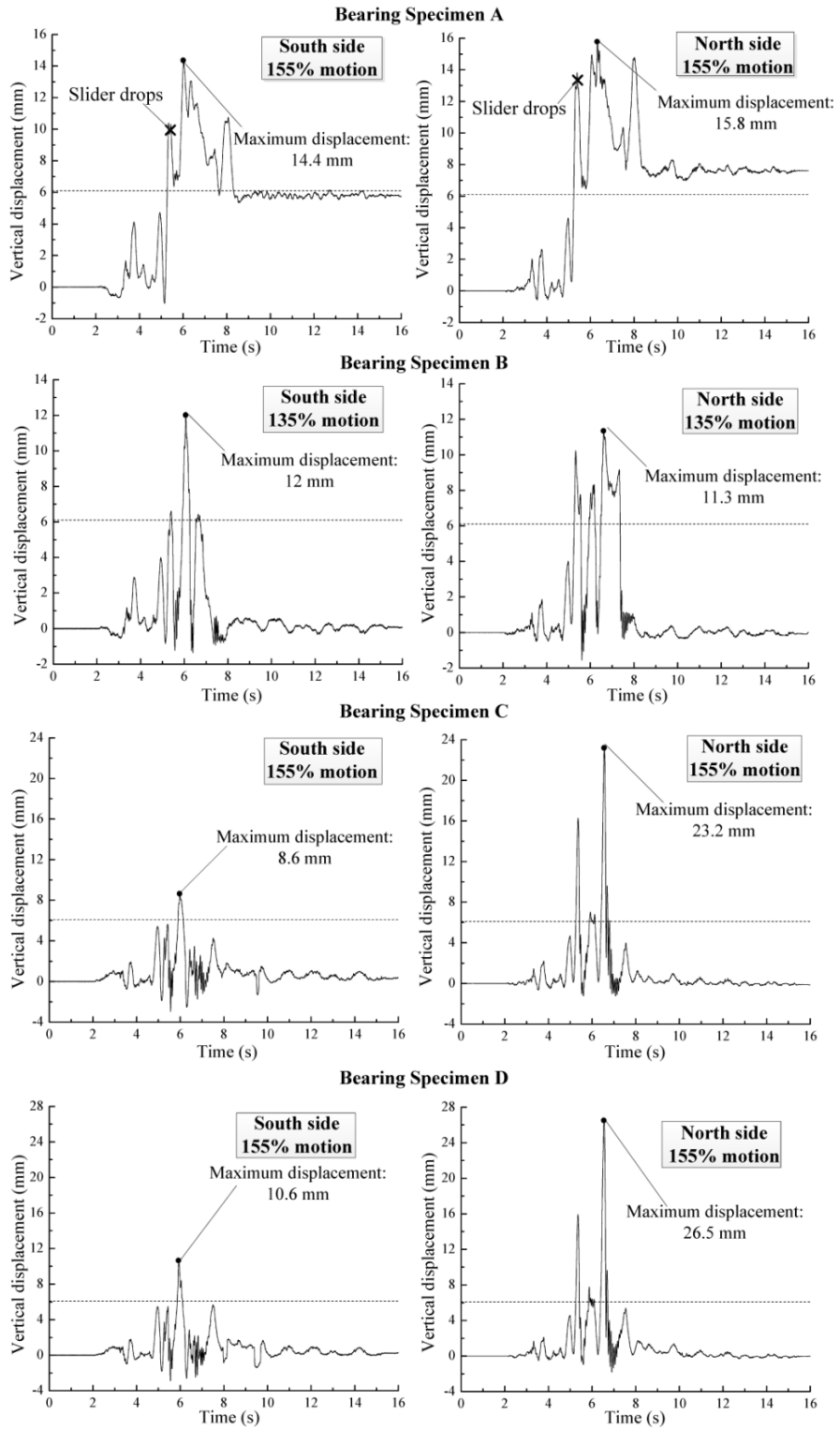
Figure 3-18 Isolation bearing vertical displacement response

3.4.2 Forces

Forces caused under extreme conditions are of great interest as they are transferred into the superstructure. Figure 3-19 shows the shear force time history while Figure 3-20 shows the hysteresis loops for each specimen. Bearing Specimen A had the smallest peak shear forces. This is expected as the lack of restraining rim means that no impact forces can be induced. The hysteresis loops of Specimen A are quite interesting. As the slider exceeded the spherical sliding surface, the shear force dropped due to the slider rotating as it moved onto the flat periphery which does not provide any secondary stiffness; this can been seen in Figure 3-21 which shows the hysteresis of the bearing only before the slider displaces beyond the bearing's capacity. After the slider landed on the adjacent bolt, sliding still continued on the top surface, and the bearing exhibited a standard bilinear hysteresis curve centered at -150 mm but now with a secondary stiffness twice that of the original stiffness. This increase in stiffness corresponds to sliding on one surface rather than two. The bearing still exhibits a jump in force, reaching roughly 30 kN or 0.56 g. This jump in force occurred after the bearing was sliding only on one surface and when the relative displacement was roughly zero. From the high speed camera videos it was inferred that this impact force may come from the slider hitting the bolt of the top connection plate, as shown in Figure 3-20.
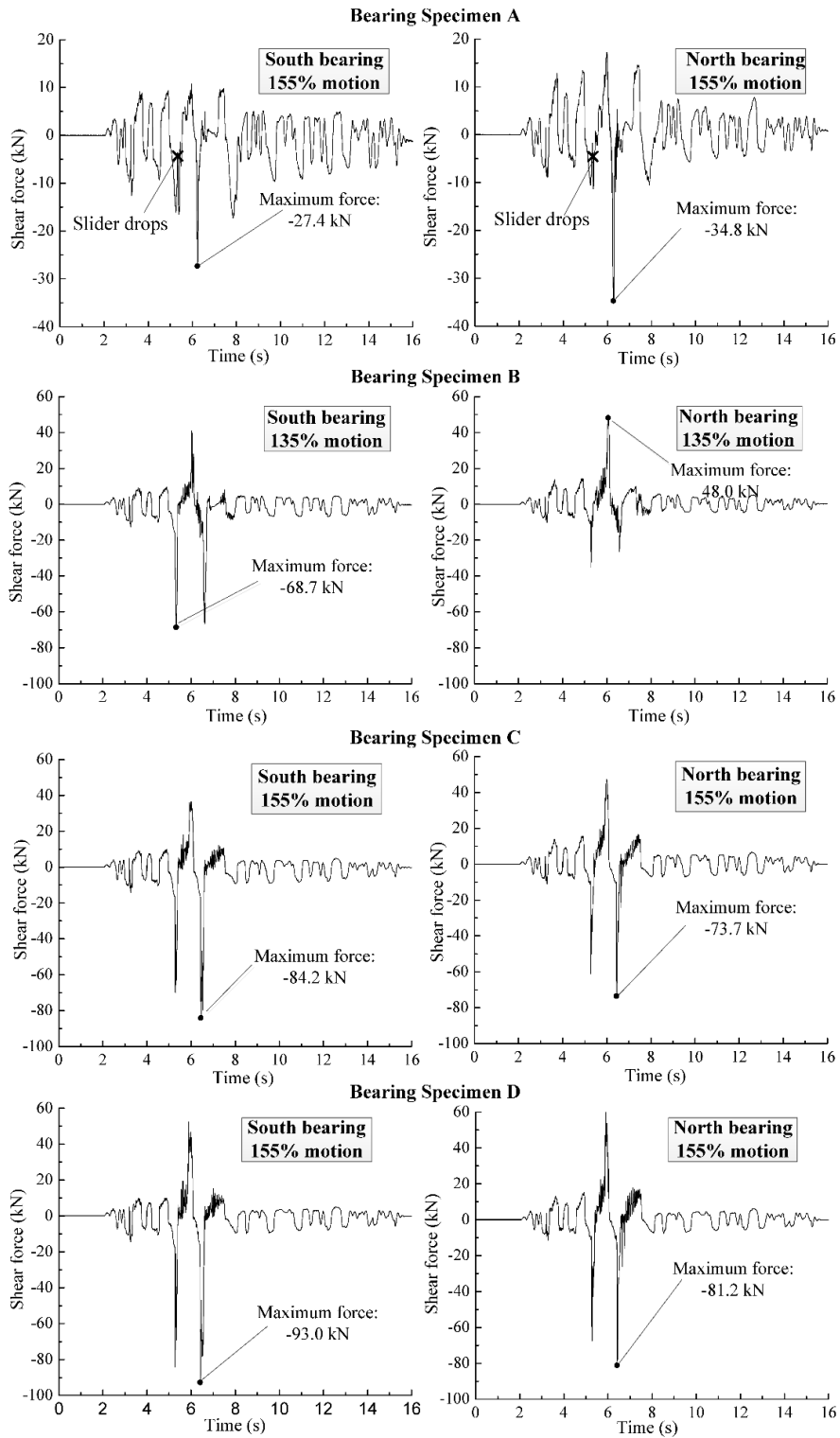
Figure 3-19 Shear force time history

For bearing Specimen B, C, and D, the shear force responses are quite similar. There are three clear impacts during the entire ground motion, consistent with the horizontal displacement. The south isolation bearing consistently had a larger peak shear force than the north isolation bearing. This may come from minor misalignment during the construction of the test setup that slightly reduced the displacement capacity of south bearing. In addition, the concrete blocks exhibited large rocking, distributing significantly larger axial load to the south isolation bearing. Specimen B had a peak shear force of 117 kN or 1.06 g, Specimen C had a peak shear force of 158 kN or 1.44 g, and Specimen D had a peak shear force of 174 kN or 1.58 g.
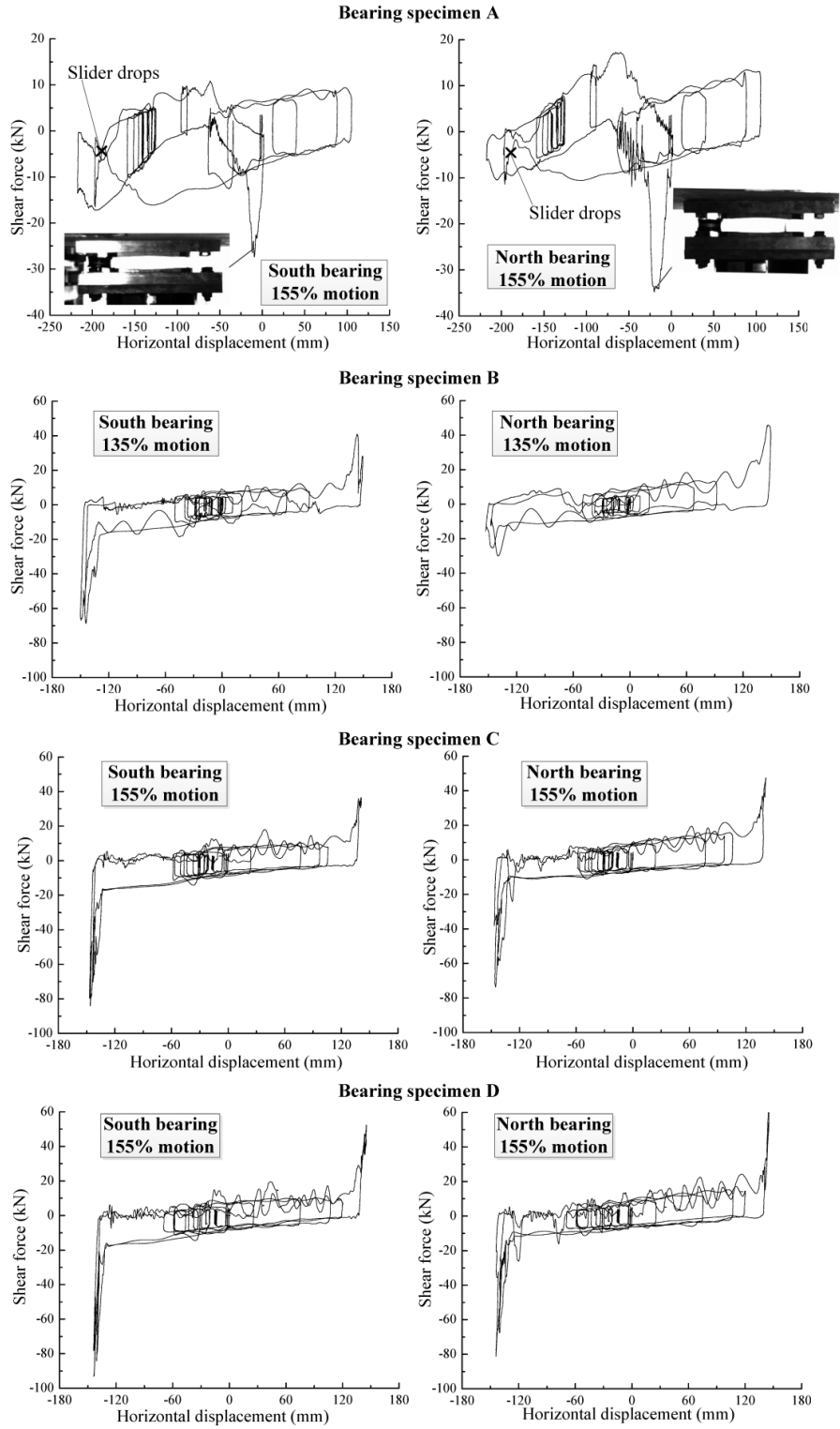
Figure 3-20 Isolation bearing hysteresis loops
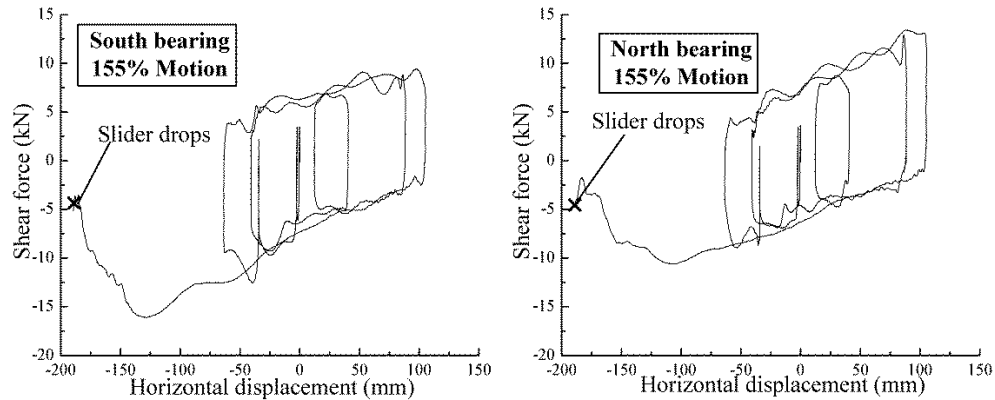
Figure 3-21 Specimen A hysteresis before slider displaces beyond limit and drops

3.4.3 Floor response spectra

The floor response spectra above the isolation layer represent the input to the superstructure. Figure 3-22 plots the 5% damped floor response spectra for all bearing specimens under their maximum run motion. As expected, because there was no impact, the response spectrum above Specimen A has the lowest amplitude across all frequency ranges. The response spectra of bearing Specimen B, C, and D are significantly larger due to the transient impact force. Specimen C and D have very similar floor response spectra shapes due to the similar magnitude of peak shear forces. For the long period region (e.g. higher than 1 s), of concern to relatively flexible superstructures, the response spectra are magnified. For the short period region (e.g. lower than 1 s), the impact causes demands twice of those seen with Specimen A which has no impact. On average all floor response spectra are significantly reduced from the input response spectrum, however, at 0.4 s the floor response spectra are close or even higher than the ground motion response spectrum.
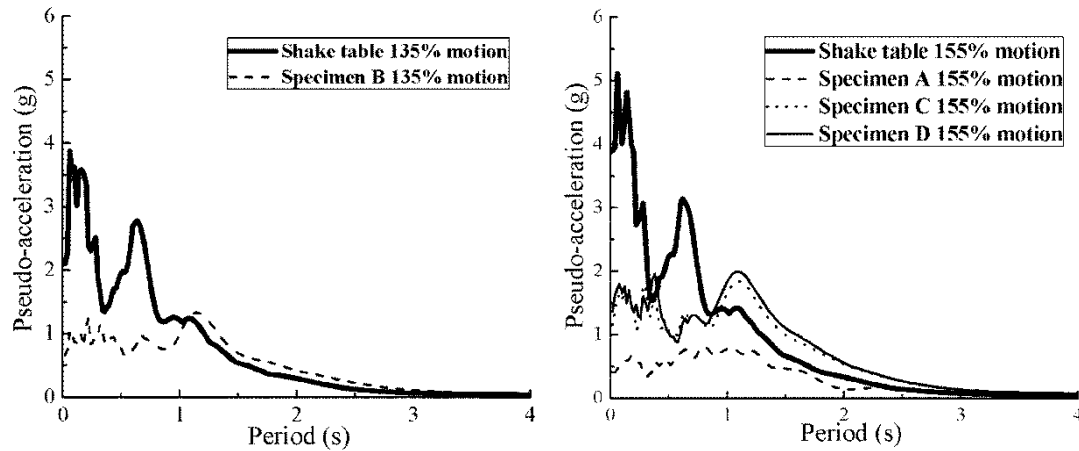
Figure 3-22 5% damped floor response spectra for different specimens

3.4.4 Incremental tests

After the 155% of the baseline motion, Specimen D, with thick restraining rims, had minimal damage, and so was tested under a series of incrementally increasing motions compare performance with Specimen A flat rim bearing and investigate the increase in impact force with magnitude of excitation. The test protocol was similar to Specimen A, at first 70% of the baseline motion was run then scaled up by 20% until 110% baseline motion, under which impact was likely to occur, after this the motion was scaled up with roughly 9% until 155% baseline motion. During the first test, under 137% baseline motion, the impact force caused two concrete blocks to slide to each other, therefore the test was terminated and the measured impact force was deemed inaccurate. During the second test under 146% baseline motion the load cell shear force was overloaded; therefore, the impact force presented is from the accelerometer measurement. Under 155% baseline motion the impact force again caused relative sliding between concrete blocks and the corresponding result is not presented here. The maximum horizontal displacement and horizontal acceleration (in lieu of maximum impact force) are

compared between bearing Specimen A and D in Figure 3-23; data points for bearing

Specimen C are also included.
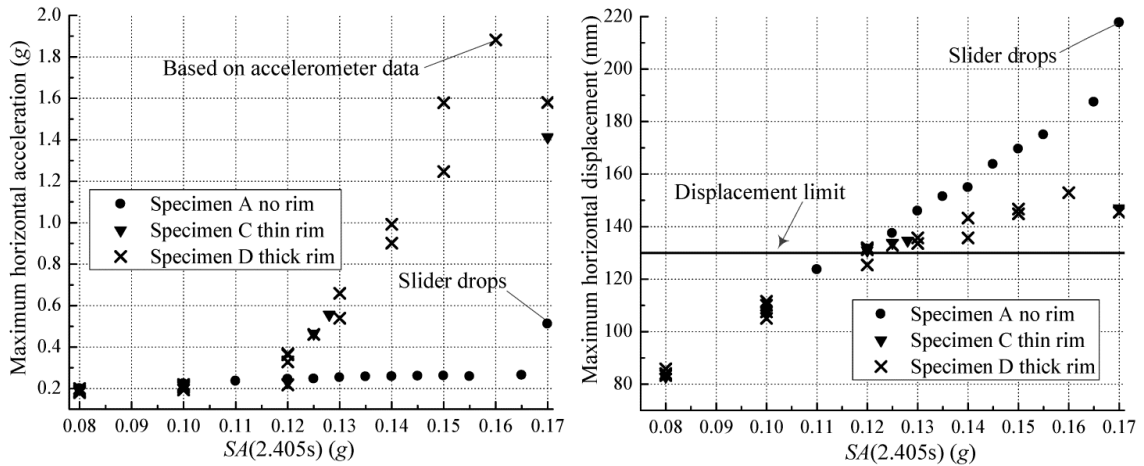
Figure 3-23 Comparison of peak acceleration and displacements under increasing ground motion input

The horizontal axis in Figure 3-23 represents the pseudo acceleration value of

input ground motion at the bearing second-stiffness period which is 2.405 s in this case,

rather than the percentage of baseline motion. The maximum horizontal acceleration is

derived by using the maximum shear force divided by the mass of the two concrete

blocks. For the case $SA(2.405s) = 0.16$ g (i.e. 146% baseline motion), due to the

overloading of load cell the maximum horizontal acceleration is from the accelerometer

data.

The comparison between Specimen A and D in terms of maximum horizontal

displacement and acceleration is straight-forward. As Specimen A does not include the

restraining rim the maximum horizontal acceleration is limited to 0.3 g, but this comes

with the trade-off that the horizontal displacement can be as large as around 200 mm,

which is more than 150% its physical limit. In contrast, Specimen D (as well as Specimen

C) has the displacement limited due to the presence of the restraining rim, but the impact force substantially increases the maximum horizontal acceleration. As the value of SA(2.405s) increases, the maximum horizontal acceleration also increases to over 1 g. During the experiments the maximum horizontal acceleration never exceeds 2 g, this may indicate the yielding of the restraining rim can limit the impact force transferring to superstructure but this still needs more investigation. An important consideration for design is that after the same 155% motion, bearing Specimen D was still functional but Specimen A was not.

3.4.5 Numerical predictions

The preliminary finite element modeling used in the design of the experiment was created with a single bearing, restraining the rotation of the mass above the bearing. However, ignoring this rotation and the presence of two bearings meant that the preliminary modeling did not predict the uplift behavior for thin rim bearing. In the experiments, the rim yielded considerably less than in the finite element prediction.

As finite element analysis is computationally expensive, a rigid body model (Bao et al. 2017) programed in MATLAB was used to predict the critical amplitude of the input ground motions (e.g. response acceleration at the first period $SA(T_b)$). As the rigid body model does not include yielding of the rim, the predictions are the same for Specimens B, C, and D. Two modeling scenarios are used: 1) a single isolation bearing supporting a rigid mass without considering rotational degree of freedom, as done in the preliminary finite element analysis; 2) two isolation bearings supporting the rigid block with actual dimensions capable of rotation. The second method reproduces the non-

uniform behavior between two isolation bearings, which demonstrates the importance to include the rotational component. Using the single bearing, the critical amplitude is 134% of the baseline where as with the two bearing model it is 155% of the baseline. As Specimens C and D both reached 155% without failure, both scenarios under predict the critical amplitude value; however, the model correctly representing the superstructure geometry clearly is superior. The under prediction may be due to the lack of rim yielding in the rigid body model which leads to significant over-predictions of the impact force.

There are multiple considerations to be made regarding the smaller-scale of the bearings, including thermal effects, geometric scaling of the bearing, and superstructure behavior. In this study the effects of temperature are most likely small due to the small size of the slider, but in full-scale isolated structures, temperature may decrease the friction coefficient considerably and therefore change the displacement demand on the isolation bearing including temperature model such as those implemented by Kumar et al. (2015) and Sarlis and Constantinou (2013) would account for these affects. In regards to the geometric scaling, there are two main issues 1) the superstructure mass versus rim thickness, which governs the rim yielding. For this finite element analysis can be used to predict the extent of yielding. 2) the aspect ratio of inner slider. This study investigated only one aspect ratio (i.e. $h_{sl}/D_{sl} = 0.52$) the same as used in the prototype bearings. Bao et al. (2017) showed that a larger aspect ratio may lead to earlier bearing failure. For this a simpler numerical model, such as the rigid body model may be used to investigate failure. Lastly, in the current study the superstructure is represented by rigid concrete blocks to concentrate on the behavior of sliding bearings; however, in real structures the

sub and superstructure are more flexible and may yield, changing the impact force. Thus the extreme behavior in the isolation bearing may not govern the system-level behavior. While the experimental observations presented should be valid in the full-scale isolated structures, the scaling effects will directly dictate at what amplitude the isolation bearing impacts and potentially fails. Either finite element model or the rigid body model (Bao et al. 2017) can be used to determine these effects on the prediction for other ground motions.

3.5 Conclusions

A series of shake table tests were conducted in the Applied Dynamic Laboratory at McMaster University to investigate the influence of restraining rim design on the extreme behavior of sliding isolation bearings. Four different types of restraining rims, representative of typical sliding bearings found in Europe, Japan, and the United States, were tested beyond their displacement limit. It is of note that the bearings were tested with motions up to 25% larger than those causing initial impact; the scale of these motions to those used in design is dependent on the methodology of the design code used. From the tests, several key observations can be made:

1) For the bearings with no restraining rim, in this particular test exceeding the displacement limit did not result in loss of load-carrying capacity. This was a chance event, not expected to happen in full implementation. As there is no impact force, the peak axial force, shear force, and floor response spectra were the lowest among the four rim designs. However, this bearing was no longer functional after the 155% motion

unless the building was physically reset and the inner sliders were replaced. In contrast, the bearings with fully connected rims were operational after 155% of the motion.

2) For the bearings with bolted rims, the impact force caused substantial plastic deformation of the stopper ring and sheared some of the connecting rim bolts. No significant uplift was observed during the impact. The peak shear was the lowest of the three isolation bearings that had restraining rims, approximately 0.56 g. It should be noted the bolted rim bearing was only tested under 135% of the baseline motion, which is less than the other three bearings. After 135% of the baseline motion was run, the bearing still functioned for a 70% motion, although there was significant damage to the slider which, in turn, gouged the sliding surface.

3) For the bearings with fully connected rims, the north isolation bearing underwent large uplift while the south isolation bearing did not. As expected, the thinner restraining rim had significantly more plastic deformation than the thick rim. The thicker rim also led to relatively larger peak shear, 1.58 g, while the thinner rim had a peak shear of 1.40 F. The impact force increased steadily with the magnitude of the input motion.

4) The amplitude of floor response spectrum has a direction relation with the magnitude of peak shear force and isolation bearing without a restraining rim has the lowest amplitude. The impact force has a significant influence on the stiffer superstructure but not on the flexible one.

5) Comparing the performance in terms of displacement and shear force can provide some insights into the influence of restraining rims. The bearings with flat rims have the lowest force but largest horizontal displacement, while other three bearings with

various restraining rim designs have much higher shear force but limited horizontal displacement.

6) Models of single bearings are not adequate in determining the extreme performance of groups of sliding bearings where the geometry of the bearing layout and superstructure aspect ratio have a considerable effect.

Acknowledgements

References

Bao Y, Becker TC and Hamaguchi H (2017). Failure of double friction pendulum bearings under pulse-type motions. *Earthquake Engineering and Structural Dynamics*, 46:715–732.

Becker TC, Bao Y and Mahin SA (2017). Extreme behavior in a triple friction pendulum isolated frame. *Earthquake Engineering and Structural Dynamics*.DOI:10.1002/eqe.2924

Becker TC and Mahin SA (2012). Experimental and analytical study of the bi-directional behavior of the triple friction pendulum isolator. *Earthquake Engineering and Structural Dynamics*, 41: 355-373.

Constantinou MC, Mokha A and Reinhorn A (1990). Teflon bearings in base isolation II: modeling. *Journal of Structural Engineering*, 116: 455-474.

European committee for standardization (2009). European standard 15129: Anti-seismic devices (English version), Brussels, Belgium.

Fenz DM and Constantinou MC (2007). Spherical sliding isolation bearings with adaptive behavior: Experimental verification. *Earthquake Engineering and Structural Dynamics*, 37(2):185–205.

Kumar M, Whittaker AS and Constantinou MC (2015). Characterizing friction in sliding isolation bearings. *Earthquake Engineering and Structural Dynamics*, 44: 1409-1425.

Masroor A and Mosqueda G (2012). Experimental simulation of base-isolated buildings pounding against moat wall and effects on superstructure response. *Earthquake Engineering and Structural Dynamics*, 41: 2093-2109.

Masroor A and Mosqueda G (2013). Impact model for simulation of base isolated buildings impacting flexible moat walls. *Earthquake Engineering and Structural Dynamics*, 43: 357-376.

Morgan TA (2008). The use of innovative base isolation systems to achieve complex seismic performance objectives. Doctoral Dissertation, University of California, Berkeley.

Sasaki T, Sato E, Ryan KL, Okazaki T, Mahin SA and Kajiwara K (2012). NEES/E-Defense base isolation tests: effectiveness of friction pendulum and lead–rubber bearing systems. *Proc. of the 15th World Conference on Earthquake Engineering*, Lisbon, Portugal.

Sarlis AA, Constantinou M and Reinhorn A (2013). Shake table testing of triple friction pendulum isolators under extreme conditions. Report No. MCEER-13-0011, University at Buffalo, Buffalo, NY.

Sarlis AA and Constantinou MC (2013). Model of triple friction pendulum bearing for general geometric and frictional parameters and for uplift conditions. Technical report MCEER-13-0010, Buffalo, NY, USA.

Chapter 4 State-space formulation of a two-dimensional Euler-Bernoulli beam element for the simulation of steel frames

Yu Bao and Tracy C. Becker. State-space formulation of a two-dimensional Euler-Bernoulli beam element for the simulation of steel frames.

Abstract

This paper presents a state-space formulation of a two-dimensional Euler-Bernoulli beam element. There are many effects of concern when conducting nonlinear analysis including nonlinear material behavior and force interaction as well as geometric nonlinearity. Material nonlinearity is implemented by using the versatile Bouc-Wen model, in which important phenomena such as stiffness and strength degradation, pinching effects, and even highly asymmetric hysteresis can be captured. Potential internal force interaction is implemented by introducing a yield surface function. Geometric nonlinearity is achieved through classical co-rotational formulation. While these methods have been presented elsewhere, this paper puts them together for a comprehensive element formulation in the state-space form. Furthermore, the treatment of the hysteretic parameters associated with the Bouc-Wen model is addressed, and it is shown that the parameters should be treated as independent variables rather than determined through interpolation. All the state

variables are evaluated simultaneously in state-space. Through several numerical examples, it is shown that the developed element can be used in nonlinear quasi-static and dynamic analysis. The element can be used to capture the flexural behavior of moment-resisting frames as well as simulate the inelastic buckling behavior of concentrically-braced frames.

4.1 Introduction

Reliable and accurate numerical modeling has increasing importance in both the research and design community. Most seismic design codes only require response spectrum analysis, with linear elastic time history analysis used as a supplementary study during the design stage; however, as current seismic design philosophy allows major yielding to develop in the seismic force resisting system in order to dissipate energy, structures can be expected to exhibit potentially large inelastic response during design basis earthquakes. Consequently, more refined numerical models are required to accurately evaluate the seismic response. In the past decades, a wide variety of structural analysis programs (e.g. SAP2000 and *OpenSees* (McKenna et al., 2002) and finite element analysis programs (e.g. ANASYS and ABAQUS) have become available. These programs greatly expand the capabilities to perform complex and accurate nonlinear dynamic analysis. However, in some particular situations it is desirable to implement models in the state space form, such as when analyzing the structures isolated by friction pendulum bearings modeled by the rigid body model (Sarlis and Constantinou, 2013; Bao et al., 2017) and examining the extreme, even failure behavior in triple friction pendulum bearings (Becker et al., 2017).

As specified in FEMA P695 (Applied Technology Council, 2009), when understanding nonlinear behavior of structures, the numerical model should incorporate, to the extent possible, deteriorating behavior (i.e. strength and stiffness degradation) and second-order geometric effects (i.e. P-Delta effects) to accurately assess the seismic performance. The majority of element formulations and structural analysis programs have implemented these characteristics within the stiffness matrix method.

There is significantly less work using the state-space approach for the dynamic structural analysis. Simeonov et al. (2000) used this approach to analyze the seismic response of a planar frame by formulating the beam element with the flexibility-based method (i.e. force interpolation), in which the material nonlinearity is represented by a Bouc-Wen model with bending moment and curvature included as state variables. Sivaselvan and Reinhorn (2000) then extended this model to include strength and stiffness degradation, pinching characteristic, and gap behavior using series and parallel springs. Within the framework of flexibility-based method, Sivaselvan and Reinhorn (2002, 2004) developed a two-dimensional finite strain beam element to incorporate geometric nonlinearity and interaction between axial force and bending moments. Recently, Schachter and Reinhorn (2011) extended this finite strain element in three-dimensions.

While this work has increased the ability to model nonlinear structural systems in state-space, one important drawback of the flexibility-based method is that, because force is used as a state variable, it will result in a differential algebraic equation (DAE) system rather than an ordinary differential equation (ODE) system. A DAE system is more

difficult to solve by standard mathematical software (e.g. MATLAB) compared to ODE systems, and sometimes results in convergence problems. An alternate approach is the stiffness-based method (i.e. displacement interpolation), in which by using a standard cubic interpolation function (Bathe, 2007) the displacement field within the element can be directly related to its node displacement.

In this paper, the framework of the stiffness-based method is used to formulate a two-dimensional Euler-Bernoulli beam element in state-space form which can account for both geometric and material nonlinearity. Although the adopted methods exist in separate literature, it is the goal of this paper to present them in a systematic way that has not been reported before. Triantafyllou and Koumousis (2012) adopted this approach to formulate a hysteretic beam element for dynamic analysis. Besides using traditional node displacements as state variables, they proposed that the hysteretic parameters associated with the Bouc-Wen model at the two end nodes of the element be used for linear interpolation to determine the hysteretic parameters along the element. However, in the formulation presented here, all the hysteretic parameters associated with the Bouc-Wen model are treated as independent state variables, and it is further demonstrated that imposing such interpolation function is inadmissible.

In addition, the co-rotational method is added to the element to account for second-order geometric effects. Several numerical examples are presented to show the accuracy of the basic element and large displacement element. Other important phenomena during cyclic motions such as strength and stiffness degradation, pinching effects, highly asymmetric hysteresis, and force interaction can be also implemented

through modification of the versatile Bouc-Wen model. In this way, a comprehensive two-dimensional Euler-Bernoulli beam element is developed. It is shown that this element can be used to capture the flexural behavior of moment-resisting steel frames well and simulate the inelastic buckling behavior of concentrically-braced steel frames with reasonable accuracy.

4.2 Basic element formulation

This section describes the mathematical formulation of the basic element. Large displacement and strength and stiffness degradation are added later. Material nonlinearity is implemented by using the Bouc-Wen model. The Bouc-Wen model at each location has its own independent hysteretic parameters. Standard cubic interpolation functions (Bathe, 2007) are used to discretize the displacement field within the element. The curvature and axial strain at any cross section can be directly found from displacements at the two end nodes using Euler-Bernoulli beam element assumptions. Node velocities are also used as state variables to update the hysteretic parameters. Element forces can be determined based on the principal of virtual work. As such, node displacements, velocities and hysteretic parameters can be rearranged in state-space and evaluated simultaneously. Although the general framework is identical to the work of Triantafyllou and Koumousis (2012), it is demonstrated that the linear interpolation function used in their work for the hysteretic parameters is inadmissible. Instead, these hysteretic parameters should be treated as independent state variables. A numerical example is presented to evaluate the accuracy of the basic element and highlight the underlying issue imposing interpolation function to hysteretic parameters.

4.2.1 Element formulation

A typical two-dimensional Euler-Bernoulli beam element with constant cross-section property is illustrated in Figure 4-1. This element has three displacements and velocities at each node *i* and *j*, there may be concentrated or distributed plasticity along the element. In the schematic drawing of the beam element shown in Figure 4-1, there are only two concentrated plastic hinges for simplicity, but the derivations below are based on distributed plasticity. Only the flexural behavior is considered as nonlinear in this section, but there is no difficulty including other nonlinear behavior (e.g. axial force) in the same manner. Node displacement, velocity, and hysteretic parameters must be related to the element forces at nodes *i* and *j* (i.e. N_i, V_i, M_i, N_j, V_j and M_j in Figure 4-1).
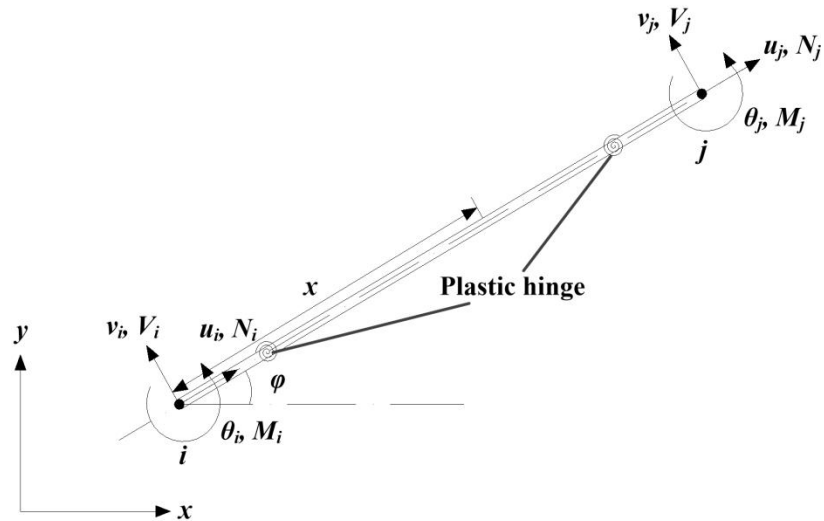
Figure 4-1 Euler-Bernoulli beam element with plastic hinges

The bending moment $M(x, t)$ along the element is represented by a Bouc-Wen model, expressed as

$$M(x, t) = \alpha EI \phi(x, t) + (1 - \alpha) EI z(t) \tag{1}$$

$$\dot{z}(t) = \dot{\phi}\left[1 - \left|\frac{z}{\phi_y}\right|^n \left(\beta + \gamma \cdot sign(z \cdot \dot{\phi})\right)\right] \tag{2}$$

where α is the ratio of post-yield stiffness to the elastic stiffness; E is the elastic modulus; I is the second-moment inertia; $z(t)$ is the hysteretic parameters associated with the Bouc-Wen model; $\phi(x,t)$ and $\dot{\phi}(x,t)$ are the curvature and its rate along the element; ϕ_y is the yield curvature; n, β and γ are the parameters controlling the shape of Bouc-Wen hysteresis loop, larger n leads to a sharper transition, $\beta + \gamma = 1$ and the Bouc-Wen model is thermodynamically admissible (Erlicher and Point, 2004) if $-\beta \leq \gamma \leq \beta$; and, sign($\cdot$) is the signum function. Equation (2) is referred as the evolution equation.

The axial force $N(x,t)$ along the element is assumed to be elastic and it can be written as

$$N(x,t) = EA\varepsilon(x,t) \tag{3}$$

where A is the cross-section area and $\varepsilon(x,t)$ is the axial strain.

Under the assumption of small strain, the longitudinal $u(x,t)$ and transverse displacement $w(x,t)$ along the element can be determined via the standard cubic interpolation functions

$$\begin{bmatrix} u(x,t) \\ w(x,t) \end{bmatrix} = [\Psi][d] = \begin{bmatrix} \Psi_1(x) & 0 & 0 & \Psi_2(x) & 0 & 0 \\ 0 & \Psi_3(x) & \Psi_4(x) & 0 & \Psi_5(x) & \Psi_6(x) \end{bmatrix} \begin{bmatrix} u_i(t) \\ v_i(t) \\ \theta_i(t) \\ u_j(t) \\ v_j(t) \\ \theta_j(t) \end{bmatrix} \tag{4}$$

in which $\Psi_1(x)$ to $\Psi_6(x)$ are the cubic interpolation functions (Bathe, 2007) expressed as

$$\Psi_1(x) = 1 - \frac{x}{L}, \Psi_2(x) = \frac{x}{L}$$

$$\Psi_3(x) = 1 - 3\left(\frac{x}{L}\right)^2 + 2\left(\frac{x}{L}\right)^3, \Psi_4(x) = x - \frac{2x^2}{L} + \frac{x^3}{L^2}$$

$$\Psi_5(x) = 3\left(\frac{x}{L}\right)^2 - 2\left(\frac{x}{L}\right)^3, \Psi_6(x) = -\frac{x^2}{L} + \frac{x^3}{L^2}$$

Under the assumption of Euler-Bernoulli beam element, the axial strain $\varepsilon(x,t)$ and curvature $\phi(x,t)$ have the following relationship with its displacement field

$$\begin{bmatrix} \varepsilon(x,t) \\ \phi(x,t) \end{bmatrix} = \begin{bmatrix} \frac{\partial u(x,t)}{\partial x} \\ \frac{\partial^2 w(x,t)}{\partial x^2} \end{bmatrix} = [B][d] = \begin{bmatrix} B_1(x) & 0 & 0 & B_2(x) & 0 & 0 \\ 0 & B_3(x) & B_4(x) & 0 & B_5(x) & B_6(x) \end{bmatrix} \begin{bmatrix} u_i(t) \\ v_i(t) \\ \theta_i(t) \\ u_j(t) \\ v_j(t) \\ \theta_j(t) \end{bmatrix} \quad (5)$$

in which $B_1(x)$ to $B_6(x)$ are derived from cubic interpolation functions which relate the node displacement directly to the strain and curvature along the element

$$B_1(x) = -\frac{1}{L}, B_2(x) = \frac{1}{L}$$

$$B_3(x) = -\frac{6}{L^2} + \frac{12x}{L^3}, B_4(x) = -\frac{4}{L} + \frac{6x}{L^2}$$

$$B_5(x) = \frac{6}{L^2} - \frac{12x}{L^3}, B_6(x) = -\frac{2}{L} + \frac{6x}{L^2}$$

In order to update the evolution equation of the Bouc-Wen model, the strain rate along the element is also required. Equation (5) the interpolation functions are independent of time, therefore the strain rate can be obtained as

$$\begin{bmatrix} \dot{\varepsilon}(x,t) \\ \dot{\phi}(x,t) \end{bmatrix} = [B][\dot{d}] = \begin{bmatrix} B_1(x) & 0 & 0 & B_2(x) & 0 & 0 \\ 0 & B_3(x) & B_4(x) & 0 & B_5(x) & B_6(x) \end{bmatrix} \begin{bmatrix} \dot{u}_i(t) \\ \dot{v}_i(t) \\ \dot{\theta}_i(t) \\ \dot{u}_j(t) \\ \dot{v}_j(t) \\ \dot{\theta}_j(t) \end{bmatrix} \quad (6)$$

With the axial strain and curvature known along the element, together with hysteretic parameters $z(t)$, the axial force $N(x,t)$ and bending moment $M(x,t)$ can be evaluated using Equation (1) and (3). Through the principle of virtual work, the element force vector $[F] = \left[N_i; V_i; M_i; N_j; V_j; M_j\right]^T$ is found as:

$$[F] = \begin{bmatrix} N_i \\ V_i \\ M_i \\ N_j \\ V_j \\ M_j \end{bmatrix} = \int_0^L [B]^T \begin{bmatrix} N(x,t) \\ M(x,t) \end{bmatrix} dx \tag{7}$$

Due to the presence of the hysteretic parameters in the expression of the bending moment, there is no closed-form solution to this integral; thus, numerical integration is used. In this study the Gauss-Lobatto quadrature rule (Hildebrand, 1956) is employed as it incorporates the two end nodes in the integration points so that their responses can also be captured. It should be noted that the displacement, velocity, and force vector defined above are in local coordinates along the element, and it is necessary to transform them back to global coordinates by

$$[F_{Global}] = [T_g]^T [F_{Local}], [d_{local}] = [T_g][d_{Global}]$$

$$[T_g] = \begin{bmatrix} \cos\varphi, & \sin\varphi, & 0, & 0, & 0, & 0 \\ -\sin\varphi, & \cos\varphi, & 0, & 0, & 0, & 0 \\ 0, & 0, & 1, & 0, & 0, & 0 \\ 0, & 0, & 0, & \cos\varphi, & \sin\varphi, & 0 \\ 0, & 0, & 0, & -\sin\varphi, & \cos\varphi, & 0 \\ 0, & 0, & 0, & 0, & 0, & 1 \end{bmatrix}$$

in which φ is the angle that the element makes with the global coordinate, as shown in Figure 4-1.

Triantafyllou and Koumousis (2012) adopted the same approach to formulate the basic element. However, motivated from the linear distribution of the bending moment along the element when no intermediate force is present, they proposed using a linear interpolation function for the hysteretic parameters. As such, only the hysteretic parameters at the two end nodes are considered as state variables which allows for a closed-form solution to Equation (7). However, this linear relationship for the hysteretic parameters along the element is inadmissible. The curvature $\phi(x,t)$ and its rate $\dot{\phi}(x,t)$ along the element can be expressed as

$$\phi(x,t) = \left(1 - \frac{x}{L}\right)\phi_i + \frac{x}{L}\phi_j \tag{8}$$

$$\dot{\phi}(x,t) = \left(1 - \frac{x}{L}\right)\dot{\phi}_i + \frac{x}{L}\dot{\phi}_j \tag{9}$$

These always hold true provided the assumptions of Euler-Bernoulli beam element and small strains. Substituting these two equations into Equation (2) results in

$$\dot{z}(t) = \left(1 - \frac{x}{L}\right)\dot{\phi}_i \left[1 - \left|\frac{z}{\phi_y}\right|^n \left(\beta + \gamma sgn(z \cdot \dot{\phi})\right)\right] + \frac{x}{L}\dot{\phi}_j \left[1 - \left|\frac{z}{\phi_y}\right|^n \left(\beta + \gamma sgn(z \cdot \dot{\phi})\right)\right] \tag{10}$$

For simplicity the curvature rate $\dot{\phi}(x,t)$ is not replaced by Equation (9). If a linear interpolation function is used for the hysteretic parameters along the element then

$$z(t) = \left(1 - \frac{x}{L}\right)z_i + \frac{x}{L}z_j \tag{11}$$

Differentiating Equation (11) with respect to time finds

$$\dot{z}(t) = \left(1 - \frac{x}{L}\right)\dot{z}_i + \frac{x}{L}\dot{z}_j \tag{12}$$

Since $\dot{z}_i$ and $\dot{z}_j$ are the rates of the hysteretic parameters at node i and j, they must satisfy the evolution equation, as a result they can be expressed as in Equation 2 as

$$\dot{z}_i = \dot{\phi}_i \left[1 - \left| \frac{z_i}{\phi_y} \right|^n \left(\beta + \gamma sgn(z_i \cdot \dot{\phi}_i) \right) \right] \tag{13}$$

$$\dot{z}_j = \dot{\phi}_j \left[1 - \left| \frac{z_j}{\phi_y} \right|^n \left(\beta + \gamma sgn(z_j \cdot \dot{\phi}_j) \right) \right] \tag{14}$$

Substituting Equation (13) and (14) into Equation (12), the hysteretic parameter rate $\dot{z}(t)$ is written as

$$\dot{z}(t) = \left(1 - \frac{x}{L} \right) \dot{\phi}_i \left[1 - \left| \frac{z_i}{\phi_y} \right|^n \left(\beta + \gamma sgn(z_i \cdot \dot{\phi}_i) \right) \right] + \frac{x}{L} \dot{\phi}_j \left[1 - \left| \frac{z_j}{\phi_y} \right|^n \left(\beta + \gamma sgn(z_j \cdot \dot{\phi}_j) \right) \right] \tag{15}$$

Comparing Equation (15) with Equation (10), putting aside the terms in the signum function, it is observed that if using a linear interpolation function then $z(t)$ in the exponential term is replaced by $z_i(t)$ and $z_j(t)$. Unless $z_i(t) = z_j(t)$ then the evolution equation at any intermediate section is violated. Consequently, adopting such interpolation function for hysteretic parameters is inadmissible. The hysteretic parameters should be treated as independent state variables in order to satisfy the evolution equation.

4.2.2 Numerical example

A one-story, one-bay moment-resisting frame analyzed by Simeonov et al. (2000) is used to evaluate the accuracy of the basic element and highlight the problem of using linear interpolation for hysteretic parameters. The frame is shown in Figure 4-2 with the dimensions and cross-section geometry. The mass was lumped at two joints each with a value of 24.96 ton. The input ground motion used is the El-Centro north-south component. This problem is analyzed using the basic element presented in Section 2.1 and the hysteretic beam element proposed by Triantafyllou and Koumousis (2012) respectively. This frame is also modeled and analyzed in *OpenSees* (McKenna et al.,

2000) as a benchmark for comparison. For the Bouc-Wen model used in both elements, the parameters and section properties are listed in Table 4-1.
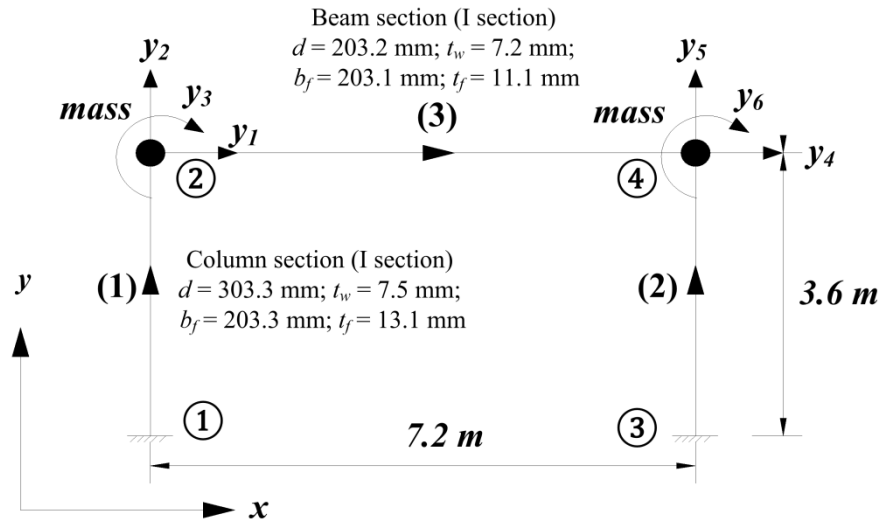
Figure 4-2 Example of one-story-one-bay moment-resisting frame

For the basic element, at nodes 2 and 4, where the mass is lumped (refer to Figure 4-2), there are six state variables including three displacements and three corresponding velocities. Along each element there are still twelve integration points, their locations are predetermined through the Gauss-Lobatto quadrature rule (Hildebrand, 1956), and there is an independent hysteretic parameter associated with each integration point. As a result, in order to fully describe the behavior of the moment-resisting frame, forty-eight state variables are required. These state variables are arranged in state-space formulation and evaluated simultaneously. This frame system is evaluated with the MATLAB ode45 solver. Usually, in dynamic analysis, only horizontal inertia is considered while static equilibrium is required in the vertical and rotational direction. However, doing so will result in a DAE system. By assigning appropriate inertia components to both the vertical and rotational direction an ODE system can be obtained (Felippa, 2005). Since the

vertical and rotational inertia are usually of less importance in the dynamic analysis, inability to satisfy the static equilibrium is not expected to affect the accuracy of the numerical model significantly.

Table 4-1 Parameters associated with Bouc-Wen model and section properties

Sections	Area (cm^2)	I (cm^4)	α	n	β	M_y (kN·m)
Beam	74	12535	0.03	5	0.5	215.7
Column	58	4505	0.03	5	0.5	117.1

For the comparative *OpenSees* model, each column and beam element is modeled using a single displacement-based BeamColumn element with eight integration points. Fiber sections are used to discretize the section to capture the nonlinear behavior of the bending moment. The material used is Steel01 with a yield stress of 248.2 MPa and hardening ratio of 0.1%. Linear transformation is used to exclude any geometric nonlinearity. The moment-curvature responses of the beam section using *OpenSees* and the basic element with Bouc-Wen model are compared in Figure 4-3 and only minor difference is observed. The comparison of the horizontal displacement history and the column hysteresis loop are shown in Figure 4-4. It is observed that the responses obtained from the basic element are in good agreement with the *OpenSees* model. However, when the same results are shown with the Triantafyllou and Koumousis element in Figure 4-5, large error is observed. It has already been demonstrated that the fundamental problem of using an interpolation function for the Bouc-Wen hysteretic parameters is the violation of the evolution equation at intermediate sections. To illustrate this, the moment-curvature responses from these two elements in the column are presented in Figure 4-6. In this figure the integration points numbered as six, seven and eight are used as examples, these

integration points are located near the mid-span of the column element where the moment-curvature responses are expected to be elastic. From the comparison in Figure 4-6, it is observed that the basic element gives an elastic response of these integration points while the Triantafyllou and Koumousis element has non-typical hysteresis loops. It is also notable that the bending moments at these integration points are well below its yield strength (i.e. 117.1 kN·m) so such yielding is not reasonable. Thus, interpolation of Bouc-Wen hysteretic parameters should be avoided.
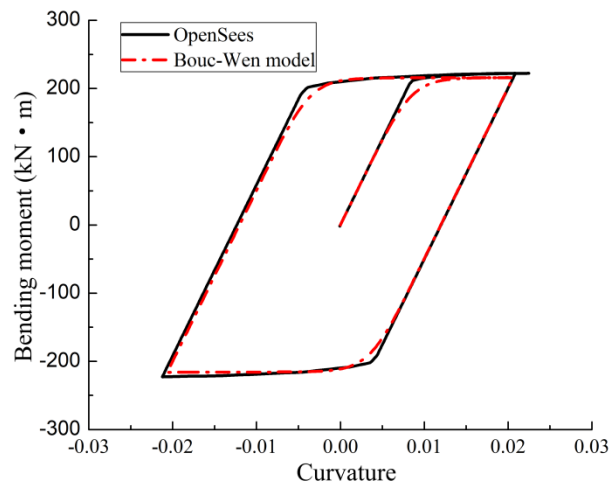
Figure 4-3 Comparison of bending moment-curvature response
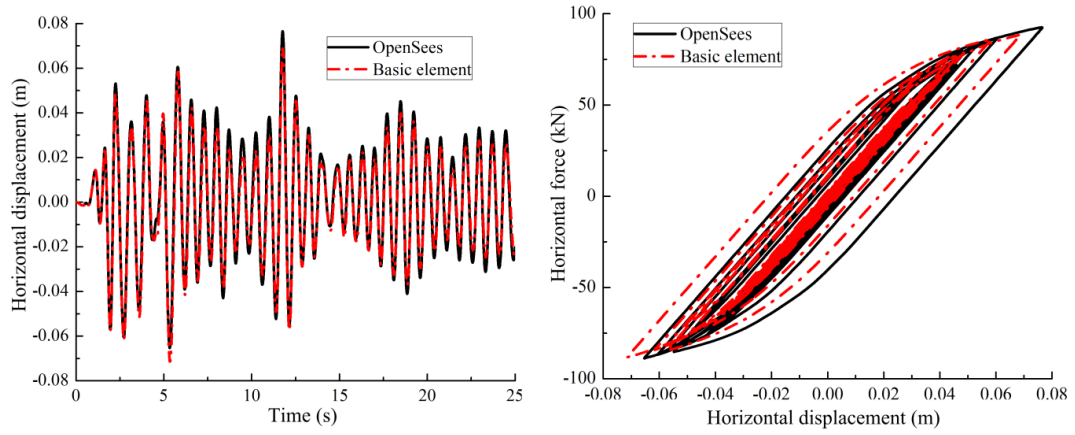
Figure 4-4 Comparison of basic element and *OpenSees* (left: horizontal displacement; right: column
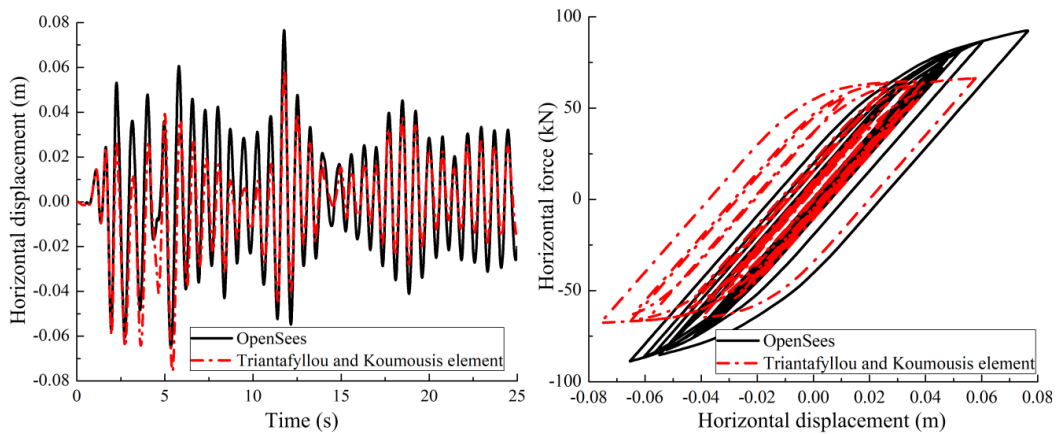
hysteresis loop)

Figure 4-5 Comparison of Triantafyllou and Koumousis element and *OpenSees* (left: horizontal

displacement; right: column hysteresis loop)
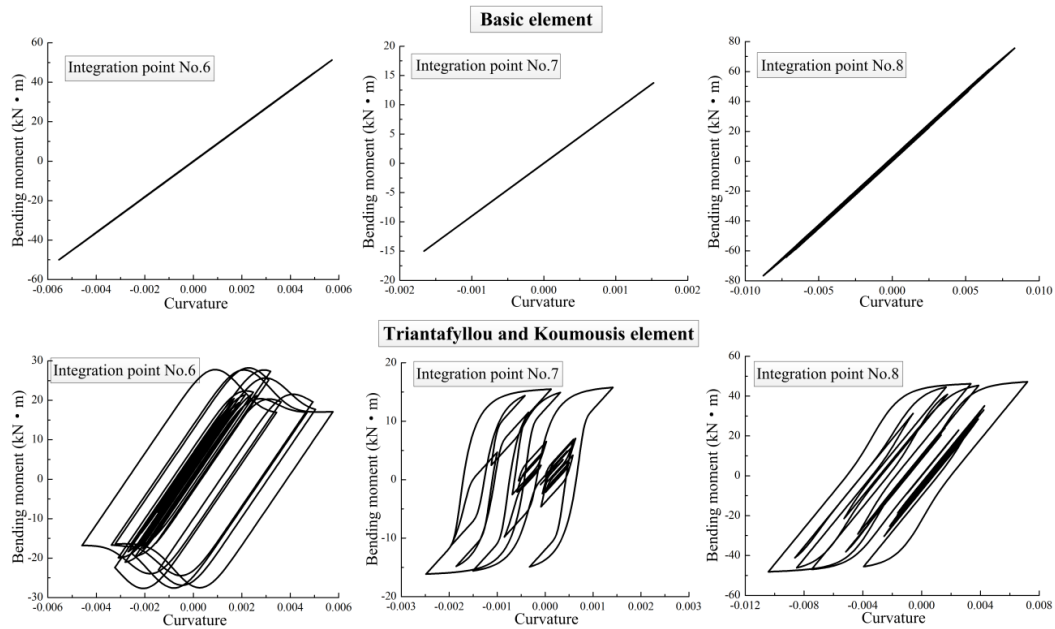
Figure 4-6 Comparison of moment-curvature responses from two different elements in the column

4.3 Large displacement element formulation

4.3.1 Co-rotational method

Large displacement effects can be added to the basic element using the co-rotational formulation (Le et al., 2011) in which the total deformation is separated into two parts: rigid body motion and element deformation. A local coordinate system is fixed to the element and translates and rotates with the element. The rigid body motion is evaluated by measuring the relative displacement of a local coordinate system to the global coordinate system. The element deformation is measured within the local coordinate system. In this study, the element deformation is assumed to be small so the standard cubic interpolation function can still be used. Beam element kinematics in the co-rotational method is schematically shown in Figure 4-7, where xy is the global coordinate

system and $x'y'$ is the local coordinate system that is attached to the beam element during its rigid body motion. Similarly to Equation (5), the global motion of this beam in the global coordinate system xy is described as

$$[d] = [u_i; v_i; \theta_i; u_j; v_j; \theta_j]^T$$

where u_i, v_i and θ_i are the horizontal, vertical and rotational displacement at node i; while u_j, v_j and θ_j are those at node j.
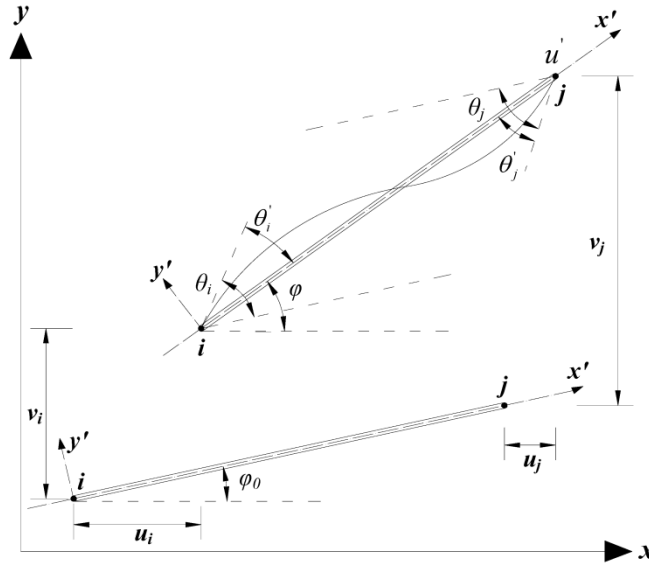
Figure 4-7 Element kinematics in the co-rotational method

The element deformation in the local coordinate system $x'y'$ is denoted as

$$[d'] = [u'; \theta_i'; \theta_j']^T$$

where u' is the axial deformation, θ_i' is the rotation at node i, and θ_j' is the rotation at node j. As to the local coordinate system is attached to the element there is no transvers deformation at two nodes during element deformation.

Assuming the global coordinate node i has a coordinate of (x_i, y_i) and node j has a coordinate of (x_j, y_j) in the undeformed configuration, the original element length l_0 can be expressed as

$$l_0 = \sqrt{(x_i - x_j)^2 + (y_i - y_j)^2}$$

After the element undergoes global motion defined as $[d]$, the current length l and current angle φ can be expressed as

$$l = \sqrt{(x_i + u_i - x_j - u_j)^2 + (y_i + v_i - y_j - v_j)^2}$$

$$\varphi = arctan \frac{y_j + v_j - y_i - v_i}{x_j + u_j - x_i - u_i}$$

Through geometric relationship, the element deformation $[d']$ in the local coordinate system can be found as

$$u' = l - l_0 = \sqrt{(x_i + u_i - x_j - u_j)^2 + (y_i + v_i - y_j - v_j)^2} - \sqrt{(x_i - x_j)^2 + (y_i - y_j)^2} \quad (16)$$

$$\theta_i' = \theta_i - (\varphi - \varphi_0) \tag{17}$$

$$\theta_j' = \theta_j - (\varphi - \varphi_0) \tag{18}$$

Similarly, it is also required to relate the global displacement rate (i.e. velocity) to the element deformation rate in order to update the evolution equation. This can be done by differentiating Equation (16) to (18) with respect to time which can be rearranged as

$$\begin{bmatrix} \dot{u}' \\ \dot{\theta}_i' \\ \dot{\theta}_j' \end{bmatrix} = \begin{bmatrix} -c & -s & 0 & c & s & 0 \\ -s/l & c/l & 1 & s/l & -c/l & 0 \\ -s/l & c/l & 0 & s/l & -c/l & 1 \end{bmatrix} \begin{bmatrix} \dot{u}_i \\ \dot{v}_i \\ \dot{\theta}_i \\ \dot{u}_j \\ \dot{v}_j \\ \dot{\theta}_j \end{bmatrix} \tag{19}$$

in which

$$c = cos\varphi = \frac{x_j + u_j - x_i - u_i}{l}$$

$$s = sin\varphi = \frac{y_j + v_j - y_i - v_i}{l}$$

With the element deformation and its rate related to the global displacement and velocity, the same derivation procedure can be used to evaluate the element force vector $[F] = \left[N_i; V_i; M_i; N_j; V_j; M_j\right]^T$. It should be noted that the transformation matrix $\left[T_g\right]$ should be updated with the current angle φ.

4.3.2 Numerical examples

4.3.2.1 Classic benchmark problems

Two benchmark problems are solved to verify the performance of the large displacement element in the state-space form: William's toggle frame (Figure 4-8) and a cantilever beam subjected to a point load (Figure 4-9). The material properties in both problems are elastic, which is achieved by setting the parameter α (i.e. the ratio of post-yield stiffness to the elastic stiffness) in the Bouc-Wen model to one. For the William's toggle frame, each beam is discretized with six large displacement elements; for the cantilever beam problem, it is discretized with ten elements. Since the large displacement element is formulated in the state-space form, these two problems are defined using a displacement-controlled method: at the node where the concentrated force is applied, a displacement history and corresponding velocity history is imposed to the target displacement. As such, the mathematical formulation inevitably results in a DAE system since the node

displacement and velocity where the force is applied must satisfy the external time history. These two problems are both evaluated using MATLAB ode15s solver.
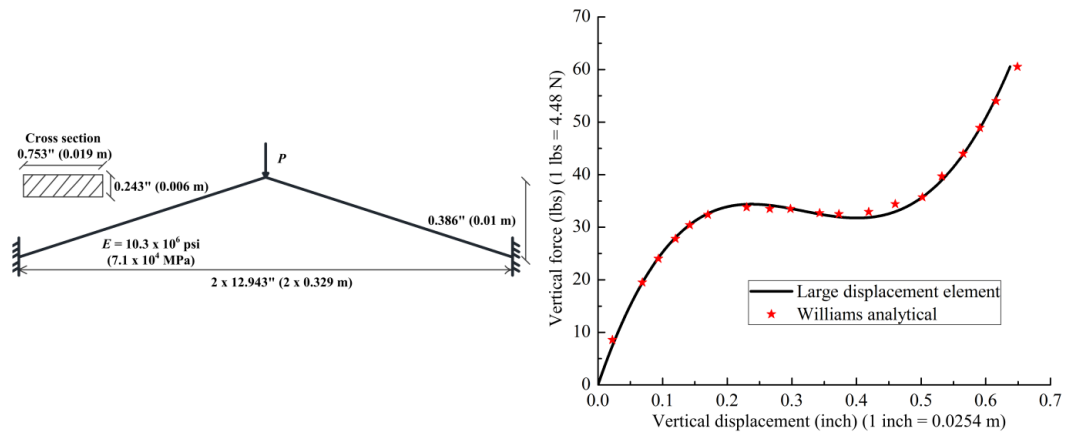
Figure 4-8 William's toggle frame
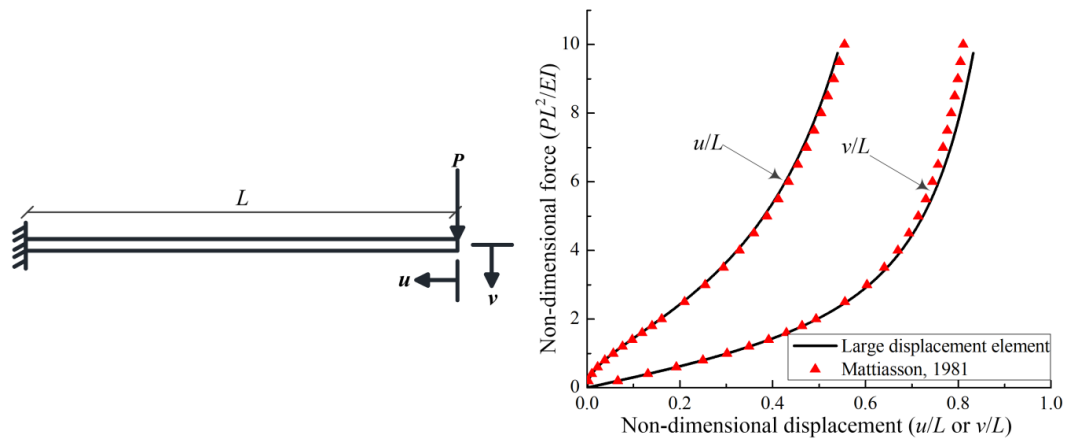
Figure 4-9 Cantilever beam subjected to vertical point load

The results of William's toggle frame, shown in Figure 4-8, are compared with the analytical solution from Williams (1964), and good agreement is observed. The cantilever beam problem is compared with the soultion provided by Mattiasson (1981) in Figure 4-9, again it shows excellent accuracy with the published results. These two

classic benchmark problems show that by adding the co-rotational method to the basic element, geometric nonlinearity can be accurately captured in the state-space formulation.

4.3.2.2 Large displacement element versus OpenSees

The two classic benchmark problems only validate the geometric nonlinearity. In order to evaluate the element accuracy with the presence of both material and geometric nonlinearity, the same single-story single-bay moment-resisting frame used in Section 2.2 is analyzed with the large displacement element and its response is compared with *OpenSees* results. For the state-space large displacement element, the modeling procedure is similar to Section 2.2, the only difference is a large displacement element with elastic behavior is added to the frame system as the leaning column, and the masses are lumped at the top of this leaning column. It should be noted in order to induce the second-order geometric effects, the gravity must be applied before the dynamic analysis to be performed.

For the *OpenSees* simulation, second-order effects are introduced by adding a leaning-column to the moment-resisting frame. The leaning-column is rigidly connected to the frame system; two zero-length elements are added at the two nodes of the leaning-column to release the bending moment. All the masses are lumped at the top of the leaning-column. All the elements are defined with a P-Delta transformation. The horizontal displacement history and column hysteresis loop are plotted and compared in Figure 4-10. It is shown that the large displacement element can provide a close estimation of seismic responses compared to the results from *OpenSees*.
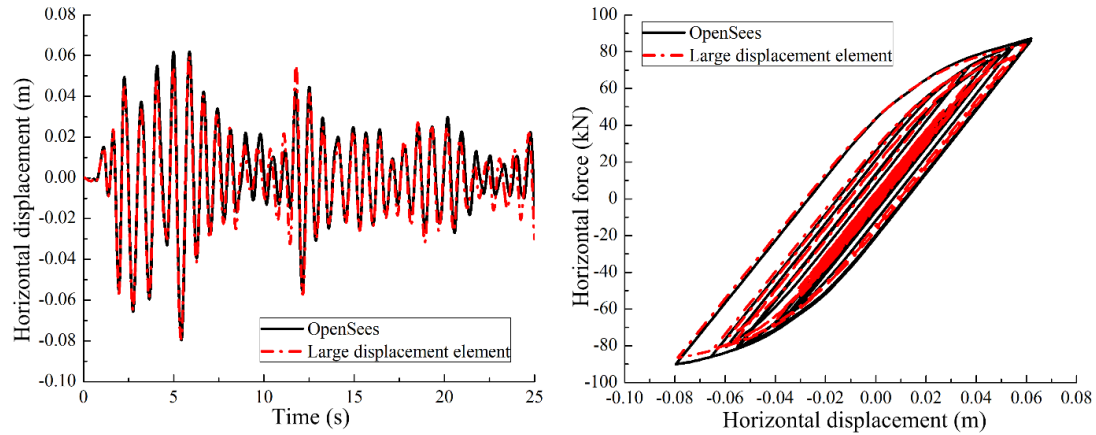
Figure 4-10 Comparison of large displacement element with *OpenSees* (left: horizontal displacement; right:

column hysteresis loop)

4.4 Degrading Bouc-Wen model and force interaction

Important phenomena such as degrading behavior during the cyclic motions and internal force interaction should also be considered. The Bouc-Wen model is extremely versatile (Ismail et al., 2009) and, through proper modifications, these effects can be incorporated in the current element. The modifications for other effects, including for pinching effects (Baber and Noori, 1984), highly asymmetric hysteresis (Song and Der Kiureghian, 2006), and compatibility with the plastic postulate (Charalampakis and Koumousis, 2009), are also available in the literature.

4.4.1 Degrading behavior

Structural components usually exhibit strength and/or stiffness degradation behavior during the cyclic motions, therefore it is necessary to incorporate these degrading properties in the Bouc-Wen model. Baber and Noori (1984) modified the standard Bouc-Wen model to the following form to explicitly consider these deteriorating effects

$$M(x,t) = \alpha EI\phi(x,t) + (1-\alpha)EIz(t)$$

111

$$\dot{z}(t) = \dot{\phi} \left[\frac{A - v \left| \frac{z}{\phi_y} \right|^n \left(\beta + \gamma \cdot sgn(\dot{\phi}z) \right)}{\eta} \right]$$

$$\dot{\xi} = (1 - \alpha)EIz\dot{\phi}$$

where A, v and η are related to the newly introduced parameter ξ through

$$A = 1 - \delta_A \xi$$

$$v = 1 + \delta_v \xi$$

$$\eta = 1 + \delta_\eta \xi$$

in which δ_A controls both the strength and stiffness degradation, δ_v only controls the strength degradation and δ_η only governs the stiffness degradation and these parameters need to be determined. In practice, δ_A is usually set to zero so that the strength and stiffness degradation can be exclusively affected by one single parameter. Sample calibration results of moment-curvature responses using data from (Lignos and Krawinker, 2013) are presented in Figure 4-11. Through calibration, good agreement with experimental results can be achieved.
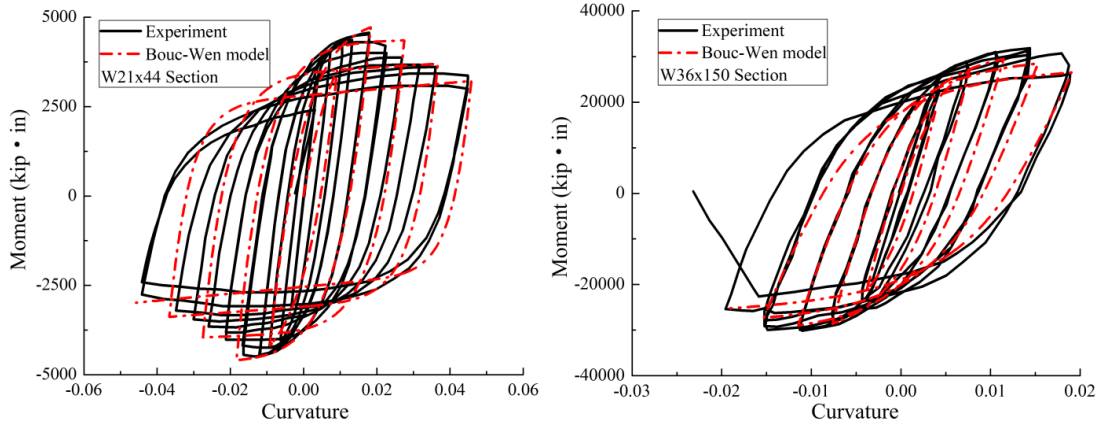
Figure 4-11 Sample calibration of degrading Bouc-Wen model

4.4.2 Force interaction

Here, the bending moment and axial force interaction (M-N interaction) is considered as the element is formulated in two-dimensions and M-N interaction is the interaction most commonly considered. For marcoscopic model such as Bouc-Wen model, a method is to introduce a yield surface function to capture the M-N interaction. Sivaselvan and Reinhorn (2002, 2004) as well as Triantafyllou and Koumousis (2011) both reported the implementation of coupling of the hysteretic component (i.e. the second term in Equation (1)) in the Bouc-Wen model. In their work, the coupling of axial force and bending moment is formulated as

$$\begin{bmatrix} \dot{z}_{axial} \\ \dot{z}_{moment} \end{bmatrix} = ([I] - H_1 H_2 [R]) \begin{bmatrix} \dot{\varepsilon} \\ \dot{\phi} \end{bmatrix}$$

in which $[I]$ is the identity matrix and $[R]$ is the interaction matrix defined later; H_1 and H_2 are smoothed Heaviside functions

$$H_1 = \|\Phi(N^h, M^h) + 1\|^n$$

$$H_2 = \beta + \gamma \cdot sgn\left([N^h; M^h]^T \begin{bmatrix} \dot{\varepsilon} \\ \dot{\phi} \end{bmatrix}\right)$$

where $\Phi(\cdot)$ is the yield surface function; N^h and M^h are the hysteretic components: $N^h = (1 - \alpha_{axial})EAz_{axial}$, $M^h = (1 - \alpha_{moment})EIz_{moment}$. The interaction matrix $[R]$ is

$$[R] = \left[\left[\frac{\partial \Phi}{\partial [F^h]}\right]^T [K] \frac{\partial \Phi}{\partial [F^h]}\right]^{-1} \times \left[\left[\frac{\partial \Phi}{\partial [F^h]}\right]\left[\frac{\partial \Phi}{\partial [F^h]}\right]^T [K]\right]$$

where $[K] = diag[\alpha_{axial}EA, \alpha_{moment}EI]$ and $[F^h] = [N^h; M^h]^T$. In this paper it is proposed to account for degrading behavior, the coupling of axial force and bending moment can be expressed as

$$\begin{bmatrix} \dot{z}_{axial} \\ \dot{z}_{moment} \end{bmatrix} = ([I_1] - H_1 H_2 [I_2][R]) \begin{bmatrix} \dot{\varepsilon} \\ \dot{\phi} \end{bmatrix}$$

where $[I_1] = diag[1/\eta_{axial}, 1/\eta_{moment}]$, $[I_2] = diag[v_{axial}/\eta_{axial}, v_{moment}/\eta_{moment}]$

There are many yield surface functions reported in the literature (e.g. Orbison et al. (1982); Duan and Chen (1990); Simeonov (1999)). In this study, the yield surface function proposed by Orbison et al. (1982) is used as it adopts a polynomial form which is easy to differentiate with respect to each hysteretic component. The surface is described as

$$\Phi = 1.15p^2 + m^2 + 3.67p^2m^2 - 1$$

where $p = N^h/N_y^h$, $N_y^h = (1 - \alpha_{axial})\sigma_y A$; $m = M^h/M_y^h$, $M_y^h = (1 - \alpha_{moment})\sigma_y Z$ and Z is the section plastic modulus.

4.5. Simulation of concentrically-braced frames

4.5.1 Numerical model

It has been demonstrated that the developed element can accurately simulate the flexural behavior of moment-resisting frames. The developed element can also be used to model the inelastic buckling behavior of braces in concentrically-braced frames. There are already many numerical models available in the literature (e.g. Ikeda and Mahin (1984, 1986); Remennikov and Walpole [(1997); Hall and Challa (1995); Jin and El-Tawil (2003)). These models can either be categorized as physical theory models (Ikeda and Mahin, 1986) or beam-column models with plastic hinges, but none are implemented in state-space form.

The element described in this paper simulates the concentrically-braced frame in a method similar to the beam-column model with plastic hinges. Each single steel brace is discretized with multiple large displacement elements with distributed plasticity. Every element has Bouc-Wen models for axial force and bending moment including stiffness degradation and M-N interaction. A small imperfection must be introduced at the mid-span of the brace to induce buckling; in this study this imperfection is selected as 0.2% of the brace length. Uriz et al. (2008) adopted a similar modeling technique, but in their work each steel brace is modeled using two force-based beam-column elements. In this study, however, it is found that at least six large displacement elements are required to capture the inelastic hysteretic response of steel braces. This is likely because the force-based element typically has better convergence than the displacement-based elements as equilibrium is satisfied exactly for the forces-based element.

4.5.2 Numerical examples

4.5.2.1 Quasi-static analysis

To validate the brace modeling capability of the proposed beam element, a quasi-static analysis of a single steel brace is presented. The strut is a 4 inch extra strong pipe section with an approximately pinned end conditions. Detailed information regarding the material properties can be found in Uriz et al. (2008).
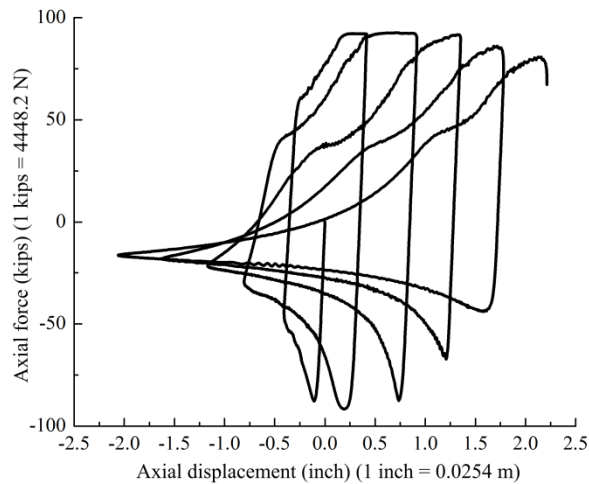
Figure 4-12 Quasi-static analysis result of a single steel brace

The hysteretic response of the steel strut is shown in Figure 4-12. Although the numerical prediction cannot reproduce the exact hysteretic shape compared to the experimental results reported by Uriz et al. (2008), it is observed that the model can capture the general hysteretic behavior of the steel brace. Upon compression, the steel brace responds linearly until inelastic buckling occurs, afterwards the compressive strength decreases as the compressive deformation continues. As the displacement reverses, unloading occurs followed by tension loading until yielding in tension. These observations are in agreement with the typical hysteretic behavior of steel brace as

116

described by Dicleli and Calik (2008). What is difficult when modeling the reversed cyclic loading, is quantifying the parameters of the Bouc-Wen model that relate to the stiffness degradation. These parameters directly influence the deterioration of the buckling capacity due to the Bauschinger effect and progressive lengthening of the steel brace (i.e. growth effect). These effects are captured in the hysteretic response presented in Figure 4-12; however, calibration with experimental results is required.

4.5.2.2 Dynamic analysis

In this section the developed beam element is used to model a single-story single-bay chevron concentrically-braced frame, which is shown in Figure 4-13 with the dimensions and cross-sections. This chevron concentrically-braced frame system was dynamically tested by Okazaki et al. (2013) under 70% of the East-West component of 1995 Kobe earthquake recorded at the Takatori station. The chevron concentrically-braced is modeled using the large displacement element with degrading behavior and M-N interaction. Each brace is represented by six beam elements with an initial imperfection of 0.2% of the brace length at its mid-point. Each column is modeled using a single element and the beam is discretized with two elements. The brace is assumed to have a fixed boundary condition.
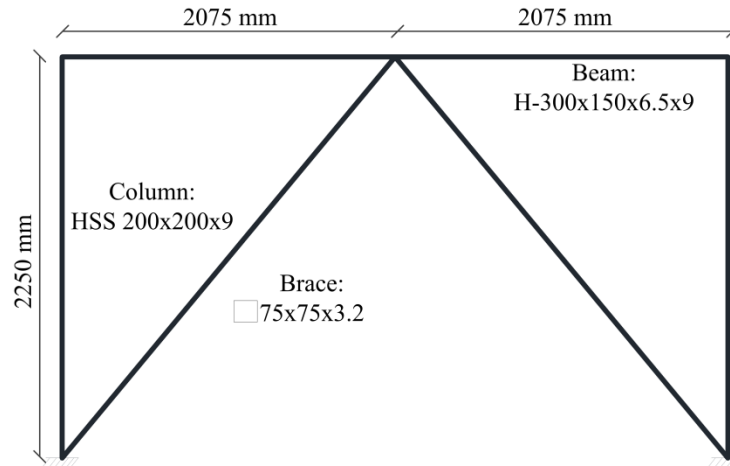
Figure 4-13 Schematic drawing of numerical model

The semi-rigid connections of the gusset plates or the panel zones are not modeled. Under the input ground motion, the seismic response from the numerical model including the shear force response of the total frame system and the axial response of a single brace is shown in Figure 4-14. The inelastic buckling of the chevron braces can be clearly observed. It is observed that during the first two major cycles, the brace experiences drift ratios from -0.015 rad to +0.0075 rad, which is very close to the experimental observations of -0.015 rad to +0.01 rad. In the experiment, the brace fractured due to low-cycle fatigue within three major cycles, which cannot be captured in the present model. The predicted peak shears are +450 kN and -520 kN, which are smaller than the reported data of +635 kN and -690 kN especially in tension, this may be because the positive drift ratio is under-predicted in the model keeping the brace inform experiencing larger tension, as shown in Figure 4-14. Similarly, Okazaki et al. (2013) predicted lower peak shears in their numerical modeling done in OpenSees, roughly -600 kN and +600 kN.

The numerical model provides a better estimation of the dynamic response of the concentrically-braced frame than the quasi-static test of the single brace. This may be because during dynamic tests the concentrically-braced frames undergo considerably fewer cycles compared to quasi-static tests. As noted earlier, in order to accurately predict the hysteretic response of steel braces under reversed cyclic motion, it is important to calibrate the stiffness degradation parameters which directly affect the Bauschinger effect and growth effect. However, in dynamic tests, since the number of cycles is relatively small, these two effects are not as significant in accurately predicting the seismic response. It is found the seismic responses of the concentrically-braced system are not heavily influenced by stiffness degrading parameters assigned to the brace model. Consequently, the developed element is more suitable for the dynamic analysis rather than the quasi-static analysis unless the element can be calibrated.
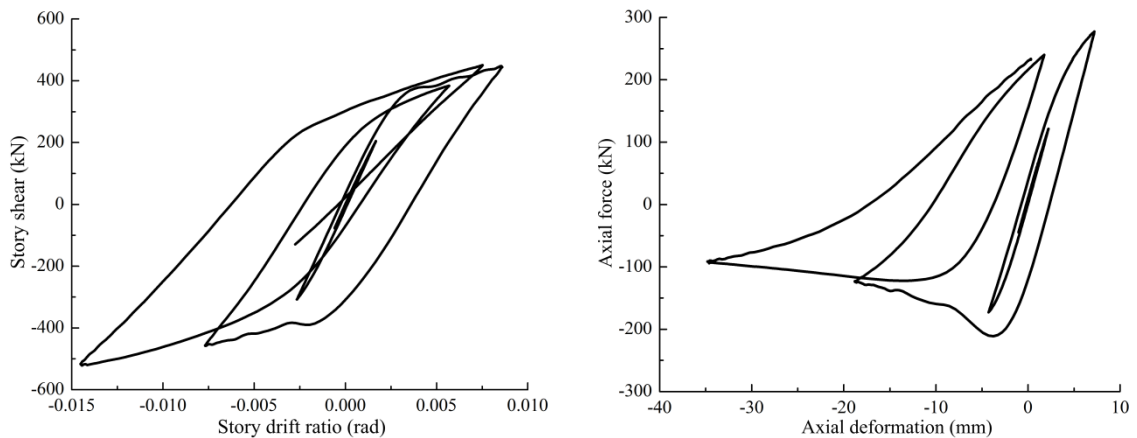
Figure 4-14 Seismic response of the concentrically-braced frame system under 70% motion

4.6 Conclusions

In this paper a two-dimensional Euler-Bernoulli beam element is formulated in state-space form. Material nonlinearity is described by the Bouc-Wen model and geometric

nonlinearity is implemented through the co-rotational method. It is demonstrated through mathematical derivation and numerical example that the hysteretic parameters of the Bouc-Wen models along an element should not be found through interpolation; rather, they should be treated as independent state variables. Other important characteristics such as strength and stiffness degradation, internal force interaction, pinching effects can be added by modifying the Bouc-Wen model.

Through several numerical examples, good accuracy is observed for the developed element to simulate the flexural behavior of moment-resisting frames with the presence of both material and geometric nonlinearity. It is also shown that the developed element is capable of simulating the complex inelastic buckling behavior of concentrically-braced frames. Through the comparisons with quasi-static and dynamic experimental results, the developed element shows reasonable accuracy but provides a better prediction in dynamic analyses. Although the major motivation for developing such an element in the state-space form is to be compatible with the rigid body isolation bearing model (Sarlis and Constantinou, 2013; Bao et al. (2017)), this element can be used for nonlinear quasi-static and dynamic analysis.

References

Applied Technology Council (2009). FEMA P695: Quantification of building seismic performance factors. Washington, D.C, USA.

Baber TT and Noori MN (1984). Random vibration of degrading, pinching systems. *Journal of Engineering Mechanics*, 111(8): 1010-1026.

Bao Y, Becker TC and Hamaguchi H (2017). Failure of double friction pendulum bearings under pulse-type motions. *Earthquake Engineering and Structural Dynamics*, 46: 715-723.

Bathe KJ (2007). Finite element procedures. Prentice-Hall, New York.

Becker TC, Bao Y and Mahin SA (2017). Extreme behavior in a triple friction pendulum isolated frame. *Earthquake Engineering and Structural Dynamics*. DOI:10.1002/eqe.2924.

Charalampakis AE and Koumousis VK (2009). A Bouc-Wen model compatible with plasticity postulates. *Journal of Sound and Vibration*, 322: 954-968.

Dicleli M and Calik EE (2008). Physical theory hysteretic model for steel braces. *Journal of Structural Engineering*, 134(7): 1215-1228.

Duan L and Chen WF (1990). A yield surface equation for doubly symmetrical sections. *Engineering Structures*, 12: 114-119.

Erlicher S and Point N (2004). Thermodynamic admissibility of Bouc-Wen type hysteresis models. *Comptes Rendus Mecanique*, 332(1): 51-57.

Felippa CA (2005). Introduction to finite element method (lecture note), University of Colorado at Boulder, CO, USA.

Hall J and Challa MVR (1995). Beam-column modelling. *Journal of Engineering Mechanics*, 121(12): 1284-1291.

Hildebrand FB (1956). Introduction to numerical analysis. McGraw-Hill, New York.

Ikeda K and Mahin SA (1984). A refined physical theory model for predicting the seismic behavior of braced steel frames. EERC report, 84/12, Earthquake Engineering Research Center, University of California at Berkeley, USA.

Ikeda K and Mahin SA (1986). Cyclic response of steel braces. *Journal of Structural Engineering*, 112(2): 342-361.

Ismail M, Ikhouane F and Rodellar J (2009). The hysteresis Bouc-Wen model, a survey. *Archives of Computational Methods in Engineering*, 16(2): 161-188.

Jin J and El-Tawil S (2003). Inelastic cyclic model for steel braces. *Journal of Engineering Mechanics*, 129(5): 548-557.

Le TN, Battini JM and Hjiaj M (2011). Efficient formulation for dynamics of corotational 2D beams. *Computational Mechanics*, 48: 153-161.

Lignos DG and Krawinker H (2013). Development and utilization of structural component databases for performance-based earthquake engineering. *Journal of Structural Engineering*, 139(8): 1382-1394.

Mattiasson K (1981). Numerical results from large deflection beam and frame problems analysed by means of elliptic integrals. *International Journal for Numerical Methods in Engineering*, 17(1): 145-153.

McKenna F, Fenves GL and Scott MH (2000). Open system for earthquake engineering simulation. University of California at Berkeley, California, USA.

Okazaki T, Lignos DG, Hikino T and Kajiwara K (2013). Dynamic response of a chevron concentrically braced frame. *Journal of Structural Engineering*, 139(4): 515-525.

Orbison JG, McGuire W and Abel JF (1982). Yield surface applications in nonlinear steel frame analysis. *Computer Methods in Applied Mechanics and Engineering*, 33: 557-573.

Remennikov AM and Walpole WR (1997). Analytical prediction of seismic behavior for concentrically-braced steel systems. *Earthquake Engineering and Structural Dynamics*, 26: 859-874.

Sarlis AA and Constantinou MC (2013). Model of triple friction pendulum bearing for general geometric and frictional parameters and for uplift conditions, 2013. Technical report MCEER-13-0010, Buffalo, NY, USA.

Schachter M and Reinhorn AM (2011). Dynamic analysis of three-dimensional frames with material and geometric nonlinearities. *Journal of Structural Engineering*, 137(2): 207-219.

Simeonov VK, Sivaselvan MV and Reinhorn AM (2000). Nonlinear analysis of structural frame systems by the state-space approach. *Computer-Aided Civil and Infrastructure Engineering*, 15:76-89.

Simeonov VK (1999). Three-dimensional inelastic dynamic structural analysis of frame systems. Ph.D. dissertation, University at Buffalo, Buffalo, NY, USA.

Sivaselvan MV and Reinhorn AM (2000). Hysteretic models for deteriorating inelastic structures. *Journal of Engineering Mechanics*, 126(6): 633-640.

Sivaselvan MV and Reinhorn AM (2002). Collapse analysis: large inelastic deformation analysis of planar frames. *Journal of Structural Engineering*, 128(12): 1575-1583.

Sivaselvan MV and Reinhorn AM (2004). Nonlinear structural analysis towards collapse simulation: a dynamical systems approach. Technical report MCEER-04-0005, Buffalo, NY, USA.

Song J and Der Kiureghian A (2006). Generalized Bouc-Wen model for highly asymmetric hysteresis. *Journal of Engineering Mechanics*, 132(6): 610-618.

Triantafyllou SP and Koumousis VK (2012). Small and large displacement dynamic analysis of frame structures based on hysteretic beam elements. *Journal of Engineering Mechanics*, 138(1): 36-49.

Triantafyllou SP and Koumousis VK (2011). An inelastic Timoshenko beam element with axial-shear-flexural interaction. *Computational Mechanics*, 48: 713-727.

Uriz P, Filippou FC and Mahin SA (2008). Model for cyclic inelastic buckling of steel braces. *Journal of Structural Engineering*, 134(4): 619-628.

Williams FW (1964). An approach to the nonlinear behaviour of the members of a rigid jointed plane framework with finite deflections. *The Quarterly Journal of Mechanics and Applied Mathematics*, 17: 451-469.

Chapter 5 Effect of Design Methodology on the Collapse of Friction Pendulum Isolated Moment-resisting and Concentrically-braced Frames

Yu Bao and Tracy C. Becker. Effect of design methodology on the collapse of friction pendulum isolated moment-resisting and concentrically-braced frames. This paper has been submitted to *Journal of Structural Engineering (ASCE)* for review and possible publication.

Abstract

Base isolation is an effective way to mitigate seismic hazards and improve seismic performance under design-level ground motions. Previous studies have typically focused on comparing performance between isolated and fixed base buildings under design-level or maximum-level earthquake without modeling the failure of the isolation bearings components. However, it is also important to include the performance of the isolation system under extreme conditions. In this study, friction pendulum isolated moment-resisting and concentrically-braced frames are designed using the ASCE 7-16 code. A numerical model which explicitly includes both impact and uplift behavior of the sliding bearings as well as degrading behavior of the superstructure is used to investigate the collapse risk of the various designs using the methodology defined by FEMA P695 with a suite of pulse-type motions. It is found that the stiffness of the superstructure has a large influence on the overall collapse risk. For flexible moment-resisting frames, increasing

the strength has considerable beneficial effects on improving its safety margin between impact and system-level failure. However, for the stiff concentrically-braced frames, due to its high stiffness and non-ductile nature, impact with the sliding bearing rim imposes a large ductility demand on the superstructure regardless of its strength, resulting in an unacceptable probability of collapse.

5.1 Introduction

It is well-recognized that base isolation is an effective way to reduce the seismic demands on superstructure, protect both the structural and non-structural components, and mitigate the seismic losses. There have been many studies on comparing the seismic performance between isolated and fixed-base structures or evaluating the effectiveness of base isolation (e.g. Erduran et al. 2011; Ordonez et al. 2003; Sayani et al. 2011; Shenton and Lin 1993; Su and Ahmadi 1989; Su and Ahmadi 1990). However, these studies examine seismic responses of isolated structures without considering extreme isolator behavior events due to excessive horizontal displacement.

The general effects of pounding of isolated buildings with adjacent buildings have been examined in previous studies (Komodromos et al. 2007; Matsagar and Jangid 2003). Both studies conclude that impact force will increase floor accelerations and excite undesirable higher mode vibration; however, these studies use simple lumped-mass models and assume elastic behavior of superstructure even after impact. The effects of pounding against the moat wall have been investigated both experimentally and numerically by Masroor and Mosqueda (2012, 2013 and 2015) and numerically by Qu et

al. (2013). These studies include the inelastic behavior of superstructure and they found that moat-wall impact can induce yielding of superstructure and increase the collapse probability of base-isolated structures.

Another concern associated with excessive horizontal displacement is the failure of the isolation bearings themselves. Recently, Bao et al. looked at the failure of double friction pendulum bearing both numerically (2017a) and experimentally (2017b), and Becker et al. (2017) explored the failure a triple friction pendulum bearing isolated frame. These studies show that for sliding isolation bearings, bearing uplift may significantly contribute to system-level failure. However, no study has determined whether designing so that superstructure yielding or bearing failure which design methodology results in the smallest collapse probability.

For the design of isolated systems, ASCE code (ASCE 2017) requires the superstructure to be designed essentially elastically under the maximum considered earthquake (MCE) level. Several researchers have looked at the influence of superstructure yielding using simplified two degree of freedom models (Kikuchi et al. 2003; Vassiliou et al. 2013) and have concluded that allowing yielding in the isolated superstructure will cause significantly larger ductility demands compared to yielding in fixed-base structures. However, these simplified studies cannot account for the complex behavior of a full frame. This paper presents the collapse assessment of several designs for moment-resisting and concentrically-braced frames isolated with sliding isolation bearings. The isolated structures are designed in accordance with ASCE 7-16 (ASCE 2017) and evaluated following the FEMA P695 (ATC 2009) framework. As isolated

buildings are particularly sensitive to long-period motions, fourteen pairs of pulse-like near-fault ground motions provided in FEMA P695 are used in this study. Compared to previous research, this study includes more comprehensive behavior as the numerical model can directly include the uplift failure of the sliding isolation bearings as well as the degrading behavior of superstructures.

In this study, three design methodologies for the isolated frames are considered: (1) a code compliant baseline design, (2) a design in which the superstructure is designed to remain elastic under moderate impact force, and (3) a design with the baseline superstructure but increased isolation displacement capacity. Through incremental dynamic analysis, the collapse margin ratio (CMR) and system-level collapse modes are evaluated. It is found for flexible moment-resisting frames, the system-level collapses modes are mixed: both bearing uplift failure and excessive superstructure yielding can contribute. But for stiff concentrically-braced frames, it is governed by excessive superstructure yielding. Increasing superstructure strength and bearing displacement capacity both have beneficial effects on increasing the CMR of the isolated moment-resisting frame; however, only the latter can have considerable beneficial effects for the isolated concentrically-braced frame. This study also finds that, all of the isolated moment-resisting frame designs have acceptable collapse probabilities at the MCE level; however, for the isolated concentrically-braced frames, only the increased bearing diameter design has an acceptable collapse probability. If the frames impact a moat wall rather than the sliding bearing restraining rim, there are similar trends for collapse

probability, although the system-level behavior is controlled exclusively through superstructure yielding.

5.2 Design of the isolated structures

Three different categories of systems are designed and evaluated in this study. In the first system, the superstructure and isolation system are designed in accordance with the most recent version of the ASCE isolation code (i.e. ASCE 7-16). In this design methodology, the building is designed to begin yielding under MCE level forces. However, the bearing's displacement capacity is only nominally larger than MCE displacement. Thus, the code does not clearly define the preferred mechanism for which nonlinear behavior will control: superstructure yielding or potential bearing failure. Thus, the system-level failure mode may be heavily influenced by the superstructure and isolation design parameters. To study the system-level failure mode and investigate which design strategy results in the smallest collapse probability, two additional systems are investigated: one with a strengthened superstructure and one with an elongated bearing displacement capacity.

The isolated buildings are located in Los Angeles, California with site class is Class C (i.e. very dense soil and soft rock). The 5% damped MCE design spectrum has spectral acceleration values $S_s = 2.35$ g and $S_1 = 0.98$ g. The superstructures are three-story three-bay steel moment-resisting and concentrically-braced frames, as depicted in Figure 5-1.
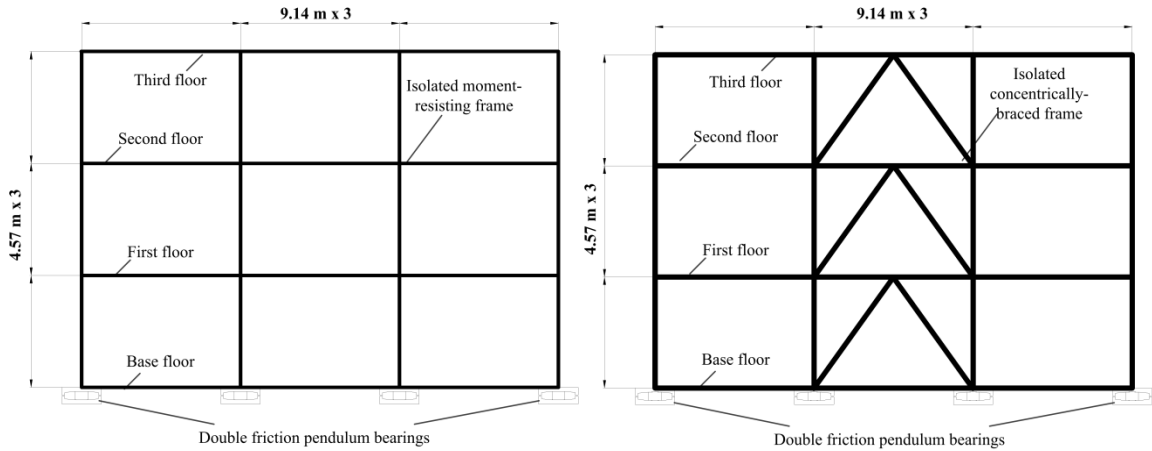
Figure 5-1 Structural layout of isolated moment-resisting and concentrically-braced frame

5.2.1 Sliding isolation bearing design

The sliding isolation bearing is selected as double friction pendulum bearing mounted below each column. The configuration of double friction pendulum bearing is shown in Figure 5-2. The target displacement under the MCE level is selected to be 0.65 m. With a sliding friction coefficient of 0.05, the radius of curvature of double friction pendulum bearing is then selected as $R = 2.75$ m, which corresponds to a second-stiffness period of 4.70 s. From the response spectrum, the predicted isolation properties and structural demands are summarized in Table 5-1. The ASCE code requires the bearings to have additional displacement capacity to account for accidental torsion; thus, the ultimate displacement capacity for the isolation bearing is set as 0.79 m.
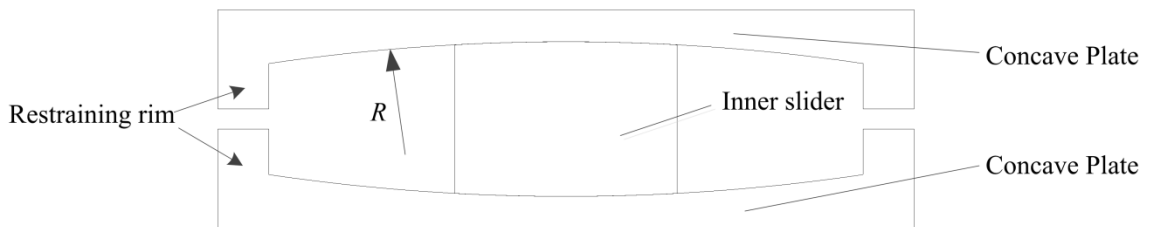
Figure 5-2 Configuration of double friction pendulum bearings (non-articulated)

Table 5-1 Design bearing responses under MCE design spectrum

Key response parameter	Value
Maximum displacement	653 mm
Effective period	3.96 s
Equivalent damping ratio	0.19
Base shear of isolation system (V_b)	0.169 g

5.2.2 Superstructure design

The systems are designed with different philosophies to explore system-level collapse probability and how the superstructure responds to the impact force. One major question is whether the superstructure should be allowed to yield prior to impact. To reflect this idea, three different systems are designed and investigated in this study:

1) System I is designed in accordance with the design code, this type of design is used as a baseline and comparison with the following two systems.

2) System II has a strengthened superstructure; it is designed so that it will develop yielding only after impact happens.

3) System III has a larger bearing capacity to minimize the probability of impact; however, major yielding is expected to develop in the superstructure before impact occurs.

System I: code compliant design

The isolation chapter of ASCE 7-16 has significant changes from the previous versions (Mayes 2014). One noticeable change is the expansion of the conditions under which equivalent lateral force procedure can be used. Now this procedure can be used provided that there is no structural irregularity and the effective period is greater than three times the fixed-base natural period; thus, it is used in this study. Another considerable revision is the calculation of the design shear force above the base level and its lateral distribution

up the height of the building, which are now a function of the fixed-base natural period, equivalent damping ratio of the isolation bearing, and the ratio of mass excluding base level to the total mass. A comprehensive description can be also found in York and Ryan (2008). The response modification factor R_I remains the same as the previous version. For an isolated ordinary steel moment frame, $R_I = 1.69$, resulting in a design shear of 0.087 times the seismic weight. For an isolated ordinary steel concentrically-braced frame, $R_I = 1.22$, resulting in a design shear of 0.118 times the seismic weight. For the isolated moment-resisting frame, the superstructure section design is drift-controlled with a drift limit of 1.5%; for the concentrically-braced frames, the design is force-controlled. The final beam, column, and brace sections for the system I designs are summarized in Table 5-2.

Table 5-2 Beam, column and brace sections of system I (code compliant design)

Isolated moment-resisting frame			
Floor	Column section	Beam section	Brace section
First floor	W14x132	W24x62	NA
Second floor	W14x132	W24x62	NA
Third floor	W14x90	W18x60	NA
Isolated concentrically-braced frame			
Floor	Column section	Beam section	Brace section
First floor	W12x72	W27x194	HSS 7x7x5/8
Second floor	W12x72	W24x176	HSS 7x7x1/2
Third floor	W12x72	W24x146	HSS 6x6x1/2

System II: stronger frame design

System II is designed using a much higher base shear coefficient to develop yielding only after impact. The procedure of designing the superstructure is identical to system I except for two differences: the response modification factor R_I is selected as 1 and the base shear is assumed to be 120% of the shear force of the isolation bearing at its maximum

displacement. The 20% increase is used to account for the impact. This results in design

shear of 0.193 and 0.198 times the seismic weight for moment-resisting frame and

concentrically-braced frame, respectively. The final beam, column, and brace sections for

system II are listed in Table 5-3. As expected, all cross sections are larger than system I

increasing the stiffness and strength of the superstructures.

Table 5-3 Beam, column and brace sections of system II (stronger frame design)

Isolated moment-resisting frame			
Floor	Column section	Beam section	Brace section
First floor	W14x176	W24x76	NA
Second floor	W14x159	W24x76	NA
Third floor	W14x120	W24x55	NA
Isolated concentrically-braced frame			
Floor	Column section	Beam section	Brace section
First floor	W18x86	W27x217	HSS 9x9x1/2
Second floor	W18x86	W27x217	HSS 8x8x5/8
Third floor	W18x86	W27x194	HSS 7x7x5/8

System III: larger bearing design

System III superstructure is designed such that the superstructure will develop

considerable yielding before bearing impact happens. This could be done by increasing

the response modification factor R_I, however, the design code explicitly constrains R_I. To

comply with the design code, the displacement capacity of the isolation bearings is

increased by 50% (i.e. displacement capacity is increased to 1.19 m) while keeping the

superstructure design identical to the system I. The 50% increase in displacement

capacity is roughly the median plus one standard deviation of displacement demand from

the suite of ground motions presented in Section 5.4.1.

5.3 Description of numerical model

In this section a brief description of the numerical models used in this study is presented. The focus of this section is not the mathematical derivations of the element as they are presented in the referred literature, but rather the limitations and underlying assumptions within the model and how they will influence the final collapse probability assessment.

5.3.1 Isolation bearing model

There are several analytical models (Becker and Mahin 2012; Constantinou and Fenz 2008) that can describe the behavior of sliding isolation bearings under regular conditions; however, these models cannot simulate the behavior of sliding isolation bearings under extreme conditions such as impact and uplift. Therefore, the bearing model developed by Sarlis and Constantinou (2013) is used in this study. As this model assumes each component of sliding bearing as a rigid body, it is referred to here as the rigid body model. As it does not include deformation of the components, this model can develop unlimited impact force and the magnitude of which is highly dependent on the assigned impact stiffness; however, shake table testing (Bao et al. 2017b) has shown that the impact forces are limited due to the yielding of restraining rim. This is a drawback of the rigid body model in the assessment of collapse probability, but this will result in a smaller, rather than artificially larger CMR, because the real impact forces should be less compared to rigid body model prediction.

   For the failure of the isolation bearings, the uplift failure is characterized by any one of the four vertexes moves outside the restraining rim of top and bottom plates, as described in Bao et al. (2017a). As noted, the rigid body model cannot predict failure due

to the restraining rim yielding, but a previous finite element study (Bao et al. 2017a) found that critical ground motion parameters such as spectral accelerations are not significantly affected by the bearing failure modes.

5.3.2 Moment-resisting frame model

In the framework of collapse probability assessment proposed by FEMA P695 (ATC 2009), the numerical model should incorporate both the degrading behavior and second-order geometric effects. The implementation of the rigid body model is in state-space form, not the traditional stiffness matrix form. In order to be compatible with rigid body model, the superstructure model is also implemented in state-space form.

The basic element formulation is already described in a previous study (Becker et al. 2017). However, second-order geometric effect and force interaction are added for this model. The second-order effect is captured using a co-rotational formulation (Le and Battini 2011), and the internal force interaction is achieved using a yield surface function (Orbison et al. 1982; Triantafyllou and Koumousis 2011).

It is necessary to calibrate the degrading Bouc-Wen model so that both the stiffness and strength degrading behavior can be accurately simulated. For this purpose, the degrading parameters are calibrated using 24 experimental tests of HSS and W sections (Lignos and Krawinker 2013). Four sample calibrated models compared with experimental results are shown in Figure 5-3. It is observed that the calibrated Bouc-Wen model can capture the degrading behavior well. It is found that parameters that explicitly control the strength and stiffness degradation stay in the same order of magnitude across the 24 experiments. Thus, constant degrading parameters are used to model all cross

sections based on the median values from all twenty-four experimental results. The yield strength and elastic stiffness associated with each cross-section section are determined from AISC specifications.
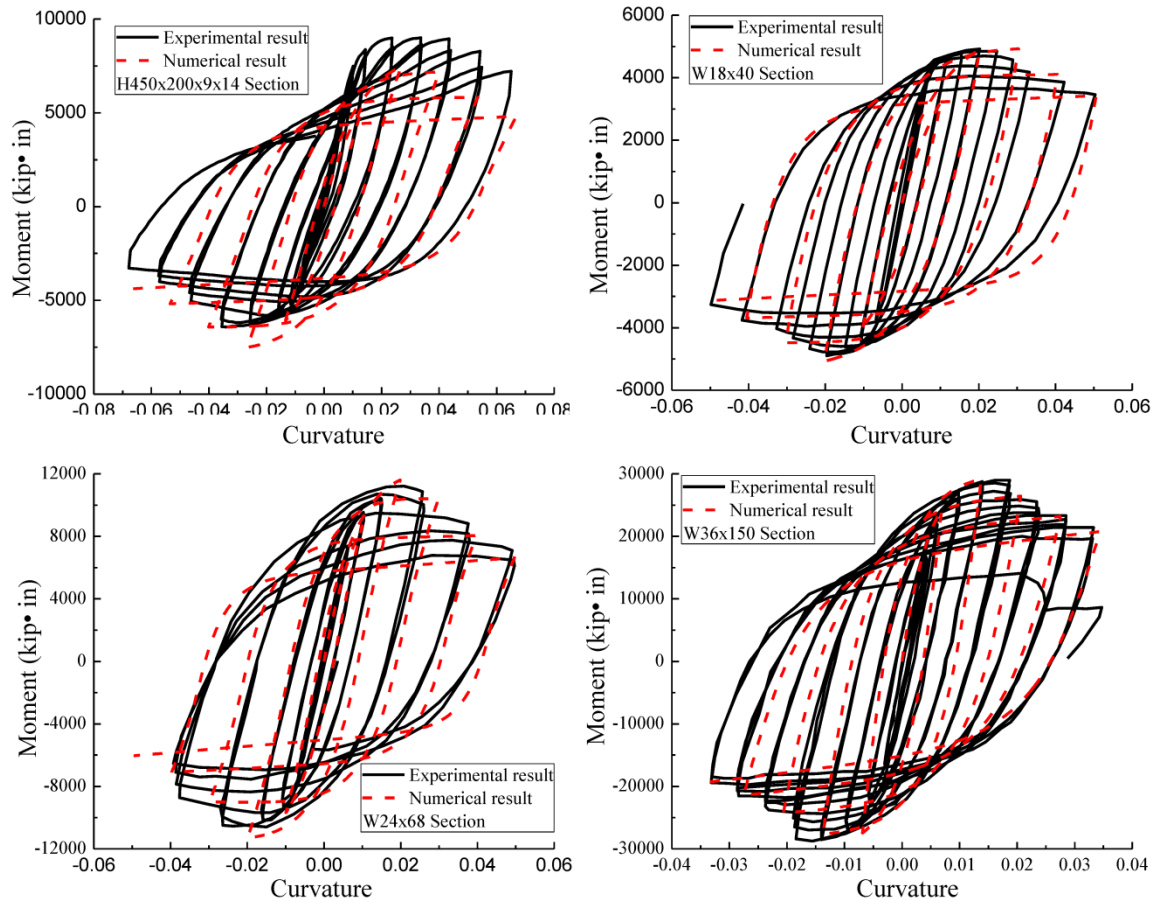
Figure 5-3 Comparison between experimental and numerical results

5.3.3 Concentrically-braced frame model

There are several models (Ikeda and Mahin 1984; Remennikov and Walpole 1997; Jin and El-Tawil 2003) to describe the inelastic buckling behavior of concentrically-braced frames. In this study, the modeling guidelines provided by Uriz et al. (2008) are followed. To capture the inelastic buckling behavior, one brace is divided into multiple beam elements, and an initial imperfection of 0.2% of its original brace length is assumed at its

midpoint. In the work of Uriz et al., it is shown that two force-based beam elements can capture the inelastic buckling behavior fairly well; however, with the displacement-based element formulation at least six elements are required to provide satisfactory performance. A typical hysteretic response of a single brace is shown in Figure 5-4, showing both buckling and deteriorating behavior.

For further model validation, a chevron braced frame presented by Okazaki (2013) and tested under 70% Takatori motion East-West component was modeled; the response is shown in Figure 5-4. Before the brace fracture occurs, the numerical model gives a relatively close estimation of peak drift ratio: -0.013 rad to +0.008 rad from the numerical model compared to -0.015 rad to +0.01 rad in the experiment. The predicted shear force is smaller than experimental results, likely due to difficulty in determining the strain-hardening ratio in the numerical model. The concentrically-braced frame model is deemed acceptable for this study.
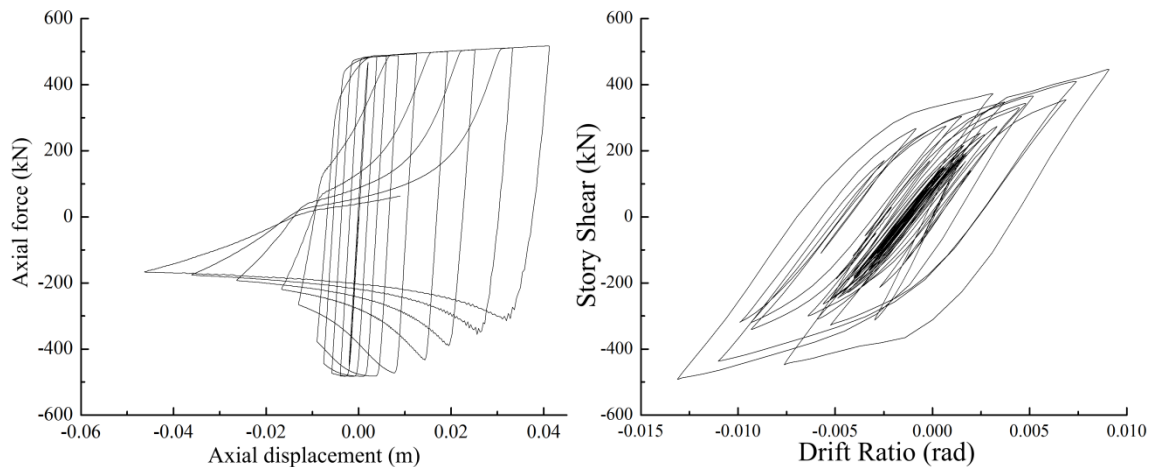
Figure 5-4 Steel brace analysis results (left: quasi-static analysis; right: dynamic analysis)

5.4 Collapse assessment using FEMA P695 methodology

The collapse evaluation of the differently designs of moment-resisting and concentrically-braced frames is presented in this section. The methodology proposed in FEMA P695 (ATC 2009) is used and several important indexes such as CMR collapse probability are quantified and compared between different designs.

5.4.1 Ground motion selection and scaling

In this study, 14 pairs of near-fault pulse-like ground motions (28 ground motions in total) are used as input to evaluate the collapse probability. The basic information regarding these motions is listed in Table 5-4. Each pair of ground motions is first normalized by their peak ground velocities using the normalization factor provided in FEMA P695 Appendix A; then all 28 ground motions are scaled as a group to match the target MCE design spectrum. The records are scaled so that the median response matches the MCE design spectrum at the effective period of the bearings at the MCE level displacement, which is 3.96 s in this study (see Table 5-1). The scaled response spectra of the twenty eight ground motions are shown in Figure 5-5. Note that the MCE design spectrum is stronger than seismic design category D_{max} defined by FEMA P695, as a result this study uses a site specific collapse probability assessment and follows the procedure outlined in FEMA P695 Appendix B.

For the scaled 28 ground motions, the median spectral displacement value at the natural period is 0.689 m, the standard deviation is 0.314 m. Considering the median value plus one standard deviation as the spectral acceleration value for type III

superstructure design, which leads to approximately 50% increase in bearing

displacement demand.

Table 5-4 Fourteen pairs of near fault pulse-like ground motions

Number	M_w	Name	Station	V_s30 (m/s)	NEHRP Class	PGA (g)
GM 1	6.5	Imperial Valley-06	El Centro Array#6	203	D	0.44
GM 2	6.5	Imperial Valley-06	El Centro Array#7	211	D	0.46
GM 3	6.9	Irpinia,Italy-01	Sturno	1000	B	0.31
GM 4	6.5	Superstition Hills-02	Parachute Test Site	349	D	0.42
GM 5	6.9	Loma Prieta	Saratoga-Aloha	371	C	0.38
GM 6	6.7	Erzican, Turkey	Erzincan	275	D	0.49
GM 7	7	Cape Mendocino	Petrolia	713	C	0.63
GM 8	7.3	Landers	Lucerne	685	C	0.79
GM 9	6.7	Northridge-01	Rinaldi Receiving Sta	282	D	0.87
GM 10	6.7	Northridge-01	Sylmar_Olive View	441	C	0.73
GM 11	7.5	Kocaeli,Turkey	Izmit	811	B	0.22
GM 12	7.6	Chi-Chi,Taiwan	TCU065	306	D	0.82
GM 13	7.6	Chi-Chi,Taiwan	TCU102	714	C	0.29
GM 14	7.1	Duzce,Turkey	Duzce	276	D	0.52
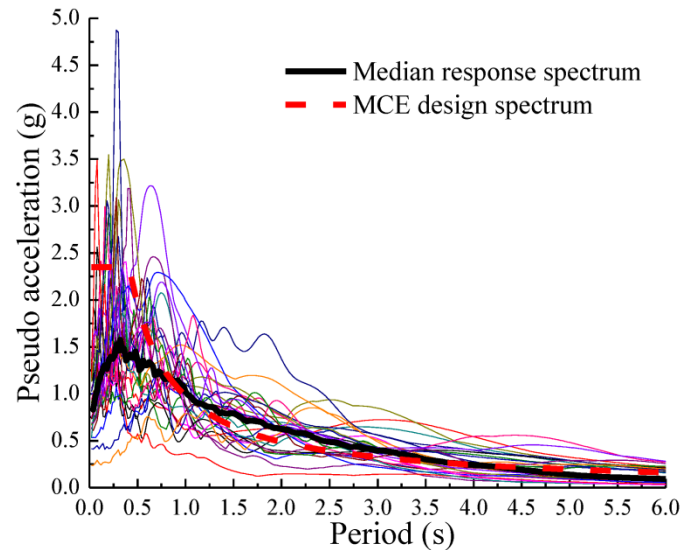
Figure 5-5 Comparison of response spectra with MCE design spectrum

5.4.2 Incremental dynamic analysis

In this section the incremental dynamic analysis (IDA) curves are first constructed for

one representative ground motion before the suite of motions to gain a better

understanding of the responses of isolated moment-resisting and concentrically-braced frames under extreme conditions. Usually the IDA curves plot intensity measures (e.g. peak ground acceleration (PGA), pseudo acceleration as the first period ($SA(T_1)$) etc.) against seismic response parameters (e.g. maximum drift ratio, floor acceleration etc.) of interest. In this study two response parameters are used: maximum story drift ratio and maximum ductility demand at the component level. For the moment-resisting frames, the ductility is the ratio of maximum curvature within a beam or column element to its yield curvature; for the concentrically-braced frames the ductility is the maximum axial compressive deformation of a single brace to the axial deformation at the buckling load, as defined in FEMA 356 (ASCE 2000). In the study presented here, collapse of the superstructure due to excessive yielding is defined by the maximum story drift ratio, which has threshold values of 5% and 2% for the moment-resisting and concentrically-braced frames, respectively. The effects on the non-structural components are currently neglected in this study. The maximum ductility is presented only to highlight the effect of yielding on the safety margin between impact and system-level failure. The concepts of impact margin ratio (IMR), CMR, and safety margin are used in the following subsections. The IMR and CMR are defined as the ratio of spectral acceleration at the isolation period to the spectral acceleration of the MCE level at which half of the suite of ground motions cause impact or collapse. Note that the term collapse here means system-level failure, either triggered by excessive superstructure yielding or bearing uplift failure. The safety margin is defined as CMR minus IMR.

5.4.2.1 Individual ground motion

The 260 degree component of ground motion No.8 (see Table 5-4) is selected as representative for the presentation of the IDA curves for moment-resisting and concentrically-braced frames; Figure 5-6 shows the maximum drift ratio and Figure 5-7 presents the maximum ductility. The percentage of MCE level is used in lieu of traditional intensity measure for consistency with IMR and CMR. The IDA curve starts from 50% of MCE level to evaluate behavior from impact to bearing uplift failure for the moment-resisting frames. For the concentrically-braced frames, the IDA curve only presented up to 10% higher than the impact intensity level. This is because concentrically-braced frame develops unrealistically large drift and ductility before bearing uplift failure occurs. As the amplitude of ground motion increases, the maximum drift ratio increases; however, when the isolation bearing exhibits uplift failure the maximum drift ratio may plateau or even decrease. This is because the analysis terminates at the instance of bearing uplift failure to avoid numerical instability. As a result, the time history response is truncated and the maximum drift ratio may not be accurate. The effect of this technical difficulty will be further discussed in the construction of the median IDA curves.

For the moment-resisting frames, varying the design has a profound influence on the system-level behavior. In terms of this particular ground motion, for the system I code compliant design, bearing impact first occurs at 90% MCE. At 110% MCE, the maximum drift ratios of the 1st and 2nd floor exceed 5%, therefore superstructure collapse is assumed at this level. Explicit bearing uplift will not happen until 130% MCE. For the system II stronger frame design, impact occurs at 90% MCE, and at 120% MCE

the bearing exhibits uplift failure but the maximum drift ratio is still less than 5%. This indicates the system-level failure mechanism shifts from superstructure yielding to bearing uplift failure, due to the increase in strength and stiffness of the superstructure. For the system III larger bearing design, impact first occurs at 130% MCE due to the increase in bearing displacement capacity, and impact immediately causes drift ratios larger than 5% in the 1st and 2nd floors. Explicit bearing uplift failure happens at 140% MCE.
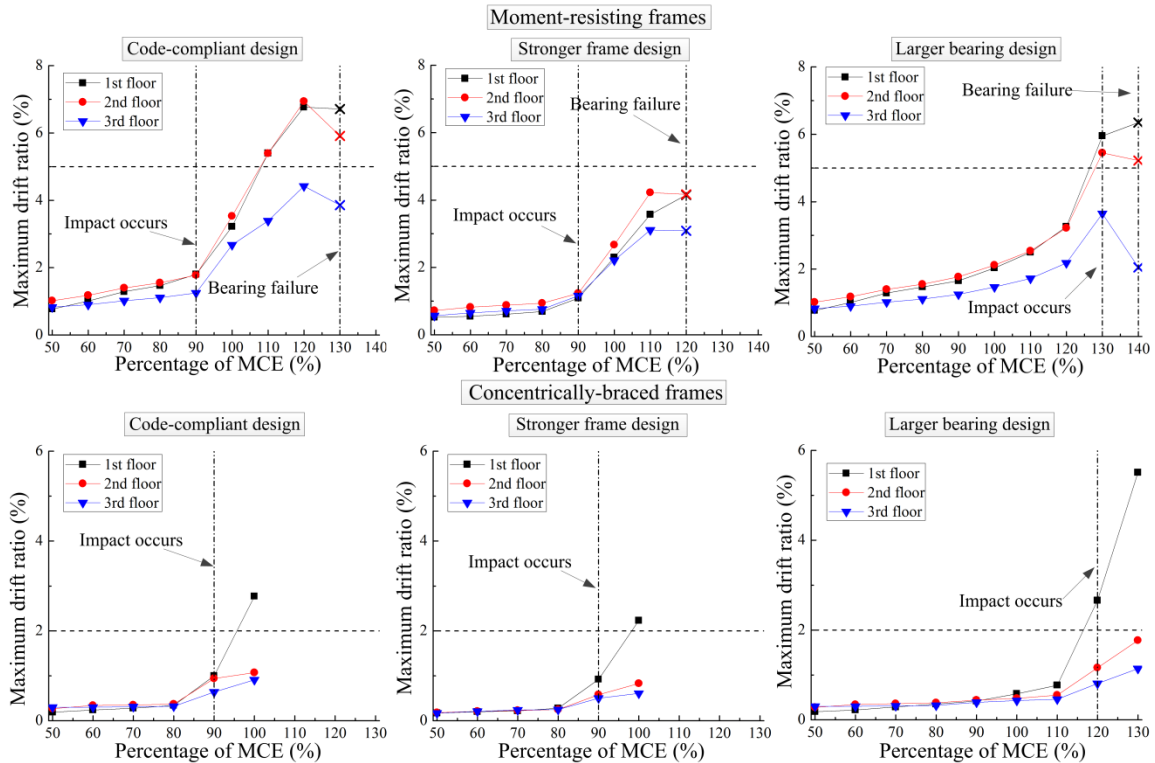
Figure 5-6 IDA curves for maximum drift ratio of the 260 degree component of GM8

For the concentrically-braced frames, the IDA curves show that the systems are very sensitive to impact force. The system-level failure comes exclusively from excessive superstructure yielding regardless of the design. For the system III larger bearing design, where impact is delayed, the 1st floor exceeds 2% drift ratio when impact first occurs,

and the other two systems exceed 2% drift ratio at 10% higher than its corresponding

IMR.
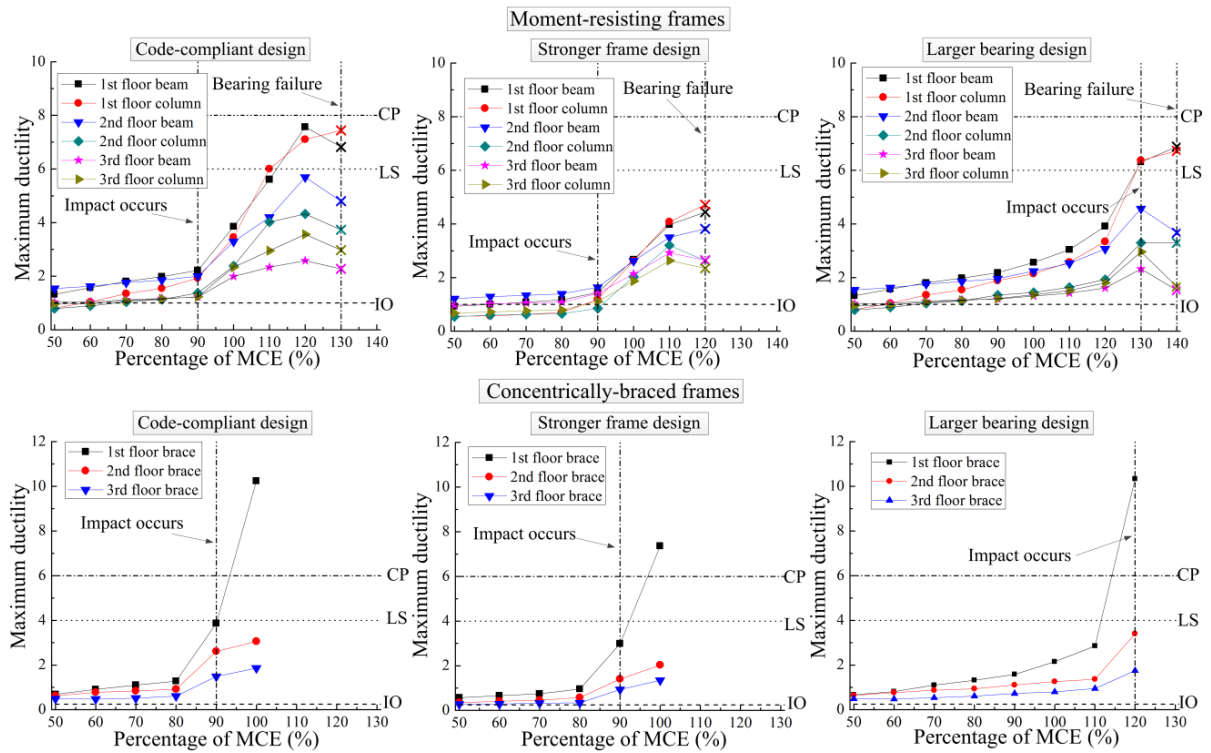
Figure 5-7 IDA curves for maximum curvature ductility of the 260 degree component of GM8

The IDA curves for maximum ductility are presented in Figure 5-7, the

abbreviations of IO, LS, and CP in the figure denote Immediate Occupancy, Life Safety,

and Collapse Prevention, with threshold values defined in FEMA 356 (ASCE 2000). For

moment-resisting frames, it is observed that the pattern for maximum ductility is

consistent with maximum drift ratio: when impact occurs, the system II stronger frame

design develops the lowest ductility while system III larger bearing design has the largest

ductility. It is also notable that for the larger bearing design, prior to impact the maximum

ductility grows to as large as 4, but for the code compliant design and stronger frame

design, this values are only 2 and 1.5 respectively.

5.4.2.2 Suite of ground motions

In order to evaluate the seismic performance of the different isolated structures under the suite of twenty-eight ground motions, it is useful to develop the median IDA curves. As noted earlier, due to the truncated time history response when bearing uplift failure occurs, the real peak drift may not be captured. This poses a challenge for developing the median IDA curves and defining the sources of system-level collapse. It is proposed that for ground motions larger than those causing bearing uplift failure, the peak response values will be based on the maximum previous values. This will avoid any misleading conclusions that maximum responses decrease after impact.

The median IDA curves for maximum drift ratio and ductility are shown in Figure 5-8 and Figure 5-9; these median IDA curves only show the behavior up to system-level collapse and do not categorize the sources of system-level failure. The source of system-level failure will be further addressed in the following Section 5.4.3. The median IDA curves from a suite of ground motions are consistent with the previous conclusion made from the individual motion.
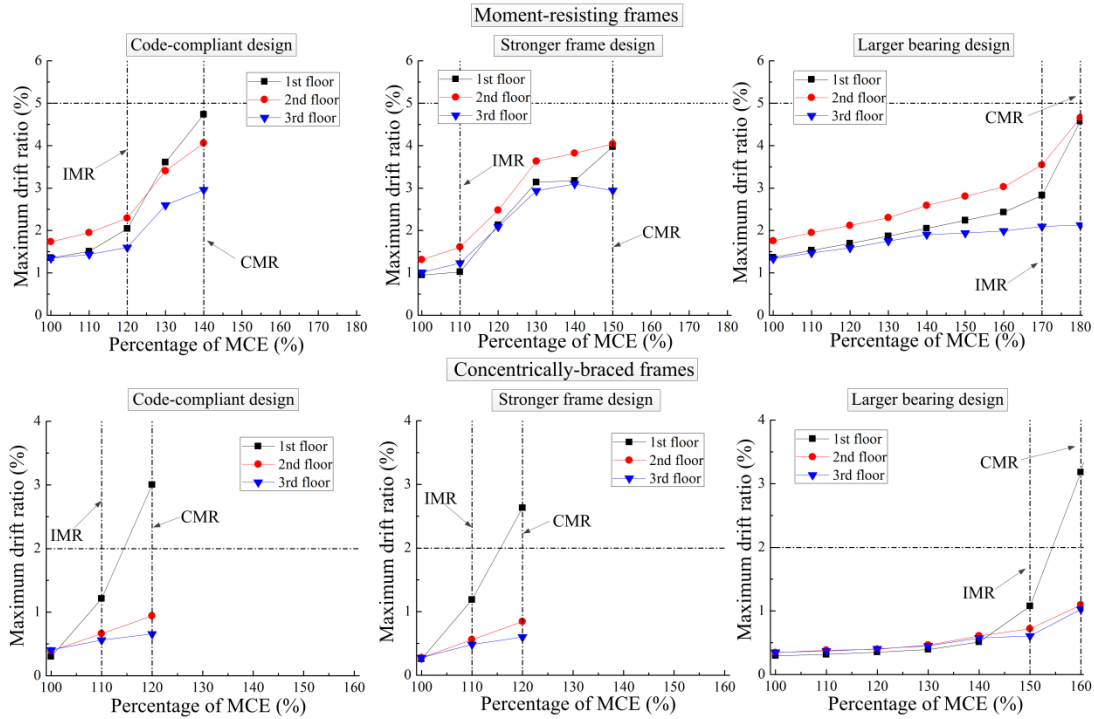
Figure 5-8 Median IDA curves for maximum drift ratio
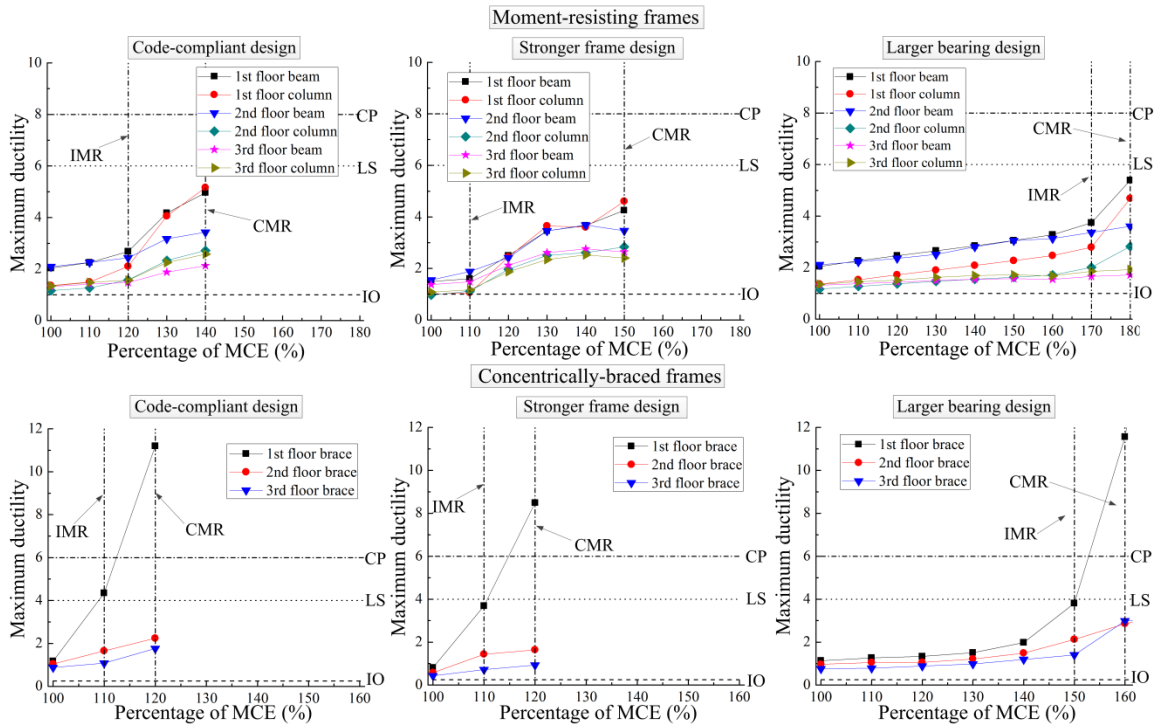
Figure 5-9 Median IDA curves for maximum ductility

For the moment-resisting frames, the IRM and CMR is 120% and 140% MCE for the code compliant design, 110% and 150% for the stronger frame design, and 170% and 180% for the larger bearing design. While the larger bearing design has the largest IMR but the safety margin between impact and collapse is only 10%. The stronger frame design has the lowest IMR but the safety margin is 40%, which is the highest among three systems. Note that for the median IDA curves for maximum drift ratio, when the CMR is reached, the median value may not exceed 5%. This is due to the bearing uplift failure contributes to system-level failure. The difference in IMR between the code compliant and stronger frame designs is because a more flexible superstructure will decrease the natural period of the isolated structure and decrease the maximum displacement in the bearing (Kelly 1990). The median IDA curves for maximum ductility also show the difference in design: prior to reaching IMR, the larger bearing design develops maximum ductility as large as 3, but the code compliant design and stronger frame design have only 2 and 1.5 respectively. These results show, for isolated flexible superstructure, the strength has an important role on its ductility demand upon impact: increasing strength has considerable beneficial effects on avoiding excessive superstructure yielding. Increasing the displacement capacity is the most straight-forward way to protect superstructure, but the consequence is the superstructure cannot survive any impact.

For the concentrically-braced frames, the median IDA curves show that the frames are extremely sensitive to impact force. For both code compliant and stronger frame design, the IMR and CMR are 110% and 120% MCE, leaving a safety margin

between impact and collapse of only 10%. For the larger bearing design, the IMR increases to 150% MCE, but the safety margin still remains 10%. The median IDA curves for maximum ductility demand also confirm that the larger bearing design develops considerable yielding compared to the other two systems; before reaching IMR, the maximum ductility is as large as 2 while the others almost remain 1. This indicates that for isolated stiff superstructures, impact force imposes large ductility demands regardless of the superstructure strength, thus the probability of any potential impact force should be minimized for stiff superstructures.

For both isolated frames, significant superstructure yielding can be observed in the larger bearing design cases, but the collapse does not occur unless an impact force is induced. This observation shows the yielding in isolated superstructure may not be as devastating as claimed by previous studies using two degree of freedoms models (Kikuchi et al. 2003; Vassiliou et al. 2013) unless impact occurs. This may be attributed to the over-strength factor in the real structural design.

5.4.3 Statistical analysis of collapse

In this section, the statistical analysis for the isolated structures is summarized and presented. As noted earlier, for the concentrically-braced frames, there is no clear difference in IMR or CMR between the code compliant and stronger frame designs; therefore, a refined 5% increment is used to scale the suite of ground motions and then a linear interpolation is used to determine these ratios. The IMR and CMR are presented in Figure 5-10. For the concentrically-braced frames, the refined IMR and CMR for system

I, II, and III are: 1.12 and 1.16; 1.11 and 1.17; 1.53 and 1.54, respectively. The difference

due to the superstructure strength is trivial for the concentrically-braced frames.
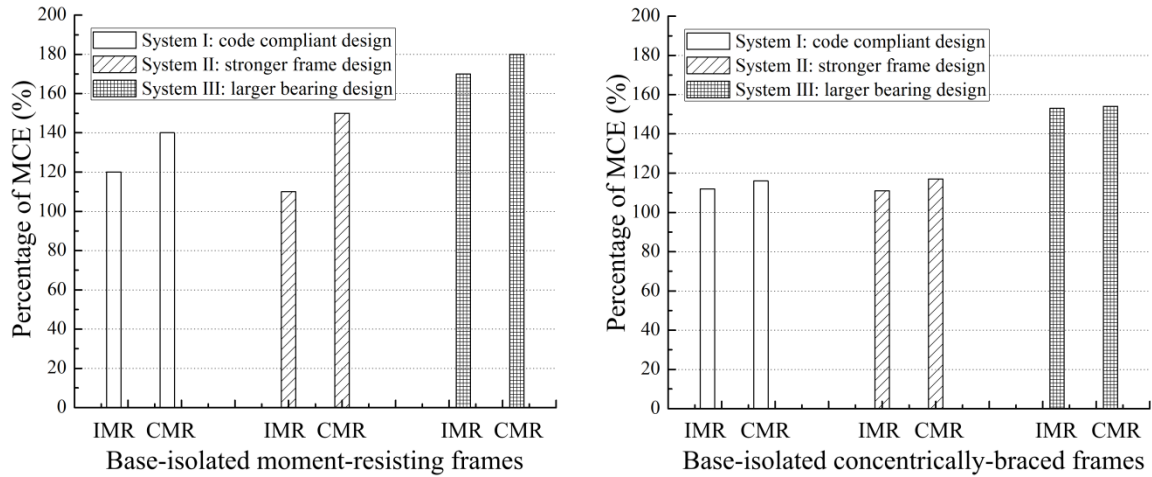
Figure 5-10 Isolated frames impact margin ratio (IMR) and collapse margin ratio (CMR)

It is also useful to categorize the sources of system-level failure for the isolated

structures with different design methodologies. In this study, whichever failure mode is

observed earlier is defined as the source of the system-level failure. For example, for

ground motion No.8 presented previously, in the moment-resisting frame code compliant

design, excessive superstructure yielding occurs at 110% MCE and bearing uplift failure

occurs at 130%, so superstructure yielding is categorized as the system-level failure. For

the same motion, in the stronger frame design, bearing uplift failure occurs at 120% MCE,

and no major superstructure yielding is observed. However, as mentioned earlier, the

truncated time history response poses a difficulty in determining the source of system-

level failure; as the analysis is terminated, it is not possible to tell whether excessive

yielding occurs after bearing failure. For this motion, only bearing uplift failure is

reported as the system-level failure mode.
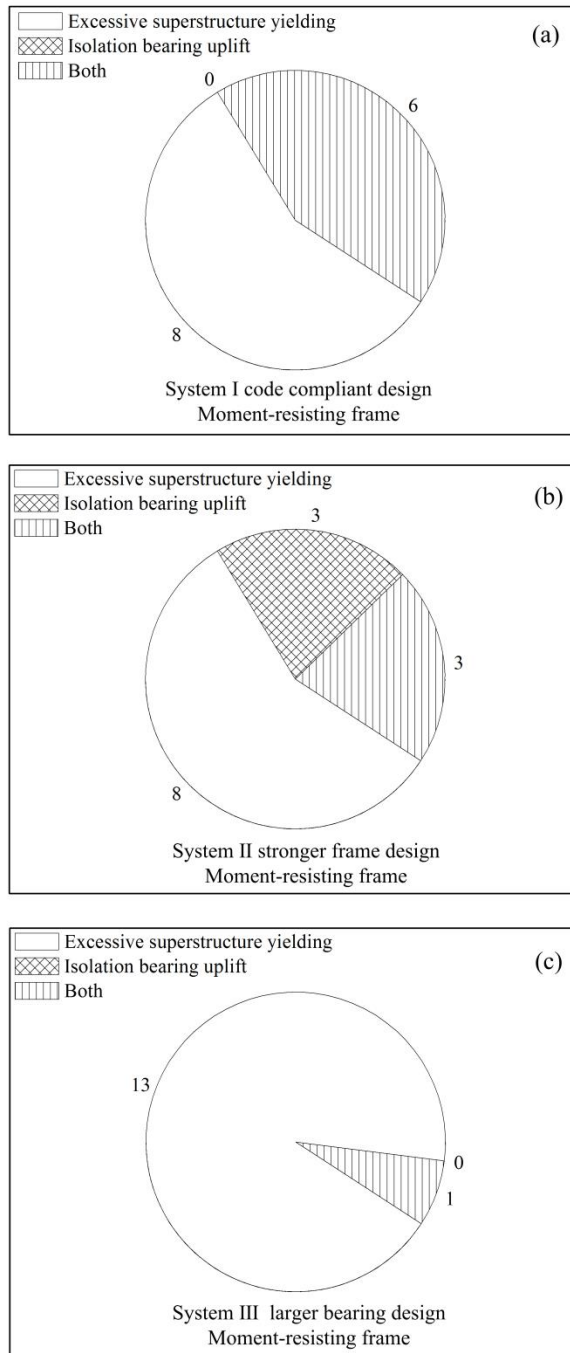
Figure 5-11 Decomposition of failure modes for the isolated moment-resisting frame

Using this definition, the decomposition of system-level failure for moment-resisting frame is depicted in Figure 5-11. For the moment-resisting frames, varying the

design can significantly change the source of system-level failure. For the code compliant

design, no system-level failure is due solely to the isolation bearings; six ground motions

exhibit a mixed failure mode where both isolation bearing uplift failure and

superstructure yielding contribute; and eight ground motions have failure from excessive

superstructure drifts. But for the stronger frame design, three ground motions have failure

due solely to the isolation bearing uplift without excessive superstructure yielding. When

using larger bearing design, superstructure yielding becomes the dominant failure mode,

causing system-level failure in thirteen out of fourteen motions.

For the concentrically-braced frames, regardless of various designs, failure solely

comes from excessive superstructure yielding; drift limits are always exceeded before

bearing uplift failure. From the findings on sources of system-level failure, it is

concluded that ignoring the bearing uplift failure as done in past studies can be justified

for stiff superstructures but not acceptable for flexible superstructures.

5.4.4 Collapse probability

In this section the collapse probabilities of isolated structures are evaluated using FEMA

P695 methodology. As the intensity of the suite of ground motions is larger than the

seismic design category D_{max} the spectral shape factor (SSF) must be calculated. The

equation provided in FEMA P695 Appendix B to calculate SSF is

$$SSF = exp[\beta_1(\bar{\varepsilon}_0 - \bar{\varepsilon}(T)_{records})] \tag{1}$$

where $\bar{\varepsilon}_0$ is the expected number of logarithmic standard deviations between the observed

spectral value and the median prediction from an attenuation function and should be

determined based on the site of interest and ground motion hazard level. For the Los Angeles region the value for ε_0 is 1.7. $\bar{\varepsilon}(T)_{records}$ is found as

$$\bar{\varepsilon}(T)_{records} = 0.2(T - 1.5) \tag{2}$$

where $0.0 \leq \bar{\varepsilon}(T)\_records \leq 0.2$ and T is the code defined natural period. The dispersion, β_1 is determined by

$$\beta_1 = 0.14(\mu_T - 1)^{0.42} \tag{3}$$

where μ_T is the period-based ductility is the ratio of the ultimate displacement δ_u to the effective yield displacement $\delta_{y,eff}$ and $\mu_T \leq 8$. To quantify μ_T, static pushover analyses are performed for the isolated structures assuming infinite bearing displacement capacity. The nonlinear pushover curves are presented in Figure 5-12 and Figure 5-13. The effective yield displacement $\delta_{y,eff}$ is calculated through

$$\delta_{y,eff} = \frac{V_{max}}{W}\left[\frac{g}{4\pi^2}\right]T_M^2 \tag{4}$$

where V_{max} is the maximum base shear of the system, shown in Figure 5-12 and Figure 5-13, W is the seismic weight, and T_M is the natural period of isolated structures which is 3.96 s in this study. The ultimate displacement δ_u is defined as the displacement that corresponds to 20% decrease from the maximum base shear.

For isolated moment-resisting frames, the effective yield displacements $\delta_{y,eff}$ for the code compliant and stronger frame designs are 1.058 m and 1.608 m respectively, the ultimate displacements δ_u are 2.552 m and 3.928 m, therefore the period-based ductility μ_T for code compliant design and stronger frame design are 2.41 and 2.44. Thus, the SSF

can be determined 1.275 for the code compliant design and 1.277 for the stronger frame design.
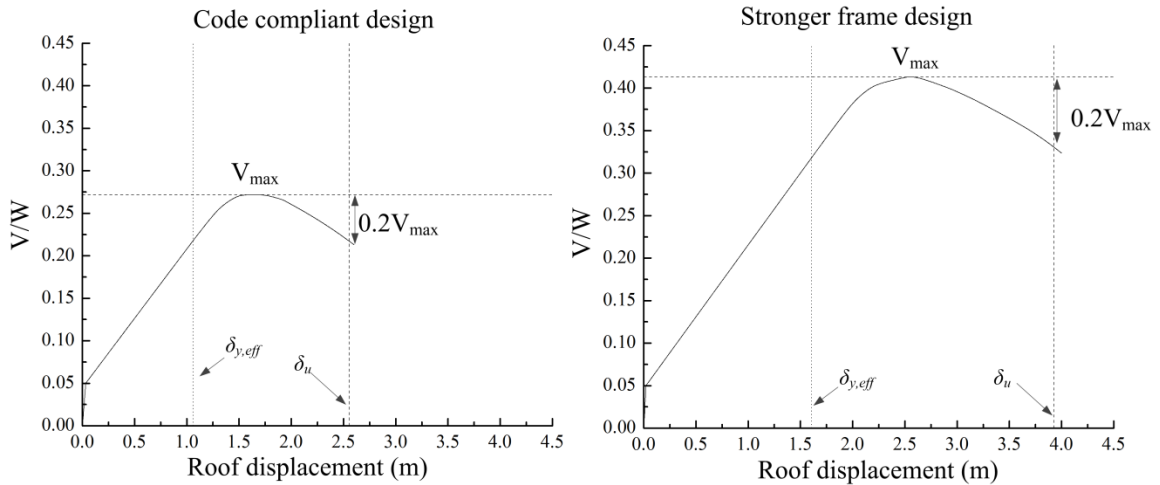
Figure 5-12 Nonlinear pushover curves for different designed isolated moment-resisting frames
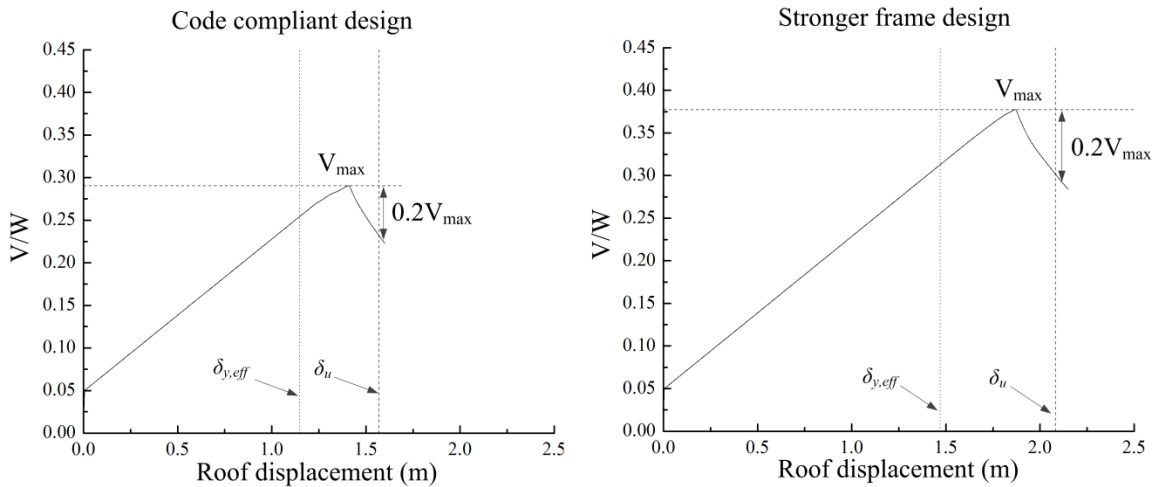
Figure 5-13 Nonlinear pushover curves for different designed isolated concentrically-braced frames

For the concentrically-braced frames, for the code compliant and stronger frame designs, the effective yield displacements $\delta_{y,eff}$ are 1.148 m and 1.469 m, the ultimate displacements δ_u are 1.568 m and 2.081 m, thus the period ductility μ_T for these two designs are 1.366 and 1.417. In the end, the SSF can be found as 1.169 for the code compliant design and 1.179 for the stronger frame design.

The adjusted collapse margin ratio (i.e. ACMR) can then be calculated from

$$ACMR = SSF \times CMR \tag{5}$$

It is also necessary to account for uncertainties when assessing the collapse probability. Four different uncertainties are introduced in the FEMA P695 methodology: 1) record to record uncertainty β_{RTR}; 2) design requirement uncertainty β_{DR}; 3) test data uncertainty β_{TD}; and 4) modeling uncertainty β_{MDL}. In this study the uncertainties are assigned ratings: (B) good for design requirement, (B) good for test data, and (B) good for modeling, respectively. Thus, the uncertainties are quantified as: $\beta_{DR} = 0.2$, $\beta_{TD} = 0.2$ and $\beta_{MDL} = 0.2$. The record to record uncertainty can be calculated as

$$\beta_{RTR} = 0.1 + 0.1\mu_T \tag{6}$$

where $0.2 \leq \beta_{RTR} \leq 0.4$. Based on the period-based ductility identified earlier, for the isolated moment-resisting frames, the record to record uncertainty is $\beta_{RTR} = 0.314$ for code compliant design and $\beta_{RTR} = 0.344$, for stronger frame design. For concentrically-braced frames, the code compliant design has a record to record uncertainty as $\beta_{RTR} = 0.237$, and the stronger frame design has a value of $\beta_{RTR} = 0.242$.
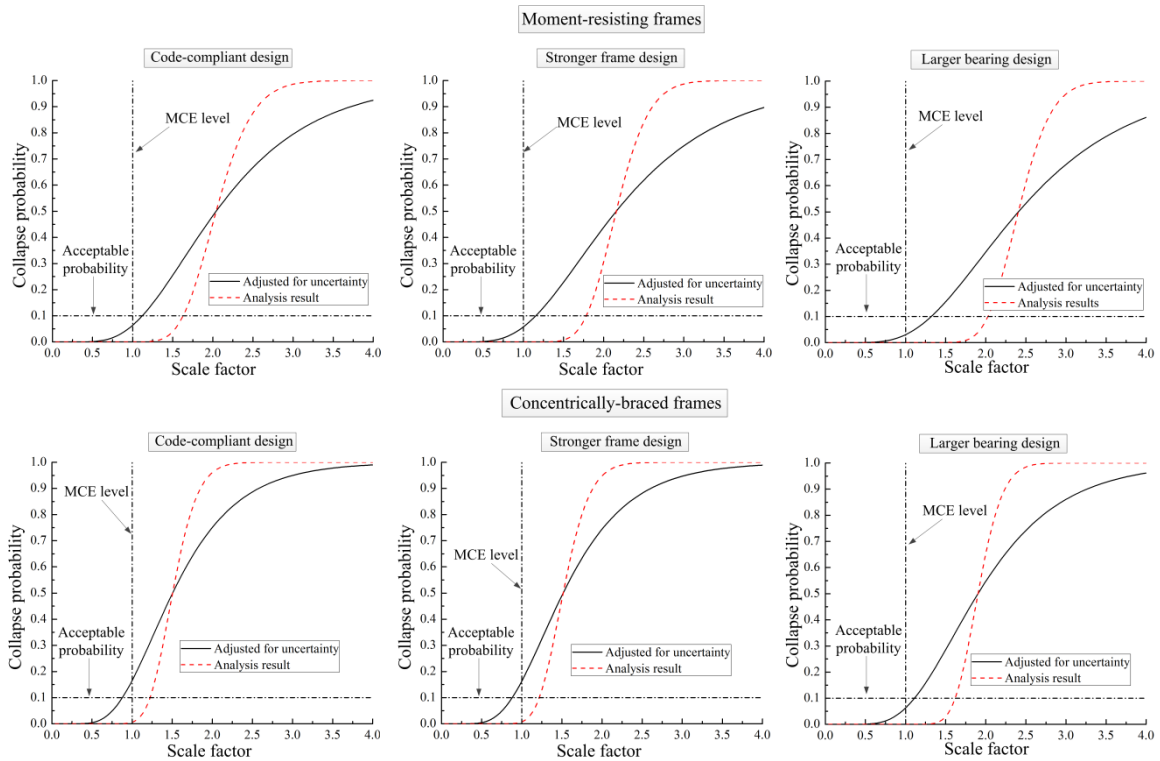
Figure 5-14 Collapse probability curves of isolated frames

The collapse probability curves of isolated structures are shown in Figure 5-14. In this figure, results are shown with and without the additional dispersion from the FEMA methodology to highlight the difference that uncertainties have on the collapse risk analysis. For the isolated moment-resisting frames, all three designs meet the required collapse probability, i.e. less than 10% collapse probability at the MCE level as specified in FEMA P695 (ATC 2009). The code compliant design has a collapse probability of 8% while the stronger frame design and the larger bearing design both have a collapse probability of 5% and 3% respectively. This demonstrates good seismic performance for isolated moment-resisting frames. However, for the concentrically braced frames, only the larger bearing design has a collapse probability of 5%, while the other two designs both exceed 10% collapse probability threshold value, showing unacceptable seismic

performance. The reason for the high collapse probability of isolated concentrically-braced frames is due to stiff superstructure which develops large ductility when subjected to impact force. Interestingly, if excluding additional uncertainty, all isolated structures meet the limit for acceptable collapse probability. This highlights the influence of uncertainty when assessing collapse probability.

5.4.5 Bearing versus moat wall impact

Although it is not the focus of this study, the case in which the isolated moment-resisting frames impact against a moat wall prior to researching the bearing restrainer is also considered. The moat wall is modeled using the impact model developed by Masroor and Mosqueda (2012). Key parameters associated with moat wall are the impact stiffness and gap distance, the first parameter is taken from Masroor and Mosqueda as 4.4×10^9 N / $m^{1.5}$, and the second parameter is selected to be equal to the bearing displacement capacities presented previously. In the configuration with the moat wall, impact and failure of the sliding isolation bearing is eliminated.

When the moat wall is considered, the CMR and collapse probability are similar when comparing impact against moat wall with isolation bearing. The only significant difference is the failure mode which is controlled exclusively through excessive superstructure yielding. Furthermore, the general findings in this study are in agreement with those of Masroor and Mosqueda (2015) which investigated the collapse of isolated frames including the moat wall but without bearing failure. This study found that, predictably, increasing the displacement limit decreased collapse probability, as with the larger bearing design presented here. In addition, the study found that that stiff braced

frames tend to impact at lower intensity levels and have higher collapse probability compared to moment-resisting frames.

5.5 Conclusion

In this paper the collapse risk of isolated moment-resisting and concentrically-braced frames considering the extreme behavior of sliding isolation bearings is evaluated. In order to examine the effect of different designs on the collapse risk, three different systems are designed in accordance with the latest ASCE 7-16 code. They are referred as code compliant design, stronger frame design, and larger bearing design. Since the isolation bearing model is implemented in state-space form, a two-dimensional beam element is developed for numerical simulation. The element can explicitly consider strength and stiffness degradation, second-order effects and internal force interaction, therefore the numerical model is suitable for collapse risk assessment. Fourteen pairs of near-fault pulse-like ground motions are selected as the suite of input motions. The numerical results show that the stiffness of the superstructure largely dictates the collapse risk and failure modes of isolated structures.

For the isolated moment-resisting frames, varying the design has a profound influence on the mode of system-level failure. For the code compliant design and stronger frame design, the system-level failure mode is mixed; both bearing uplift failure and superstructure yielding contribute. In contrast, for the larger bearing design, system-level failure is dominated by superstructure yielding. While the larger bearing design has the largest CMR, it has the smallest safety margin between impact and collapse, and the

stronger frame design has the largest safety margin. All three designs meet the requirement of acceptable collapse probability at the MCE level.

For the isolated concentrically-braced frame, changing the design has limited effect on the mode of system-level failure and total collapse risk. For the stiff superstructure, impact force imposes substantial ductility demand on the superstructure regardless of its strength, therefore, the system-level failure comes solely from superstructure yielding, and only increasing bearing displacement capacity can improve collapse risk in extreme events. This observation suggests that for isolated stiff superstructures the impact should be avoided. For this study, only the larger bearing design has a satisfactorily small the collapse probability.

References

American Society of Civil Engineers (2000). FEMA 356: Prestandard and commentary for the seismic rehabilitation of buildings, Washington, D.C.

American Society of Civil Engineers (2017). ASCE 7-16: Minimum design loads and associated criteria for buildings and other structures, Reston, VA, USA.

Applied Technology Council (2009). FEMA P695: Quantification of building seismic performance factors, Washington, D.C, USA.

Bao Y, Becker TC and Hamaguchi H (2017a). Failure of double friction pendulum bearings under pulse-type motions. *Earthquake Engineering and Structural Dynamics*, 46: 715-723.

Bao Y, Becker TC, Sone T and Hamaguchi H. (2017b). Experimental study of the effect of restraining rim design on the extreme behavior of friction pendulum bearings. (submitted on April 2017 to *Earthquake Engineering and Structural Dynamics*)

Becker TC, Bao Y and Mahin SA (2017). Extreme behavior in a triple friction pendulum isolated frame. *Earthquake Engineering and Structural Dynamics*. Available online. DOI:10.1002/eqe.2924.

Becker TC and Mahin SA (2012). Experimental and analytical study of the bi-directional behavior of the triple friction pendulum isolator. *Earthquake Engineering and Structural Dynamics*, 41:355-373.

Constantinou MC and Fenz DM (2008). Spherical sliding isolation bearings with adaptive behavior: Theory. *Earthquake Engineering and Structural Dynamics*, 37:163-183.

Erduran E, Dao ND and Ryan KL (2011). Comparative response assessment of minimally compliant low-rise conventional and base-isolated steel frames. *Earthquake Engineering and Structural Dynamics*, 40: 1123-1141.

Ikeda K and Mahin SA (1984). A refined physical theory model for predicting the seismic behavior of braced steel frames. EERC report, 84/12, Earthquake Engineering Research Center, University of California at Berkeley, USA.

Jin J and El-Tawil S (2003). Inelastic cyclic model for steel braces. *Journal of Engineering Mechanics*, 129(5): 548-557.

Kelly JM (1990). Base isolation: linear theory and design. *Earthquake Spectra*, 6(2): 223-244.

Kikuchi M, Black CJ and Aiken ID (2003). On the response of yielding seismically isolated structures. *Earthquake Engineering and Structural Dynamics*, 37: 151-164.

Komodromos P, Polycarpou PC, Papaloizou L and Phocas MC (2007). Response of seismically isolated buildings considering poundings. *Earthquake Engineering and Structural Dynamics*, 36: 1605-1622.

Le T and Battini J (2011). Efficient formulation for dynamics of corotational 2D beams. *Computational Mechanics*, 48:153-161.

Lignos DG and Krawinker H (2013). Development and utilization of structural component databases for performance-based earthquake engineering. *Journal of Structural Engineering*, 139(8): 1382-1394.

Masroor A and Mosqueda G (2012). Experimental simulation of base-isolated buildings pounding against moat wall and effects on superstructure response. *Earthquake Engineering and Structural Dynamics*, 41: 2093-2109.

Masroor A and Mosqueda G (2013). Impact model for simulation of base-isolated buildings impacting flexible moat walls. *Earthquake Engineering and Structural Dynamics*, 42: 357-376.

Masroor A and Mosqueda G (2015). Assessing the collapse probability of base-isolated buildings considering pounding to moat walls using FEMA P695 methodology. *Earthquake Spectra*, 31(4): 2069-2086.

Matsagar VA and Jangid RS (2003). Seismic response of base-isolated structures during impact with adjacent structures. *Engineering Structures*, 25: 1311-1323.

Mayes RL (2014). The next generation of codes for seismic isolation in the United States and regulatory barriers to seismic isolation development. *Tenth US national conference on earthquake engineering*, Anchorage, AK, USA.

Okazaki T, Lignos DG, Hikino T and Kajiwara K (2013). Dynamic response of a chevron concentrically braced frame. *Journal of Structural Engineering*, 139(4): 515-525.

Orbison JG, McGuire W and Abel JF (1982). Yield surface applications in nonlinear steel frame analysis. *Computer Methods in Applied Mechanics and Engineering*, 33: 557-573.

Ordonez D, Foti D and Bozzo L (2003). Comparative study of the inelastic response of base isolated buildings. *Earthquake Engineering and Structural Dynamics*, 32: 151-164.

Qu Z, Kishiki S and Nakazawa T (2013). Influence of isolation gap size on the collapse performance of seismically base-isolated buildings. *Earthquake Spectra*, 29(4): 1477-1494.

Remennikov AM and Walpole WR (1997). Analytical prediction of seismic behavior for concentrically-braced steel systems. *Earthquake Engineering and Structural Dynamics*, 26: 859-874.

Sarlis AA and Constantinou MC (2013). Model of triple friction pendulum bearing for general geometric and frictional parameters and for uplift conditions. Technical report MCEER-13-0010, Buffalo, NY, USA.

Sayani PJ, Erduran E and Ryan KL (2011). Comparative response assessment of minimally compliant low-rise base-isolated and conventional steel moment-resisting frame buildings. *Journal of Structural Engineering*, 137(10): 1118-1131.

Shenton HW and Lin AN (1993). Relative performance of fixed-base and base-isolated concrete frames. *Journal of Structural Engineering*, 119(10): 2952-2968.

Su L and Ahmadi G (1989). A comparative study of performances of various base isolation systems, part I: shear beam structures. *Earthquake Engineering and Structural Dynamics*, 18: 11-32.

Su L and Ahmadi G (1990). A comparative study of performances of various base isolation systems, part II: sensitivity analysis. *Earthquake Engineering and Structural Dynamics*, 19: 21-33.

Triantafyllou SP and Koumousis VK (2011). An inelastic Timoshenko beam element with axial-shear-flexural interaction. *Computational Mechanics*, 48:713-727.

Uriz P, Filippou FC and Mahin SA (2008). Model for cyclic inelastic buckling of steel braces. *Journal of Structural Engineering*, 134(4): 619-628.

Vassiliou MF, Tsiavos A and Stojadinovic B (2013). Dynamics of inelastic base-isolated structures subjected to analytical pulse ground motions. *Earthquake Engineering and Structural Dynamics*, 42: 2043-2060.

York K and Ryan KL (2008). Distribution of lateral forces in base-isolated buildings considering isolation system nonlinearity. *Journal of Earthquake Engineering*, 12: 1185-1204.

Chapter 6 To limit forces or displacements:

comparative study of steel frames isolated by sliding

bearings with and without restraining rims

Yu Bao, Tracy C. Becker, Takayuki Sone and Hiroki Hamaguchi. To limit forces or displacements: comparative study of steel frames isolated by sliding bearings with and without restraining rims. This paper has been submitted to *Soil Dynamics and Earthquake Engineering* for review and possible publication.

Abstract

Sliding isolation bearings can provide enhanced seismic performance for both structural and non-structural components under design level earthquakes. However, the ultimate performance once the physical displacement limit is reached or exceeded, has received little attention. One major difference in sliding isolation bearing designs around the world is the restraining rim design. In Europe, the code explicitly forbids any restraining rim in order to eliminate transmission of impact forces to the surrounding structure. However, in North America, all bearings have some form of rim to keep the inner slider from falling out of the bearing. In this study, one moment-resisting frame and one concentrically-braced frame both isolated with sliding bearings using these two rim designs are investigated under extreme conditions. The collapse risks of these base-isolated frames are quantified and compared. Due to the flexibility of the moment-resisting frame, the collapse margin ratios vary slightly between the rim designs with a slight benefit seen

with the bearing design without rims. But for the stiff concentrically-braced frame, eliminating the restraining rim consistently results in a larger collapse margin ratio. This is because the impact force from the rim tends to impose large ductility demands on the concentrically-braced frames causing excessive yielding soon after impact. Generally, using flat rim bearings has a lower collapse probability for both isolated frames, indicating better performance.

6.1 Introduction

One major type of seismic isolation system, sliding bearings, consists of a slider, one or more spherical sliding surfaces, and surrounding rims. The superior seismic performance of sliding isolation bearings under design level excitations compared to fixed-base counterparts, regardless of the specific configuration, has been extensively studied and verified (Zayas et al. 1990; Mokha et al. 1990; Mokha et al. 1991; Fenz and Constantinou 2006; Tsai et al. 2006; Becker and Mahin 2012; Tsopelas et al. 1996; Morgan and Mahin 2006; Fenz and Constantinou 2008). However, most studies have not investigated the ultimate behavior of sliding isolation bearings under extreme conditions. One major concern is that sliding isolation bearings can exhibit large horizontal displacements, which in extreme events may cause pounding against the retaining wall or impact within sliding isolation bearings, potentially resulting in major yielding or collapse of the superstructure.

Pounding of base-isolated building against the moat wall has been investigated in several studies (Masroor and Mosqueda 2012; Masroor and Mosqueda 2013; Qu et al.

2013) with the finding that pounding can result in yielding of the superstructure and increase in the collapse probability. Studies on the extreme behavior of double and triple friction pendulum bearings isolated structures have been conducted by Bao et al. (2017a) and Becker et al. (2017), respectively. However, both of these studies focus on the fully connected restraining rim design (Figure 6-1, left), which is widely used in the United States but may not be representative in the other regions. In Japan the sliding isolation bearings are manufactured either with a flat rim (Figure 6-1, right) or a restraining rim that is bolted on, while in Europe only flat rims are permitted for sliding isolation bearings (European committee for standardization 2009). A recent shake table test using double sliding pendulum bearings (Bao et al. 2017b) demonstrated that the restraining rim designs have substantial influence on the extreme behavior of the bearings themselves. With a fully connected restraining rim, although the bearing can withstand stronger seismic excitation compared to a flat rim design, the bearings transmitted shears as large as 180% of the superstructure's weight. In real structural design, such high base shear may induce considerable yielding and potentially resulting in collapse. For the sliding isolation bearing with a flat rim design, assuming that the bearing fails once the nominal displacement capacity is exceeded may be unnecessarily conservative. In fact, in the experimental study by Bao et al. (2017b) the flat rim bearing experienced displacements larger than 150% of its nominal capacity before becoming non-functional. These two observations motivate the study of examining and comparing the collapse risk of base-isolated frames using the two aforementioned rim designs.

In this paper one moment-resisting frame and one concentrically-braced frame are isolated with double friction pendulum bearings. Two bearing designs are used: one with fully connected rims and one with flat rims. A comprehensive numerical model which can capture both the isolation bearing failure and inelastic superstructure behavior is used. By comparing the seismic responses using the two restraining rim designs, it is found that the stiffness of the superstructure has a profound influence on ultimate performance. For the flexible moment-resisting frame, the impact force does not significantly increase the superstructure ductility demand, resulting in similar collapse margin ratio using the two rim designs. However, for the stiff concentrically-braced frame, the impact force from the rigid restraining rims generates large ductility demand on the superstructure, resulting in a smaller collapse margin ratio compared to flat rim design. When further examining the individual record collapse margin ratios, it is concluded using the flat rim bearing has considerable beneficial effects in reducing the collapse probabilities for both isolated frames.
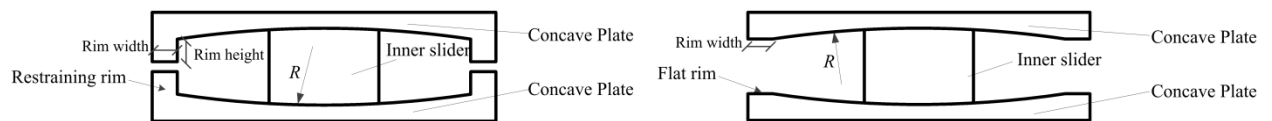
Figure 6-1 Configurations of non-articulated double friction pendulums with different rim designs (left: rigid rim bearing, right: flat rime bearing)

6.2 Design of base-isolated structures

A representative base-isolated moment-resisting frame and concentrically-braced frame designed in accordance with the latest ASCE design code (American Society of Civil Engineers 2016) are used. The isolated structures are located in Los Angeles, California with a site class C (i.e. very dense soil and soft rock). The 5% damped maximum

considered earthquake (MCE) design spectrum, with a 2% probability of exceedance in 50 years, has spectral acceleration values $S_s = 2.35$ g and $S_1 = 0.98$ g. The target bearing displacement under MCE level spectrum is 0.65 m; after iteration and considering accidental torsion, the design properties of double friction pendulum isolation bearing are summarized in Table 6-1. The equivalent damping ratio is 19% and corresponding base shear coefficient is 0.17 g at effective period of 3.96 s.

The configurations of superstructure are shown in Figure 6-2, both superstructures are three-story-three-bay frame structures. After considering the response modifications specified in the design code, which are $R_I = 1.69$ for isolated intermediate steel moment resisting frame and $R_I = 1.22$ for isolated ordinary steel concentrically-braced frame, the total design base shears for moment-resisting and concentrically-braced frame are 0.087 and 0.118 times the corresponding seismic weight. The moment-resisting frame design is displacement-controlled and the limit is 1.5%, as specified in ASCE 7-16. The design of concentrically-braced frame is force-controlled. The selected beam, column and brace section are listed in Table 6-2.

In order to evaluate the collapse risk of the isolated structures, the superstructure models include stiffness and strength degrading behavior and second order geometric effects. For this purpose, a two-dimensional Euler-Bernoulli beam element is formulated (Becker et al. 2017; Bao and Becker 2017c) in the state-space form to be compatible with the isolation bearing models discussed in the following section. This element can simulate the flexural behavior of moment-resisting frames, and when multiple elements

are used, can capture the inelastic buckling behavior of concentrically-braced frames.

Only hysteretic damping is considered in the models.
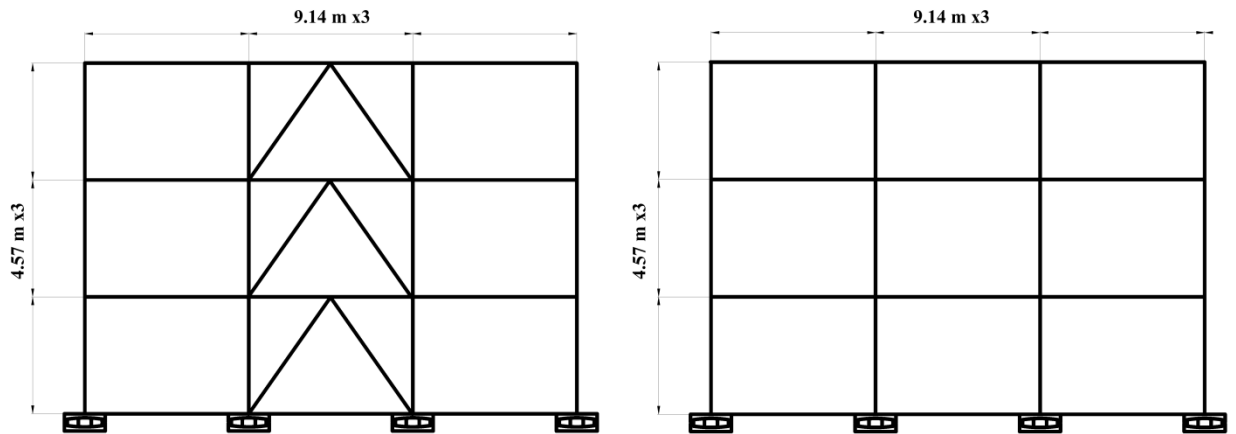
Figure 6-2 Structural layout of base-isolated concentrically-braced and moment-resisting frame

Table 6-1 Design parameters of double friction pendulum bearing

Key response parameter	Value
Displacement capacity (mm)	790
Radius of curvature R (m)	2.75
Second-stiffness period (s)	4.70
Friction coefficient	0.05
Rim height (mm)	12
Flat rim width (mm)	25
Slider height (mm)	150
Slider width (mm)	250

Table 6-2 Beam, column, and brace sections of base-isolated frames

Isolated moment-resisting frame			
Floor	Column section	Beam section	Brace section
First floor	W14x132	W24x62	NA
Second floor	W14x132	W24x62	NA
Third floor	W14x90	W18x60	NA
Isolated concentrically-braced frame			
Floor	Column section	Beam section	Brace section
First floor	W12x72	W27x194	HSS 7x7x5/8
Second floor	W12x72	W24x176	HSS 7x7x1/2
Third floor	W12x72	W24x146	HSS 6x6x1/2

6.3 Validation of numerical bearing models

The rigid body model capable of predicting failure for the double friction pendulum bearings follows the methodology presented by Bao et al. (2017a) which is modified from the formulation of Sarlis and Constantinou (2013). By assuming each bearing component is rigid, the location of any point within the component can be determined from rigid body kinematics. In this section, the numerical predictions of bearing models are compared with experimental uniaxial shake table tests conducted by the Bao et al. (2017b) on double pendulum bearings with both rigid restraining rims and flat rims to evaluate the accuracy of the numerical models and identify possible shortcomings. A detailed description regarding the experimental study can be found in Bao et al. 2017b, the schematic drawing of the experimental setup is shown in Figure 6-3. The superstructure is a 2.8 m by 0.8 m rigid block, weighing roughly 11 tons. The superstructure is supported by two identical double friction pendulum bearings with a length scale factor of 3.5 (i.e. the ratio of dimension of prototype bearing to model bearing). A time scale of $\sqrt{3.5} = 1.87$ is used for the ground motions. The East-West component of the 1995 Kobe earthquake recorded at Takatori station was used. Incremental testing was done from $SA(2.405 \text{ s}) = 0.08$ g up to $SA(2.405 \text{ s}) = 0.17$ g, under which the flat rim bearings lost their functionality and the fully connected thick rim bearings had some minor rim yielding and damage to the slider but remained functional.

To validate both the rigid rim and flat rim bearing models, a numerical model is developed to reproduce the real experimental configuration. In this numerical model, the rigid superstructure has two translational and one rotational degree of freedom, which are

measured at its centroid. The rigid block is supported by two identical double friction pendulum bearings, and each bearing is independently modeled. The input motion is gradually scaled up until any isolation bearing exhibits failure.

6.3.1 Rigid rim bearing model

To model a rigid restraining rim, Bao et al. (2017a) replaced the linear spring found in Sarlis and Constantiou's formulation with the Hertz nonlinear spring to incorporate energy dissipation during impact. While the model cannot capture yielding of the rim, uplift failure, defined as when any vertex of the inner slider moves horizontally beyond the region confined by restraining rims of the top plate or bottom plate can be captured. The comparisons between the experimental results and the numerical predictions of the maximum horizontal displacement and acceleration are shown in Figure 6-4. The maximum horizontal acceleration is defined as the maximum base shear divided by the superstructure mass. It is observed that, generally, the maximum horizontal displacement predicted by the numerical model is in good agreement with the experimental results, but that the prediction of the acceleration becomes less accurate as the impact grows stronger. In the experimental study, the maximum horizontal acceleration never exceeded 2 g, but the numerical model predicts accelerations as high as 3.5 g. This is believed to be due to minor yielding of the restraining rim which can limit the impact force. As the model assumes all components of the isolation bearing to be rigid, the rim yielding is not captured. Due to the prediction of larger impact forces, the rigid rim model results in a smaller estimation of critical ground motion intensity measure for predicting failure of the bearing system. In fact, the numerical model predicts tbearing uplift failure occurs at

SA(2.405 s) = 0.17 g; however, in the experimental study the isolation bearings remained operational under this motion.

Over-prediction of the impact force could potentially lead to premature yielding and collapse of the superstructure. To address this, one possibility is to limit the impact force to 2 g. This is implemented through modifying the nonlinear Hertz spring which models the impact force so that it plateaus. Although this treatment does not represent the real mechanism of rim yielding, it does constrain the impact force. However, numerical analyses of the full building system found that the critical ground motion intensity measures presented in later sections are not heavily influenced by whether the impact force is limited or not. Therefore, the original rigid rim bearing model is used. The lack of strong dependence of the results on the exact peak bearing force may be because the seismic response of superstructure is governed by a combination of both the amplitude and duration of the impact force or simply that impact forces are significantly large that the superstructure will yield regardless.
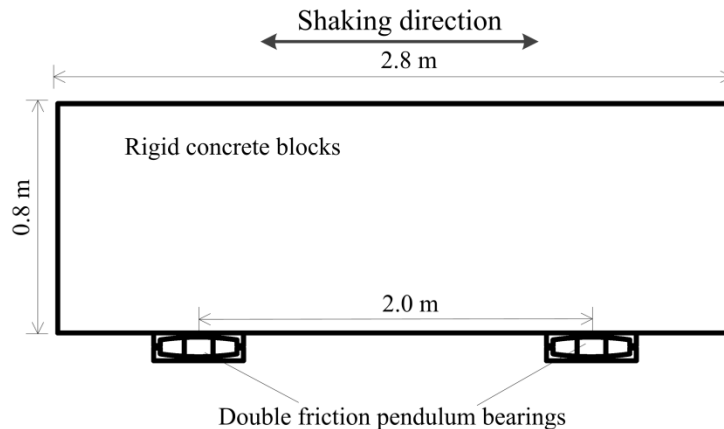
Figure 6-3 Schematic drawing of experimental setup

Figure 6-4 Comparisons between rigid rim bearing model and experiment (left: maximum horizontal

displacement; right: maximum horizontal acceleration)

6.3.2 Flat rim bearing model

The double friction pendulum bearing with flat rim model is an extension of the rigid

body model developed in previous studies (Bao et al. 2017a; Sarlis and Constantinou

2013). The major difference is the removal of the Hertz nonlinear spring so that no

impact force is developed. To account for the presence of the flat rim, additional contact

points are added to the model to consider the transition phase of the inner slider from the

concave surface to the flat rim. Failure of this model is triggered directly by the loss of

stability of inner slider due to the centroid of the slider moving beyond the edge of the

flat rim.
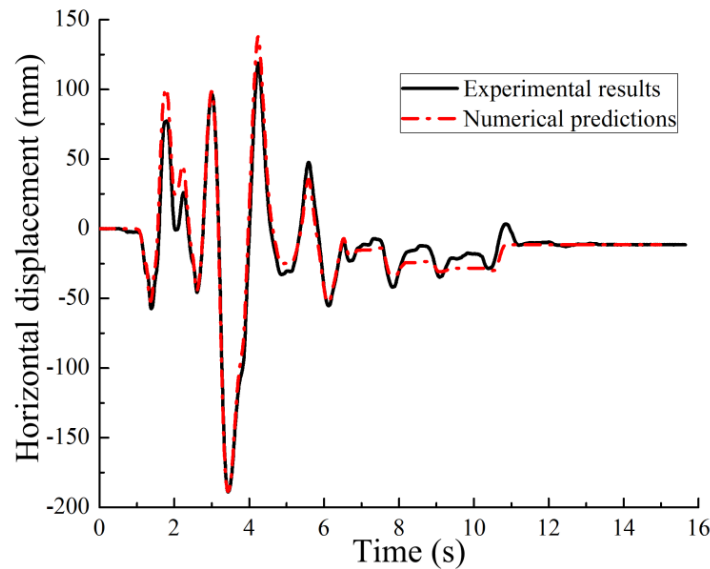
Figure 6-5 Comparison of horizontal displacement time history under $SA(2.405\ s) = 0.165$ g

Again, the experimental data from Bao et al. (2017b) is used for validation. For the ground motion with intensity of $SA(2.405\ s) = 0.165$ g, the horizontal displacement time histories are compared in Figure 6-5. In this was the penultimate ground motion intensity before the bearings failure experimentally. Note that in Figure 6-5 the maximum horizontal displacement is 190 mm, which is much larger than the nominal displacement capacity of the bearing, which is 130 mm. As such, the inner slider moves onto the flat rim range; this is in good agreement between the experimental results and numerical predictions demonstrate the accuracy of the flat rim bearing model. Under the same ground motion, the general motion is compared in Figure 6-6. The model does a good job of capturing the behavior, even showing the non-symmetric response on the top and bottom plate due to catching on the flat rim. The numerical model predicts this catching on the top plate while the experimental results show catching on the bottom.

The maximum horizontal displacements and accelerations from all testing levels from the experimental results and numerical predictions are presented in Figure 6-7. For the maximum displacements, the numerical prediction is in good agreement with experimental results, but the numerical model tends to under-predict the maximum acceleration. Note here the maximum acceleration shown in Figure 6-7 is defined using the whole time history response including the behavior after the slider drops, which is not captured in the flat rim bearing model. In terms of predicting failure, in the experiments the flat rim bearings failed (were non-functional) after the SA(2.405 s) = 0.17 g while the numerical failure predicts failure at SA(2.405 s) = 0.18 g. The ultimate displacement before failure is very close: 217 mm in the experiment and 214 mm in the numerical model; these are well above the nominal displacement limit of 130 mm. The hysteresis loops upon failure of the isolation bearings are compared in Figure 6-8, note these hysteresis loops are obtained under the same ground motion but at different scaling factors as the numerical model predict failure at a slightly larger motion. For the numerical model, as the slider approaches the flat rim, the hysteresis loop becomes flat followed by a sudden drop due to the slider loses its stability. In the experiment, there is no discernible flat region but a gradual drop in the horizontal force. As a result, the numerical model over-predicts the force. In the subsequent section, the maximum superstructure drift ratio is remains close to 1% as the ground motion intensity increases to bearing failure, showing that the larger forces transmitted to the superstructure are not a concern.
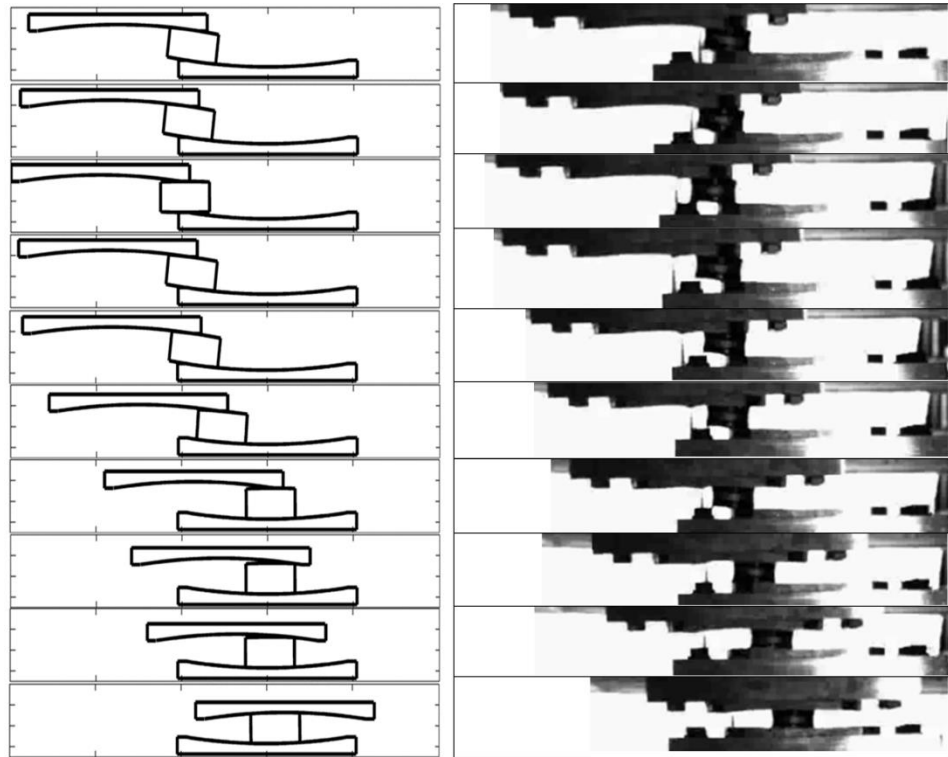
Figure 6-6 Comparison of behavior of flat rim bearings (left: numerical model, right: experimental)
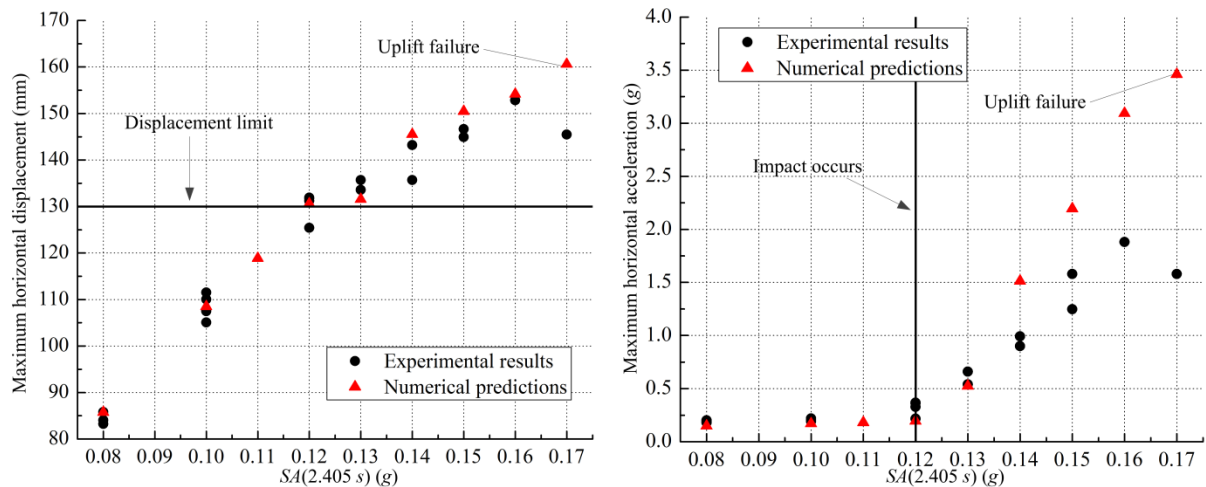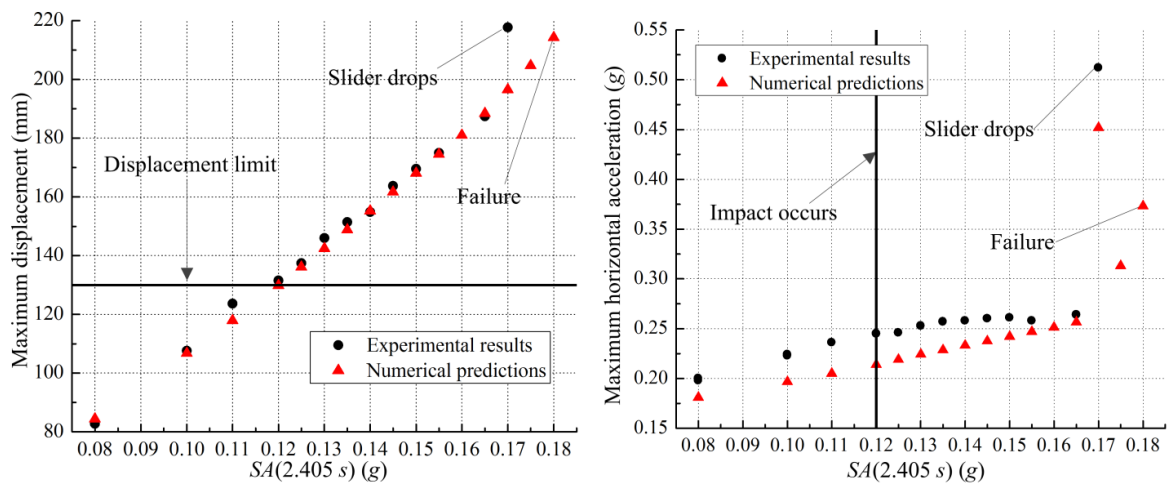

Figure 6-7 Comparisons between flat rim bearing model and experiment (left: maximum horizontal

displacement; right: maximum horizontal acceleration)
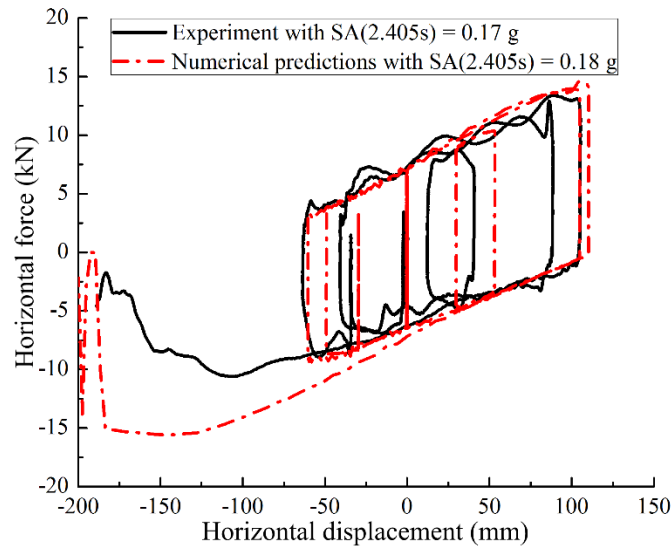
Figure 6-8 Comparison of hysteresis loops upon failure of isolation bearing with flat rim

6.4 Collapse risk of isolated frames with different rim designs

6.4.1 Pulse-like ground motions and scaling

As isolated structures have elongated natural period, they are more vulnerable to pulse-like motions; therefore, fourteen pairs of pulse-like ground motions recommended in FEMA P695 (Federal Emergency Management Agency 2009) are used as the suite of input ground motions. Ground motion details can be found in Table 6-3. Each ground motion contains two orthogonal components, the East-West and North-South component, which are applied independently resulting in twenty-eight input motions. As the frames are designed using the MCE level response spectrum, the suite is initially scaled to be compatible with the design response spectrum. This can be done with multiple methods (American Society of Civil Engineers 2010; Federal Emergency Management Agency 2009); in this study, the scaling method outlined by FEMA P695 (Federal Emergency Management Agency 2009) is followed. The suite of ground motions is scaled so that the median spectral acceleration value at 3.96 s, which is the secant stiffness-based period at

the MCE level earthquake, equals the target spectral acceleration value, which is 0.247 g.

The response spectra of the suite of ground motions and its median response spectra are

plotted in Figure 6-9.
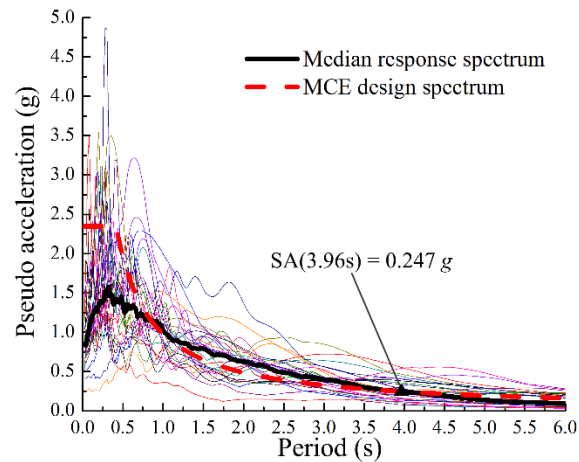
Figure 6-9 5% damped response spectra and median response spectra

Table 6-3 Fourteen pairs of pulse-like ground motions recommended in FEMA P695

Number	M_w	Name	Station	V_s30 (m/s)	NEHRP Class	Unscaled PGA (g)	Scale factor
GM 1	6.5	Imperial Valley-06	El Centro Array#6	203	D	0.44	1.42
GM 2	6.5	Imperial Valley-06	El Centro Array#7	211	D	0.46	1.52
GM 3	6.9	Irpinia,Italy-01	Sturno	1000	B	0.31	2.72
GM 4	6.5	Superstition Hills-02	Parachute Test Site	349	D	0.42	1.64
GM 5	6.9	Loma Prieta	Saratoga-Aloha	371	C	0.38	2.57
GM 6	6.7	Erzican, Turkey	Erzincan	275	D	0.49	1.72
GM 7	7	Cape Mendocino	Petrolia	713	C	0.63	1.71
GM 8	7.3	Landers	Lucerne	685	C	0.79	1.22
GM 9	6.7	Northridge-01	Rinaldi Receiving Sta	282	D	0.87	1.09
GM 10	6.7	Northridge-01	Sylmar_Olive View	441	C	0.73	1.26
GM 11	7.5	Kocaeli,Turkey	Izmit	811	B	0.22	4.40
GM 12	7.6	Chi-Chi,Taiwan	TCU065	306	D	0.82	1.17
GM 13	7.6	Chi-Chi,Taiwan	TCU102	714	C	0.29	1.36
GM 14	7.1	Duzce,Turkey	Duzce	276	D	0.52	1.71

6.4.2 Incremental dynamic analysis

In order to evaluate which bearing design results in lower collapse risk, incremental

dynamic analysis (IDA) is conducted for each building using the suite of motions. The

IDA is terminated when half of the ground motions cause explicit bearing uplift failure or bearing instability in the rigid rim bearing design and flat rim bearing design, respectively. For each ground motion, the initial scaling factor may be less than 1.0 to capture seismic responses from the initial bearing impact up to explicit bearing failure. All the input ground motions are scaled up in increments of 10%.

In the following two subsections, the IDA curves for isolated frames with different rim designs are presented for individual motions as well as the suite. The IDA curve, which plots an engineering demand parameter against an intensity measure, describes the seismic response of a particular structure with increasing ground motion. Here, the maximum drift ratio and maximum ductility at the component-level are used as demand parameters. While both values can be used in defining superstructure collapse, in this study only the drift ratio is used to judge the collapse of superstructure due to excessive yielding, as specified in FEMA 356 (Federal Emergency Management Agency 2000); the threshold drift ratio values for moment-resisting frames and concentrically-braced frames are 5% and 2% respectively. The component ductility is used only to highlight the difference in ductility demands between the superstructures due to the impact force.

When constructing the IDA curves there is some difficulty due to truncation of the time history response which is done to avoid numerical instability after bearing failure. Due to the truncation, if a peak engineering demand parameter occurs after bearing failure, it will not be captured. As a result, the IDA curve may plateau or drop at

the critical intensity measure. In this study, it is proposed that once bearing failure occurs, for the ground motions with higher intensity, the previous maximum value is used.

6.4.2.1 Individual ground motions

In this section, the IDA curves for three representative ground motions, GM1 East-West (EW), GM2 North-South (NS) and GM11 East-West (EW), are presented. For the isolated moment-resisting frames, the IDA curves are terminated when explicit bearing failure is observed, which is bearing uplift for rigid rim bearing and bearing instability for flat rim bearing. However, when judging the system-level failure mode, both bearing failure and excessive superstructure yielding are considered. In this study, whichever failure mode comes first is defined as the source of the system-level failure. For the concentrically-braced frames, the IDA curves are only constructed to one intensity level beyond initial impact. This is because the concentrically-braced frames typically develop unrealistically large drift ratios before bearing uplift failure occurs; therefore, this portion of the IDA curve is not meaningful.

The IDA curves in terms of maximum drift ratio considering all floors for the isolated moment-resisting frame are depicted in Figure 6-10. The maximum drift ratio tends to occur at the first floor as the ground motion intensity increases. For the moment-resisting frames isolated with the rigid rim bearings, for GM1 EW, impact occurs at 130% of MCE and at 140% of MCE the maximum drift ratio exceeds the 5% threshold drift, but bearing uplift failure does not occur until 160% of MCE. When using the flat rim bearings, even after the nominal displacement limit is exceeded, the maximum drift ratio remains at roughly 2% until bearing instability occurs at 160% of MCE. For this ground

motion, the failure mode for the moment frame isolated with the rigid rim bearings is excessive superstructure yielding at 140% of MCE, and for the flat rim bearing, the failure mode is bearing failure at 160% of MCE. Clearly, for GM1 EW, using flat rim bearing provides better performance. However, for GM2 NS the reverse is true; with rigid rim bearings the system-level failure comes from excessive superstructure yielding at 110% of MCE, while with flat rim bearings, bearing instability occurs at 90% of MCE. For GM11 EW, both bearing designs result in the same intensity at failure. Thus, while the failure mechanisms remain clearly distinct between the two bearing designs (i.e. excessive superstructure yielding versus bearing instability), there is no general conclusion for the moment-resisting frames on which rim design gives a better collapse margin.

The maximum drift IDA curves for the concentrically-braced frames are shown in Figure 6-11. For the rigid rim bearing design, after bearing impact occurs, the maximum drift ratio quickly exceeds the 2% drift ratio threshold, well before bearing uplift failure occurs. As a result, the system-level failure mode is governed exclusively by excessive superstructure yielding. For the flat rim design, due to the elimination of the impact force, the maximum drift ratio remains well below 2% and the system-level failure comes exclusively from bearing instability. Although in general using flat rim bearings results in higher collapse margins for the isolated concentrically-braced frames (e.g. 140% versus 120% of MCE level for GM1 EW), there are still exceptions. For example, under GM2 NS, the system-level failure occurs at the same intensity level (i.e. 80% of MCE).

By comparing the responses of moment-resisting and concentrically-braced frames under different ground motions, it is clear that both the stiffness of the superstructure and complex nature of earthquakes contribute to the issue of which rim design should be adopted. The high stiffness of the concentrically-braced frame makes it very sensitive to impact forces. In general, the flexible moment-resisting frame can withstand the earthquake intensities well beyond those causing impact, while the stiff concentrically-braced frame reaches excessive drifts when impact is just initiated.

The IDA curves for maximum ductility of isolated moment-resisting and concentrically-braced frames are also presented in Figure 6-12 and Figure 6-13. The IO, LS and CP in these figures are abbreviations of Immediate Occupancy, Life Safety, and Collapse Prevention; their threshold values are defined in FEMA 356 (Federal Emergency Management Agency 2000). Similar trends can be observed for the maximum ductility as for the drift. When using rigid rim bearings, the maximum ductility increases as the scale factor exceeds impact, but the concentrically-braced frame tends to be more sensitive to the impact force, and its ductility demand quickly goes beyond CP. In contrast, the maximum ductility remains relatively low with the flat rim bearings due to the elimination of the impact force.
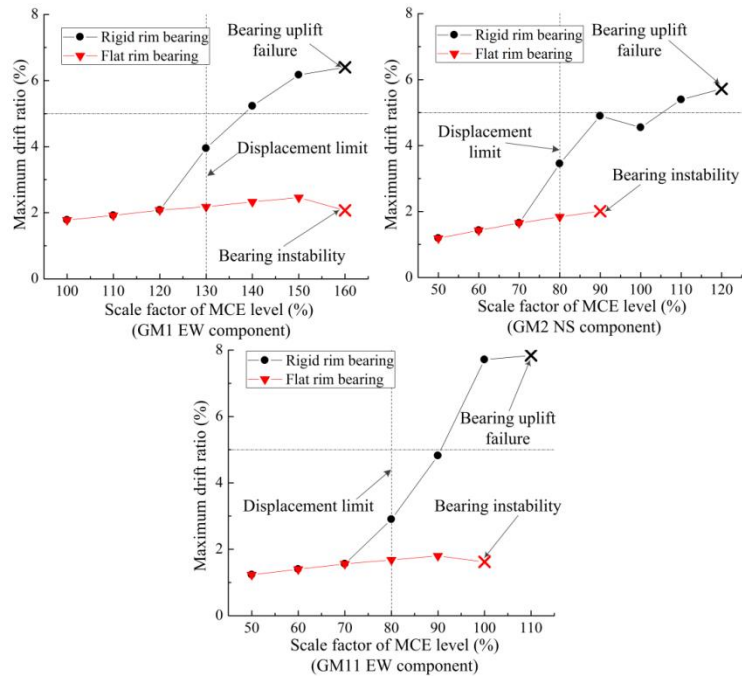
Figure 6-10 IDA curves of maximum drift ratio of isolated moment-resisting frames under three different
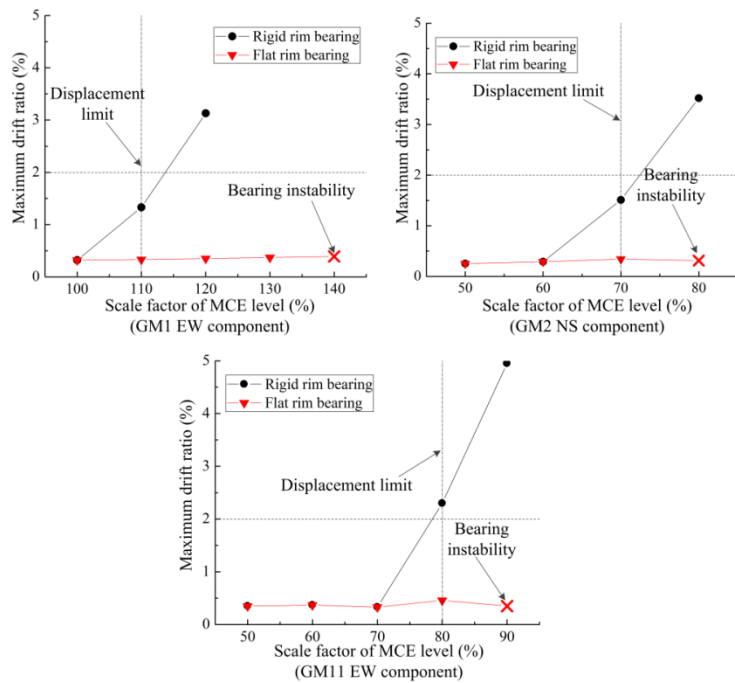
motions

Figure 6-11 IDA curves of maximum drift ratio of isolated concentrically-braced frames under three
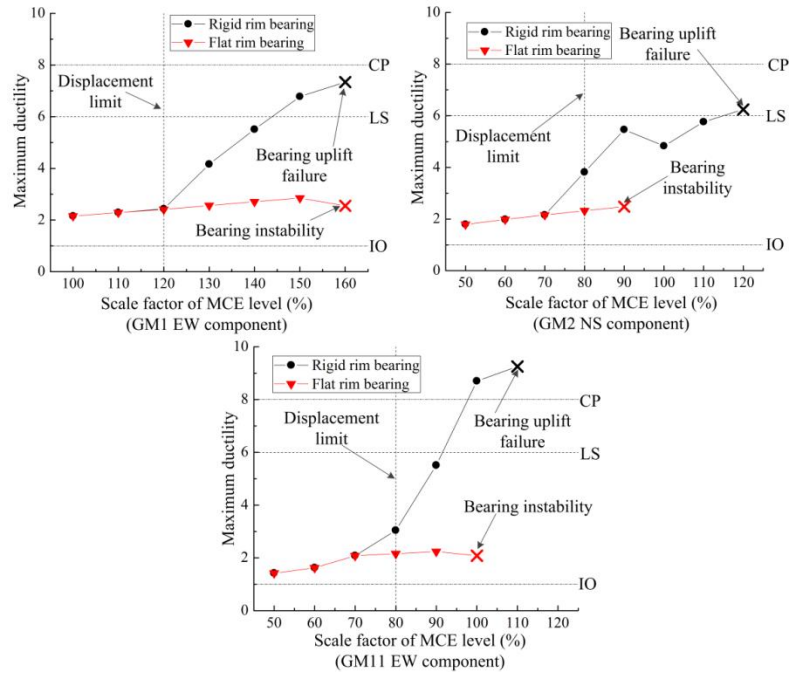
different motions

Figure 6-12 IDA curves of maximum ductility of isolated moment-resisting frames under three different
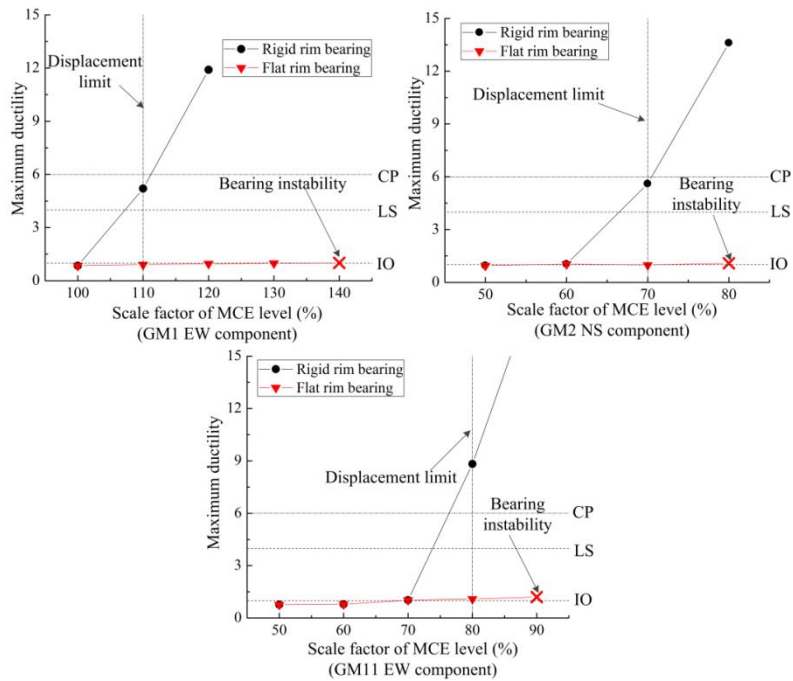
motions

Figure 6-13 IDA curves of maximum ductility of isolated concentrically-braced frames under three

different motions

6.4.2.2 Suite of ground motions

Since no general conclusions can be made by examining individual ground motions, especially for the moment resisting frame, it is useful to evaluate the seismic responses under the suite of motions. For the suite of ground motions, the collapse margin ratio (CMR), which is defined as the ratio of spectral acceleration at the isolation period of the MCE level to the spectral acceleration at which half of the suite of ground motions cause collapse. Similarly, the concept of impact margin ratio (IMR) can be defined in the same way. The IMR and CMR are used to evaluate the performance of the isolated frames under the suite of ground motions.

The median IDA curves for the maximum drift ratio of the isolated frames are shown in Figure 6-14 with the IDA curves for all ground motions. For the moment-resisting frames with rigid rim bearings, the IMR is 120% of MCE; after the IMR is reached, the average maximum drift ratio increases gradually to 5% when half of the ground motions exhibit system-level failure at 140% of MCE which is the CMR. When using flat rim bearings, the IMR, which simply denotes when the nominal displacement limit is reached rather than impact, is still 120% MCE as the rim design does not affect displacements prior to impact. After reaching the IMR, the maximum drift ratio remains below 2%, well below the collapse threshold of 5%, until half of the ground motions have resulted in system-level failure at 150% of MCE. Thus, the flat rim bearings result in a higher CMR than the rigid rim bearings.

The bearing design also affects the collapse mechanism. For the isolated moment-resisting frame with rigid rim bearings, the system-level failure is dominated by

excessive superstructure yielding; this is the case for eight out of fourteen ground motions. The other motions have failure attributed to a combination of bearing uplift failure and superstructure yielding. In contrast, when flat rim bearings were used, bearing instability accounted for the failure in all of the ground motions.

For the concentrically-braced frames with rigid rim bearings, the CMR value is only 10% higher than its IMR value of 110% of MCE. Excessive superstructure yielding is the sole system-level failure mode. For the flat rim bearings, after exceeding the IMR at 110% of MCE, the maximum drift ratio remains around 0.3% until the CMR at 140% of MCE is reached, due exclusively to bearing instability. For the concentrically-braced frames, the flat rim bearing design provides significantly larger safety margin compared to the rigid rim bearing design. Again, this is due to the sensitivity of the stiff concentrically-braced frames to the impact force from rigid rims.

The CMR for the suite of ground motions ignores the record to record variability. Therefore, it is also helpful to examine the CMR for individual ground motions that result in the system-level failure. The comparison of CMR for individual ground motions using two different rim designs is shown in Figure 6-15. In this figure eleven ground motions (i.e. half of the suite of ground motions) are compared, the ground motion number and its component are also listed in Figure 6-15. It can be observed that generally speaking, using flat rim bearings leads to larger CMR value compared to rigid rim bearings for the stiff concentrically-braced frames, but there is no consistent observation for the flexible moment-resisting frames. For example, for GM6 NS component using flat rim bearings

results in a CMR 10% higher than for rigid rim bearing, but for GM2 NS component, the

rigid rim bearing design results in a CMR value 20% larger than with flat rims.
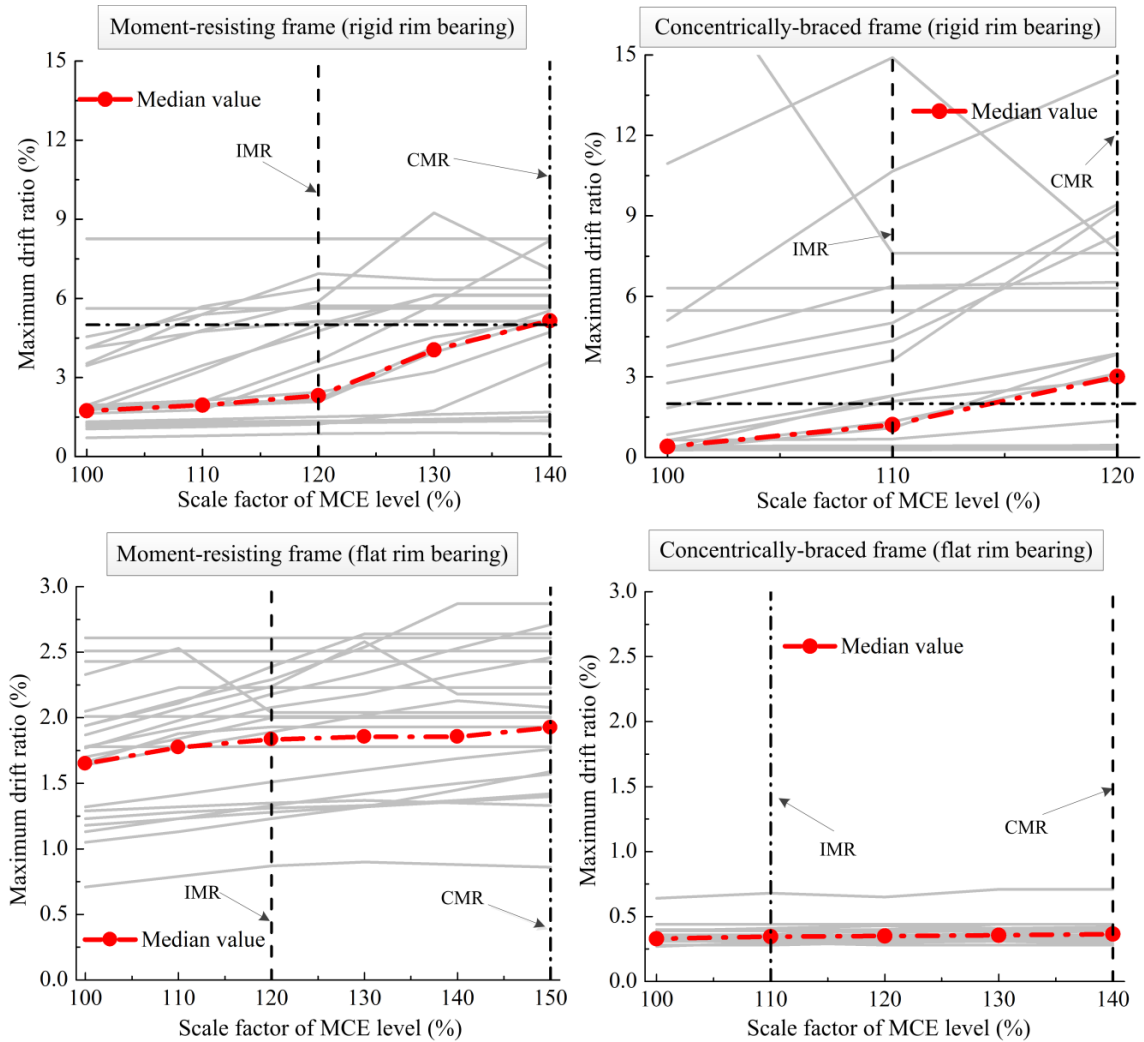
Figure 6-14 IDA curves of maximum drift ratio under the suite of ground motions
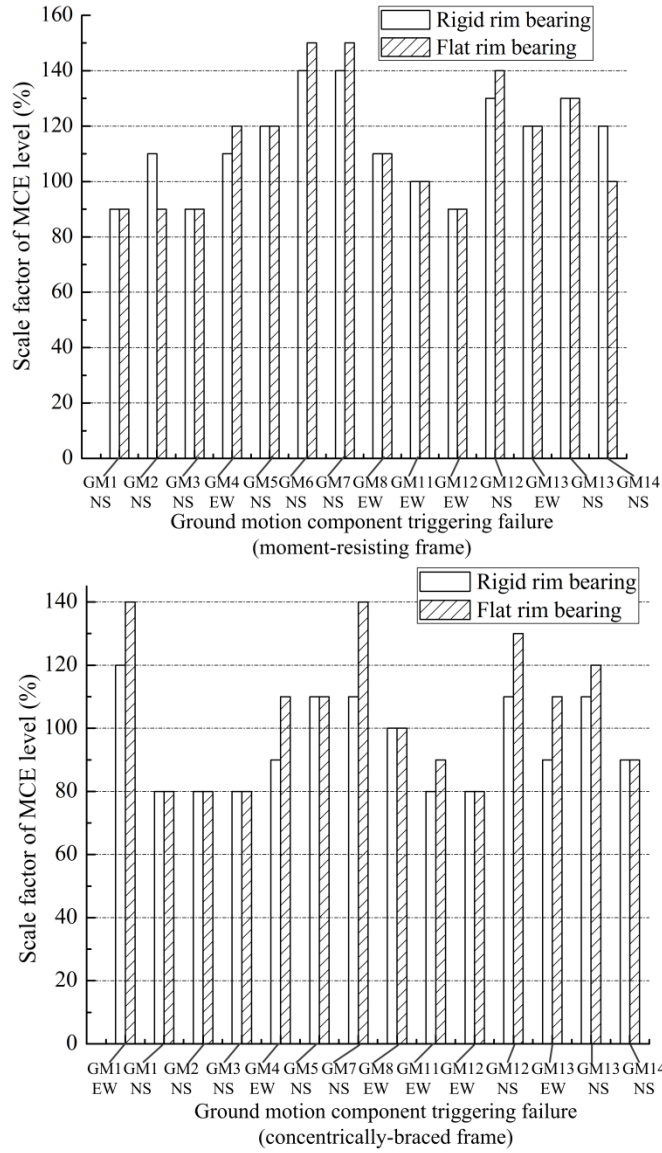
Figure 6-15 CMR for individual ground motion triggering system-level failure (left: moment-resisting

frame; right: concentrically-braced frame)

6.4.3 Collapse probability

The collapse probabilities of frames isolated with different rim design bearings are

presented in this section. In the methodology specified in FEMA P695 (Federal

Emergency Management Agency 2010), the collapse probability should be evaluated

after introducing the following four sources of uncertainties: 1) record-to-record uncertainty β_{RTR}; 2) design requirement uncertainty β_{DR}; 3) test data uncertainty β_{TD}; and 4) modeling uncertainty β_{MDL}. The last three uncertainties are specified in FEMA P695 based on qualitative ratings; they are assigned as $\beta_{DR} = 0.2$, $\beta_{TD} = 0.2$, and $\beta_{MDL} = 0.2$ which indicate levels of 'good'. The first uncertainty requires site-specific seismic hazard analysis and nonlinear pushover analysis; it is found as: $\beta_{RTR} = 0.314$ for the moment-resisting frame and $\beta_{RTR} = 0.237$ for the concentrically-braced frame.

The collapse probabilities of the moment-resisting and concentrically-braced frames isolated with rigid and flat rim bearings are shown in Figure 6-16. The horizontal axis is in terms of scale factor of MCE level ground motion. In FEMA P695, the acceptable collapse probability is defined as less than 10% under the MCE level ground motion. For the moment-resisting and concentrically-braced frames isolated with rigid rim bearings, at MCE level the collapse probability is 8% and 15% respectively. However, when replacing the isolation bearings with flat rim designs, the collapse probability reduces to 4% for the moment-resisting frame and 10% for the concentrically-braced frame. Thus, the flat rim is useful in reducing the collapse probability for both the concentrically-braced frames and moment-resisting frames. The beneficial effects are particularly apparent for the concentrically-braced frame; using flat rim design can achieve an acceptable collapse probability compared to the rigid rim design.

One major consideration in any collapse analysis is the limitations in the models. While the models used here are able to explicitly model failure of the isolation layer as well as yielding and degradation of the superstructures, it does not model the building

behavior post isolation bearing failure. For rigid rim bearings, failure for both frames types was dominated by superstructure nonlinear behavior. However, with the flat rims all collapses were triggered by bearing instability. There is actually no knowledge of the superstructure performance after the bearing failure, and thus, the collapse margin ratio and collapse probability are the lower bounds. This further boosts the benefit of the flat rim bearings especially for the concentrically-braced frames.
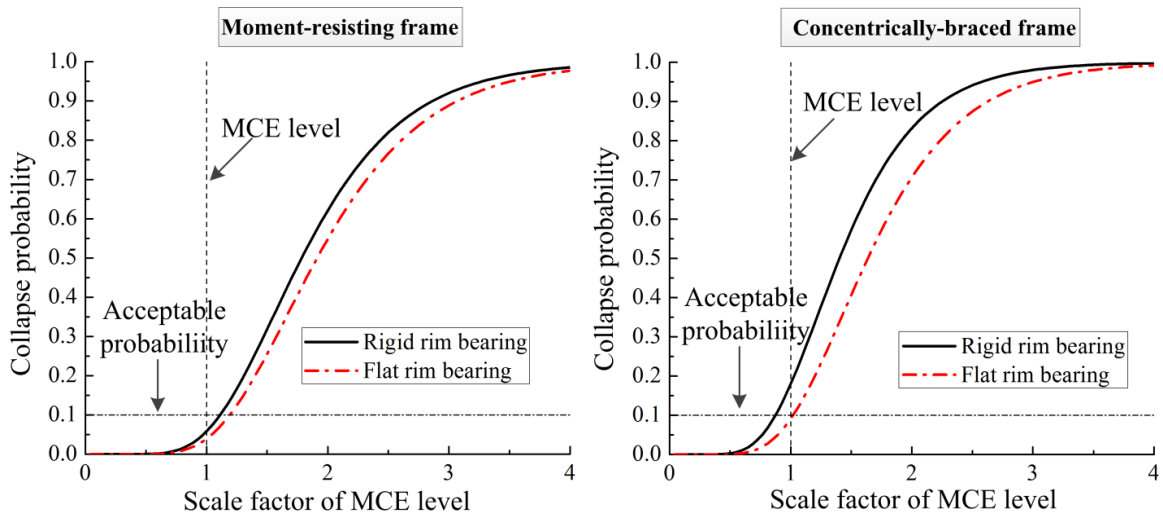
Figure 6-16 Collapse probabilities of isolated frames with different rim designs

6.5 Conclusions

This paper conducts a comparative study of moment-resisting and concentrically-braced frames isolated by double friction pendulum bearings with two distinct rim designs: rigid rims and flat rims. In order to be used in the collapse risk assessment, a rigid rim bearing model, which previously existed in the literature, and a flat rim bearing model, which is introduced in this paper, were compared with the experimental study. For the rigid rim bearing model, the predicted maximum displacement is generally in good agreement with the experiment but the acceleration under large impacts is significantly higher. The over-

prediction of the maximum horizontal acceleration (and resulting maximum shear force) is expected as the model does not consider rim yielding. However, even if the impact force is intentionally capped, the critical ground motion intensity measures for the isolated frames are not heavily influenced. The flat rim bearing model provides sufficient accuracy to predict the critical intensity measures.

The moment-resisting and concentrically-braces frames respond differently to the impact with the rigid rim. For the moment-resisting frame, the superstructure can withstand considerable impact force without exhibiting excessive yielding. When examining the record-to-record CMR values, it is found there is no clear conclusion which bearing design is better; only after comparing the CMR for the suite of ground motions and collapse fragility it is found that using flat rim bearings design has a small beneficial effect. The concentrically-braced frame, however, is extremely sensitive to the impact force. The CMR for the suit of ground motions for this system with rigid rim bearings is only slightly higher than the IMR, and this is due to excessive superstructure yielding under small levels of impact. Consequently, using a flat rim design results in a consistently larger CMR. More importantly, using flat rim bearings for the stiff concentrically-braced frame reduces the collapse probability to an acceptable level.

Varying the rim design also changes the system-level failure mode. When using the rigid rim design, the system-level failure modes for the moment-resisting frames are mixed; both bearing uplift failure and excessive superstructure yielding contribute, but the latter is more prevalent. For the concentrically-braced frame, failure comes exclusively from the superstructure yielding when using rigid rim bearings. However,

when isolating these frames with the flat rim bearing design, for both superstructures, the system-level failure mode is dictated solely by bearing instability.

Acknowledgements

References

American Society of Civil Engineers. ASCE 7-10: Minimum design loads and associated criteria for buildings and other structures, 2010, Reston, VA, USA.

American Society of Civil Engineers. ASCE 7-16: Minimum design loads and associated criteria for buildings and other structures, 2016, Reston, VA, USA.

Bao Y, Becker TC and Hiroki H. Failure of double friction pendulum bearings under pulse-type motions. *Earthquake Engineering and Structural Dynamics*, 2017a, 46: 715-723.

Bao Y, Becker TC, Sone T and Hamaguchi H. Experimental study of the effect of restraining rim design on the extreme behavior of friction pendulum bearings. *Earthquake Engineering and Structural Dynamics,* 2017b. Available online. DOI:10.1002/eqe.2997.

Bao Y and Becker TC. Effect of design methodology on collapse of friction pendulum isolated moment-resisting and concentrically-braced frames. (submitted to *Journal of Structural Engineering,* August 2017c)

Becker TC and Mahin SA. Experimental and analytical study of the bi-directional behavior of the triple friction pendulum isolator. *Earthquake Engineering and Structural Dynamics*, 2012, 41: 355-373.

Becker TC, Bao Y and Mahin SA. Extreme behavior in a triple friction pendulum isolated frame. *Earthquake Engineering and Structural Dynamics*, in press, 2017. DOI:10.1002/eqe.2924

European committee for standardization. European standard 15129: Anti-seismic devices (English version), Brussels, Belgium, 2009.

Federal Emergency Management Agency. FEMA P695: Quantification of building seismic performance factors, 2009, Washington, D.C, USA.

Federal Emergency Management Agency. FEMA 356: Prestandard and commentary for the seismic rehabilitation of buildings, 2000, Washington D.C, USA.

Fenz DM, Constantinou MC. Behaviour of the double concave friction pendulum bearing. *Earthquake Engineering and Structural Dynamics*, 2006, 35: 1403-1424.

Fenz DM and Constantinou MC. Spherical sliding isolation bearing with adaptive behavior: experimental verification. *Earthquake Engineering and Structural Dynamics*, 2008, 37: 185-205.

Masroor A and Mosqueda G. Experimental simulation of base-isolated buildings pounding against moat wall and effects on superstructure response. *Earthquake Engineering and Structural Dynamics*, 2012, 41: 2093-2109.

Masroor A and Mosqueda G. Assessing the collapse probability of base-isolated buildings considering pounding to moat walls using FEMA P695 methodology. *Earthquake Spectra*, 2015, 31(4): 2069-2086.

Morgan TA and Mahin SA. Achieving reliable seismic performance enhancement using multi-stage friction pendulum isolators. *Earthquake Engineering and Structural Dynamics*, 2010, 39: 1443-1461.

Mokha A, Constantinou MC and Reinhorn AM. Teflon bearings in base isolation I: testing. *Journal of Structural Engineering*, 1990, 116(2): 438-454.

Mokha A, Constantinou MC, Reinhorn AM and Zayas VA. Experimental study of friction-pendulum isolation system. *Journal of Structural Engineering*, 1991, 117(4): 1201-1217.

Qu Z, Kishiki S and Nakazawa T. Influence of isolation gap size on the collapse performance of seismically base-isolated buildings. *Earthquake Spectra*, 2013, 29(4): 1477-1494.

Sarlis AA and Constantinou MC. Model of triple friction pendulum bearing for general geometric and frictional parameters and for uplift conditions. Technical report MCEER-13-0010, 2013, Buffalo, NY, USA.

Tsai CS, Chen WS, Chiang TC and Chen BJ. Component and shaking table tests for full-scale multiple friction pendulum system. *Earthquake Engineering and Structural Dynamics*, 2006, 35: 1653-1675.

Tsopelas P, Constantinou MC, Kim YS and Okamoto S. Experimental study of FPS system in bridge seismic isolation. *Earthquake Engineering and Structural Dynamics*, 1996, 25: 65-78.

Zayas VA, Low SS and Mahin SA. A simple pendulum technique for achieving seismic isolation. *Earthquake Spectra*, 1990, 6(2): 317-333.

Chapter 7 Conclusions and Recommendations

Base isolation is a well-established technology to protect both structural and non-structural components from being damaged during earthquakes. Its superior seismic performance has been validated by many studies under regular conditions. However, there is still concern regarding excessive horizontal displacement in the isolation system as it could potentially induce the failure of the isolation bearing itself or pounding against the moat wall. Sliding isolation bearings or, more specifically, friction pendulum bearings are one major type of isolation bearing; however, there has been little work on its extreme behavior when the displacement limit is reached or exceeded. This represents a critical hole in our knowledge. Thus, in order to understand the bearing's ultimate performance and evaluate the safety margin in design, this thesis presented a comprehensive study on the extreme behavior of friction pendulum bearings as well as the steel moment-resisting and braced frame buildings isolated with these bearings. For simplicity, the double friction pendulum bearing with a non-articulated slider was used throughout. Major conclusions found in this study are presented below.

7.1 Conclusions

7.1.1 Failure modes of double friction pendulum bearings

There are two major failure modes for the double friction pendulum bearings with a fully-connected rim. For a standard bearing design, when the superstructure mass is sufficiently large (e.g. 50 MPa on the slider, which is the standard operating pressure), the dominant failure mode is yielding of the restraining rim. On the other hand, when the superstructure mass is relatively small (e.g. 10 MPa slider pressure), the failure is

governed by bearing uplift. For the bearings with flat rim available in Japan and Europe, the failure mode is straight-forward; it comes from the loss of stability of the isolation bearing from the internal slider moving off the edge of the sliding surface.

7.1.2 Failure prediction under pulse-like ground motions

As seismically isolated structures are particularly vulnerable to long-period motions, the failure of double friction pendulum bearings under pulse-like motions is investigated. Under the excitation of Ricker pulses, used for their mathematical simplicity as there are only two parameters, the response (no impact, impact without failure and failure) of double friction pendulum bearings can be summarized in the impact region spectrum. Using wavelet analysis, the dominant Ricker pulses can be extracted from the pulse-like ground motions. Combined with the impact region spectrum, the failure of double friction pendulum bearings under pulse-like ground motions can then be predicted. It is found that this method can provide good predictions compared to directly using real pulse-like ground motions, allowing this method to be used as a preliminary guidance for selection of bearings.

7.1.3 Extreme bearing behavior: experimental results

To validate the extreme behavior of double friction pendulum bearings and evaluate the accuracy of the developed numerical model, an experimental study was also conducted. Four scale isolation bearings with different rim designs, which represent typical sliding isolation bearings in Europe, Japan, and North America, were tested well beyond their displacement capacities. For bearings with fully connected rims, used in North America, two rim thicknesses were used. Both bearings had large uplift due to the impact force.

The bearing with thin rims had significant rim yielding while the bearing with thick rim only had minor yielding.

For the bolted rim design, available in Japan, the uplift behavior was eliminated but significant rim yielding occurred accompanied with significant damage to the internal slider; the impact force caused large plastic deformation of the stopper ring and shears the connection screw off.

For the bearings with flat rim, available in Japan and standard in Europe, due to the elimination of the impact force, there is no uplift behavior; the failure of isolation bearing is characterized by the loss of its load-carrying capacity. During the whole test, only the flat rim bearing loses its load-carrying capacity. The other three bearings with restraining rims remain functional after the test, although increases in friction coefficient due to slider damage was observed, again most notably for the bolts rim bearing.

7.1.4 Transmitted forces in extreme events: experimental results

For the bearing with flat rim, the bearings reached a maximum horizontal displacement 50% larger than its nominal displacement capacity. This is dependent on the bearing geometry but demonstrates that there is an additional margin of safety for this bearing design. As there was no impact force, the maximum shear force in the bearings was limited to 0.3 g, the theoretical maximum shear force at the displacement limit is 0.22 g, which is around 25% less than the recorded value.

For the bolted rim design, the bearing reached a displacement 15% larger than its capacity. The maximum shear is around 1.0 g, the uplift amount is also the lowest among the bearings with restraining rims, partially due to the lowest input intensity.

For fully connected rim bearings, their horizontal displacements were limited to 10% larger than their capacity. Due to the impact, large shear forces were observed: 1.44 *g* and 1.58 *g* for the thin rim and thick rim bearing, respectively. Additionally, the uplift amount was 26 mm.

7.1.5 Numerical models of double friction pendulum bearings

Two numerical models were used in this study to investigate the extreme behavior of double friction pendulum bearings: the finite element model and the rigid body model. The finite element model is more comprehensive as it captures both uplift and rim yielding, but it is computationally expensive. The rigid body model, on the other hand, is more efficient but only captures the uplift failure mechanism. It was found that if supporting a rigid mass, two numerical models give close estimations of ground motion critical intensity measures.

When comparing to the experimental results of the fully-connected rim bearings, the finite element model effectively captures the rim yielding and bearing uplift behavior. However, modeling a single bearing with a superstructure mass rather than the physical system which has overturning results in a significant under-prediction of the critical ground motion intensity.

The same is true for the rigid body model. However, when the real dimension and configuration of the experimental setup is considered, the non-uniform behavior of two bearings can be reproduced and the prediction of the critical intensity measure is improved. However, as the rigid body model does not consider rim yielding, it tends to over-predict the impact force and under-predict the critical intensity measure.

Using the original rigid body model as a basis, a model for the flat rim design was developed. Compared to the experimental results, the maximum displacements which occur once the slider travels onto the flat rim are well captured while the maximum shear force in the bearing is slightly under-predicted. This numerical model gives a close estimation of critical intensity measure compared to experiments.

7.1.6 State-space element formulation

In order to perform the system-level study which includes the extreme behavior of sliding isolation bearings, a two-dimensional Euler-Bernoulli beam element in the state-space form was developed. This element incorporates degrading behavior, second-order effects, and internal force interaction, making it suitable for collapse assessment. The stiffness and strength degradation behavior is implemented through the degrading Bouc-Wen model, which includes two hysteretic parameters. The second-order effects are achieved using co-rotational method, and internal force interaction is implemented through a yield surface function. This element can be used to simulate the flexural behavior of moment-resisting frame or the inelastic buckling behavior of concentrically-braced frame.

7.1.7 Collapse of isolated moment-resisting frames

For the flexible moment-resisting frame designed to the United States isolation design code with bearings with full rims, the collapse modes are mixed: both bearing uplift failure and excessive superstructure yielding contribute. The collapse probability is below the acceptable threshold value of 10% at MCE level. When a larger base shear is used to design the superstructure, the collapse probability decreases and while the modes of failure are till mixed, more motions result in bearing failure rather than structure yielding.

Only when a larger bearing design is introduced is the system-level collapse mode is governed by the superstructure yielding. This results in the lowest collapse probability; however, it also results in the smallest margin between bearing impact and system-level failure.

7.1.8 Collapse of isolated concentrically-braced frames

The stiffness of the superstructure largely dictates its collapse probability and system-level collapse modes. Due to the large stiffness of concentrically-braced framed, the impact force tends to impose a large ductility demand on the superstructure regardless of the design strength. As a result, for the braced frame designed to the United States isolation design code with bearings with full rims, the system-level failure mode comes exclusively from the excessive superstructure yielding and the probability of failure under the MCE event is greater than 10%. Only by increasing the bearing's displacement capacity can the system meet the required collapse probability. Therefore, it is recommended for isolated stiff superstructure the impact force should be avoided.

7.1.9 Effects of restraining rim designs on extreme performance

The collapse risk of moment-resisting and concentrically-braced frames isolated by double friction pendulum bearings with two different rim designs, rigid rim and flat rim design, were compared. For the rigid rim bearing, the conclusions are identical to those given above. For the flat rim bearing, as there is not impact force, superstructure maximum drift is limited and the system-level failure modes for both isolated frames are exclusively controlled by the bearing failure. For both superstructures isolated by flat rim bearings, the collapse margin ratio is increased, indicating enhanced seismic performance.

Moreover, using flat rim bearing for stiff concentrically-braced frame can meet acceptable collapse probability requirement while using rigid rim bearing design cannot.

7.2 Recommendations for future study

7.2.1 Analytical isolation bearing model

It is desirable to develop a more advanced analytical model that can simulate the extreme behavior of sliding isolation bearings. One necessary step is to develop a three-dimensional model; another is to consider the effect of rim yielding. The latter is motivated from the shake table tests. It was found that the impact forces from the experiments are usually smaller than the predictions from the current numerical model. This is because to the current numerical model cannot consider rim yielding, and, as a result, it over-predicts the impact force. It may be more conservative using current bearing model in the collapse assessment since it increases the force transmitting to the superstructure, but an accurate prediction is always desirable especially when comparing systems.

7.2.2 Experimental failure and rim yielding

Due to the facility capacity and potential safety issues, the isolation bearings with restraining rims were not physically tested to dynamic failure. Future study may consider test these isolation bearings to dynamic failure to gain a more comprehensive understanding. The effect of rim yielding is also of interest. In the experimental study the maximum shear did not exceed 2 *g*; it is inferred this is due to yielding of the restraining rim that can limit the impact force transmitting to the superstructure. This inference needs further experimental studies to validate.

7.2.3 Other configurations of friction pendulum bearings

The experimental study presented in this thesis only validates the extreme behavior of double friction pendulum bearings with a non-articulated slider. This configuration may be of limited interest outside Japan. In the United States, for example, the friction pendulum bearings usually have an articulated slider. Also, there are also other types of friction pendulum bearings (e.g. single friction pendulum bearings, triple friction pendulum bearings, etc.) in the world. The configuration of friction pendulum bearings may have influence on the extreme behavior, which needs to be addressed in the future study.

7.2.4 Other issues

For simplicity, two major simplifications were made in this study. First, in this study the friction coefficient is assumed to be a constant value for simplicity; however, friction is dependent on temperature, velocity, and pressure. Changes in the friction coefficient will change the maximum displacement and velocity at impact. Secondly, only the horizontal ground motions were considered. However, vertical ground motion may also be important as it may affect the axial load on the bearing prior to impact, influencing the bearings ability to uplift. It is recommended these considerations are included in future studies.

Appendix I: Extreme Behavior in a Triple Friction Pendulum Isolated Frame

Abstract

While isolation can provide significantly enhanced performance compared to fixed-base counter parts in design level or even maximum considered level earthquakes, there is still uncertainty over the performance of isolation systems in extreme events. Researchers have looked at component level stability of rubber bearings and on the effect of moat impact on behavior of structures isolated on general bilinear isolators. However, testing of triple friction pendulum (TFP) sliding bearings has not been done dynamically or incorporated into a building system. Here, 1/3rd scale laboratory tests were conducted to on a two-story two-bay TFP isolated structure. Input motions were increasingly scaled until failure occurred at the isolation level. As the superstructure was designed with a yield force equivalent to the force of the bearing just at their ultimate displacement capacity, there was minimal yielding. A numerical model is presented to model the isolated building up-to and including bearing failure. Forces transferred to the superstructure in extreme motions are examined using both experimental and numerical

data. Additionally, the effect of the hardening stage of the TFP bearing is evaluated using the numerical model, finding slight benefits.

1 Introduction

It is well accepted that seismic isolation can provide enhanced performance for structures under a range of earthquake ground motions, reducing accelerations for non-structural components as well as displacements to the benefit of both structural and non-structural elements. However, only limited studies have been conducted on the behavior of isolated buildings under extreme, potentially unpredicted, ground motions. This is an important area that has received significant attention for traditional fixed-base design methodologies, but lacks in seismic isolation design.

A handful of numerical studies have looked at the performance of isolated buildings, up to and including collapse (FEMA 2009; Erduran et al. 2011; Sayani et al. 2011; Terzic et al. 2012), some with the purpose of lifetime cost assessment. However, these studies did not include any extreme bearing behavior or restriction from seismic moats; isolators were allowed to displace indefinitely. Unless the isolation system is designed with sufficient displacement capacity to give confidence that yielding and subsequently collapse will first occur in the superstructure and the distance to the moat is sufficient that impact will not occur, these studies cannot accurately capture the extreme behavior of the isolated structure.

Masroor and Mosqueda (2012) experimentally tested a single bay of a moment frame isolated with single friction pendulum bearings. Their setup included a moat wall

with soil backfill. For these tests, the moats were positioned so that the friction pendulum bearings never reached their ultimate displacement capacity. They found that the forces from moat impact amplified story drift and accelerations responses and could induce yielding in the superstructure, although no collapse was observed in the testing. Using a model for the moat impact developed from their experimental testing (Masroor and Mosqueda 2013), Masroor and Mosqueda (2015) looked at the collapse probability of braced and moment frame buildings, with general bilinear isolators. Cutfield et al. (2016) looked at the same braced frame structure with the included moat impact to investigate the effect of moat impact on life cycle cost. These studies showed that, indeed, presence of a moat increased collapse probability and expected annual repair costs.

While these studies take a major step forward into understanding extreme behavior in isolation buildings, they still have not included the possibility of bearing impact or failure, defined here as when the bearing loses intended functionality due to extreme loading. Similar to fixed-base buildings constructed of different materials, the failure mechanisms of elastomeric and sliding type isolation systems vary significantly, and thus the extreme behavior of each system must be studied in its own right. Significant research, both numerical and experimental, has been conducted on the stability of elastomeric bearings at the component level (Simo and Kelly 1984; Buckle et al. 2002; Cardone and Perrone 2012; Sanchez et al. 2013; Han and Warn 2014; Vemuru et al. 2014; Kumar et al. 2015; Montuori et al. 2016). Fewer tests of full structural systems on elastomeric bearings have been conducted to extreme levels. Monzon et al. (2016) tested a curved bridge in which the elastomeric bearings became unstable under excessive

displacements, however, due to the unsymmetric geometry of the structure sufficient restoring force remained in the isolation level, not all bearings exhibited this instability and the seismic inertia force returned the system to zero displacement.

As sliding bearings are comparatively newer, less research has been conducted on their behavior under extreme events. Triple friction pendulum bearings, or other sliding bearing with multiple components have complex dynamic failure behavior due to the multiple unconnected parts, each with their own inertial forces. Many dynamic tests (Morgan 2008; Fenz and Constantinou 2007; Becker and Mahin 2012; Sasaki et al. 2012; Sarlis et al. 2013), both on the triple friction pendulum bearing itself as well as full frame systems, have tested the bearings up to maximum considered earthquake levels and even to maximum isolation capacity but have stopped short of failure. For prototype bearings tests, quasistatic extreme loading tests are often conducted. However, these tests cannot capture contributions from dynamic uplift behavior; thus these tests find yielding in the restraining rim where as a combination of the two mechanisms would most likely be expected. Bao et al. (2017) looked numerically at the failure of double friction pendulum bearings at their component level, finding that, depending on the mass of the structure, uplift played a large role in the ultimate behavior of the bearings.

This paper presents the results of a dynamic unidirectional shake table test of a steel frame isolated with triple friction pendulum (TFP) bearings. The ground motion input was increased until failure occurred in the isolation level. In these tests, no seismic moat was included to simplify the experiment and gain knowledge on the system behavior in this previously untested condition. A numerical model, validated against the

experimental data, is presented to observe how changes to the experimental TFP design

would affect the magnitude of the ground motion at which bearing failure occurs. The

trends of the forces transmitted into the superstructure and the force distribution in the

superstructure under the increasing ground motions through impact and ultimately

bearing failure are presented.

2 Experimental Setup

For these tests, a unidirectional shake table was constructed in the UC Berkeley NEES

lab. The shake table, shown in Figure I-1 and Figure I-2, consists of a large steel platform

isolated on low-friction linear bearings. The steel platform is 5.8 m long by 2.0 m wide

and is supported at six points, directly below the locations of the six isolators used in the

experiment. The shake table is driven by a dynamic MTS actuator with +/- 0.5 m of

stroke and +/- 667 kN force capacity.
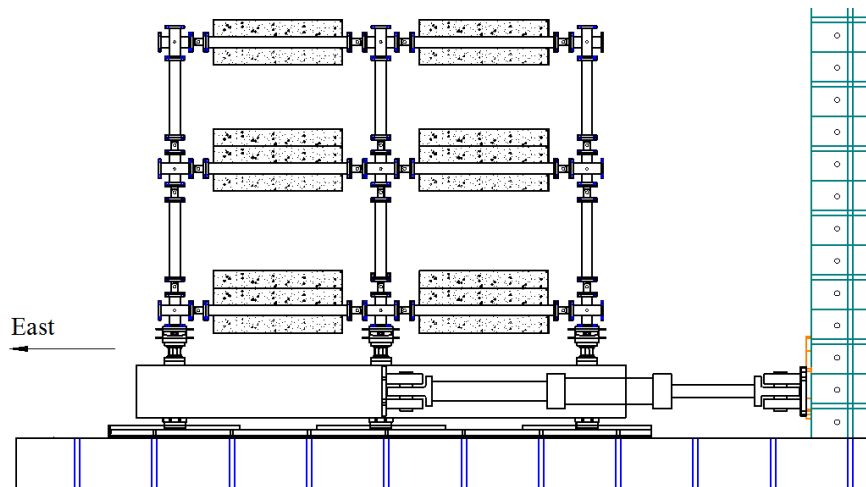
Figure I-1 Isolated frame on the unidirectional shake table

(a)

(b)
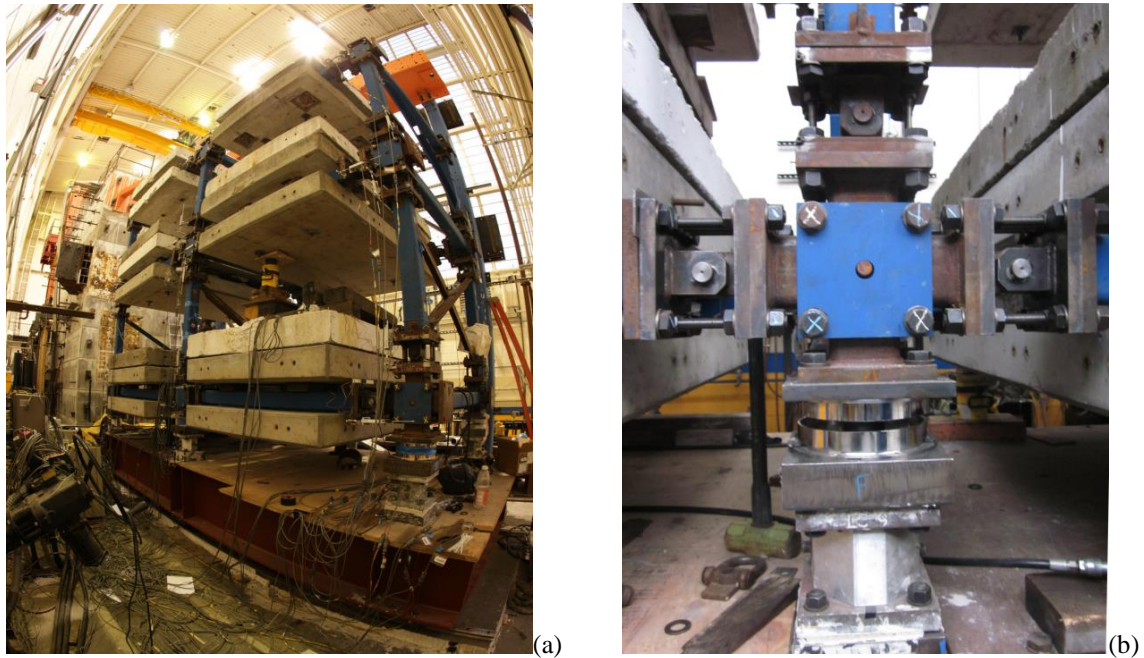
Figure I-2 (a) Isolated frame on shake table and (b) close-up of isolator and clevises

2.1 Design of the specimen

A two-story steel moment frame was designed and constructed at 1/3rd scale to fit on the unidirectional shake-table. The first and second story heights are 1.7 m and 1.5 m, respectively. The frame has two bays in the direction of loading with a span of 2.44 m. The frame was one bay in the out-of-plane direction. The frame was constructed using the NEES REconfigurable Platform for EArthquake Testing (REPEAT frame) which uses clevises with replaceable steel coupons at locations of expected plastic hinges, as seen in Figure I-2b. Each clevis can accommodate three pairs of coupons. Coupon pairs are spaced 178 mm on-center.
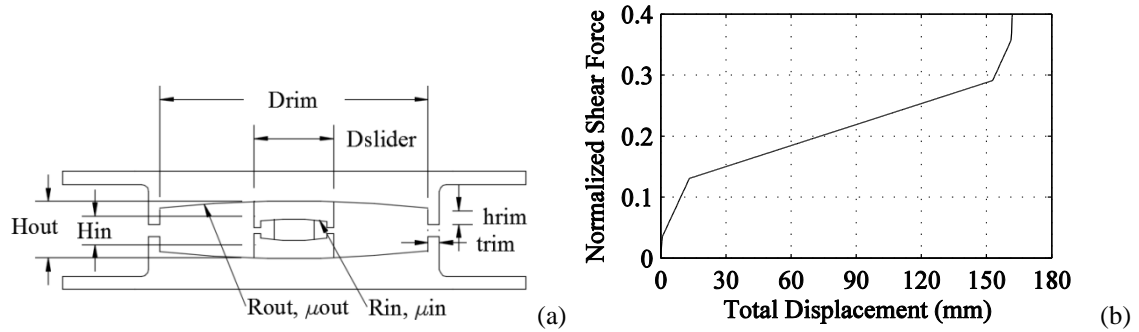
Figure I-3 (a) Triple friction pendulum bearing and (b) backbone curve

Table I-1 Triple friction pendulum properties

	Inner surfaces	Outer surfaces
R	76 mm	474 mm
μ	0.03	0.13
D_{rim}	64 mm	229 mm
D_{slider}	38 mm	76 mm
t_{rim}	6 mm	12 mm
h_{rim}	10 mm	20 mm
H	38 mm	64 mm

The frame was isolated on six triple friction pendulum (TFP) bearings, shown in Figure I-3 with properties given in Table I-1. The ultimate displacement capacity of the model-scale isolators is 163 mm. The equivalent elastic period of the bearings is 1.32 s at 100 mm and the post-yield second sliding stage period is 1.87 s (2.29 s and 3.24 s at full scale respectively). The bearings had a flexible rubber seal between the 76 mm diameter sliders, encasing the innermost slider. This seal did not change the backbone behavior of the bearing. The frame was loaded with concrete blocks and lead weights to reach a total weight of 380 kN so that the pressure on the sliding surfaces in the isolators would be sufficiently large (~10 N/mm2 on the outer sliding surface of a corner isolator) to ensure

stable friction behavior. The weights were distributed so that the mass on the roof level was half of that on the other two levels.

The coupons in the REPEAT frame clevises were sized so that the frame would have an *R* factor (ductility factor) of 1 under beyond maximum considered event loads. For these experiments, the base shear was taken as the force after impact of the TFP bearings, just under 0.4 g. It should be noted that this experiment represents a specific design strategy in which the building is protected even at as the bearings fail. Both current and future versions of ASCE 7 (ASCE 2010) aim to maintain essentially elastic behavior up until a maximum considered event (Mayes 2014), but this would result in a base shear of less than 0.3 g for the bearings used in these tests.

The forces in the superstructure were distributed using the linear distribution prescribed in ASCE 7-10. To provide a rigid diaphragm above the isolators, three pairs of coupons with the maximum diameter were used in the Level 1 Beam clevises. All other locations had only one pair of coupons; the diameters at each location are listed in Table I-2. The coupon sizes were calculated using a yield stress of 635 MPa, found from a subassembly test of a simple clevis and column-set up. The column coupon diameters were increased so that they were just greater than those in the Level 2 Beams. The first and second fixed base periods of the superstructure are approximately 0.43 s and 0.14 s, which were found by matching a numerical model to the experimental data.

Table I-2 REPEAT frame coupon diameters

	Column	Level 1 Beams	Level 2 Beams	Roof Beams
Coupon diameter (mm)	15.1	19.1	14.7	10.3

2.2 Instrumentation

Multi-axis loads cells were places below each isolator to measure axial loads and shears at the base of the specimen. Accelerometers measuring horizontal acceleration were located at every floor level used to find story shear forces. Strain gages applied to the columns were used to find moments, from which the story shear forces were calculated to verify those found from the accelerometers. Horizontal displacements were measured at each joint using a pair of diagonal wire potentiometers. All the sensors were sampled at 200 samples/s and filtered at 80 Hz to reduce signal noise.

2.3 Input Motions

Three ground motions were used to investigate the behavior of the structure, listed with their design basis event (DBE) and maximum considered event (MCE) scaling factors in Table I-3. These levels correspond to earthquakes with 10% and 2% probability of exceedance in 50 years respectively. In addition, the ground motions were used with a time scale of $\sqrt{3}$ to match the length scaling of the specimen. The ground motions were scaled to a uniform hazard spectrum at site in Oakland, CA (Baker et al. 2011) but then reduced by 25%, corresponding to the bearing sliding capacity, so that in an MCE level motion the TFP bearings would have significant residual displacement before hardening phase. The fault normal component of each motion was used.

The expected displacement under MCE level motions, predicted using equivalent bearing properties with the uniform hazard spectrum, was roughly 120 mm. At this displacement the equivalent damping in the bearing is 27%. This large damping value is

due to the large friction coefficient (0.13) on the outer sliders. At the DBE displacement, 45 mm, the equivalent damping is even higher at 36%.

Table I-3 Ground motions

Earthquake	Station	DBE Scaling	MCE Scaling	Pulse Period (model
Superstition Hills, 1987	Westmoreland Fire Station	1.75	2.91	-
Northridge, 1994	Jensen Filter Plant	0.71	1.2	2.0 s
Loma Prieta, 1989	Gilroy Array #4	1.70	2.88	-

3 Numerical Model

There are several existing analytical models (Becker and Mahin 2012; Fenz and Constantinou 2008) capable of describing the complex behavior of triple friction pendulum bearing under seismic excitations. These analytical models may be adequate to describe the bearing behavior under regular conditions; however, they do not consider the extreme behavior of the bearing including impact and uplift. In order to investigate these extreme behaviors in triple friction pendulum bearings, a rigid body model originally developed by Sarlis and Constantinou (2013) is used in which the horizontal, vertical and rotational momentum of each sliding component is considered. This analytical model is the only currently available model which can simulate the impact and uplift behavior directly. However, the model uses linear springs to simulate the impact force, resulting in no energy dissipation during impact. To account for energy loss, the linear spring model is replaced by Hertz's contact law with non-linear damping (Muthukumar and DesRoches 2006) in which the damping is related nonlinearly to the penetration depth and velocity; more details regarding this modification can be found in Bao et al. (2017). Numerically,

failure is triggered when the vertex of one slider displaces beyond the opposite vertex of the adjacent slider. The top and bottom of the bearings are modeled as rigidly connected to the frame and shake table, respectively.

The superstructure is also modeled nonlinearly. Since, the rigid body model of the bearing element is implemented in state-space form, the superstructure is also implemented in state-space form. Simeonov et al. (2000) used this approach to analyze the seismic response of a planar frame by formulating the beam element in flexibility-based method (i.e. force interpolation). Within the framework of the flexibility-based method, Sivaselvan and Reinhorn (2000) developed a Bouc-Wen model that incorporates deteriorating properties of the structure. Using the flexibility-based method results in a DAE (differential algebraic equation) system rather than an ODE (ordinary differential equation) system; however, the DAE system is more difficult to solve by standard mathematical software program (e.g. Matlab) compared to the ODE system. Thus, in this study, a stiffness-based method (i.e. displacement interpolation) is adopted for the formulation of a two-dimensional Euler-Bernoulli beam element in state-space form, following the formulation of Triantafyllou and Koumousis (2012). The only modification made in the formulation is that instead of using interpolating hysteretic parameters across the beam, they are treated as independent state variables. By assigning appropriate inertia components, this formulation results in an ODE system.

The numerical model of the isolated frame is schematically depicted in Figure I-4. As the experiments were conducted unidirectionally, only a single frame was modeled. Each coupon is considered as a concentrated plastic hinge and described by a Bouc-Wen

model with degrading hysteretic properties. In this formulation, small deformations are assumed, and only the bending moment behavior includes deteriorating properties while other behaviors (e.g. axial behavior) are assumed to be linear. The masses from the concrete blocks and lead plates at each element are assumed equally distributed at the two beam-end nodes; the solid dots in Figure I-4 represent these concentrated masses.

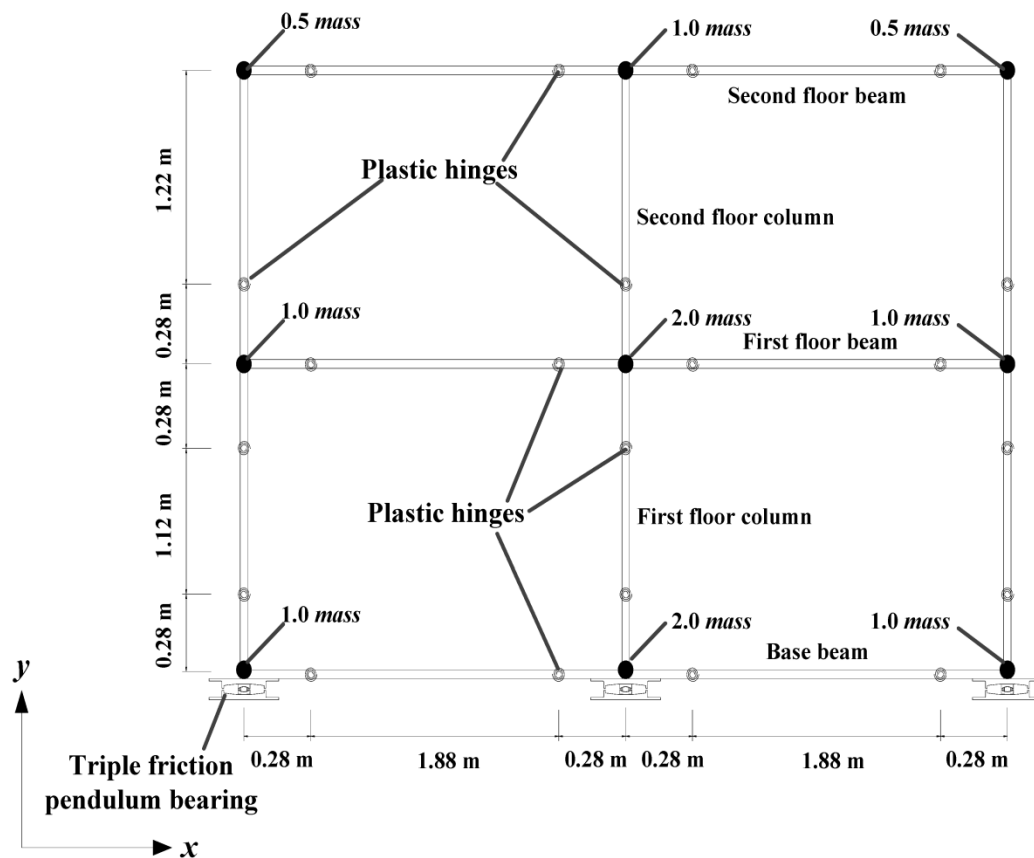Figure I-4 Illustration of numerical model of the isolated frame

The accuracy of this model primarily depends on to what extent the Bouc-Wen model can represent the nonlinear behavior of the clevises with coupons. Before the full experiments were conducted, tests of a single column-clevis subassembly with various sized coupons were conducted to find the moment-rotation behavior of the connection.

The test using coupons with 5/8 inch (15.9 mm) in diameter were selected to calibrate the Bouc-Wen model as this diameter was the closest to the coupons installed in the actual isolated frame. Experimental results for the single clevis behavior are compared with the numerical clevis in Figure I-5.
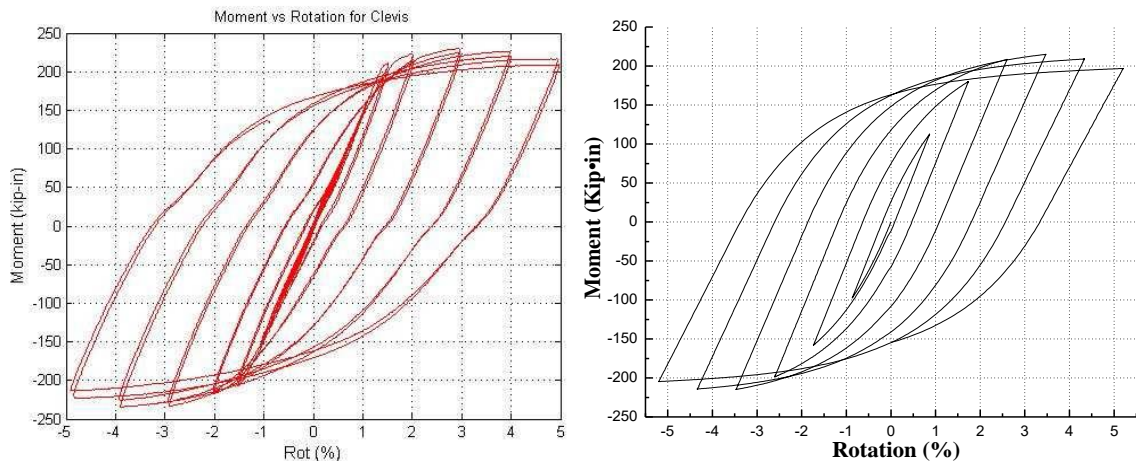

Figure I-5 Comparison between clevis experimental behavior (left) and numerical model (right) for 5/8 inch (15.9 mm) coupons

3.1 Validation with experimental results

The bearing and story drift time histories found numerically are compared against the experimental results in Figure I-6 to Figure I-8 for the MCE motions. The peak story drifts for all experimentally run motions are compared against the numerical predictions in Figure I-9. It can be seen that, for the majority of motions, the model accurately predicted the behavior of the isolation layer. However, after the first peak, the model did significantly under predict the subsequent peaks for the MCE level of the Northridge motion. Story drifts were generally under predicted by the numerical model, particularly for the 1st story. In general, these predictions improved with increased ground motions intensity, with very close predictions for the MCE level and beyond Loma Prieta motions.

In the experimental tests, all three ground motions were run at their DBE and MCE scalings. Afterwards, the Loma Prieta motion was run at 120% MCE, 140% MCE, and finally 160% MCE. As in the experimental testing, the numerical model predicts bearing failure in the 160% MCE level Loma Prieta, while impact (reaching the ultimate displacement of the bearings) was neither experimentally observed nor numerically predicted under the 140% MCE level.
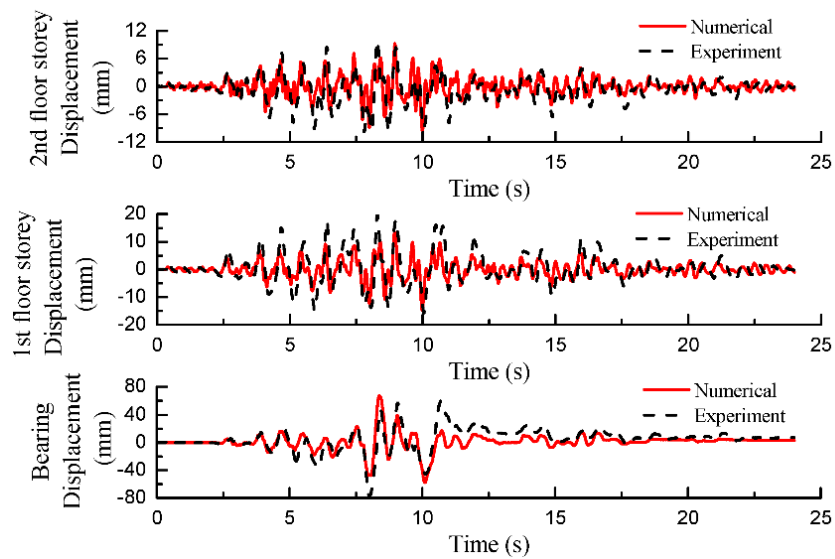

Figure I-6 Drifts under the Superstition Hills MCE level
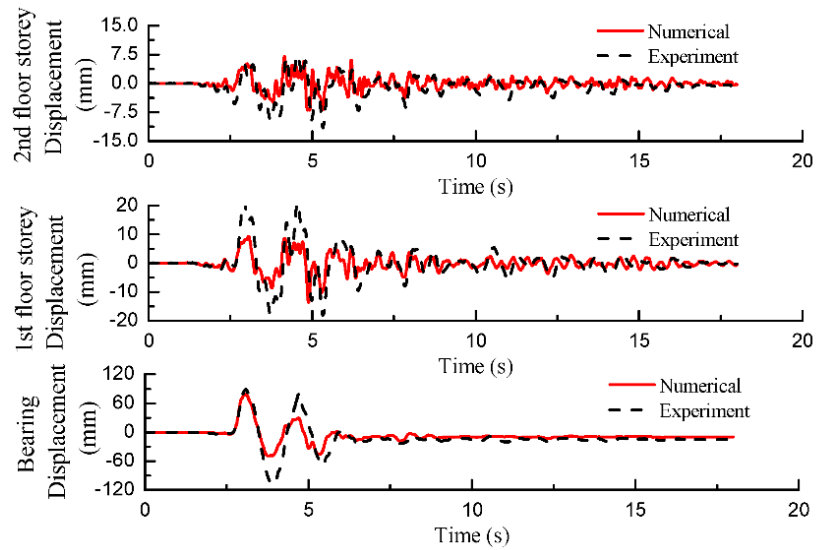
Figure I-7 Drifts under the Northridge MCE level
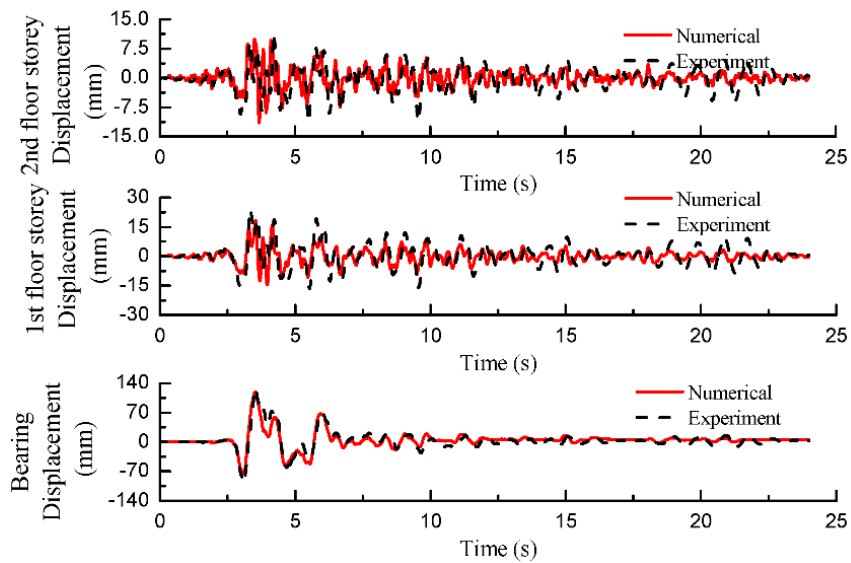
Figure I-8 Drifts under the Loma Prieta MCE level
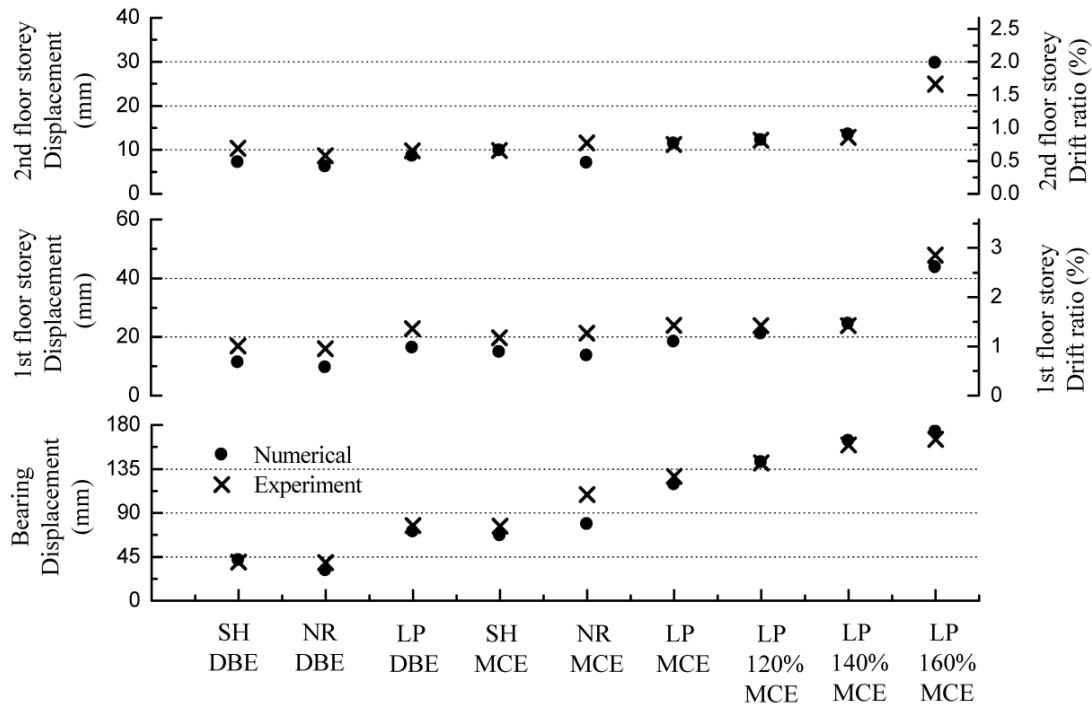
Figure I-9 Comparison of peak relative story drifts for all motions

4 Ultimate Behavior

4.1 Experimental observations

In the experimental testing, failure of the isolation layer occurred during the 160% MCE

level of the Loma Prieta motion. Due to the high design base shear for the superstructure

there was negligible permanent drift in the frame. The six bearings are shown post-failure

in Figure I-10. Bearing 1 is located on the South East corner all other bearings in the

figure correspond to their relative layout in the experiments; Bearings 1, 3, and 5

supported the South frame and Bearings 2, 4, and 6 supported the North frame.

While holes were provided for eight 3/8 in (9.5 mm) diameter bolts to connect the

bearings, only four were used. As seen in Figure I-10, in Bearings 1, 3 and 5, the bolts

connecting one of the outer plates sheared off and the outer plate of the bearing slid. This

has been proposed by some researchers as a potentially desirable behavior for friction pendulum bearings under extreme loading. In theory, this would allow the bearing to continue to displace beyond its ultimate capacity, adding a final cushion to protect the bearing and limit the force transferred to the superstructure. While this is sound reasoning, the test results illustrate potential issues that should be considered. Perhaps obviously, the bolts of the top outer plate should not be allowed to shear; a loss of this connection will result in the collapse of the bearing (Bearing 5) at best and the outer plate flying out (Bearing 3, see top plate and sliders sitting on shake table) at worst.
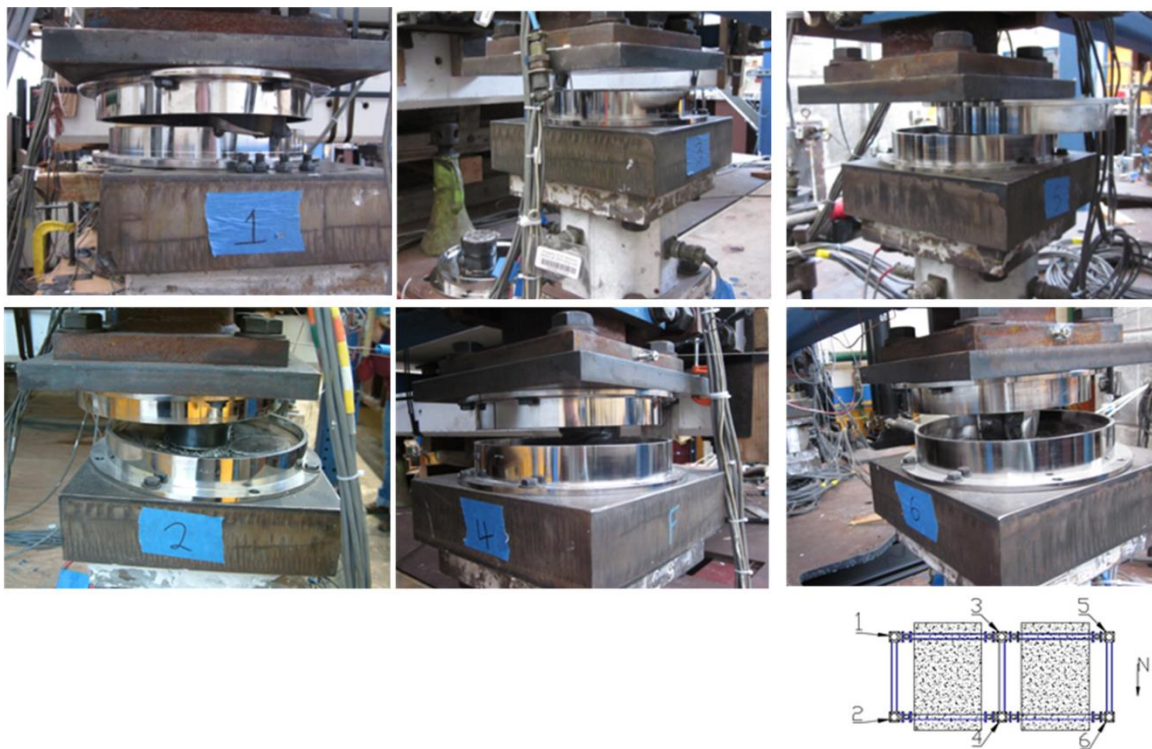

Figure I-10 TFP bearings post-failure. Arrows on the plan-view indicate the direction from which the

picture was taken

Detailed video was taken of Bearing 1. Still frames from the bearing at ultimate behavior are shown in Figure I-11. For this bearing, uplift of the top plate occurred

immediately after impact and the inner sliders, connected by their rubber seal, rotated. This uplift behavior is caused by the force couple exerted on the sliding components during impact (Bao et al. 2017). As the top plate came back down, the restraining rims of the top and bottom outer plates helped to separate the inner sliders, which then became sandwiched. After the bearing was seated, the resisting force in the bearing increased as sliding was no long possible. Thus, stiffness increased, and on the return motion the bolts on the bottom plate sheared. The bottom plate then slid relative to the pedestal until motion stopped. From this, it is clear that to avoid damage to the bearing by bolt shearing, the bolt connection must be designed so that shearing occurs at forces significantly lower than would cause uplift behavior. If the bottom plate is designed to shear (Bearing 1), the bearing pedestal must have adequate area to accommodate the sliding displacement.
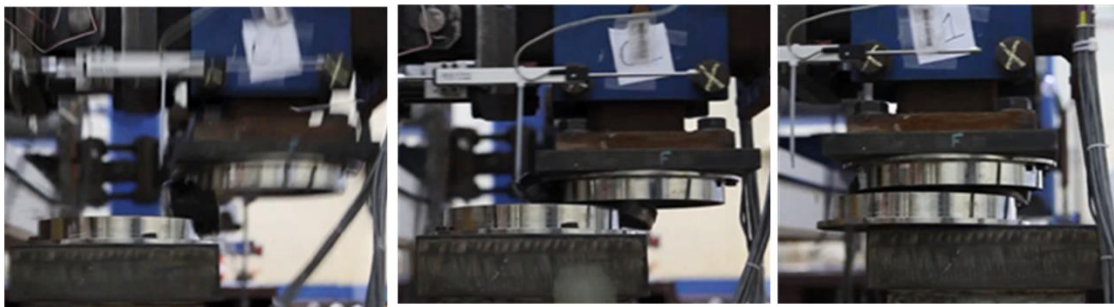
Figure I-11 Ultimate behavior sequence of Bearing 1, left to right: uplift of bearing and rotation of inner sliders; separation of inner bearing components; shearing of bottom plate bolts on the return motion

In Bearings 2, 4, and 6, the connection bolts did not shear. In sliding bearings, the shear force is proportional to the axial load. Before loading, Bearing 3 had the highest axial load (108 kN vs 86 kN on Bearing 4). As a result, bolt shearing occurred first in Bearing 3. After losing the top outer plate, Bearing 3 could no longer support load, and the axial load was redistributed so that it was supported solely on Bearings 1, 4, and 5.

This pattern is most likely due to the loss of the top plate in Bearing 3 completely eliminating its axial load carrying capacity. The diaphragm layer was sufficiently stiff to transfer the loads to the adjacent bearings. However, even a small amount of bending in the frame due to the support removal at Bearing 3 brought the loads on Bearings 2 and 6 to nearly zero. With higher axial loads, the shear forces in Bearings 1, 4, and 5 increased and the bolts sheared in Bearings 1 and 5. It is unclear why Bearing 4, which ultimately reached the highest shear forces of all the bearings, did not have bolt shearing. However, the restraining rim of Bearing 4 did have a small amount of residual deformation from yielding. In Bearing 6 the inner sliders turned on their side, and in Bearings 2 and 6 the frictional surfaces on the sliders detached (Figure I-10). Of all the bearings, only Bearing 4 would potentially be immediately reusable.

Due to the high base shear used in the design of the superstructure, after the bearings failed, the superstructure remained upright. During the motion that resulted in bearing failure, the peak shear force in the isolation layer, V_b, was measured as 408 kN, roughly 107% of the weight of the structure. However, the maximum shear force at the first floor of the superstructure, V_s, was 143 kN, 35% of the isolation layer shear. For the 140% MCE motion this ratio of V_s to V_b was 77%, indicating that the impact force is not fully transferred to the superstructure most likely due to the short pulse duration. Under the 140% MCE motion ($V_s = 95$ kN), the peak story drifts of the 1st and 2nd floors were 1.5% and 0.7% respectively and there was no residual displacement. During the 160% MCE motion, the drifts increased to 2.9% and 1.7% respectively, with residual drifts of

0.2% and 0.3%. While large drifts were reached, the behavior of the superstructure remained stable and only minor yielding was observed.

4.2 Numerical results

As in the experimental testing, the numerical model shows that failure occurred in the isolation layer with minimal yielding in the superstructure. The numerical model was run at increasing levels of excitation at 5% increments. The model predicts that impact of the bearings occurs under a 145% MCE level of the Loma Prieta motion, but that bearing failure does not occur until 160% MCE. The ultimate behavior sequence of the TFP bearings under the 160% MCE level motion, predicted by the model is shown in Figure I-12. The numerical model does not include the bolted connections of the bearings and thus cannot capture the bolt shearing observed in the experiments. In addition, the model does not include the rubber gasket surrounding connecting the inner sliders; however, the gasket is unlikely to result in changes in the predicted behavior of the numerical model.

Similarly to the experiments, the behavior varies across the bearing plane. This variation in behavior is caused by the overturning moments in the superstructure that decreased the pressure in Bearing 1 and increased the pressure in Bearing 5 directly before impact. After impact, the bearings rebound, as in the experiment. Bearing 1 experiences large uplifting behavior during which the internal bearing components rotate. Eventually, the restrainer of the top outer slider displaces beyond the vertex of the adjacent slider. This signals failure of the bearing in the analysis. While the exact bearing failure mechanism is not predicted, the model does predict the magnitude at which

bearing failure occurs and the non-uniform behavior of the bearings across the isolation plane.

For the numerical model, the peak force predicted in the isolation layer during ultimate behavior of the bearing is 455 kN, 12% greater than measured in the experiments. The maximum shear force at the first floor of the structure was predicted to be 150 kN, 33% of the isolation layer. This is in very good agreement with the experimental testing where the ratio of isolation layer force transferred to the structure was 35%.

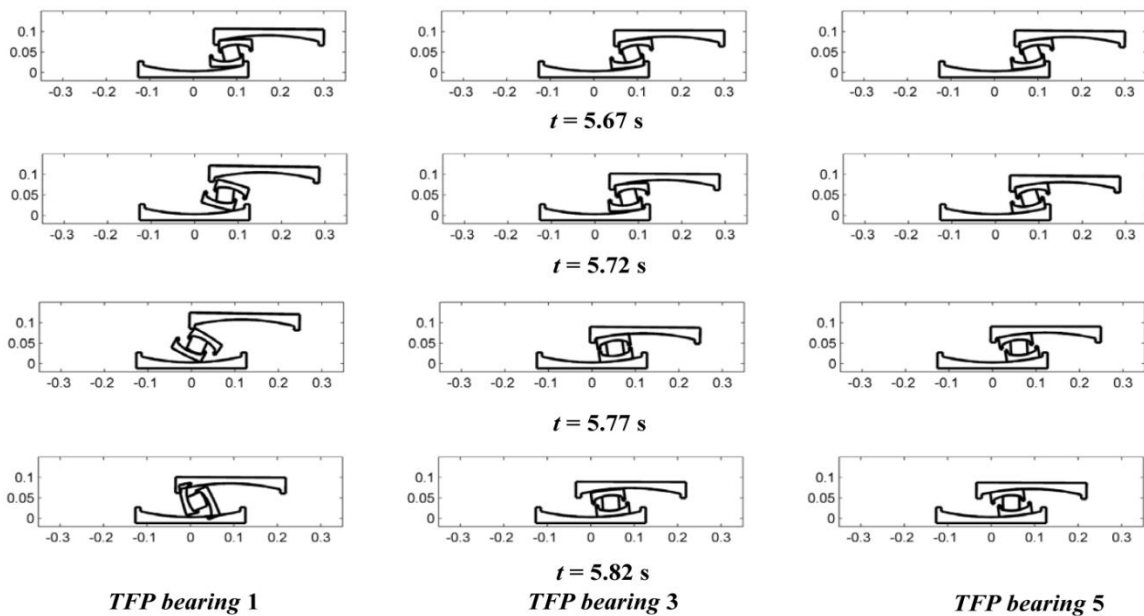Figure I-12 Sequence of modeled TFP bearing ultimate beahvior under 160% MCE level Loma Prieta motion

4.3 Effect of bearing hardening stage

There are two major reasons behind the final stiffening stages of the TFP bearing: (1) to gradually transfer forces to the superstructure rather than impart an impact force and (2) to delay impact and significantly decrease the velocity when impact occurs. To evaluate

the effect of the TFP bearing stiffening stage on the extreme behavior of the system, three

alternate designs for the bearing were explored while leaving the superstructure design

unchanged. For all designs, the backbone curve of the bearing prior to the hardening

stage was unchanged. The first design allowed the hardening stage to continue for twice

the distance, from 9 mm in the original design to 18 mm; to do this the outer diameter of

the bearing had to be increased by 12 mm. The second design eliminated the hardening

stage, but retained the same displacement capacity of the original bearings; to achieve

this the inner slider was designed to reach its maximum displacement as sliding

transitioned to the outer sliders, in between the first and second sliding phase. The final

design again eliminated the hardening phase but elongated the displacement capacity to

match the elongated hardening bearing. The backbone curves for the two altered designs
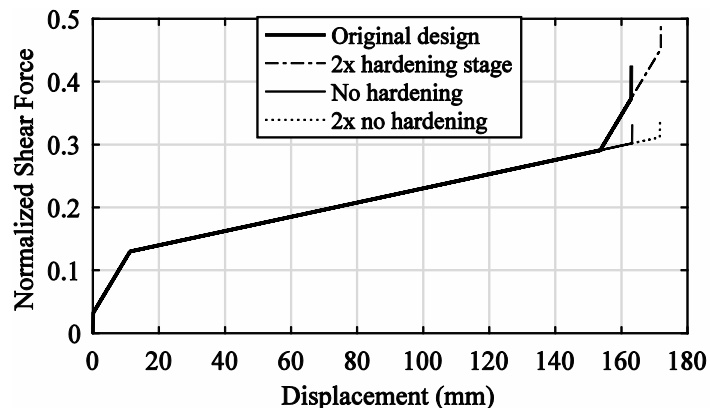
are shown in Figure I-13.

Figure I-13 Backbone curve of the original and modified bearing designs

Intuitively, the hardening phase should delay both impact and bearing failure.

However, the analysis did not corroborate this. For no hardening design, impact occurred

at the same earthquake level (145% MCE) as the original design. Where the original

design failed at 160% MCE, the no hardening design continued until 170% MCE. Comparing the axial load time histories of the two systems, the bearing without hardening had less fluctuation in load. One possibility is that the increase in bearing forces causes larger overturning moments, reducing bearing axial loads and leading to uplift in the bearing components. The extended displacement bearings with and without hardening are also compared. Without hardening, impact occurred at 150% MCE. Including the hardening phase increased this to 155% MCE. However, both bearing designs failed at 175% MCE. Thus, for the ground motion investigated here, the hardening phase was not effective at delaying bearing failure for either the original or extended displacement designs.

The top row of Figure I-14 shows relative velocity of the base of the superstructure at the instant when the bearing reaches 154 mm (the point at which hardening occurs in the original design) and at impact for all of the bearing designs. For the original displacement capacity designs, there was no little difference in the reduction of velocity between the bearings with and without hardening, indicating the hardening phase was not effective at slowing the structure. However, this is not true when the displacement capacity was extended. For these bearings, the hardening phase was significantly reduced the velocities of the structure at impact. While this did not increase the bearing's ability to avoid failure, it did decrease the bearing forces at impact, shown in the bottom row of Figure I-14.
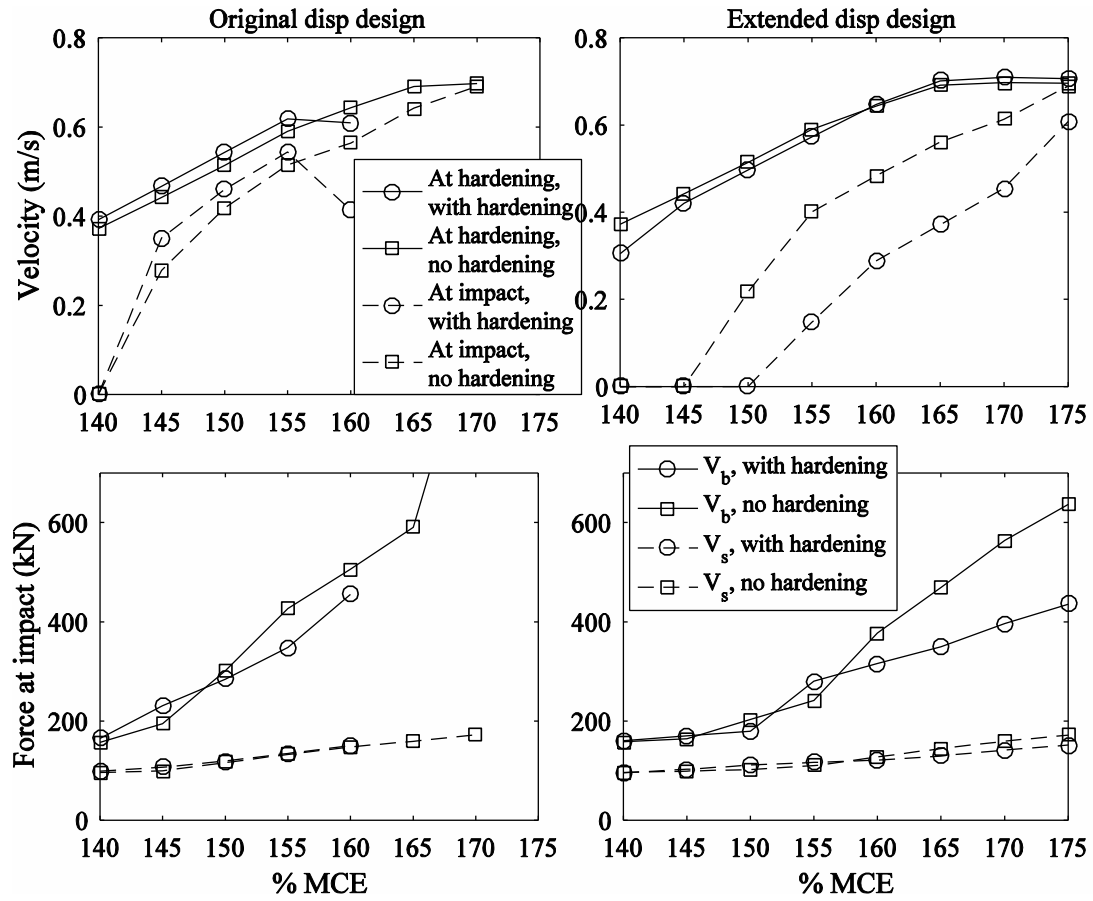
Figure I-14 Top row: Velocity at initiation of hardening (or the same displacement for bearings without the hardening phase) and at impact for different bearing designs. Zero velocity indicated that the bearing did not research ultimate displacement. Bottom row: Force at impact at the isolation layer (V_b) and at the base of the superstructure (V_s) for different bearing designs

Before discussing the bearing forces, it should be noted that the values are highly dependent on modeling assumptions. The Hertz contact law used in the TFP modeling has an associated penalty stiffness associated with the amount of displacement beyond the restrainer limits. If the stiffness is too small, the model predicts very large, unrealistic penetration of the sliders with the restrainers. If the stiffness is too big, the impact force predictions become unrealistically large. For this study, the impact stiffness ($1x10^9$

N/m$^{1.5}$) was found through comparison with experimental test results, and reflects a middle value. While, the penalty stiffness does not significantly alter the ultimate behavior of the bearings (whether or not the bearings fail), it does have a direct impact on the forces predicted by the model. Thus, the exact forces presented may not be accurate, but the trends are useful.

Including the hardening phase in the bearing design reduces the impact forces that occur when the bearing reaches its maximum displacement. This is particularly noticeable for the elongated bearing designs. The impact force is directly tied to the impact velocity. As the velocity reduction was greater for the elongated displacement bearings, the same holds true to force. However, reducing the bearing forces had little impact on reducing the superstructure forces the forces were almost identical under motion levels in which hardening without impact occurred. When impact occurred, the structure forces with the bearings with no hardening were larger for some of the motion levels but were within 10% of the hardening bearing forces. This means that, as in the experiments, the large impact forces were not fully transferred due to the short duration of impact forces. At bearing failure, the yield force of the superstructure was reached in all bearing design scenarios.

From this study, the benefits of the hardening phase of the TFP bearing are not strong. The hardening phase may reduce the impact forces experienced by the bearing, which will directly affect the design of the attaching components; however, this is only true when the hardening phase is sufficiently long. For the original bearing displacement capacity, the hardening was actually detrimental to the bearing failure, but this result

requires further investigation before it should inform design decisions. One clear and straight forward conclusion is the benefit of increasing the bearing displacement capacity; here, increasing the diameter of the bearing by 5% resulted in a 10% increase in bearing amplitude before failure occurred in the isolation level.

5 Force Distribution

In previous iterations of the ASCE code, isolated superstructures designed with equivalent static forces F were designed with a linear distribution ($k = 1$) in the standard force distribution equation

$$F_i = V_s \frac{w_i h_i^k}{\sum w_i h_i^k} \tag{1}$$

where w is the weight of the floor, h is the height of the floor, and V_s is the base shear experienced by the superstructure. Considering typical first mode behavior in a linear isolation system, a more appropriate distribution would have $k = 0$ as accelerations would be equal at all floors. However, most isolation systems incorporate nonlinear behavior increasing higher modes. York and Ryan (2008) used a parametric numerical study with a range of nonlinear isolation systems and superstructure properties and proposed $k = 13\xi T_s$, where ξ is the equivalent damping in the bearing and T_s is the fixed-base period of the superstructure, as better representative force distribution.

York and Ryan (2008) also proposed an approximation for the relationship for the superstructure base shear, V_s, to the shear in the isolation layer, V_b. The difference between V_s and V_b is the inertia force of the level directly above the isolators. Assuming linear isolation behavior, this ratio would be proportional to the relationship of the masses: M_s representing the weight of the superstructure minus the floor directly above the

isolation system and M the total weight of building. However, due to nonlinear behavior in the isolator York and Ryan (2008) proposed a relationship

$$\frac{V_s}{V_b} = \left(\frac{M_s}{M}\right)^{(1-\alpha\xi)} \tag{2}$$

where α is 2.2. A modified version of both the ratio of the forces and the force distribution in the superstructure is incorporated ASCE 7-16 (Mayes 2014). The isolation models used to derive these relationships are bilinear; they do not incorporate any hardening as is seen at large displacements in the triple friction pendulum bearing or high damping rubber bearing nor do they investigate impact or bearing failure. Masroor and Mosqueda (2014) experimentally found increased forces in an isolated superstructure when the building impacted a moat; however, the ratio of forces was not investigated.

Ratios of V_s to V_b normalized by the ratio of M_s to M (0.6 for the structure) are shown in Figure I-15 for experimental and numerical results as well as the theoretical values from Eq. 2. To validate the experimental data, the ratio of the sum of the floor inertia forces to the load cell shear. The ratio ranged from 0.91 to 1.05 with an average of 0.99 for all motions excluding the 160% Loma Prieta motion where the ratio was 1.15, showing general agreement between sensor data. The results of $(V_s/V_b)/(M_s/M)$ from the Loma Prieta motion show a downward trend as the bearing displacement increases. As the displacements increase, the damping decreases and V_s/V_b decreases towards M_s/M. Thus, Eq. 2 well predicts this trend. The numerical results for the Loma Prieta motion consistently under predicted the force ratio (causing the under prediction of superstructure displacements seen in Figure I-9) but showed the same trends; even as the bearing entered the hardening region the ratio stayed just above M_s/M. However, for

earthquake magnitudes which resulted in bearing impact, the ratio of force transferred to

the superstructure decreased below M_s/M and continued to decrease until bearing failure.

The trends of V_s/V_b were true for all of the numerical bearing designs investigated in the

previous section, including bearings both with and without hardening regions. This

decrease in V_s/V_b was not due to yielding of the superstructure, as the superstructure did

not reach yield forces until penultimate motion (e.g., 155% MCE in the numerical results
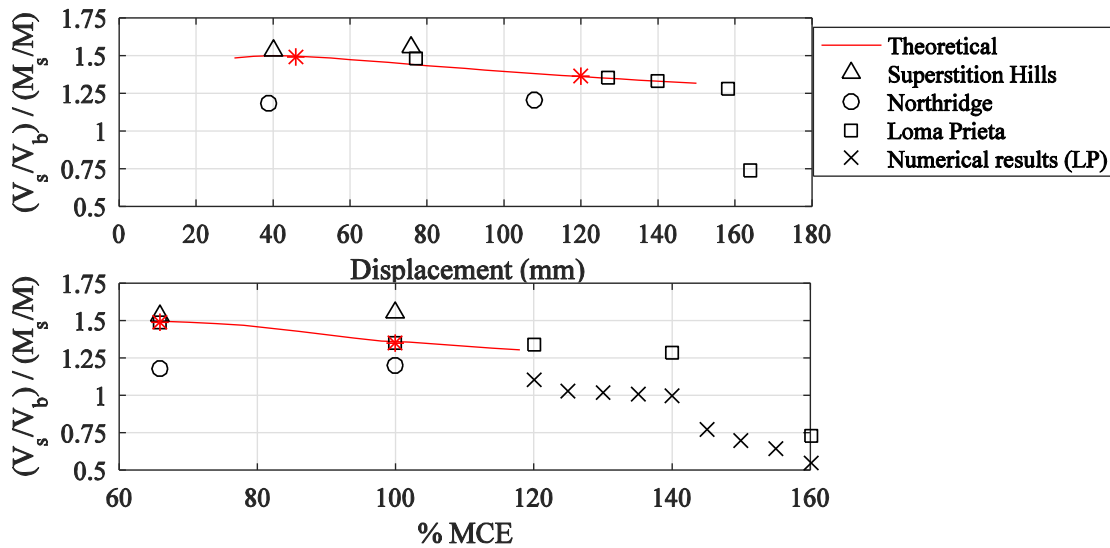
presented in Figure I-15).

Figure I-15 Theoretical, experimental, and numerical results for the ratio of the superstructure shear to the

isolation layer shear versus bearing displacement (top) and % MCE (bottom)

The ratio of the second floor shear force V_2 to the superstructure shear force V_s are

shown in Figure I-16. The predictions from Eq. 1 are plotted as well; for the DBE level k

$= 1.96$, and for the MCE level, when the damping is lower, $k = 1.5$. For this set up, Eq. 1

and the numerical model over predicted the ratio of the force transmitted to the second

story. If the acceleration were constant at each floor, the value of V_s/V_b would be 0.33,

proportional to its mass. The experimental results which hover around 0.5 show a force

distribution to be in-between those predicted in Eq. 1 and the constant acceleration case. Designing to Eq. 1 may potentially be an issue if the superstructure was allowed to yield as over designing upper floors could lead to a soft story mechanism.
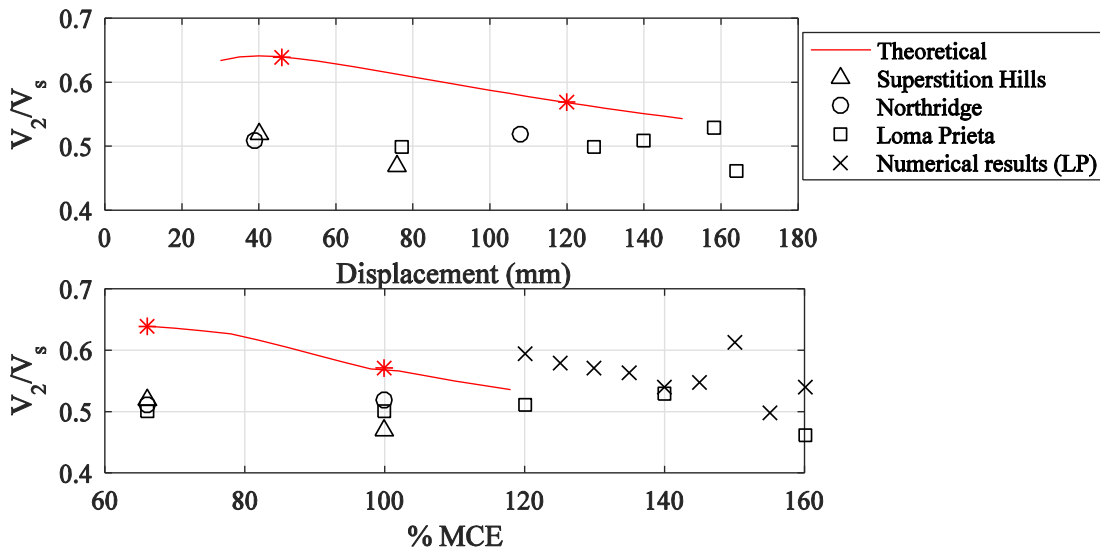

Figure I-16 Theoretical, experimental, and numerical results for the ratio of the second story shear to the superstructure shear versus bearing displacement (top) and % MCE (bottom)

The ratio of V_2/V_s for the increasing magnitudes of the Loma Prieta motions for all of the alternate bearing designs considered in the previous section are presented in Figure I-17. For both the original design and the extended hardening region design, the hardening stage was reached at 135% MCE. The magnitude at which each bearing design first reached the ultimate displacement is circled. The results show that the ratio decreases as the bearing displacement increases, as Eq. 1 would predict due to decreasing equivalent damping. Interestingly, initiation of the hardening stage does not affect this trend. After impact, the bearings without the hardening stage have consistently higher ratios of V_2/V_s. This may indicate that the impact force without the transitional hardening stage is exciting higher modes in the structure.
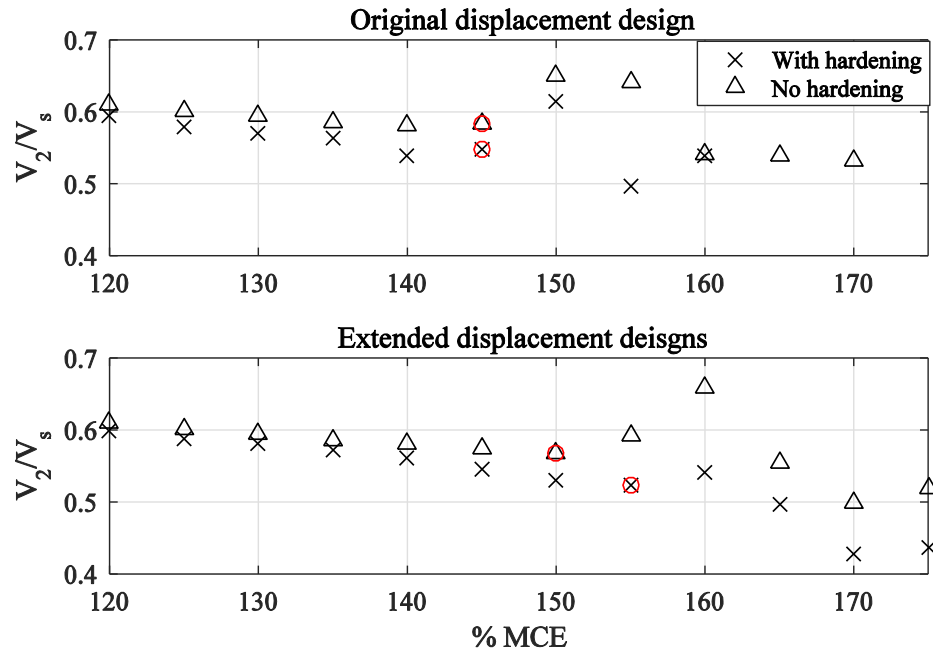
Figure I-17 Numerical results for the ratio of second story shear force to superstructure shear for increasing

levels of the Loma Prieta ground motion considering the four bearing designs presented in the previous

section

6 Conclusions

To investigate the behavior of TFP isolated structures in extreme earthquake loading, a

unidirectional test was conducted on a two story two bay frame. As the superstructure

was designed with a large base shear, failure occurred in the isolation layer. The ground

motions were scaled so that the bearing displacement did not reach the hardening stage in

the MCE level event. The bearings failed under the 160% of the MCE level motion, far

beyond design expectations. The experiments found varying behavior across the isolation

plane, with each bearing exhibiting a unique post-failure behavior. Shearing of

connecting bolts played a large role in the bearings' failure mechanisms. A major, and

perhaps obvious, takeaway is that the bolts at the top of the bearing should not be

designed to fail as the motion of the plate after bolt shearing is difficult to predict and complete loss of the top plate would result in loss of the bearing's load carrying capacity. All but one of the bearings was non-functional after the isolation system failure. However, in most cases the only the inner sliders would need to be replaced; of course, if the bolts for the top or bottom sheared, the plate would have to be reinstalled.

A numerical model was developed to investigate the effect of the bearing design on the isolation layer failure. While the force transferred into the superstructure and resulting superstructure drifts were under predicted, the overall performance of the model was good. The effect of the bearing hardening stage was investigated by looking at four different bearing designs, two with hardening stages and two without with different displacement capacities. It was found that the hardening stages decreased the velocity at impact, and thus decreased the force in the isolation layer at impact. However, the force transmitted into the superstructure was not reduced by including the hardening stage. Also, the hardening stage did not delay failure in the isolation layer.

Lastly, changes to how superstructures shear forces are calculated in ASCE 7-16 were compared against the forces observed both experimentally and numerically. It was found the code predicted ratio of the force transferred to the superstructure to the force in the bearing level was a good estimate for the DBE and MCE motions. This was true even when the bearings reached their hardening range. However, after impact, outside of the scope addressed by the code, there was a reduction in the ratio of forces transmitted to the structure. This reduction continued as the impact force became larger. The distribution of the superstructure shear forces over the first and second floor was less well predicted by

the updated code provisions, but was also poorly predicted by the model. However, the model found that the addition of the hardening stage had a significant effect on the forces transmitted to the upper story when bearing rim impact occurred.

Acknowledgements

References

American Society of Civil Engineers (2010). Minimum Design Loads for Buildings and Other Structures. Standard ASCE/ SEI 7-16: Reston, VA.

Baker JW, Lin T, Shahi SK and Jayaram N (2011). New ground motion selection procedures and selected motions for the PEER transportation research program. Report No. PEER 11/03, Pacific Earthquake Engineering Research Center, University of California, Berkeley, CA.

Bao Y, Becker TC and Hamaguchi H (2017). Failure of double friction pendulum bearings under pulse-type motions. *Earthquake Engineering Structural Dynamics*, 46: 715-732.

Becker TC and Mahin SA (2012). Experimental and analytical study of the bi-directional behavior of the triple friction pendulum isolator. *Earthquake Engineering and Structural Dynamics*, 41: 355-373.

Buckle IG, Nagarajaiah S and Ferrell K (2002). Stability of elastomeric isolation bearings: experimental Study. *Journal of Structural Engineering*, 128(1):3–11.

Cardone D and Perrone G (2012). Critical load of slender elastomeric seismic isolators: an experimental perspective. *Engineering Structures*, 40:198–204.

Cutfield M, Ryan K and Ma Q (2016). Comparative life cycle analysis of conventional and base isolated buildings. *Earthquake Spectra*, 32(1): 323-343.

Erduran E, Dao ND and Ryan KL (2011). Comparative response assessment of minimally compliant low-rise conventional and base-isolated steel frames. *Earthquake Engineering and Structural Dynamics,* 40: 1123-1141.

Federal Emergency Management Agency (2009). Quantification of Building Seismic Performance Factors, Chapter 10.3. FEMA P695: Washington DC.

Fenz DM and Constantinou MC (2007). Spherical sliding isolation bearings with adaptive behavior: Experimental verification. *Earthquake Engineering and Structural Dynamics*, 37(2):185–205.

Fenz DM and Constantinou MC (2008). Modeling triple friction pendulum bearings for response-history analysis. *Earthquake Spectra*, 24(4): 1011-1028.

Han X and Warn GP (2014). Mechanistic model for simulating critical behavior in elastomeric bearings. *Journal of Structural Engineering*, 141(5): 04014140.

Kumar M, Whittaker AS and Constantinou MC (2015). Experimental investigation of cavitation in elastomeric seismic isolation bearings. *Engineering Structures*, 101:290-305.

Masroor A and Mosqueda M (2012). Experimental simulation of base-isolated buildings pounding against moat wall and effects on superstructure response. *Earthquake Engineering and Structural Dynamics*, 41: 2093-2109.

Masroor A and Mosqueda M (2013). Impact model for simulation of base isolated buildings impacting flexible moat walls. *Earthquake Engineering and Structural Dynamics*, 42: 357-376.

Masroor A and Mosqueda M (2015). Assessing the collapse probability of base-isolated buildings considering the pounding to moat walls using the FEMA P695 methodology. *Earthquake Spectra*, 31(4): 2069-2086.

Mayes RL (2014). The next generation of codes for seismic isolation in the United States and regulatory barriers to seismic isolation development. *Proceedings of the 10th US National Conference in Earthquake Engineering*. Anchorage, Alaska, July 21-25.

Morgan TA (2008). The use of innovative base isolation systems to achieve complex seismic performance objectives. Doctoral Dissertation, University of California, Berkeley.

Montuori GM, Mele G, Marrazzo G, Brandonisio G and De Luca A (2016). Stability issues and pressure–shear interaction in elastomeric bearings: the primary role of the secondary shape factor. *Bulletin of Earthquake Engineering*, 14(2):569–97.

Monzon EV, Buckle IG and Itani AM (2016). Seismic performance and response of seismically isolated curved steel I-girder bridge. *Journal of Structural Engineering*, DOI: 10.1061/(ASCE)ST.1943-541X.0001594.

Muthukumar S and DesRoches R (2006). A Hertz contact model with non-linear damping for pounding simulation. *Earthquake Engineering and Structural Dynamics*, 35:811-828.

Sarlis AA, Constantinou M and Reinhorn A (2013). Shake table testing of triple friction pendulum isolators under extreme conditions. Report No. MCEER-13-0011, University at Buffalo, Buffalo, NY.

Sarlis AA and Constantinou MC (2013). Model of triple friction pendulum bearing for general geometric and frictional parameters and for uplift conditions. Technical report MCEER-13-0010, Buffalo, NY, USA.

Sayani PJ, Erduran E and Ryan KL (2011). Comparative response assessment of minimally compliant low-rise base-isolated and conventional steel moment-resisting frame buildings. *Journal of Structural Engineering*, 137(10), 1118-1131.

Sanchez J, Masroor A, Mosqueda G and Ryan KL (2013). Static and dynamic stability of elastomeric bearings for seismic protection of structures. *Journal of Structural Engineering*, 139(7):1149–59.

Sasaki T, Sato E, Ryan KL, Okazaki T, Mahin SA and Kajiwara K (2012). NEES/E-Defense base isolation tests: effectiveness of friction pendulum and lead–rubber bearing systems. *Proc. of the 15th World Conference on Earthquake Engineering*, Lisbon, Portugal.

Simeonov VK, Sivaselvan MV and Reinhorn AM (2000). Nonlinear analysis of structural frame systems by the state-space approach. *Computer-Aided Civil and Infrastructure Engineering*, 15: 76-89.

Sivaselvan MV and Reinhorn AM (2000). Hysteretic models for deteriorating inelastic structures. *Journal of Engineering Mechanics*, 126(6): 633-640.

Simo JC and Kelly JM (1984). Finite element analysis of the stability of multilayer elastomeric bearings. *Engineering Structures*, 6(3):162–74.

Terzic V, Merrifield SK and Mahin SA (2012). Lifecycle cost comparisons for different structural systems designed for the same location. *Proc. of the 15th World Conference of Earthquake Engineering*, Lisbon, Portugal.

Triantafyllou S and Koumousis V (2012). Small and large displacement dynamic analysis of frame structures based on hysteretic beam elements. *Journal of Engineering Mechanics*, 138(1): 36-49.

Vemuru VSM, Nagarajaiah S, Masroor A and Mosqueda G (2014). Dynamic lateral stability of elastomeric seismic isolation bearings. *Journal of Structural Engineering*, 140(8): 4014014.

York, K and Ryan KL (2008). Distribution of lateral forces in base-isolated building considering isolation system nonlinearity. *Journal of Earthquake Engineering*, 12:1185-1204.